Modeling and Control of Multi-Elastic-Link Robots under Gravity

From Oscillation Damping and Position Control to Physical Interaction

DISSERTATION

submitted in partial fulfillment
of the requirements for the degree

Doktor Ingenieur
(Doctor of Engineering)

in the

Faculty of Electrical Engineering and Information Technology
at TU Dortmund University

by

Dipl.-Ing. Jörn Malzahn

Essen, Germany

Date of submission: 10th February 2014

First examiner: Univ.-Prof. Dr.-Ing. Prof. h.c. Dr. h.c. Torsten Bertram
Second examiner: Univ.-Prof. Dr.-Ing. Dr. h.c. Burkhard Corves

Date of approval: 27th October 2014

Preface

Robotics is a fascinating scientific discipline. By developing robots we assemble metal or plastic parts, wires as well as integrated circuits. Through software, we try to equip this assembly of lifeless components with a certain degree of apparent autonomy, which makes it move and interact with our environment. We struggle to convert basic movements and interactions into useful skills enabling e.g. robust locomotion on uneven terrain or dexterous manipulation of arbitrary objects. The harder we struggle, the more exciting becomes the moment, when a robot finally accomplishes some desired task. The struggle also completely changes our everyday perspective on how impressively rapid, easy and reliable humans learn and adapt to the various complex situations in life. Just look at young children starting their first grasping experiments...

When I started studying electrical engineering at TU Dortmund University, my plan was to dive into this fascinating world of robotics with all its facets as a robot developer. While writing these lines I can look back and say the plan seems to have worked out pretty well so far. *It would not have worked out without the continuous unconditional support and patience of my parents Traudel and Hein-Peter Malzahn, for which I am deeply grateful.*

I also thank Prof. Dr.-Ing. Prof. h.c. Dr. h.c. Torsten Bertram for his feedback and forward-looking strategic debates as well as the freedom to develop my work in the direction I wanted and to the extent it finally has.

I would like to thank Prof. Dr.-Ing. Dr. h.c. Burkhard Corves, who agreed to review my thesis as the second examiner. Furthermore I would like to thank Prof. Dr.-Ing. Peter Krummrich for his valuable comments about my work as well as for being the third examiner.

Many thanks go to my colleague Anh Son Phung, not only for all the time we spent working on TUDOR and writing papers together, but also for introducing me into the Vietnamese cuisine.

A person who deserves many thanks is Jan Braun, who is not only a good friend to me. He proved to have a lot of patience with my personal impatience in learning SolidWorks and thought me a lot about mechanical design. He is a reliable source of valuable feedback on my ideas. This also applies to Johannes Krettek, who, as a friend, has played a good devil's advocate so many times.

I am thankful for the friendliness and the comradeship of the remaining staff at the Institute of Control Theory and Systems Engineering (RST). In particular I would like to mention Martin Keller and Malte Oeljeklaus for our discussions and their

Contents

Nomenclature

The following list explains all abbreviations and symbols used throughout this work. In general scalar symbols are represented by normal font letters. Vectors are expressed as bold lower case letters, matrices are indicated by bold upper case letters. If not obvious, coordinate frames of reference are given by leading superscripts to the symbol. For coordinate transformations the leading superscript indicates the original frame, while the leading subscript denotes the target frame. Where required, integration variables are written in Gothic print.

L	general beam length
$\hat{a}_{1...4}$	coefficients of the hyperbolic solution to the beam deflection ODE
$\hat{a}_{5,6}$	coefficients of the solution to the beam temporal ODE
$^{+}\hat{a},\ ^{-}\hat{a},\ ^{+}\hat{a}_n,\ ^{-}\hat{a}_n$	amplitudes of propagating wave and near field components
$^{+}\mathbf{a},\ ^{-}\mathbf{a}$	vectors of rightwards and leftwards directed wave components
$^{+}a,\ ^{-}a,\ ^{+}a_n,\ ^{-}a_n$	wave variables for the propagating wave and near field components
$\mathbf{a}_g$	vector of gravitational acceleration
$\mathbf{C}$	joint referred robot matrix of Coriolis and centrifugal torques
$\mathbf{C}_\varepsilon$	strain referred robot matrix of Coriolis and centrifugal torques
v_c	camera velocity
c_u	modal stiffness
D_u	modal attenuation factor
d_u	modal damping
E	Youngs modulus
$\mathbf{E}$	unit matrix
a_E	end effector acceleration
v_E	end effector velocity
$\mathbf{e}_{uv}$	image space control error
$f_1,\ f_2$	friction model switching functions
f_{ext}	external force density
F_L	load force
f_r	collision reaction frictional parameter
f_u	modal force
$F_x,\ F_y,\ F_z$	force in x-, y- and z-direction
$G(z),\ G(s)$	transfer function in s- or z-domain
G_d	first order filter for the joint velocity

$\mathbf{g}$	joint referred robot vector of gravitational torques
$\mathbf{g}_\varepsilon$	strain referred robot vector of gravitational torques
g	gravitational acceleration
G_B	beam transfer function
G_{CVL}	closed velocity control loop transfer function
G_d	oscillation damping admittance
G_{FIR}	FIR filter transfer function
G_{IIR}	IIR filter transfer function
G_l, ^+G_l, ^-G_l	lumped transfer function
G_M	motor transfer function
G_{PD}	PD controller transfer function
G_{PI}	PI controller transfer function
G_r	collision reaction admittance
H	Heaviside distribution
$\mathbf{I}$	joint referred robot inertia matrix
$\mathbf{I}_\varepsilon$	strain referred robot inertia matrix
u_i	horizonctal image coordinate
v_i	vertical image coordinate
I_l	lumped inertia
I_L	payload volume moment of inertia about the bending axis
I_M	joint rotor and gear moment of inertia
i_M	motor current
$I_z(x)$	area moment of inertia about the z-axis
$\mathbf{J}_c$	image Jacobian matrix
$\mathbf{J}_r$	robot Jacobian matrix
k_ω	wave number
k_{Amp}	power amplifier gain
$\mathbf{K}_c$	visual servoing gain matrix
k_c^+, k_c^-	Coulomb friction coefficients
$k_{dyn,u}$	dynamic modal gain
k_ε	oscillation damping gain
$\mathbf{K}_I$	generalized momentum gain
K_r	rotational spring stiffness at the joint-link boundary
k_l	lumped siffness
k_M	aggregated motor gain
k_{or}	collision overreaction gain
k_{PD}	PD controller gain
k_{PI}	PI controller gain
$\hat{K}_r$	normalized version of K_r
k_r	collision reaction spring parameter
$k_{stat,u}$	static modal gain
K_t	translational spring stiffness at the joint-link boundary
$\hat{K}_t$	normalized version of K_t
k_τ	actuator torque constant
k_v, k_v^+, k_v^-	viscous friction coefficients
l_1, l_2, l_3	lengths associated with the 1st, 2nd and 3rd link body

$\mathbf{L}_c$	hybrid visual servoing interaction matrix
m_L	payload mass
m_r	collision reaction inertial parameter
m_u	modal mass
N_{FIR}	number of FIR filter coefficients
n_l	number of lumped masses
n_M	gear ratio
n_u	number of considered modes
$\mathbf{p}_\varepsilon$	strain referred generalized momentum
$\mathbf{R}$	rotation matrix
$\mathbf{r}_\varepsilon$	direct strain residual vector
$\mathbf{r}_p$	generalized momentum residual vector
s	Laplace variable
t	time variable
$_B^A\mathbf{T}$	homogenous coordinate transform from B to A
T_{CS}	settling time
t_d	joint velocity filter time constant
t_l	lag time constant
t_{PD}	PD controller time constant
t_{PI}	PI controller time constant
Vcc	supply voltage
v_M	Motor amplifier input voltage
w	weighting function
$\mathrm{d}x$	infinitesimal element of quantity x
$\tilde{x}$	mean deliberated quantity x
x, y, z	coordinates along the x-, y- and z-axes
$\mathbf{x}, \mathbf{y}, \mathbf{z}$	x-, y- and z-axes
$x_{s,j}$	location of the j-th strain gauge pair
Y_1, Y_2	nonlinear regressors for the inverse kinematics
y_b	half beam thickness
$\mathbf{Y}_\varepsilon$	strain referred dynamics regressor matrix
z	discrete domain shift operator
Z_w	lumped wave impedance
α_{IIR}	IIR filter exponential discount factor
β_L	product of k_ω and L
χ_ε	strain referred dynamics parameter vector
δ	Dirac distribution
$\boldsymbol{\varepsilon}$	vector of measured strains
ε	link surface strain
ε_c	collision strain
ε_{ex}	strain measurement extremum
ε_f	collision free strain
Λ	focal length
λ	eigenvalue
$\hat{\mu}_x$	estimated mean for the quantity x
X	

μ_x	mean of the quantity x
ν	temporal deflection amplitude
$\boldsymbol{\Omega}$	transmission matrix
ω	frequency
ω_l	lumped frequency
Φ	deflection shape function
$\boldsymbol{\Psi}$	reflection matrix
ρ_b	beam mass per unit length
σ_x	variance of quantity x
$\Delta\tau$	offset between the load torque at the strain gauges and at the joint
τ_b, $\tau_{b,i}$	bending moment, lumped bending moments
$^+\check{\tau}_b$, $^-\check{\tau}_b$	lumped bending torque wave components
$\boldsymbol{\tau}_c$	vector of collision torques
τ_E	joint electrical torque
τ_F	joint friction torque
τ_J	joint load torque
τ_M	joint mechanical torque
$\boldsymbol{\theta}$	vector of joint angles
θ_b, $\theta_{b,i}$	bending angle, lumped bending angles
$^+\check{\theta}_b$, $^-\check{\theta}_b$	lumped bending angle wave components
$\dot{\theta}_\varepsilon$	angular velocity commanded for oscillation damping
θ_ε	set angle commanded for oscillation damping
$\dot{\theta}_{PD}$	angular velocity commanded by the position controller
$\dot{\theta}_r$	commanded collision reaction angular velocity
θ_w	set angle
ζ_u	logarithmic decrement

Abbreviations and acronyms

AMM	**A**ssumed **M**odes **M**ethod
APRBS	**A**mplitude **M**odulated **P**seudo **R**andom **B**inary **S**ignal
BLDC	**B**rushless **D**irect **C**urrent
ELM	**E**xtreme **L**earning **M**achine
FEM	**F**inite **E**element **M**ethod
FIR	**F**inite **I**mpulse **R**esponse
HSV	**H**ue **S**aturation **V**alue color model
IATE	**I**ntegral **A**bsolute **T**ime-Weighted **E**rror
IATS	**I**ntegral **A**bsolute **T**ime-Weighted **S**train Surface
IIR	**I**nfinite **I**mpulse **R**esponse
IMU	**I**nertial **M**easurement **U**nit
IR	**I**nfra **R**ed
ISS	**I**nternational **S**pace **S**tation
ITER	**I**nternational **T**hermonuclear **E**xperimental **R**eactor
MEMS	**M**icro-**E**lectro-**M**echanical-**S**ystem
NRMSE	**N**ormalized **R**oot **M**ean **S**quared **E**rror
ODE	**O**rdinary **D**ifferential **E**quation

PID	**P**roportional **I**ntegral **D**erivative
PMD	**P**hotonic **M**ixing **D**evice
RGB-D	**R**ed **G**reen **B**lue - **D**epth
RMSE	**R**oot **M**ean **S**quared **E**rror
RS-232	serial data interface standard
TCP/IP	**T**ransmission **C**ontrol **P**rotocol / **I**nternet **P**rotocol
TOF	**T**ime **O**f **F**light
TUDOR	**T**echnische **U**niversität **D**ortmund **O**mnilastic **R**obot
UDP	**U**ser **D**atagram **P**rotocol
USB	**U**niversal **S**erial **B**us
WTF	**W**ave **T**ransfer **F**unction

1

Introduction

"I was up to here in *Flexible Frank*. [...] I had a bee in my bonnet about the perfect, all-work household automaton, the general-purpose servant. [...] I wanted a gadget which could do *anything* inside the home – cleaning and cooking, of course, but also really hard jobs, like changing a baby's diaper or replacing a typewriter ribbon. [...] I wanted a man and wife to be able to buy one machine for, oh say about the price of a good automobile [...]. This meant that you need to cause *Flexible Frank* to clear the table and scrape the dishes and load them into the dishwasher only once, and from then on he could cope with any dirty dishes he ever encountered" Heinlein (1957).

1.1. Motivation

This passage from the novel "The Door Into Summer" by Robert Heinlein written in 1957 represents an early detailed reference to the fascinating anticipation of introducing robotic assistants in our everyday life. *Flexible Frank* is the imagination of an artificial butler that takes care of recurrent, time consuming and annoying tasks of the daily grind. Heinlein clearly documents that more than half a century ago – even years before the advent of the first industrial robot in 1961 (Devol 1961) – robot assistants have been envisioned to commonly enter our households to save our valuable time and to improve quality of life. Since those days the vision steadily enfetters young and old.

However, still today the cognition and motor skills of robots remain far away from matching their Science-Fiction ideals. Yet around the turn of the millennium Khatib et al. (1999) point out that in industrial production "typical operations are composed of various tasks, some of which are sufficiently structured to be autonomously performed by a robotic system, while many others require skills that are still beyond current robot capabilities. The introduction of a robot to assist a human [...] will reduce fatigue, increase precision, and improve quality; whereas the human can bring experience, global knowledge and understanding to the execution of task". However, with today's conventional robots physical assistance is frequently inconceivable or at least strongly restricted. The reason is the associated risk potential emerging from their rigid and precise but also very massive construction.

If in the industrial production a human process specialist can intuitively program
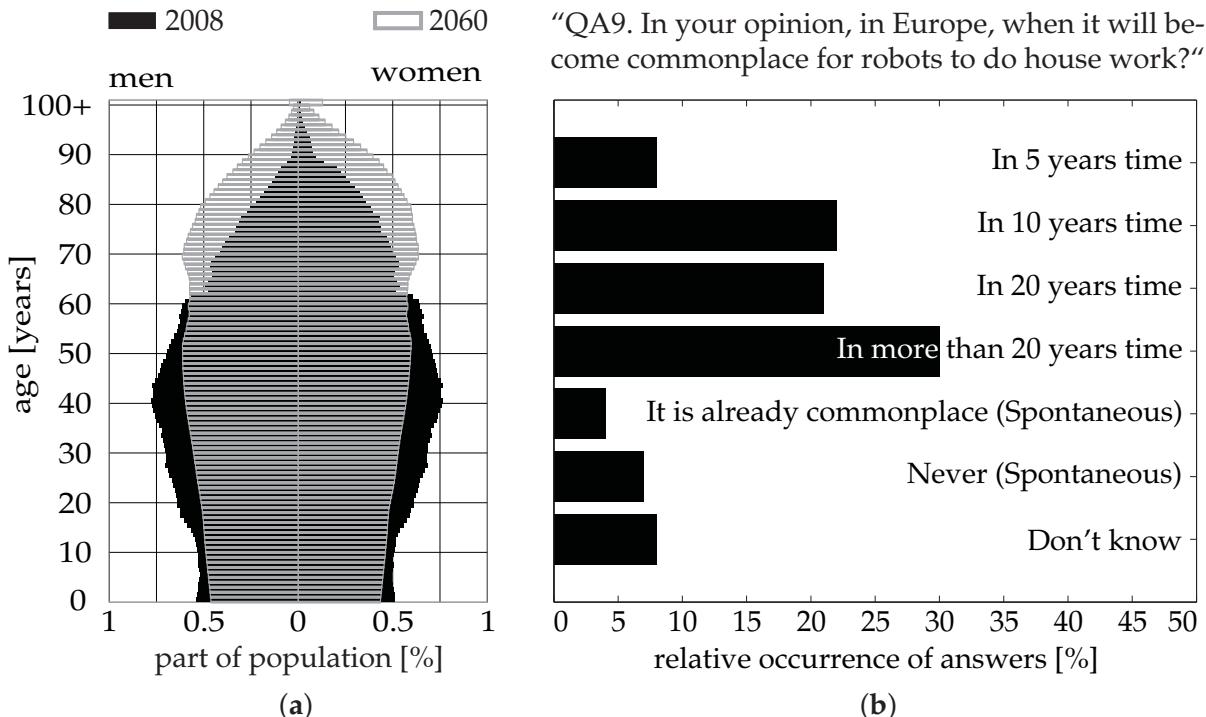
Figure 1.1.: The projected European demography pyramid (**a**) (Giannakouris 2008) and results of a survey regarding "public attitudes towards robots" (TNS Opinion and Social 2012) (**b**).

the robot or adjust an existing program for example by kinesthetic teaching (Billard, Calinon and Guenter 2006), a costly and time consuming textual programming by a robotic specialist would become obsolete. While the robot fulfills the demonstrated task the human worker would be free to organize the subsequent assembly steps or to instruct additional robots. This idea is called robot farming, where the human worker acts as a herdsman looking after a herd of manufacturing robots. This way robotic automation is envisioned to become economically efficient also for small and medium sized enterprises (SME) and preserves competitiveness of high quality production in high wage countries (German Federal Ministry of Education and Research 2007).

While the industrial process specialist would be specially trained, robots in domestic environments will inevitably get into contact with untrained interaction partners. In industrialized countries demographers project the emergence of elderly dominated societies in the near future as visible in figure 1.1 (**a**). From this perspective the German Federal Ministry of Education and Research (2007) identifies "great opportunities in the growing market for industrial and service robots, which has doubled in size over the last ten years". Hence, the conception of human robot cooperation must not halt in industrial workshops. It will surely enter domestic environments as well. First robotic lawn mowers, vacuum cleaners and pool or window cleaning robots slowly begin to explore such markets for a restricted number of low-level tasks at present time. But still, according to a broad survey conducted by the TNS Opinion and Social (2012), "all of this is future talk to most Europeans, as very few imagine that it will soon become commonplace for robots to do housework" (see figure 1.1 (**b**)). Today, this more than ever motivates the research efforts all over the world to bring robots and humans into physical cooperation for high-level tasks. If anyone can "cause"

a robotic assistant "to clear the table and scrape the dishes and load them into the dish-washer only once" by kinesthetic or any other teaching method (Argall et al. 2009), we finally arrive at a point very close to Heinlein's vision of *Flexible Frank*.

Recently Alami et al. (2006); Santis et al. (2008) identified that "safety and dependability are the keys to a successful introduction of robots into human environments". Moreover, "the first step towards intrinsically safe and dependable design is to reduce the weight of the moving parts of the robot". Bicchi and Tonietti (2004) propose that the next step "to increasing the safety level of robot arms interacting with humans is to intentionally introduce mechanical compliance in the design". It decouples the link inertia from the effectively larger actuator inertia, which reduces the reflected overall robot inertia during collisions. Additionally it protects gears and joint-sensors against external shocks. The insights lead Alami et al. (2006) to formulate an "integrated approach to the co-design of robots for safe physical interaction with humans, which revolutionizes the classical approach for designing industrial robots – rigid design for accuracy, active control for safety – by creating a new paradigm: design robots that are intrinsically safe and control them to deliver performance". Guizzo and Ackerman (2012) conclude: "If you want a robot that's going to deal with an unstructured environment, it can't be stiff".

According to Guizzo and Ackerman (2012) within the recent half-decade companies like ABB, Adept Technology, Barrett Technology, DLR, Kawada Industries, Redwood Robotics, Universal Robots and recently Rethink Robotics are developing robot co-workers to assist humans in SME production lines. They all feature lightweight structures and intrinsic compliance collocated with the joint actuators. Among the mentioned examples Universal Robots as well as Rethink Robotics explicitly declare the robots to be affordable by any small to medium sized enterprise as a main goal. The rated prices are less than 22 000 USD, which pretty much agrees with Heinlein's idea of "one machine for [...] about the price of a good automobile" (Heinlein 1957).

Guizzo and Ackerman (2012) see the key to cutting the costs in giving the robot through software "the ability to autonomously compensate for its own mechanical irregularities as well as changes in its environment". This approach waives the need for costly components by the development of advanced control algorithms. Following this paradigm, it is noticeable that recent lightweight robot assistant prototypes still share one important aspect with conventional robots. It is the strict rigid-link-design aiming at the preservation of durability and moreover positioning accuracy by hardware. It appears that the paradigm of affordable robots through sophisticated software instead of expensive hardware has not yet been driven to the end.

The undesired side effects of intrinsic compliance are structural oscillations and static deflections. In contrast to a non-collocated distributed elasticity in the robot links, their attenuation is way simpler from a control point of view, if their origin is collocated in the actuators as with the examples above. Up to now, the preservation of link rigidity remains a strong demand, even if it constitutes a substantially time consuming mechanical design difficulty, which easily inveigles to use pricy novel materials. Such materials yield lighter structures and allow for less powerful actuators on one hand, but usually come with a larger ecological footprint during production on the other hand.

Albeit, Benosman and Le Vey (2004) experience that in large scale industrial pro-

elastic beam
sensor
actuator

whisker

skin with
nerve cells

extrinsic
muscles

intrinsic
muscles

(**a**)

link

strain
gauges

motor

(**b**)
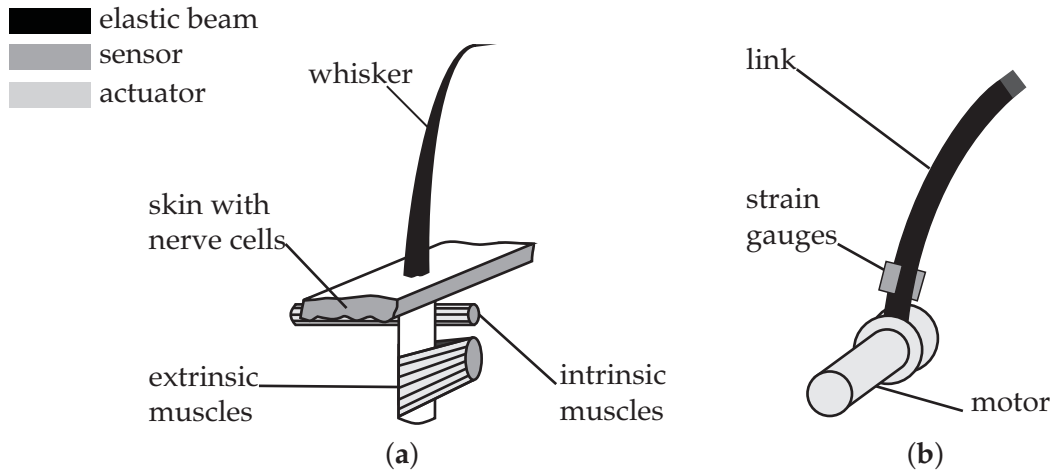
Figure 1.2.: Simplified schematic of a whisker (**a**) and an elastic joint-link-module (**b**).

duction with conventional robots the link mass trimming together with emerging link elasticity gain importance due to steady reduction of cycle times and increasing accuracy specifications. Tao et al. (2006) provide a practical example of a Scara type robot for wafer handling applications in semiconductor manufacturing. Besides robotics we find link elasticity being a problem to avoid in the constructions of cherry pickers (Pridgen et al. 2011), fire rescue turntable ladders (Zimmert, Kharitonov and Sawodny 2008), automobile concrete pumps (Cazzulani et al. 2011) and many other machines. As a consequence, if the problems associated with link elasticity can be solved in robotics, the developed concepts are supposed to be transferable to the aforementioned applications as well.

Once the undesired effects of link elasticity are sufficiently compensated, a promising new perspective is to exploit the intrinsic link compliance for the detection and sensing of contact forces. Behn et al. (2013) explain that the vibrissae of rodents "can be moved either passively or actively through alternate contractions of the intrinsic and extrinsic muscles". This enables the passive detection of contact forces as well as the tactile scanning of surfaces. Miersch et al. (2011) report that even in murky water pinnipeds use their whiskers to locate and track the hydrodynamic trails of their pray. While the species differ in the details, figure 1.2 (**a**) shows a very basic schematic of a single whisker with the skin realizing the neural connection as well as the actuation mechanism composed of extrinsic and intrinsic muscles. For comparison, figure 1.2 (**b**) presents a single joint-link-module of an elastic-link robot with strain gauges and an electrical motor. The whiskers as well as the arm consist of an elastic beam, which is actuated on one end. The deflection sensor is mounted close to this actuator on the beam surface. This identical structural arrangement evokes the biological inspiration by the whiskers of rodents and pinnipeds. It gives raise to the hypothesis that the intrinsic link compliance can indeed be exploited for the detection and sensing of contact forces.

The present thesis approaches the promising and still open research direction concerned with the control of elastic link robots. If the hypothesis is correct, the strong requirements for link rigidity and the associated challenges can be relaxed and elastic

link robots may become indistinct from compliant joint robots on the way to the intrinsically safe "household automaton [...] about the price of a good automobile" (Heinlein 1957).

1.2. Related work

The research interest in elastic link robotic arms dates back to the early seventies. At that time the demands for increased speed and accuracy of robot manipulators as well as applications of light but long reach robotic manipulators for space applications were the main driving motivators (Whitney, Book and Lynch 1974). After 40 years of research on the modeling and control of elastic link robots, the booms of space shuttles (Scott, Gilbert and Demeo 1993) and the remote manipulation systems installed on the international space station (ISS) (Sawada et al. 2005) are the only widely visible examples for practically applied elastic link robots in public. Dwivedy and Eberhard (2006) supplement examples of long reach inspection and nuclear waste retrieval manipulators. Recently, Dubus, David and Measson (2009) investigated the application of a long reach elastic link inspection robot for the International Thermonuclear Experimental Reactor (ITER). While space manipulators operate in a zero-gravity environment this one is a rare example for a terrestrial application.

In spite of the potentials outlined in the previous section, the compensation of the detrimental effects of link elasticity by control algorithms is obviously yet an unsolved challenge. According to Benosman and Le Vey (2004), "it can be seen that even for the simple end effector regulation problem, research has been conducted still recently". Promising results have been achieved with respect to safety and energy efficiency using elastic joints (Ham et al. 2009), so that one might wonder about the cardinal differences between joint and link elasticity. The following literature survey yields a tangible notion of these differences. Therefore it is organized in three subsections. The first subsection structures available modeling techniques. The second reviews control challenges and approaches. The third subsection focuses and concludes on experimental works reported in literature.

Modeling and dynamics analysis

A first literature survey on modeling and control of elastic link robots with 45 contributions between 1975 and 1990 has been carried out by Book (1990). The survey is written as a "Tutorial Review" and summarizes the additional challenges compared to the control of purely rigid and elastic joint robots.

Besides the kinetic energy contained in the motion of inertias and the potential energy due to the posture within the gravitational field, elastic robots store potential energy in their structural deflection. For elastic joint robots the compliance is spatially concentrated at the actuation mechanism. A spring model collocated with the actuator suffices to model the equations of motion. Link bending however is governed by its dispersive distributed nature. This is where the additional challenges for the modeling and control of elastic link robots originate. The common modeling approaches in literature aiming at the simulation and control of elastic link robots can be categorized into three main directions:

Lumped mass approach: The elastic links are spatially discretized into lumped masses interconnected by massless spring-damper-elements. The number of lumped masses trades off accuracy and model complexity. An example for this approach is given by Konno and Uchiyama (1996) as well as Konno, Uchiyama and Murakami (1997), who investigate the horizontal motion of a two link experimental setup. Feliu, Rattan and Brown (1992) realize a controller for a single massless elastic link with distributed lumped masses. This view on the system decouples the influence of the link geometry and the mass properties on the elastic dynamics. The decoupling enables the load adaptation scheme for a single link experimental setup under exclusion of gravitational forces proposed by Feliu, Feliu and Cerrada (1999).

Euler-Lagrange approach: The equations of motion are derived in analogy to rigid robots based on the energy balance using the Euler-Lagrange formalism. Link elasticity adds to the potential and the deflection rates contribute to the kinetic energy. The additional generalized coordinates required to describe the deflection states are obtained from a modal analysis. The modal analysis provides eigenfrequencies and deflection shapes. Even with single links analytical solutions to the involved fourth order partial differential equations are feasible only for a very limited number of simple link geometries and rather basic boundary conditions. Popular beam configurations are covered in fundamental textbooks on structural dynamics (Dukkipati and Srinivas 2005; Meirovitch 2001). Approximate techniques employ generic polynomials, finite element solutions or empirical data obtained from experiments to assess the assumed relevant eigenfrequencies as well as a mathematical description of the associated mode shape functions. The achievable accuracy is determined by the considered number of assumed modes, the body geometry and validity of the selected boundary conditions.

Frequency domain approach: Frequency domain techniques are an alternative to the time domain approaches above. According to Book (1990) the serial and parallel connection of joint as well as both rigid and flexible links is straightforward using transfer function models. Book and Majette (1983) report that the extension to transfer matrices generally allows the propagation of the deflection, bending angle, shearing force and bending moment through entire kinematic chains. Krauss (2012) recently published an efficient Python implementation of this approach. Nevertheless, frequency domain transfer matrix methods have experienced far less attention in the past than the other two approaches. The reason may be, that many powerful advanced controller design methods require time domain models. The conversion between the frequency and time domain models for nonlinear systems is tedious. Detailed analyses provided by Krauss (2006) as well as Krauss, Book et al. 2010 are still restricted to linear models.

More citations for each category can be found in the extensive literature survey conducted by Dwivedy and Eberhard (2006), which reviews a total of 433 modeling papers. As a summary, the first two categories clutch to modeling concepts that are well established for the concentrated parameter case of conventional rigid robots and

seek to extend them for distributed parameter systems. Following Meirovitch (2001, p. 464), both approaches "model distributed-parameter systems as discrete systems, which amounts to spatial discretization and truncation". The lumped parameter approach "is more physical in nature, but lacks rigor", while the assumed modes model "is more abstract, but has a solid mathematical foundation" and "also tends to be more predictable and accurate". The frequency domain approach also discretizes the continuous system to a finite series of assumed modes. Book (1990) remarks that the obtained models are rather inaccurate with respect to the large robot motions, but mathematically compact and thus attractive for the description of small oscillatory motions.

In all these common modeling approaches the spatial and modal truncation entails crucial consequences for the subsequent controller design. A model based controller may potentially excite the unmodelled eigenfrequencies, which can destabilize the closed loop. This effect is known as modal spillover (Balas 1978). A cost analysis may be carried out to reduce model complexity by considering a smaller number of eigenfrequencies with acceptable degradation of accuracy (Tsujisawa and Book 1989). However, no theoretical technique exists, that guarantees relief from spillover. This must be carefully investigated in real experiments.

In order to circumvent the spillover problematic, a few researchers such as Halevi and Wagner-Nachshoni (2006) have investigated nonlinear infinite dimensional transfer functions. The transfer functions are derived for different sensor and actuator configurations as well as generalized second order boundary conditions at both ends of a single beam. On this basis a controller is designed by Halevi (2004). The parameter tuning and stability analysis is carried out with respect to the generalized boundary conditions. Although very promising the investigations are limited to elastic systems governed by second order partial differential equations such as vibrations of strings or torsional or lateral oscillations in rods.

The accuracy of the modeling techniques discussed so far strongly depends on the knowledge of the boundary conditions for each link in the kinematic chain. The introductory boundary value problems discussed in fundamental textbooks on structural dynamics (Dukkipati and Srinivas 2005; Meirovitch 2001) usually consider static boundary conditions. In real multi-elastic-link robots the boundary conditions of each individual link already vary with the joint controller parameters as well as the relative joint configuration. In spite of exponentially growing computation power the model complexity under consideration of time varying boundaries "can swamp even large memories" (Book 1990) and render the resulting dynamics equations poorly inspectable. That is why most multi-link models such as the one proposed by Luca and Siciliano (1991) or Chen (2001) argue the replacement of the varying boundary conditions by fixed approximations.

Beyond the joint configuration dependent time variance, imperfect clamping and finite drive train stiffness add non-negligible uncertainty to the boundary model. Backlash may lead to chaotic or at least non-deterministic boundary dynamics. Finally, payload changes and physical contacts with the environment unpredictably but drastically and abruptly alter the boundary conditions. Such events must not destabilize the closed control loop.

Control approaches

A broad variety of controllers have been investigated in search of a solution to the oscillation damping and positioning tasks for elastic link arms simultaneously. Benosman and Le Vey (2004) structure a total of 119 papers into control concepts such as input-output linearization through stable inversion using a state feedback designed in the frequency and time domain, singular perturbation and sliding mode control, optimal, robust and adaptive control, feedforward filtering and input shaping.

Identically to rigid robots, the position control objective for elastic link robots is to perform point-to-point motions or to follow a predefined trajectory. This commonly implies the actuator torques to be the control inputs and the end effector pose to be the control output of the plant. However, for elastic link robots this choice of control inputs and outputs leads to a plant with unstable zero dynamics. The rigid links of conventional robots cause a control action at the joints to instantaneously affect the end effector motion. The distributed nature of link elasticity causes the control action to propagate along the structure with finite speed. As a consequence well known control concepts from rigid robots such as the computed torque and inverse dynamics control cannot be applied directly. Luca, Panzieri and Ulivi (1998); Moallem and Patel (2001); Wang and Vidyasagar (1991) circumvent the difficulties using a method known as output redefinition, where the actual end effector deflection is replaced by an artificial control output. The plant with the artificial output shows stable zero dynamics.

Approaching from the hardware side, oscillations can, at least up to some extend, be damped passively by using multi-layered link designs with intermediate visco-elastic layers for energy dissipation or parallel arm structures. Some researchers distribute additional actuators such as piezo electric ceramic actuators (Khorrami, Zeinoun and Tome 1993) or dielectric electroactive polymer actuators (Bailey and Ubbard 1985) along the structure. These devices also show integrated deflection sensing capabilities. Their arrangement accounts for the distributed nature of the elastic links and they are controlled to actively stabilize the zero dynamics. Moreover, Konno, Uchiyama and Murakami (1997) discover in certain joint configurations the modal controllability through the joint actuators to get lost. In such configurations it might become infeasible to stabilize or attenuate oscillations of particular modes. The effect does not occur with elastic joint robots, because of the collocation between the concentrated elasticity and the actuation mechanism. The distributed actuators mentioned above can be optimally placed to ensure modal controllability throughout the whole workspace. However, a practically very inconvenient property of piezo ceramics as well as dielectric electroactive polymers are the high operating voltages, which necessitate thorough insulation.

Most researchers use strain gauges as deformation sensors. They are fast, cheap, operate at low voltages and can be easily glued onto the link surface. An investigation towards more expensive optical fibers with Bragg gratings as strain sensing device for increased precision and a larger signal to noise ratio is performed by Franke et al. (2009).

The strain measurement close to the joint provides stable zero dynamics, which motivates researchers such as Luo (1993) to directly close proportional and integral

feedback loops for oscillation damping. In their experiments Luo and Guo (1995) use a single link in the horizontal plane. Malzahn et al. (2010a) augment the direct proportional feedback for a single link under gravity using feedforward input shaping filters discussed by Vaughan, Yano and Singhose (2008). The resulting two degree of freedom control structure joins the individual strengths and alleviates the shortcomings of the feedforward and feedback approaches. Malzahn et al. (2011b) extend the concept to a multi-link arm under gravity with a more advanced cascaded joint controller complemented by a jerk minimizing online trajectory planner.

The most promising property of the linear strain feedback is the independence of any dynamics computation at runtime. Ge, Lee and Zhu (1998) suggest a nonlinear integral feedback law sharing this property in a purely simulative study. The concept looks at the dissipation of oscillation energy following a direct Lyapunov synthesis approach, which avoids a truncation of the arm dynamics and possible spillover effects.

Experimental studies with this energy based control have emerged simultaneously and independently by Mansour et al. (2008) as well as within the scope of this thesis by Franke et al. (2009).

The experiments carried out in a wide workspace and under gravitational influence reveal an unexpected difficulty with the nonlinear integral feedback law. If any elastic link passes through a vertical orientation the damping scheme starts a limit cycle. In the vertical pose the static strain changes the sign, so that an imperfect static strain cancellation in combination with the integral nature of the concept is suspected to cause the observed effect. The observation from multiple experiments is, that such limit cycles do not occur, if link orientations remain on either side of the vertical pose. Experiments with a backlash free experimental setup allow the exclusion of the gear backlash as a reason.

While a mathematical proof to this observation is still an open challenge, Malzahn (2008)[1] develops a remedy later published by Franke et al. 2009. The idea is to supervise each link orientation and adapt the sign of the feedback term accordingly. However, the experiments under gravity indicate that the damping results do not justify the additional efforts compared to the linear feedback.

The strain measurements close to the joints allow only poor tip position information inferred by means of a properly identified dynamics model. Tip sensors provide accuracy with respect to static configuration and load dependent deflections but introduce unstable zero dynamics into the control system. This gives raise to the following, still open question stated by Book (1990): "how can one combine strain and tip position sensors to achieve a robust and accurate controller"?

For example, Kharitonov, Zimmert and Sawodny (2007) propose the use of strain gauges close to the joint with a gyroscope at the tip. During the past decade camera sensors with fast frame rates and high resolutions became widely available at low cost, which renders them a promising option as tip sensors. This has motivated researchers such as Bascetta and Rocco (2006a,b); Dubus, David and Measson (2009); Jiang, Konno and Uchiyama (2007) to work on the use of cameras as a sensor for oscillation damping as well. During preparation of this thesis Malzahn, Phung

---

[1]The cited thesis narrowly focuses on the experimental investigation of the particular nonlinear integral feedback. The main result is the sign adaptation to circumvent the observed instability.

and Bertram (2012c); Malzahn et al. (2010b) contribute experimental results on the oscillation sensing relying solely on an eye-in-hand camera with a special emphasis on unstructured and potentially dynamic scenes with varying texture and geometric structure. Malzahn, Phung and Bertram (2012b) compare three approaches for online identification of a signal model describing the perceived oscillations. The proposed method allows to compensate for the sensor delay. Malzahn et al. (2012) aggregate these works and present the purely camera based oscillation damping using the control concept explained in chapter 5. While the actual image processing with delay compensation is beyond the scope of this thesis, chapter 9 includes a brief application of the camera for end effector positioning.

Experimental studies

Experimental investigations of control concepts are as yet dominated by single link setups operating in the horizontal plane under exclusion of the variable gravitational influence. Becedas et al. (2009) propose a generalized PI-controller for a horizontal single-link setup supported by an air table. Diaz et al. (2010) propose a robustified variant of the impulse based input shaping technique developed in earlier works of Singhose (2009). The variant shows an abbreviated filter duration. The increased robustness results from a numerical optimization, which adapts to changes in the system dynamics due to varying payload masses.

Publications on multi-elastic-link robots are as yet mostly limited to simulative studies. They comprise model predictive approaches for up to four-link mechanisms (Boscariol, Gasparetto and Zanotto 2010). Korayem et al. (2010); Subudhi and Morris (2009) combine fuzzy approaches with variable structure controllers or neural networks. Rong et al. (2010) supplement a PID-controller by an artificial neural network to form an adaptive controller based on velocity feedback for oscillation damping with piezo actuators. Benosman and Le Vey 2004 find the reason in "the complexity of the nonlinear multi-link models, since it is difficult even if not impossible to apply directly some theoretical closed-loop control strategies, which need closed-form manipulations of these complex system dynamics".

Along with all the uncertainties associated with the dynamics modeling described in section 1.2, it is frustrating, tedious and error prone to derive and especially to identify a holistic dynamics model of a real robot, suited to precisely describe the structural oscillations along with the static deflections in the entire workspace. In particular, Book (1984) discusses the complexity and computational burden of a recursive Lagrangian formulation with respect to different mode shape approximations and compares them to rigid robot models. Theodore and Ghosal (1995) provide simulations for the model of a multi-link arm in the absence of gravity and compare the analytical assumed mode method (AMM) with the finite element method (FEM). The FEM overestimates stiffness which can drive a model based controller unstable. Their AMM model considers time dependent boundary conditions under simplifying conditions. Book (1984) supplements the investigation of computational complexity. Even with today's available computational power a model of that type most probably lacks real-time capabilities and such a model would not yet have captured payload changes and interactions with the environment.

The complexity and uncertainty aggravate the experimental proofs of concept for model based controllers, so that researchers argue that contributions in the control of elastic link robots should intensify experimental works "to keep realism in the research" (Book 1990). Hu (1993); Tokhi and Azad (2008) collect and picture experimental setups developed all over the world. The works clearly document the dominance of single link experimental setups. Multi-link setups are almost exclusively operating in the horizontal plane thereby excluding the influence of gravity. Just a few multi-link setups moving in the vertical plane exist. Two of them are FLEBOT II and ADAM in the Space Machines Laboratory at Tohoku University as well as ELLA and ElRob at the Institut für Robotik, Linz University.

The number of publications concerning the exploitation of link elasticity for force control or contact detection is vanishingly small. Bazaei and Moallem (2011) follow the output redefinition approach control the tip force of a single link operating in the horizontal plane. Garcia and Feliu (2000) as well as Garcia, Feliu and Somolinos (2001) compare implicit and explicit force control schemes as well as collision detection with a single-link setup and a modified PID framework. So far, neither simulative nor experimental studies on force control or collision detection are known that consider elastic link robots under the influence of gravity or with multiple links.

1.3. Contribution and outline

This work is first and foremost driven by the idea that elasticity in the robot links does not ultimately need to be a problem, which must be avoided by costly and momentous constructional efforts. The hypothesis formulated in section 1.1 claims, that link elasticity can be exploited to sense and control contact forces. The work represents a first experimental study towards this hypothesis. It considers multi-link arms under gravitational influence. As a prerequisite, the work develops and exemplifies solutions to the challenges of oscillation damping and position control under the conditions summarized in the previous section. This whole path is visualized in figure 1.3 and reflected by the following outline:

Chapter 2: The preparation of this thesis included the development and installation of the three degree of freedom elastic link robot named TUDOR along with the additional external reference sensors. The arm is intentionally designed to show clearly visible elastic effects, which allows for illustrative evaluations of the devised control concepts. The chapter introduces the complete experimental equipment and the communication among all individual units.

Chapter 3: The chapter models and identifies the joint actuators. It describes the choice and tuning of the cascaded joint angular controllers. The chapter closes with an experimental evaluation of the control objectives and describes a generalized controller architecture for the unified joint-level integration of all different oscillation damping control concepts investigated in this work.

Chapter 4: The chapter introduces the mathematical prerequisites of the elastic link dynamics for the remainder of this work. Supported by experiments, it contributes detailed theoretical analyses of the oscillatory link dynamics of multi-
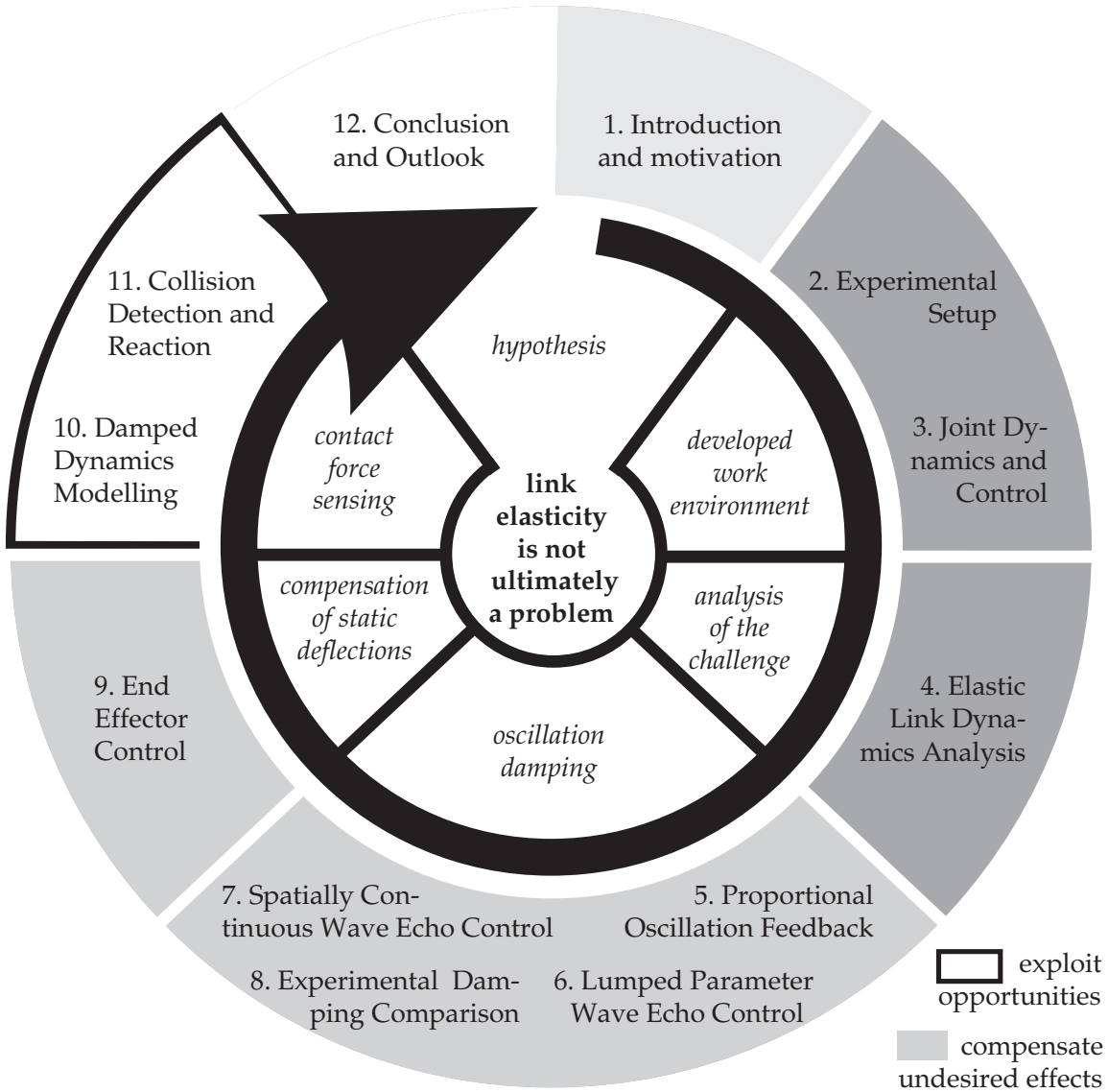
Figure 1.3.: Structure of this thesis centered around the motivating hypothesis.

elastic-link arms. The analyses particularly focus on the influences of payload changes, varying joint configurations and uncertainty in the boundary conditions on the eigenfrequencies as well as mode shapes. The discussion of the analyses founds the basis for the controller design in the chapters 5 to 7.

Chapter 5: This is the first chapter devoted to oscillation damping control. Uncertainties and unpredictable influences on the complex dynamics of multi-elastic link robots seem to prevent the practical success of common model based controllers for simultaneous oscillation damping and end effector positioning so far. This chapter focuses on the strain based oscillation damping without consideration of the tip positioning task in first place. It proposes a solution to this sub-challenge by discussing different direct proportional strain feedback approaches based on a truncated transfer function model. The concept relies on a minimum amount of model knowledge and does not compute any dynamics at run-time.

Chapter 6: The second chapter on oscillation damping control uses a lumped para-

meter model of the elastic link dynamics. It revisits the identification of wave properties in the lumped structure introduced by O'Connor (2007b). The wave properties are exploited to an alternative derivation of a damping controller based on the absorption of emitted and echoed wave components. Again, a minimum knowledge of the link dynamics is required at run-time. With a structural reduction this thesis reveals a very close relation to the proportional oscillation feedback presented in chapter 5.

Chapter 7: The models and control concepts presented so far all involve discretization or truncation of the oscillatory elastic link dynamics. Following the concept of mechanical waves this third chapter on oscillation damping control accepts the continuous spatial distribution of the elastic properties and introduces the concept of wave reflection and transmission at junctions as well as boundaries. The chapter discusses three different variants to shape the wave reflection matrix at the actuator boundary. Cross-relations to the previously derived controllers are highlighted.

Chapter 8: This final chapter on oscillation damping control provides an extensive experimental comparison of the oscillation damping concepts presented in this work. The experimental results cover the whole workspace of the multi-elastic-link robot TUDOR and include investigations towards varying payloads, step-like as well as harmonic external disturbances and damping actions at just a single actuator.

Chapter 9: With the structural oscillations readily damped, the end effector positioning task in this chapter drastically simplifies. Two position control approaches are presented. The first one is a 3D visual servoing controller implemented with an eye-in-hand mounted RGB-D camera. The second one employs a data driven inverse kinematics algorithm. A ball catching scenario with a human thrower sequentially throwing multiple balls towards the robot serves as a testbed towards the question whether time critical positioning tasks can be accomplished by an elastic link robot arm with sufficient precision.

Chapter 10: In addition to the inverse kinematics also the dynamics of the elastic link arm are way simpler to model in the presence of an underlying robust and fast oscillation damping controller. With this chapter the thesis derives a linear relation between the measured strain and the joint torques, which allow the damped strain referred dynamics to be formulated with exactly the same mathematical structure as the dynamics of conventional rigid robots.

Chapter 11: With the oscillations damped, the end effector position controlled as well as the identified damped dynamics model at hand, the work finally arrives at the investigation of the hypothesis about the potentials of link elasticity in robot arms for collision detection and reaction. The chapter provides collision experiments with blunt and sharp impacts, both carried out with durable and stiff but also with compliant and fragile objects as well as a human arm.

Chapter 12: The work comes full circle with a concluding discussion about the accomplished results and suggests directions for future works.

2

Experimental Setup

For the experimental evaluation of the theoretical concepts developed in this work, the three degree of freedom multi-elastic-link robot arm TUDOR (**T**echnische **U**niversität **D**ortmund **O**mnielastic **R**obot) along with additional external reference sensors has been developed. The robot is depicted in figure 2.1 (**a**). The robot links are intentionally designed to be visibly elastic. This simplifies the illustration of oscillation damping results as well as the compensation of static deflections. This chapter details the individual components of the experimental setup.

2.1. Joints and links

The robot comprises three brushless DC (BLDC) motors with planetary ceramic gears and two spring steel blades as elastic links. The equivalent rigid body kinematics in figure 2.1 (**b**) shows the joint zero configuration and illustrates the actual robot dimensions. It defines the coordinate frames of the base, the end effector as well as the intermediate joints. The first actuator with the joint variable θ_1 is installed within the cylindrical base and rotates the arm structure in the horizontal plane around the axis ^1z. The mechanical connection between the first and second joint is considered to be the rigid first link of the robot. The second and the third joints have horizontal axes of rotation with θ_2 about ^2z and θ_3 about ^3z. Both actuators are interconnected via the elastic second link. The elastic third link is mounted at the shaft of the third actuator. The parameters of the actuators are collected in appendix A.3.

The design criterion for the elastic links was to enable clearly visible structural oscillations being easily excited by joint motions and physical interactions. This paves the way for convenient illustration of the results effected by the proposed control schemes. The dominant frequencies of each link should reside in the order of magnitude of 10 Hz. Therefore different types of quenched and tempered aluminum as well as steel blades with varying cross section have been investigated. As a result spring steel blades with rectangular cross section and the parameters listed in appendix A.1 are used throughout the thesis. These links provide sufficient fatigue strength under the repeated bending stresses associated with the targeted oscillation amplitudes, frequencies and end effector payloads. For the payloads, steel plates with dimensions 80 mm by 80 mm by 2 mm can be mounted at the end effector. Each plate adds a payload mass of 100 g.
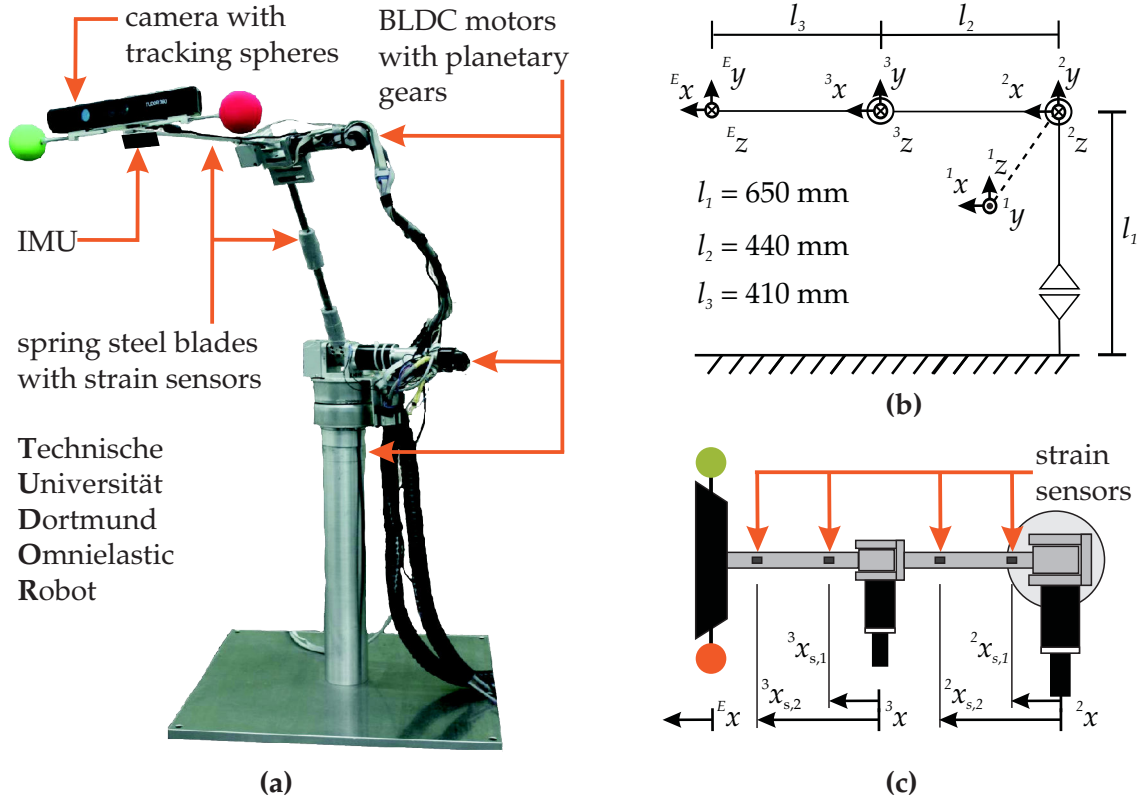
Figure 2.1.: Photograph of the multi-elastic-link robot arm TUDOR (**a**) with equivalent rigid body kinematics (**b**) and top view schematic (**c**) including the strain sensor locations.

The thesis accounts for the effect of gravity on the elastic links. To emphasize the appearance of this effect, the elastic link area moments of inertia about axes parallel to the joint ^{2}**z**-axes are designed to be small. This way the structural oscillations mainly occur in the vertical ^2x-^2y plane incorporating the gravity vector. Nevertheless deviation moments due to the unbalanced mounting of the third joint also cause smaller torsional and horizontal oscillations of the arm.

2.2. Strain sensors

Strain gauge pairs are applied on the top and bottom surfaces of the elastic links according to the schematic shown in figure 2.1 (**c**). Each link carries two pairs of strain gauges. One pair close and one pair more distant to the preceding joint. The pairwise installation in connection with a Wheatstone half-bridge circuit allows for the compensation of temperature dependent strain drift in the measurements. The sensor parameters are listed in appendix A.4. For simplicity, the notation

$$\varepsilon_2 = \varepsilon(^2x_{s,1}) \quad \text{and} \quad \varepsilon_3 = \varepsilon(^3x_{s,1}) \tag{2.2.1}$$

is used as a convention in the remainder of this thesis.
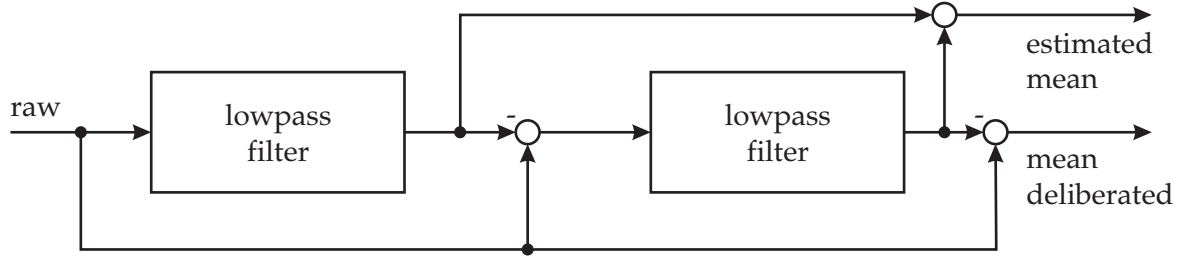
Figure 2.2.: Filter architecture for second order smoothing.

The key difference between elastic link arms that operate under gravity and those that do not is the presence of configuration and load dependent static deflections. The static deflections effect non-zero static strain readings, which have to be cancelled in preparation to oscillation damping control. Otherwise they introduce substantial steady state positioning and tracking errors or even destabilize an oscillation damping controller.

There are basically two options to perform static strain cancellation: a model based or a filter based approach. The static deflection nonlinearly depends on the joint configuration. The transitions between two static deflections due to changes in the joint motion are dominated by the mechanical actuator time constants. The adaptation of a model based static strain cancellation to unpredicted load changes as well as to static strains during contacts with the environment requires fast online identification and dependable reasoning from a higher cognitive level. A more fundamental limitation of a model based approach arises from the finite accuracy of any model. This necessitates the implementation of a deadzone around the residual modelling error. Oscillations with measurements remaining in this deadzone cannot be damped by the controller.

For low level damping control of the structural oscillations this work therefore proposes a filtering approach. It has no limiting deadzone, it is simpler from a computational as well as less demanding from a cognitive point of view. It automatically adapts to varying load conditions. The model based prediction of strain measurements is left for the collision detection and reaction in the chapters 10 and 11.

Highpass filtering of the strain measurements is an obvious first idea for static strain cancellation. There exist numerous automated filter design algorithms for both finite impulse reponse filters (FIR) as well as infinite impulse response filters (IIR). Most of these algorithms compute the filter coefficients based on amplitude gain and cut-off frequency specifications for the stop- and pass-band. As a result from section 4.7 the lowest natural frequencies are found to come close to 1 Hz. FIR filters with sharp filter edges involve a large number of filter coefficients, which increases computational cost and decreases responsiveness. IIR filters can be desigend with less filter coefficients at the cost of a more complicated phase characteristic. Large phase shifts aggravate or even destabilize the oscillation damping control. Phase constraints are more difficult to set in most automated filter design algorithms. Understanding the relationship between the typical frequency domain design specifications and the time domain filtering result requires extensive filter design experience.

The filter design suggested in this work is based on the subtraction of the estimated static strain signal portion. Besides the static strain cancellation, the availability of this

FIR based highpass   IIR based highpass
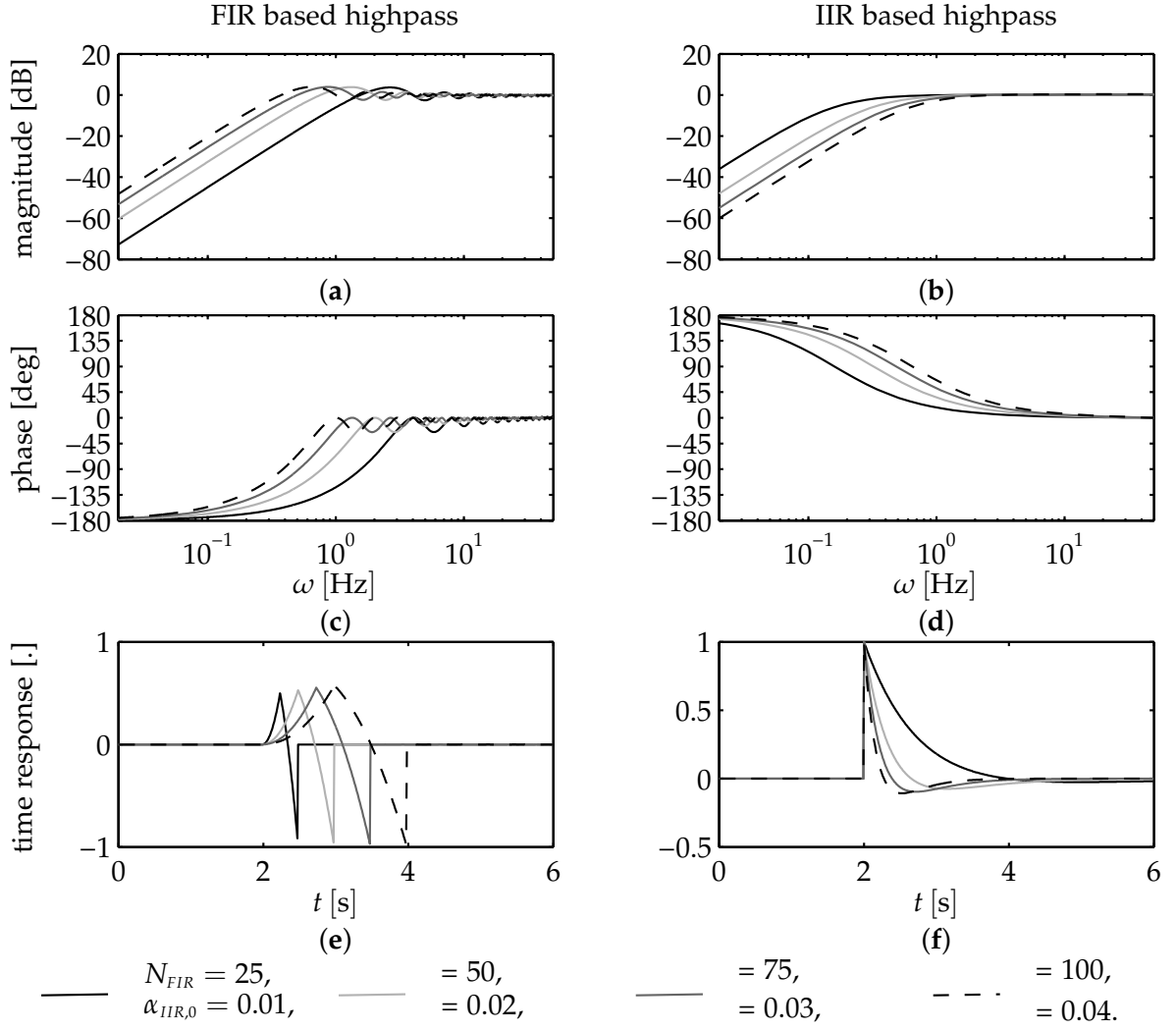
Figure 2.3.: Magnitude (**a**) and (**b**), phase diagrams (**c**) and (**d**) as well as time responses (**e**) and (**f**) of the highpass filters for different design paramters N_{FIR}, α_{IIR}. For the time response the highpass transfer functions are excited by: $H(t - 2s) + 0.5\,(t - 2s)$ with the Heaviside distribution H. The sampling time is 0.01 s.

estimate is beneficial also for the forward and inverse kinematics modelling discussed in chapter 9.

Principally, the estimation process represents a lowpass filtering. Two options for the realization of the lowpass filter are discussed in the following. The first one is the equally weighted moving average filter with the FIR transfer function:

$$G_{FIR} = \frac{\hat{\mu}_\varepsilon(z)}{\varepsilon(z)} = \frac{1}{N_{FIR}} \sum_{i=0}^{N_{FIR}-1} z^{-i}. \tag{2.2.2}$$

The only design parameter is the number N_{FIR} of averaged samples. The second option is an exponentially weighted moving average filter with the IIR transfer function:

$$G_{IIR} = \frac{\hat{\mu}_\varepsilon(z)}{\varepsilon(z)} = \frac{\alpha_{IIR}}{1 - (1 - \alpha_{IIR})\,z^{-1}}. \tag{2.2.3}$$

The only design parameter is the exponential discount factor $\alpha_{IIR} \in [0, 1]$.
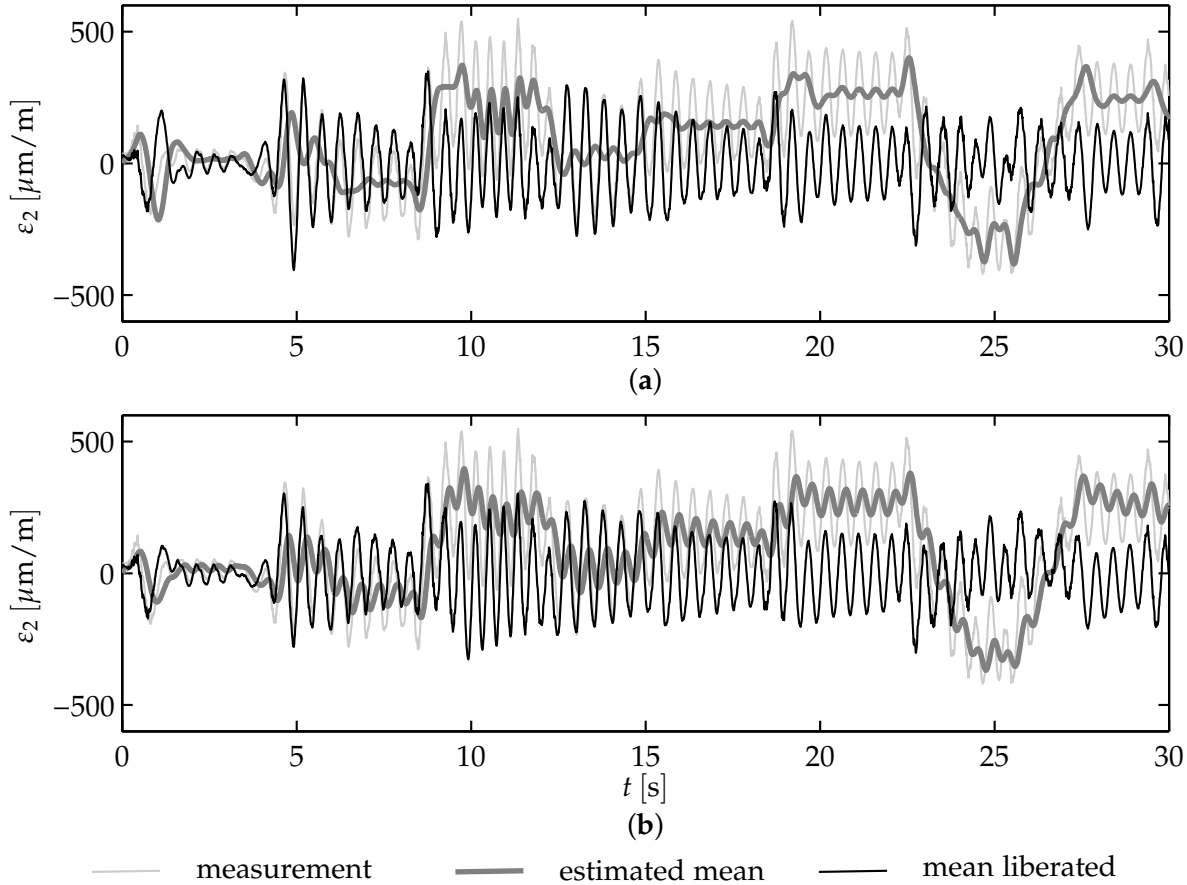
Figure 2.4.: Experimental filtering results for the FIR (**a**) and the IIR (**b**) filter with $N_{FIR} = 50$ and $\alpha_{IIR} = 0.02$. The sample time of both filters is 0.01 s.

Both filters can estimate the running average of stationary input signals. They lag behind any trend in the signal. With TUDOR trends emerge during joint motions. To also remove the trend the same filter can be subsequently applied twice as shown in figure 2.2. In the case of the IIR filter this is known as double exponential smoothing or second order smoothing. This is in particular important for the control concepts with integral strain feedback such as described in chapter 6.

The difference $\tilde{\varepsilon} = \varepsilon - \hat{\mu}_\varepsilon$ is the actually highpass filtered signal. The transfer functions of the corresponding highpass filter is computed from the differences $1 - G_{FIR}$ as well as $1 - G_{IIR}$. Their Bode diagrams are shown in figure 2.3 (**a**) to (**d**) for different design parameters. The magnitudes show an edge steepness of 40 dB/decade. The phase shift in the pass band is close to zero for both filters. The IIR filter basically has smoother magnitude and phase responses, whereas the FIR filter responses both display a slight ripple in the pass-band.

The time domain response to a step input with superposed linear trend is depicted in the figures (**e**) and (**f**).

It is apparent that a larger number N_{FIR} of averaged samples results in a smoother signal, but poorer reactiveness and phase shift. Similarly a smaller discount factor α_{IIR} results in a smoother signal with poorer reactiveness and phase shift.

Experimental results on strain measurements are depicted in figure 2.4. The strain is measured on the second link. To generate the strain curve the joints follow an

input stimulus. The stimulus for each individual joint consists of angle steps with random amplitude at random time steps. The mean liberated stimulus responses $\tilde{\varepsilon}$ for both filters properly oscillate around zero with comparably fast reactions to changing operating points. From the figures, the phase shift between the mean liberated signal $\tilde{\varepsilon}$ and the original measurement ε appears marginal. The intended convergence of the mean liberated signal $\tilde{\varepsilon}$ to zero in static scenarios becomes evident in the damped single step experiments provided in the chapters 5 to 8 of this work.

Both filters have been designed to show basically the same reactiveness. Under this conditions the IIR filter shows a larger ripple in the estimated mean. In essence, both filters can be tuned to have equivalent cut-off frequencies or effective filter durations. Good trade-offs between phase-shift and bandwidth are observed for $N_{FIR} = 50$ and $\alpha_{IIR} = 0.02$. With these settings the occurring phase shifts within the relevant frequency range are acceptable. However, from the experimental results it is found that the FIR filter practically allows a better trade-off in terms of reactiveness and ripple in the moving average. That is why the remainder of this work uses FIR variant despite the larger computational efforts in comparison to the IIR filter.

2.3. Eye in hand camera

The robot can be equipped with an eye in hand camera for visual servoing purpose as done in section 9.1. The idea is to minimize the relative pose error between an actual and a desired view of the scene by commanding appropriate joint velocities. This elegantly allows to position the end effector of an elastic link arm without the need for an accurate model of the load and configuration dependent static structural deflections. The exploitation of the already available sensor as a multi purpose sensor also for oscillation sensing and damping is beyond the scope of this thesis, but has nevertheless been investigated during preparation of this work. The oscillation reconstruction from unstructured and possibly dynamic scenes has been published by Malzahn et al. (2010b) as well as Malzahn, Phung and Bertram (2012c), while the compensation of additional delays introduced by the image acquisition and processing are
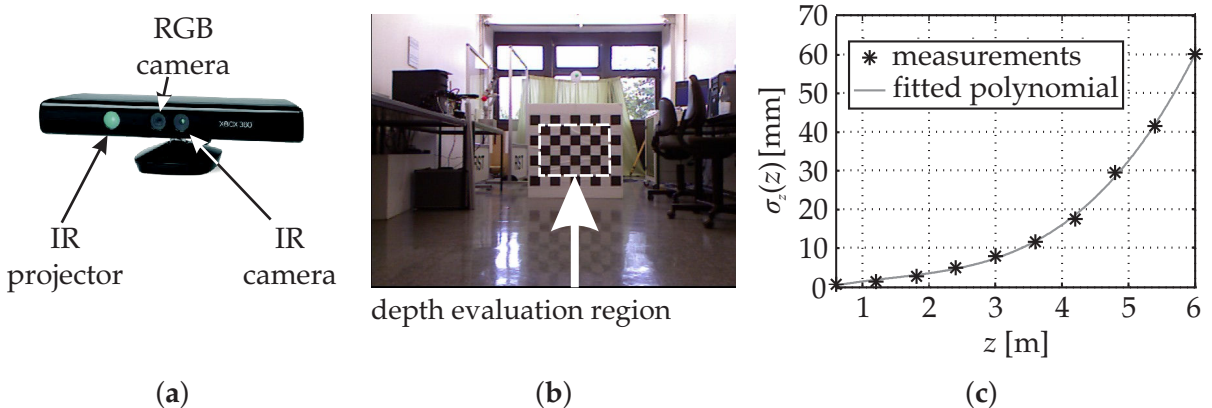

Figure 2.5.: RGB-D camera close-view (**a**). Planar region within a calibration pattern (**b**). Average standard deviation of depth measurements (**c**) evaluated on the pattern at distances between 0.6 and 6 m to the camera. Fitted polynomial: $\sigma_z(z) = 0.51z^3 - 2.1z^2 + 5.12z - 2.18$.

adressed by Malzahn, Phung and Bertram (2012b). The oscillation damping concept Malzahn, Phung and Bertram (2012b) use, is the one described in section 5.

The eye-in-hand configured camera is the Microsoft Kinect (Freedman et al. 2008) depicted in figure 2.5 (**a**). The Kinect integrates a conventional RGB camera with the infrared (IR) projector and the IR camera as depth (D) sensor in a single housing. Therefore it is termed to be an RGB-D sensor.

The sensor provides RGB images at a spatial resolution of 640×480 pixels at a frame rate of 30 Hz. Each color pixel is augmented by a depth measurement. The depth measurement principle relies on the projection of a pseudo random structured light pattern into the scene. The reflected pattern is observed by the IR camera. The per pixel depth image is computed onboard from the reflected pattern via triangulation. The camera together with the mechanical mounting and the tracking spheres has an overall mass of 450 g.

In this work, the effective usable depth range has been determined experimentally to be within 0.6 to 6.0 m. To obtain this range, the checkerboard pattern visible in figure 2.5 (**b**) has been placed at different depths in front of the RGB-D camera perpendicular to the optical axis. The depth uncertainty is considered to be the average standard deviation $\sigma_z(z)$ over all depth measurements and 100 sequentially recorded images per distance step within the planar depth evaluation region indicated in the figure. The result is plotted against the actual distance z in figure 2.5 (**c**). Within the aforementioned effective range the average standard deviation remains below 10 %. An extrapolation indicates that the uncertainty disproportionally increases beyond this range.

Alternatives to the use of the Kinect have been considered. A passive stereo camera setup with comparable accuracy would most probably have a baseline less suitable for eye-in-hand mounting. Additionally the requirement to search for the correspondences within the image pairs contributes additional error sources. An RGB-D camera circumvents this issue.

The loss of the scene depth information due to the perspective projection of a conventional camera could have been tackled by software using "structure from motion" (Oliensis 1999), "depth from focus" (Ens and Lawrence 1993) or "depth from defocus" (Subbarao and Surya 1994) algorithms. Basic techniques are found in textbooks for example by Hartley and Zisserman (2006) or Wöhler (2013). However, this likely leads to degradation of the oscillation sensing accuracy due to error propagation in conjunction with motion reconstruction algorithms applied afterwards.

Data fusion with a motion model incorporating the elastic arm dynamics would contradict the motivating idea of using the camera to precisely position the end effector without exact knowledge about the actual link deflections.

Data fusion with a laser scanner would represent the most precise, but also the most expensive and very bulky alternative.

A technology quite similar to the Kinect is the so-called "Time Of Flight" (TOF) camera (Hansard et al. 2013). TOF cameras measure the delay of IR light impulses emitted by a triggered source and reflected by the scene. The depth information is computed from the known speed of light. The unique measurement range depends on the trigger frequency. Especially those TOF cameras where the triggered light impulses are received with Photonic Mixing Devices (PMD) (Xuming Luan 2001) are

very insensitive to disturbing light sources such as direct sunlight. In this regard the Kinect is restricted to indoor applications. However, the investigation of the camera based oscillation sensing for an elastic arm in this work is pursued in an indoor laboratory environment without direct sunlight. Future technology advances similar to the PMD are assumed to solve disturbing light issues. In the end the low price of about 100 € and especially the higher spatial resolution render the Kinect to be the best choice for the purpose of this work.

2.4. Reference sensors

This section details the reference equipment developed and installed to asses training data as well as ground truth information about the end effector motion and contact forces.

Inertial measurement unit

TUDOR can be equipped with an inertial measurement unit (IMU). The one used here is a CHR-6D unit by CH Robotics. It comprises a ADXL335 3-axes accelerometer and a LPR510AL 3-axes MEMS gyroscope. The main properties of the sensor are summarized in appendix A.4. The sensor is used as a ground truth reference for the camera based oscillation reconstruction. The 6D inter-frame camera motion vector reconstructed by the techniques described by Malzahn, Phung and Bertram (2012c) represents the finite difference approximation of the camera velocity. Therefore the IMU is boxed and mounted directly at the end effector of TUDOR underneath the camera as visible in figure 2.1 (**a**).

External stereo camera system

With conventional rigid robot arms the measurement of the joint angles and knowledge about the link lengths is sufficient to accurately compute the end effector pose with respect to the robot base frame. In contrast, the forward kinematics modeling of elastic link robots is complicated by static deflections. Beyond that, the determination of the end effector pose during oscillations requires a precise model of the elastic link dynamics. Two aspects motivate the development of an external stereo camera setup in this work. The first one is the identification of the forward as well as inverse kinematics models decribed along with the determination of the position accuracy in chapter 9. The second aspect is the evaluation of the proposed oscillation damping concepts presented by Malzahn et al. (2011b). The implementation, calibration and analysis of the setup has been performed within the scope of a supervised thesis by Mr. Bürger (February 2011).

The stereo camera setup is depicted in figure 2.6. It is a convergent camera configuration mounted close to the walls underneath the laboratory ceiling. The optical axes point towards the robot base frame. This way a baseline of 3 m is achieved, while the field of view covers nearly the entire robot workspace.

The two cameras are VRmC-3+ models manufactured by VRmagic. Each camera has a resolution of 640 × 480 pixels and provides 50 frames per second. A complete
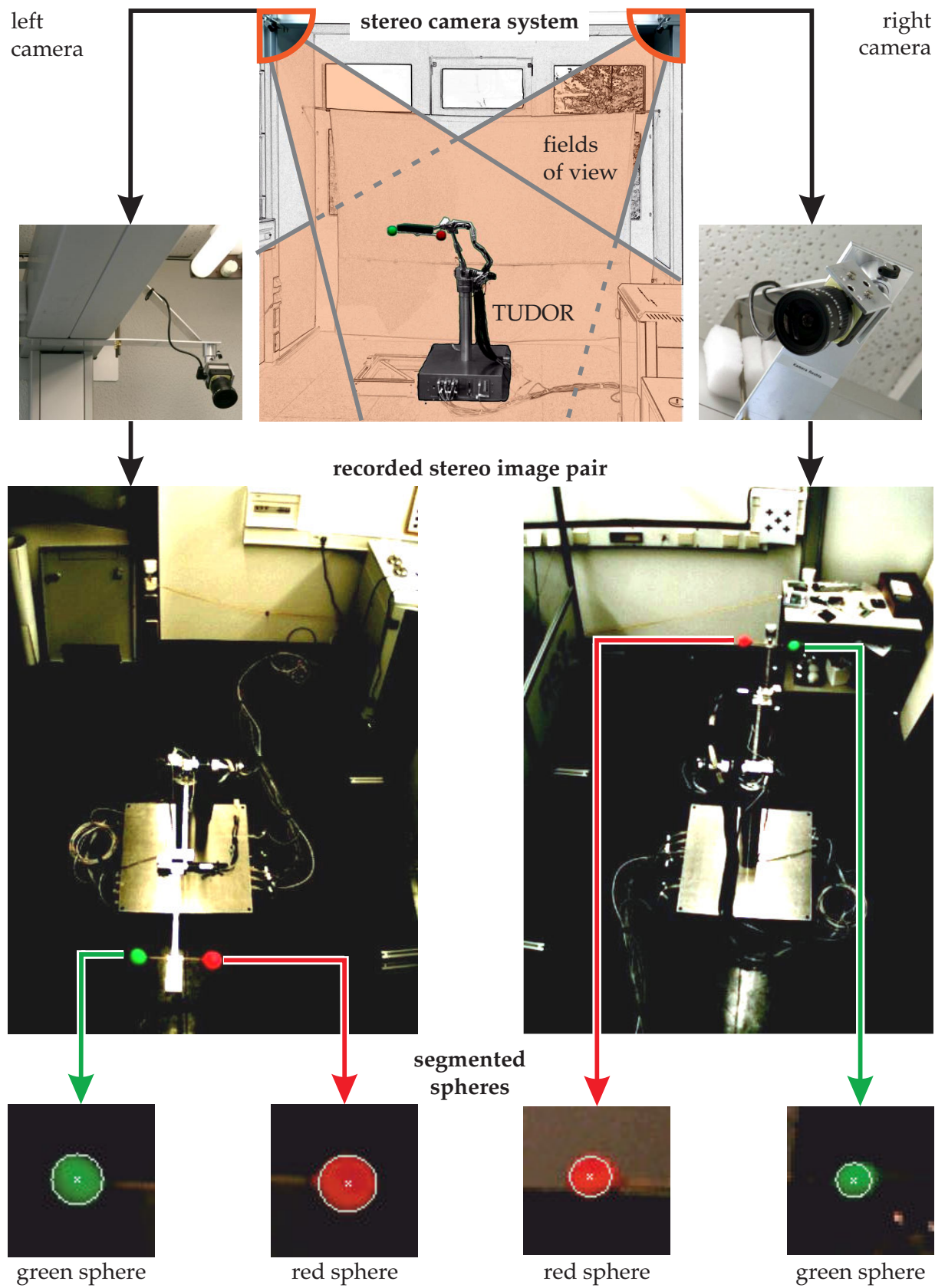
Figure 2.6.: TUDOR within the laboratory environment with illustration of the stereo camera field of view and tracking sphere extraction.

summary of the stereo camera hardware parameters is collected in appendix A.4.

The position measurement is based on the spheres mounted on both sides of the end effector and visible in figure 2.1 (**a**) as well as 2.6. One sphere is green. The other one is red. Therefore the solution to the correspondence problem among the stereo image pairs is straightforward. The colors further simplify the sphere segmentation. The segmentation algorithm is a three step process. Similar to histogram back projection (Swain and Ballard 1990) a normalized Gaussian color model for the spheres is determined in the first step. The color model is determined for each channel of the RGB as well as the HSV color space.

The appearance of the sphere colors in the images strongly depends on the properties of the individual camera sensor as well as the lighting. In the laboratory a mix of varying daylight and artificial ceiling lighting can be found. The color models for both cameras are thus semi-automatically calibrated once per recorded image sequence. A center pixel and an edge pixel are selected for each sphere in a single stereo image pair. The two selected points per pixel define a circle. All pixels within this circle are used to compute the Gaussians.

The per-channel Gaussians reflect the probability that a particular channel value belongs to a sphere pixel. A naive Bayes approach aggregates the individual channel models and yields a probability estimate for a pixel to belong to either the red or green sphere. This way the single color image of one camera is transformed into two probability images, one image for each sphere.

In the second step morphological erosion removes all disturbing pixels in the probability images. The result of this second step finally serves as seed for the region growing algorithm (Adams and Bischof 1994) operating on the probability image results of the first step. The centroid of the region growing output represents the estimate of the sphere location in the image. A result is exemplified in the zoomed views of figure 2.6.

The intrinsic and extrinsic stereo camera calibration is done with the checkerboard pattern visible in figure 2.5 (**b**) and the Camera calibration toolbox for Matlab based on the work by Bouguet (2008). For calibration of the stereo camera system with respect to the robot base frame the robot samples the operating range of the first joint. The second and third joints are kept in their zero configurations. This way the end effector moves on a circular trajectory parallel to the ^1x-^1y-plane. The normal through the circle center is collinear to the ^1z axis. The static deflection of the arm due to its own weight introduces an offset between the circle and the actual ^1x-^1y-plane. This offset is removed based on the known arm length in a vertical arm configuration with $\boldsymbol{\theta} = [0°, 90°, 0°]^{\mathrm{T}}$.

After rectification the position of the segmented spheres with respect to the stereo camera reference frame is computed via triangulation as discussed by Hartley and Zisserman (2006, p. 318). The midpoint of the straight line connecting the sphere centroids is considered to be the end effector position. The tracking of this point from frame to frame allows the reconstruction of end effector motions such as the one illustrated in the figures 2.7 (**a**) to (**d**).

The high end effector velocity causes the motion blur exemplified in figure 2.7 (**e**). It is visible that the first moment of the segmented image regions represents plausible mean locations of the spheres during the camera integration time.
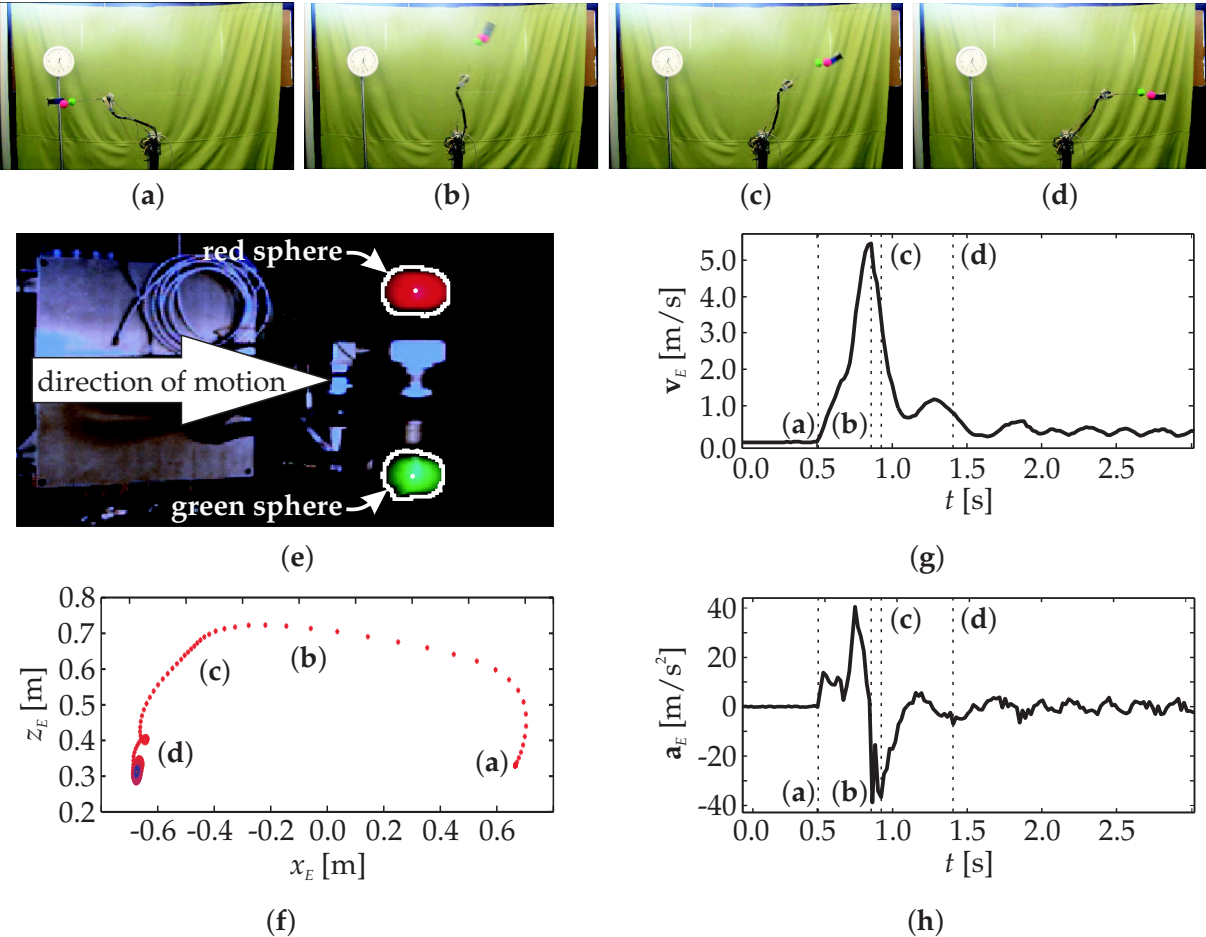
Figure 2.7.: Snapshots of a joint step motion from $\theta = [0°, 45°, -45°]^T$ to $\theta = [0°, 135°, 45°]^T$ (**a**)-(**d**). Motion blurr observed by the stereo camera and sphere segmentation result (**e**). Reconstructed trajectory (**f**) as well as derived velocity (**g**) and acceleration (**h**).

The complete reconstructed end effector trajectory is visible in figure 2.7 (**f**). The trajectory segments with higher velocities are indicated by the larger spacing between the samples. The circular motion close to the trajectory end attributes to the torsional and horizontal oscillations mentioned in section 2.1.

The high frame rate enables the end effector velocity depicted in figure 2.7 (**g**) and the end effector acceleration shown in figure 2.7 (**h**) to be computed from finite differences.

The peak velocity of this motion amounts to 5.5 $\frac{m}{s}$. The maximum absolute acceleration is 40 $\frac{m}{s^2}$.

The end effector localization accuracy amounts to 2 mm. This value is determined from the theoretical and experimental investigation described in the appendix B.5.

Contact cube

The investigation of concepts to exploit the link flexibility in the context of force control, collision detection and reaction necessitates a contact device with force and torque sensing capability to enable ground truth evaluations. The contact cube depicted in figure 2.8 serves as such a device in this work. It is a hollow aluminum cube
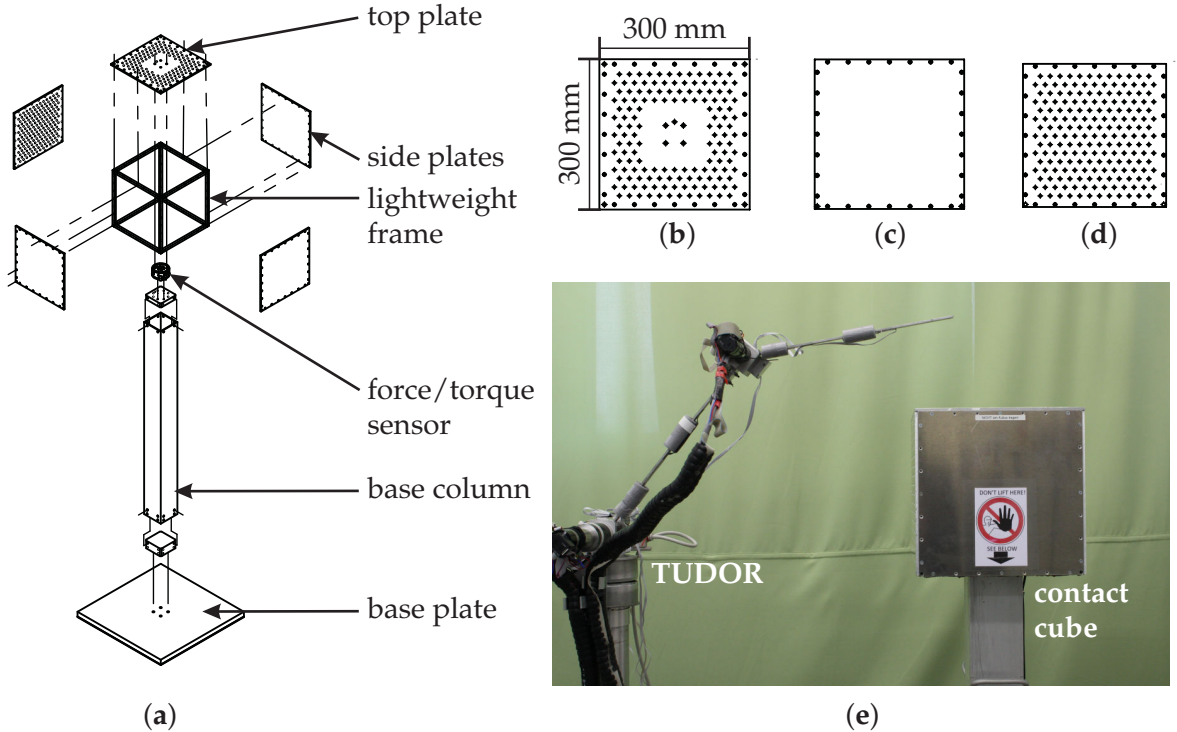
Figure 2.8.: The exploded view of the contact cube (**a**), top plate (**b**), side plate (**c**), side plate with mounting holes (**d**), picture of the contact cube with TUDOR (**e**)

attached to the 6D force/torque sensor. The exploded view in figure 2.8 (**a**) depicts holes in two side plates of the cube. They enable the application of additional surface elements to modify the object characteristics such as shape and impedance. The edge-length of the cube amounts to 300 mm. The measurement range for the vertical contact force F_z is ± 200 N with a resolution of 0.05 N. Further properties are listed in appendix A.4.

2.5. Communication architecture

A total number of four PC systems is involved in the data acquisition and control of TUDOR. The communication setup for these computers is illustrated in figure 2.9. The first PC (xPC) is mounted in the 19" industrial rack with the xPC-Target real-time operating system by Mathworks. All control algorithms for TUDOR run on this PC. The fundamental sample time is 0.5 ms. Measurements such as the encoder readings, motor currents and link strains arrive at the xPC via the main supply cable tree. The main supply cable tree also includes the power supply and hall sensor cables for the motors.

Contact torques and forces are sent from the contact cube to the xPC via RS-232. IMU readings from TUDOR also arrive via RS-232 on a second port.

A console PC serves as programming device for TUDOR. On this PC the controllers are implemented and uploaded to the xPC. The function library developed in this work allows sending motion commands, switching operating modes of TUDOR and downloading measurement data via a TCP/IP connection between the console PC

— USB 2.0
- - ethernet (UDP)
— ethernet (TCP/IP)
..... RS-232
≡ main supply
  cable tree
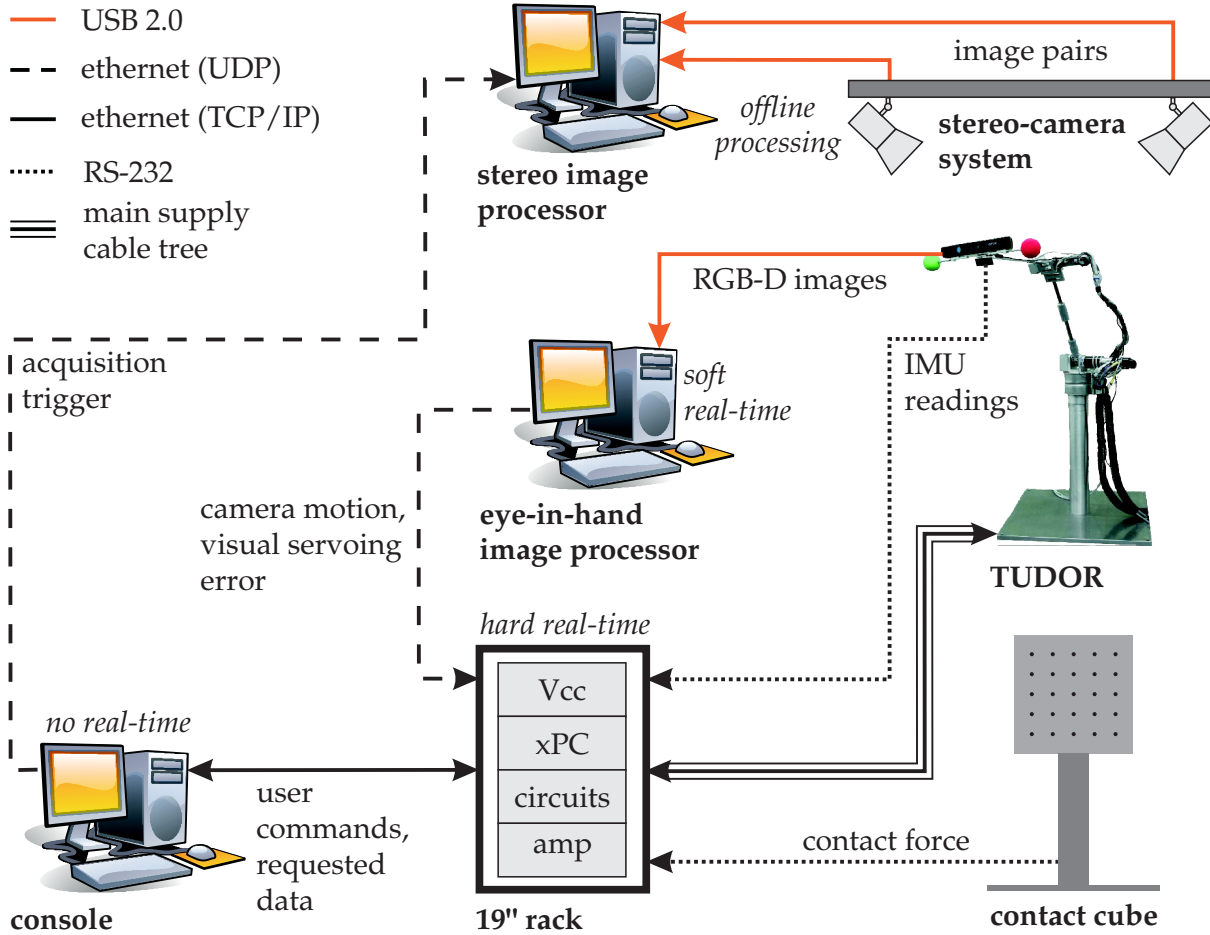
Figure 2.9.: Communication setup for TUDOR

and the xPC.

The console PC triggers the stereo image processor PC to start the stereo image acquisition via UDP.

The image processing for the eye in hand camera is computationally intensive. Most image processing algorithms are rarely realizable to meet hard real-time constraints. Frequently the actual computation time is influenced by the scene contents. Thus, the image processing takes place on the fourth PC under soft real-time conditions. This PC communicates the information extracted from the image sequences to the xPC using UDP. The operating system on this image processing system is Ubuntu-Linux. As a consequence, services running besides the image processing program contribute to the variance of the delay associated with the extracted information. A method to compensate this delay is reported by Malzahn, Phung and Bertram 2012b.

All Ethernet connections are realized within a closed network to avoid package loss and additional delays due to arbitrary network traffic. The characteristic parameters of the individual computers are collected in appendix A.2.

3

Joint Dynamics and Control

The thesis follows an independent joint control strategy, where the whole arm is interpreted as a chain of independent joint link modules. The actuator identification, controller synthesis and evaluation is explained in the following subsections. The last subsection abstracts a general controller architecture as a common basis for the material presented in the subsequent chapters.

3.1. Joint dynamics

The actuators in the joints of TUDOR are brushless DC motors. The power amplifiers for each actuator ship with integrated PI current controllers using the input voltage v_M as reference. The combined amplifier and current controller dynamics are identified as a second order system from multiple step responses spread in the whole operating range as depicted in figure 3.1 (**a**). The second order system with gain k_{amp} and cut-off frequency ω_{amp} achieves an average goodness of fit of 86 % according to the definition given in appendix B.4. The identified parameters are listed in appendix A.3.

The torque balance for the actuator yields:

$$\tau_M = \tau_E - \tau_J - \tau_F. \tag{3.1.1}$$

In this equation τ_M is the mechanical torque actually causing the joint acceleration $\ddot{\theta}$ inversely proportional to the combined rotor and gear inertia I_M. The electrical torque:

$$\tau_E = n_M \, k_\tau \, k_{Amp} \, v_M = k_M \, v_M \tag{3.1.2}$$

is generated from the winding current i_M. The high current controller dynamics compared to the mechanical subsystem enable the closed current loop to be merged with the motor torque constant k_τ and gear ratio n_M to yield a mere gain k_M. The joint load torque τ_J originates from the arm dynamics as well as external interaction torques.

For the joint friction τ_F two different models are used in this work. The first one is taken from Zeng (1999):

$$\tau_F = k_v^+ \, \dot{\theta} + \left(k_v^- - k_v^+ \right) f_1 \left(\dot{\theta} \right) + k_c^+ + \left(k_c^- - k_c^+ \right) f_2 \left(\dot{\theta} \right), \tag{3.1.3}$$
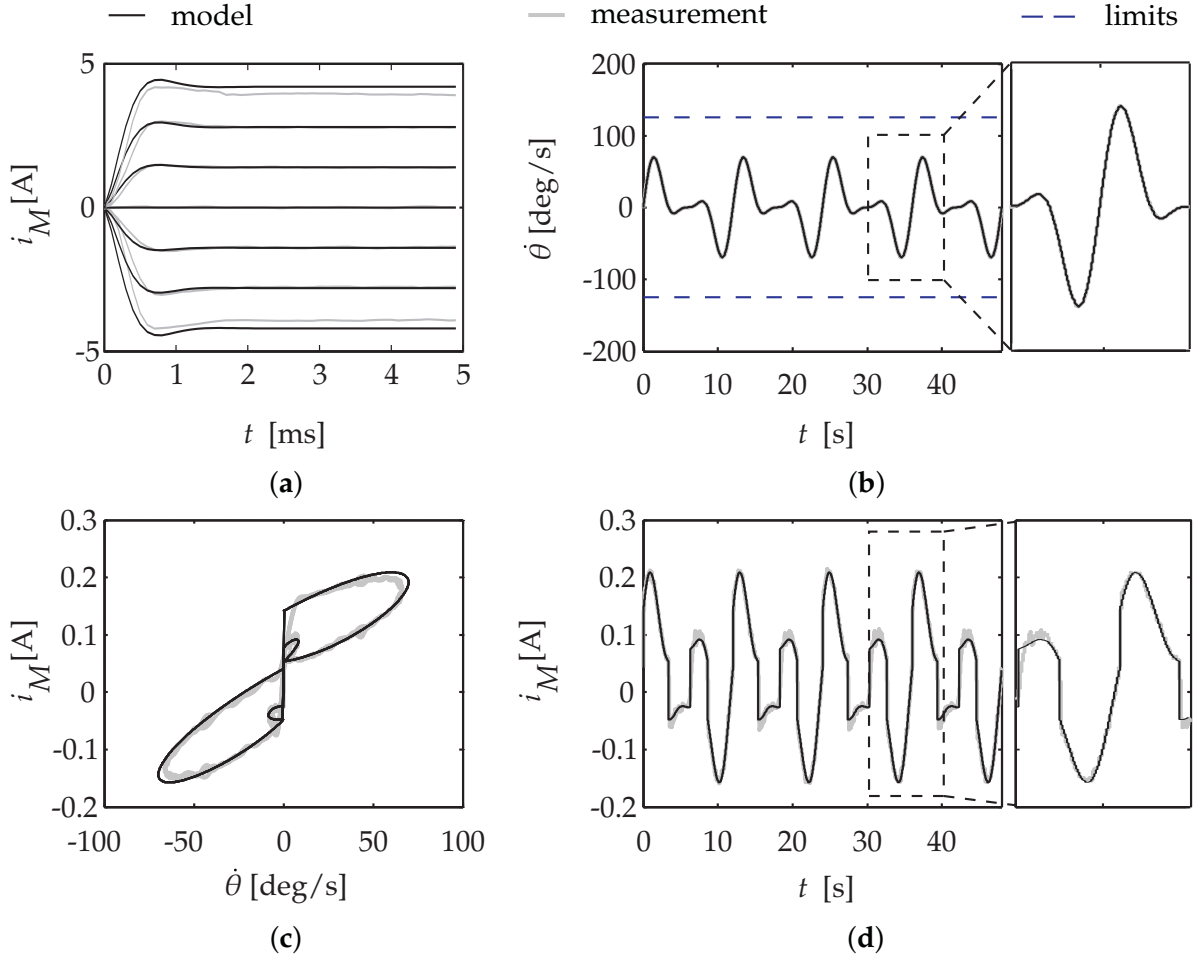
Figure 3.1.: Identification results for the second joint without load. Measured and identified amplifier step response (**a**), planned and realized joint angular velocity stimulus with velocity limits (**b**), measured and identified joint current plotted over joint velocity (**c**) and time (**d**).

with

$$f_1\left(\dot{\theta}\right) = \begin{cases} 0 & \text{if} \quad \dot{\theta} \geq 0 \\ \dot{\theta} & \text{if} \quad \dot{\theta} < 0 \end{cases} \tag{3.1.4}$$

and

$$f_2\left(\dot{\theta}\right) = \begin{cases} 0 & \text{if} \quad \dot{\theta} \geq 0 \\ 1 & \text{if} \quad \dot{\theta} < 0. \end{cases} \tag{3.1.5}$$

The parameters k_v^+ and k_v^- are the velocity-direction dependent viscous friction coefficients while k_c^+ and k_c^- are the corresponding coulomb friction coefficients. This model structure is required for the damped dynamics modelling in chapter 10 as well as detection of collisions between the robot and its environment in chapter 11.

The second and simplified friction model has the form:

$$\tau_F = k_v\,\dot{\theta}, \tag{3.1.6}$$

where k_v is called the symmetric viscous friction coefficient obtained by averaging over the asymmetric coefficients from equation (3.1.3). In section 3.2 this second friction model serves the design of the joint angular controllers based on the linear trans-

fer function model:

$$G_M(s) = \frac{\theta(s)}{v_M(s)} = \frac{k_M}{s(I_M s + k_v)}.$$
(3.1.7)

For identification, the velocity controller described in section 3.2 is designed based on the motor parameters provided by the vendor. The multi-sinus velocity stimulus depicted in figure 3.1 (**b**) excites the joint dynamics. The periodicity allows the noise free computation of higher order signal derivatives based on Fourier analysis as proposed by Swevers, Verdonck and Schutter (2007). The stimulus operates in both the upper and the lower velocity range. The corresponding measured and estimated motor currents are plotted over the joint velocity in figure 3.1 (**c**) and over time in figure 3.1 (**d**). The asymmetric nature of the coulomb friction is clearly visible. The asymmetry in the viscous friction is insignificant and justifies the direction independence of the linear model (3.1.7). The average goodness of fit computed from the motor current i_M on 10 experiments is 89 %. This static result is more than satisfactory against the background that changes in lubrication and temperature drastically influence these parameters over time. The parameters for all joints are listed in appendix A.3.

3.2. Joint angular control

The control objective for each joint is the realization of point-to-point movements without overshoot and vanishing steady state error.

For robotic arms according to Sciavicco and Siciliano (2001) independent joint control is probably "the simplest control strategy that can be thought of". It interprets a robot arm as a chain of independent single-input single-output systems (SISO). It is enabled by the high gear ratios, which reduce coupling forces and torques. In consequence, coupling effects between the individual systems may be considered as disturbances.

For the reasons detailed in section 1.2 centralized concepts such as the inverse dynamics or computed torque control approach known from rigid robots are difficult to apply to elastic link robots. Section 1.2 introduces and chapter 4 experimentally exemplifies the challenges connected with the precise holistic modelling of a multi-elastic-link robot in realistic manipulation scenarios. It renders the achievable benefit questionable in comparison to the required mathematical and computational effort.

On the other hand, the analyses show that the natural oscillation frequencies of all links appear to be measurable with good phase alignment on each of the individual links. This insight leads to the transfer function model in section 5.1. The independent joint control strategy fits well with this modelling approach in view of oscillation damping control of a multi-elastic-link arm.

The independent joint controller described in the following has a cascaded architecture. The cascaded nature simplifies the controller design. At each cascade level the plant is treated as a second order SISO system. In equivalence to a state feedback the closed loop dynamcis can be rigorously shaped whereas rejection of disturbances and nonlinearities improves with each cascade level. The concept is outlined in textbooks such as Sciavicco and Siciliano (2001) or Schröder (2009).

The innermost cascade level comprises the joint current controller shipped with the power amplifiers. This controller is a PI type controller, which rejects nonlinear

effects in the electrical part of the plant and compensates for the mutual induction for instance. Section 3.1 identifies the fast response of the closed current control loop.

The next cascade level is a PI velocity control loop with the transfer function:

$$G_{PI} = \frac{k_{PI}(t_{PI}s + 1)}{s}.$$ (3.2.1)

A sampling frequency of 2 kHz justifies the quasi continuous design. The feedback is based on numerical derivatives of the incremental encoder readings filtered by a first order transfer function G_d with a time constant t_d. The PI controller time constant t_{PI} cancels the slow mechanical time constant of the motor. This mechanical time constant $t_M = \frac{\dot{\theta}_{max}}{\tau_{M,max}} \frac{I_{M,eff}}{k_v}$ includes the effective inertia $I_{M,eff}$ estimated from the geometries and masses of the joint as well as attached subsequent bodies in the joint zero configuration. The gain k_{PI} is tuned according to the symmetrical optimum so that the closed loop exhibits a damping of $D_{PI} = 1/\sqrt{2}$.

Schröder (2009); Sciavicco and Siciliano (2001) realize the position cascade level by applying a proportional controller. However, in view of the linear oscillation feedback proposed in chapter 5, the extension to the PD controller with first order lag element:

$$G_{PD} = \frac{k_{PD}(t_{PD}s + 1)}{t_l s + 1}$$ (3.2.2)

is advantagous for oscillation damping. The PD time constant t_{PD} is tuned to cancel the time constant of the first order approximation of the closed velocity loop. The gain k_{PD} is selected so that the position control loop displays unity gain. A first order filter with lag time constant t_l reduces noise and ensures causality.

A motion planner generates a sinusoidal acceleration profile as detailed by Wenz (2008, p. 89) for each commanded joint motion. For self-containment the underlying equations are summarized in the appendix B.6. The profile is continuously differentiable of infinite order and elegantly avoids impulsive jerk, which minimizes gear wear. The absence of impulsive jerk already contributes to a reduced excitation of structural oscillations. The planner ensures that the controller adheres the acceleration and velocity limits (see appendix A.3), which becomes apparent in the next section.

3.3. Controller evaluation

Figure 3.2 (**a**) depicts the joint angle stimulus response of the second joint. During this experiment TUDOR carries three test mass plates with a total mass of 300 g. All three joints simultaneously respond to individual stimuli comprising of angle setpoint steps with random amplitudes at random timesteps. All joints have been operated with maximum acceleration as well as maximum speed (see appendix A.3).

Figure 3.2 (**b**) provides a close view on the stimulus response. The close view illustrates the smooth acceleration phases and the constant velocity phase generated by the sinusoidal motion planner. The PI velocity controller compensates gravitational load torques as well as joint friction so that the steady state angular position error vanishes below the encoder resolution. There is no overshoot. Even at higher zoom levels disturbances due to the link oscillations are not visible.
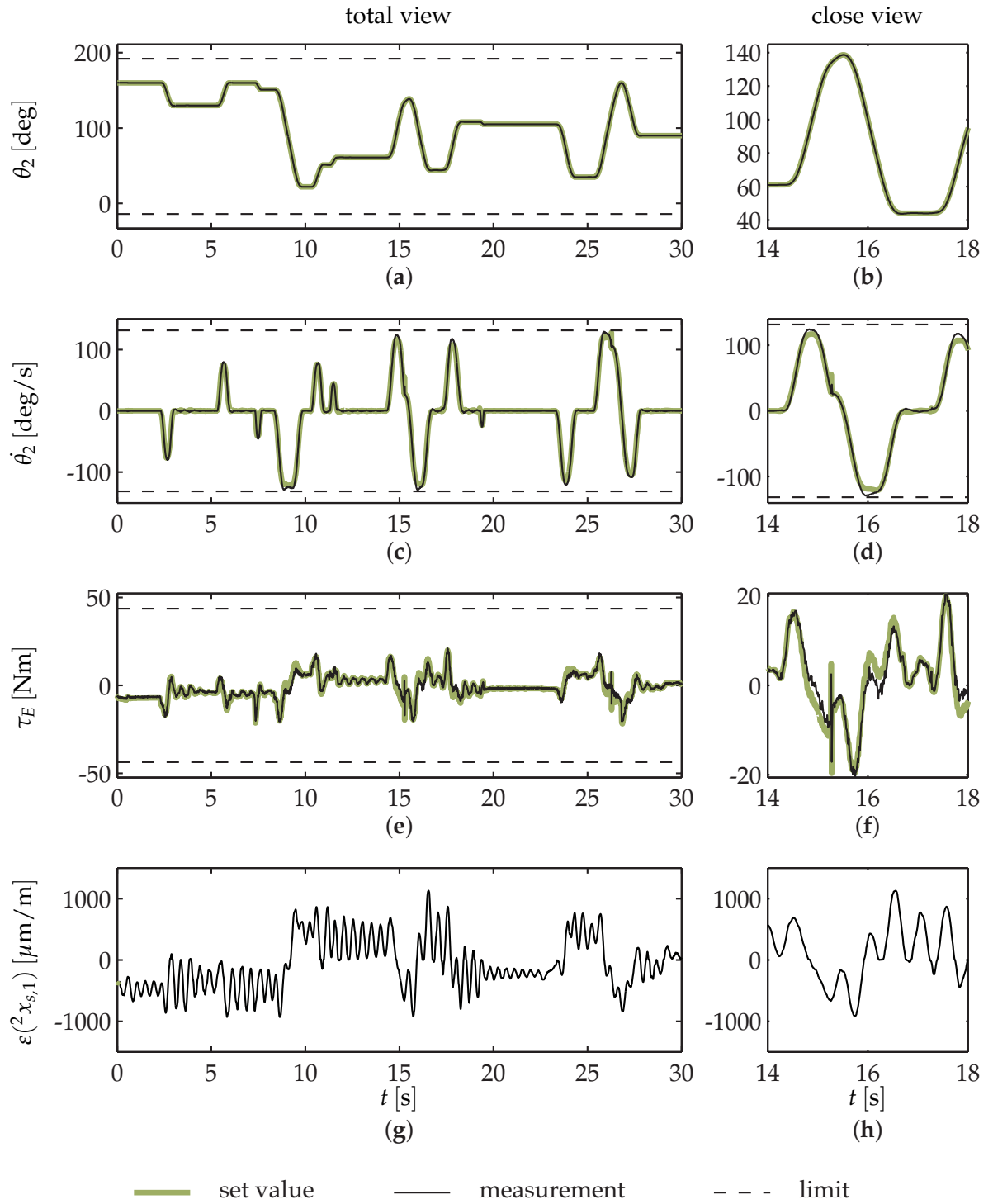
Figure 3.2.: Joint angular position stimulus response (**a**) with close-up (**b**), corresponding velocity profile (**c**) with close-up (**d**) along with the electrical motor torque (**e**), (**f**) and strain (**g**), (**h**) measured on the second link. The responses are recorded for the second joint with TUDOR carrying a 300 g payload at maximum speed and acceleration.
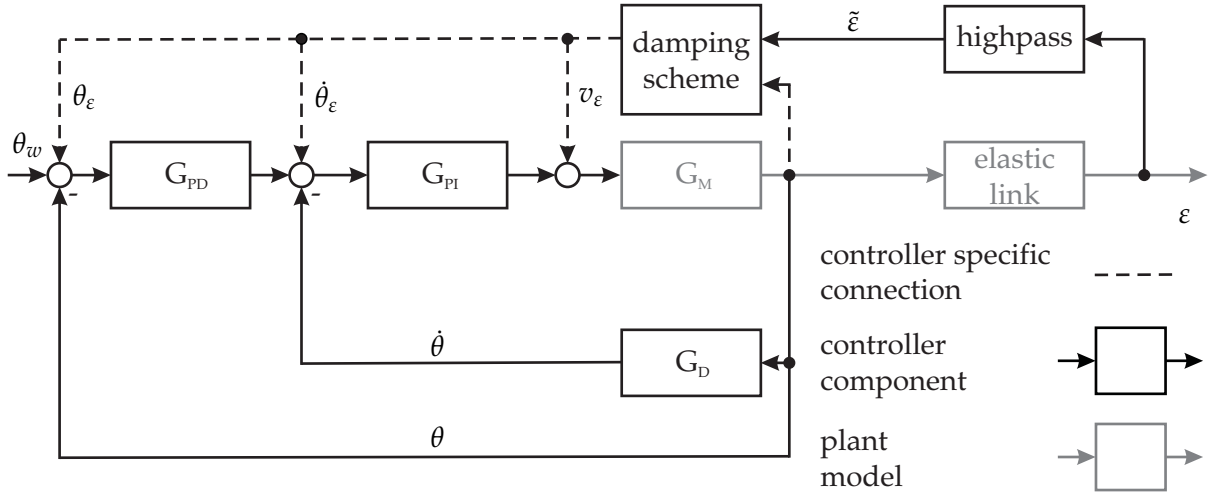
Figure 3.3.: The general independent joint controller architecture developed in this work.

The velocity profile of the stimulus response is depicted in figure 3.2 (**c**). A close view is provided in figure 3.2 (**d**). The velocity profile shows only slight oscillatory disturbances.

Figure 3.2 (**e**) depicts the electrical torque produced by the winding current during the stimulus. Figure 3.2 (**f**) is the corresponding close view. Besides the larger measurement noise originating from the current readings, the torque signal has clearly visible harmonic components. They can be interpreted as the action of rejecting disturbances due to the link oscillations before they influence outer cascade levels. The oscillations are depicted in the figures 3.2 (**g**) and (**h**) based on strain measurements. As a conclusion it may be stated that the joint controller accomplishes the design objectives.

3.4. General control architecture

The independent joint angular controllers are augmented by the oscillation damping schemes presented in the chapters 5 to 7. Figure 3.3 illustrates the integration of the individual damping actions within a general controller architecture. The plant consists of the motor transfer function (3.1.7) with a controller specific oscillatory dynamics representation for the subsequent link connected in series. The oscillations are superposed by the static strain due to gravity. The strain measurement ε is liberated from this static signal portion using the technique explained in section 2.2. The mean liberated measurement $\tilde{\varepsilon}$ is fed to the damping controller. Depending on the particular oscillation damping scheme, additional joint angle feedback may be required. The cascade level at which the damping action enters the joint controller also varies with the concept under consideration. Such optional signals are indicated by dashed lines in the generalized visualization of the controller architecture in figure 3.3.

4

Elastic Link Dynamics Analysis

The chapter initially introduces the terminology and mathematical relations required for the remainder of this work. Beyond that, the theoretical analyses and experimental investigations carried out confirm the notion acquired from the literature survey regarding the complexity of the elastic arm dynamics as well as the applicability of controllers relying on holistic plant models. This chapter constitutes the foundation of the decisions, which lead to the control strategy proposed in this work.

4.1. Preliminary assumptions

The derivations presented in the remainder of this chapter are based on a set of assumptions, which are summarized in the following.

Assumptions 4.1.1: *The elastic links are modeled as Euler-Bernoulli-beams, so that:*

(a) ...*the deflections are small in comparison to the beam length,*

(b) ...*the neutral fiber has constant length,*

(c) ...*the deflections are elastic and reversible so that Hooke's law applies,*

(d) ...*the rotation of a differential beam element is negligible compared to the translation so that cross sections perpendicular to the neutral fiber remain perpendicular,*

(e) ...*the angular distortion of a beam element is small in relation to the transversal bending deformation,*

(f) ...*the beam is uniform and homogenous.*

4.2. The equation of motion

Consider the planar differential beam element of infinitesimal length dx sketched in figure 4.1. In accordance to the rigid body kinematics in figure 2.1 (**b**) the deflection of the beam at a time instant t is measured in the preceding joint frame as the y-coordinate at a location x along the undeflected neutral fiber.

Figure 4.1.: Undeformed differential beam element (*left*) and bent differential beam element (*right*) with bending moments and forces

From assumption 4.1.1 (**a**) we find that the bending angle θ_b corresponds to the first spatial derivative of the bending curve $y(x,t)$:

$$\theta_b(x,t) \approx \tan\theta_b(x,t) = \frac{\partial y(x,t)}{\partial x}. \tag{4.2.1}$$

With assumption 4.1.1 (**b**) all bent beam fibers are concentric arc segments, such that a fiber at a distance y_b to the neutral fiber is subject to the strain $\varepsilon(x,t)$:

$$\varepsilon(x,t) = y_b \frac{\partial\theta_b(x,t)}{\partial x} = y_b \frac{\partial^2 y(x,t)}{\partial x^2}. \tag{4.2.2}$$

Based on assumption 4.1.1 (**c**) Hooke's law relates the strain $\varepsilon(x,t)$ to the bending moment τ_b:

$$\tau_b(x,t) = -\frac{EI_z(x)}{y_b}\varepsilon(x,t) = -EI_z(x)\frac{\partial^2 y(x,t)}{\partial x^2}, \tag{4.2.3}$$

where E represents the Young's Modulus and $I_z(x)$ describes the area moment of inertia about the bending axis. The product $EI_z(x)$ is called the beam stiffness.

The assumptions 4.1.1 (**d**) and (**e**) are known as the Bernoulli hypotheses (Meirovitch 2001, p. 384). Their validity allows the cross sectional rotary inertia as well as the shear modulus to be neglected in the beam equations of motion. This way, for the infinitesimal beam element in figure 4.1 the force balance in the vertical direction equates to:

$$F_y(x,t) - \left(F_y(x,t) + \frac{\partial F_y(x,t)}{\partial x}\mathrm{d}x\right) + f_{ext}(x,t)\mathrm{d}x = \rho_b(x)\mathrm{d}x\frac{\partial^2 y(x,t)}{\partial t^2}. \tag{4.2.4}$$

Similarly, the moment balance is:

$$\tau_b(x,t) - \left(\tau_b(x,t) + \frac{\partial \tau_b(x,t)}{\partial x}\mathrm{d}x\right) + \frac{1}{2}f_{ext}(x,t)\mathrm{d}x\,\mathrm{d}x + \dots$$
$$- \left(F_y(x,t) + \frac{\partial F_y(x,t)}{\partial x}\mathrm{d}x\right)\mathrm{d}x = 0. \tag{4.2.5}$$

The variable $\rho_b(x)$ denotes the beam mass per unit length, F_y is the inner shearing force and f_{ext} is the external force density function.

From the infinitesimal perspective, second order terms of dx may be neglected, so that both balances simplify to:

$$-\frac{\partial F_y(x,t)}{\partial x} + f_{ext}(x,t) = \rho_b(x)\frac{\partial^2 y(x,t)}{\partial t^2}, \tag{4.2.6}$$

$$F_y(x,t) = -\frac{\partial \tau_b(x,t)}{\partial x}. \tag{4.2.7}$$

Using assumption 4.1.1 (**f**) the area moment of inertia I_z as well as the mass per unit length ρ_b becomes constant. Combining equations (4.2.6), (4.2.7) and expressing the bending moment by the right side of equation (4.2.3) yields the Bernoulli Beam partial differential equation (PDE):

$$\rho_b\frac{\partial^2 y(x,t)}{\partial t^2} + EI_z\frac{\partial^4 y(x,t)}{\partial x^4} = f_{ext}(x,t). \tag{4.2.8}$$

Unlike the transversal oscillations of strings, the longitudinal oscillations of rods or the torsional oscillations of shafts this PDE is fourth order. The consequences become apparent in chapter 7 for example.

4.3. The general solution

The common approach to solve equation (4.2.8) is to assume a separability of the spatial and temporal dependances (Dukkipati and Srinivas 2005; Meirovitch 2001):

$$y(x,t) = \Phi(x)v(t), \tag{4.3.1}$$

where $\Phi(x)$ describes the deflection shape and $v(t)$ reflects the temporal amplitude.

Consider the harmonic case with $f_{ext} = 0$. The substitution in the PDE (4.2.8) leads to:

$$-\frac{EI_z}{\rho_b}\frac{d^4\,\Phi(x)/d\,x^4}{\Phi(x)} = \frac{d^2\,v(t)/d\,t^2}{v(t)} = \omega^2. \tag{4.3.2}$$

Note, the dependance on the spatial variable x is collected on the left while the temporal dependance is kept on the right side of the equation. The equality holds for all times t and $0 \leq x \leq L$. Hence, the ratios on both sides of the equations must be constant. This constant is the eigenvalue denoted by ω^2. Both sides of equation (4.3.2) are independent ordinary differential equations (ODE).

The first ODE depends on the spatial variable x. With the introduction of the wave number k_ω:

$$k_\omega = \sqrt[4]{\frac{\omega^2\,\rho_b}{EI_z}}, \tag{4.3.3}$$

it follows:

$$\frac{d^4\,\Phi(x)}{d\,x^4} + k_\omega^4\,\Phi(x) = 0. \tag{4.3.4}$$

By substitution of the exponential form $\Phi(x) = \hat{a}\,e^{\lambda\,x}$ in equation (4.3.4) we find the characteristic equation $\lambda^4 + k_\omega^4 = 0$. Its roots provide the general solution to the ODE:

$$\Phi(x) = {}^{+}\hat{a}\,e^{-j\,k_\omega\,x} + {}^{-}\hat{a}\,e^{j\,k_\omega\,x} + {}^{+}\hat{a}_N\,e^{-k_\omega\,x} + {}^{-}\hat{a}_N\,e^{k_\omega\,x}. \tag{4.3.5}$$

With the equivalences provided in the appendix B.1, this solution can be rewritten in terms of hyperbolic functions:

$$\Phi(x) = \hat{a}_1 \sinh(k_\omega x) + \hat{a}_2 \cosh(k_\omega x) + \hat{a}_3 \sin(k_\omega x) + \hat{a}_4 \cos(k_\omega x), \qquad (4.3.6)$$

where:

$$^{+}\hat{a} = \frac{\hat{a}_4 + j\hat{a}_3}{2}, \quad ^{-}\hat{a} = \frac{\hat{a}_4 - j\hat{a}_3}{2}, \quad ^{+}\hat{a}_N = \frac{\hat{a}_2 - \hat{a}_1}{2}, \quad ^{-}\hat{a}_N = \frac{\hat{a}_2 + \hat{a}_1}{2}. \qquad (4.3.7)$$

The task of finding the amplitudes $\hat{a}_i$ is called the solution of the boundary value problem defined by (4.3.4) and a total number of four boundary conditions.

The second ODE depends on the time variable t:

$$\frac{d^2 v(t)}{dt^2} + \omega^2 v(t) = 0. \qquad (4.3.8)$$

The solution has the exponential form $v(t) = a\, e^{j\lambda t}$. The substitution of this form in equation (4.3.8) leads to the characteristic polynomial $\lambda^2 + \omega^2 = 0$ with the roots $\lambda_{1,2} = \pm\sqrt{-\omega^2}$. Hence, with the equivalences provided in appendix B.1 a general solution to the ODE is:

$$v(t) = \hat{a}_5 \sin\omega t + \hat{a}_6 \cos\omega t. \qquad (4.3.9)$$

The task of finding the amplitudes $\hat{a}_5$ and $\hat{a}_6$ is called the solution to the initial value problem defined by (4.3.8) and a total of two initial values of $v(t)$ or its derivatives.

4.4. Special solutions to the boundary value problem

In a number of publications on the control of elastic link robot arms the beams are considered to be clamped at the joint hub side and free at the tip side. Luca and Siciliano (1991) point out, that "it is more correct to consider mass boundary conditions representing balance of moment and shearing force" at the other end. In the context of an elastic link robot it should be noted, that the rigid clamping at the hub implies a strong disturbance rejection of the joint controller as well as a rigid joint shaft and link flange. A weak rejection or a flexible shaft is rather reflected by a spring at the hub.

As a conclusion the boundary value problem discussed in the following is an elastic beam with a rotary spring support at the hub and a load mass m_L as well as a load
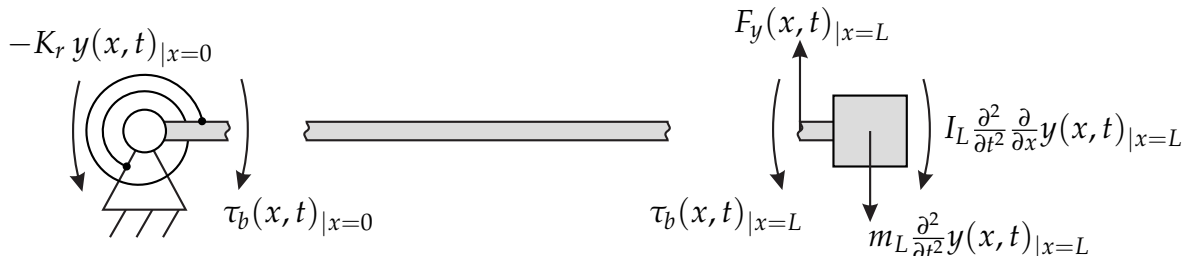

Figure 4.2.: Free body diagrams for the boundary conditions of a beam with a rotary spring support at the hub and a load mass and inertia at the tip.

inertia I_L at the tip. This boundary value problem models the situation for a particular planar link within a kinematic chain of a multi-elastic-link robot arm having only revolute joints. The influence of gravity is neglected for a moment at this point. The boundary conditions are illustrated in the free body diagrams of figure 4.2. From equation (4.3.8) a second order temporal derivative corresponds to a multiplication by $-\omega^2$. Mathematically the boundary conditions are stated as follows:

$$y(x,t)|_{x=0} = 0, \tag{4.4.1}$$

$$\frac{\partial y(x,t)}{\partial x}\bigg|_{x=0} = \frac{EI_z}{K_r}\frac{\partial^2 y(x,t)}{\partial x^2}\bigg|_{x=0}, \tag{4.4.2}$$

$$\frac{\partial^2 y(x,t)}{\partial x^2}\bigg|_{x=L} = -\frac{I_L}{EI_z}\frac{\partial^2}{\partial t^2}\frac{\partial y(x,t)}{\partial x}\bigg|_{x=L} \qquad = k_\omega^4\frac{I_L}{\rho_b}\frac{\partial y(x,t)}{\partial x}\bigg|_{x=L}, \tag{4.4.3}$$

$$\frac{\partial^3 y(x,t)}{\partial x^3}\bigg|_{x=L} = \frac{m_L}{EI_z}\frac{\partial^2}{\partial t^2}y(x,t)|_{x=L} \qquad = -k_\omega^4\frac{m_L}{\rho_b}y(x,t)|_{x=L}. \tag{4.4.4}$$

The spring stiffness K_r models the elasticity of the link flange as well as the disturbance rejection properties of the joint angular controller. The load represents the aggregated mass and inertia of subsequent joints and links in the chain including the payload at the end effector.

The characteristic equation of the boundary value problem is:

$$\frac{k_\omega EI_z}{K_r}\left(\cos\left(\beta_L\right)\sinh\left(\beta_L\right) - \cosh\left(\beta_L\right)\sin\left(\beta_L\right) + \ldots\right.$$

$$-\frac{2k_\omega m_L}{\rho_b}\sin\left(\beta_L\right)\sinh\left(\beta_L\right) - \frac{2k_\omega^3 I_L}{\rho_b}\cos\left(\beta_L\right)\cosh\left(\beta_L\right) + \ldots$$

$$-\frac{k_\omega^4 I_L m_L}{\rho_b}\left(\cos\left(\beta_L\right)\sinh\left(\beta_L\right) + \cosh\left(\beta_L\right)\sin\left(\beta_L\right)\right) + \ldots$$

$$+ m_L\frac{k_\omega}{\rho_b}\left(\cos\left(\beta_L\right)\sinh\left(\beta_L\right) - \cosh\left(\beta_L\right)\sin\left(\beta_L\right)\right) + \ldots$$

$$- I_L\frac{k_\omega^3}{\rho}\left(\cos\left(\beta_L\right)\sinh\left(\beta_L\right) + \cosh\left(\beta_L\right)\sin\left(\beta_L\right)\right) + \ldots$$

$$+ I_L m_L\frac{k_\omega^4}{\rho_b^2}\left(1 - \cos\left(\beta_L\right)\cosh\left(\beta_L\right)\right) + \ldots$$

$$+ 1 + \cos\left(\beta_L\right)\cosh\left(\beta_L\right) = 0, \tag{4.4.5}$$

with $\beta_L = k_\omega L$. The detailed derivation is provided in the appendix B.3.

Under the conditions of a perfectly rigid clamping the characteristic equation reduces to:

$$1 + \cosh\left(\beta_L\right)\cos\left(\beta_L\right) + \ldots$$

$$+ m_L\frac{k_\omega}{\rho_b}\left(\cos\left(\beta_L\right)\sinh\left(\beta_L\right) - \cosh\left(\beta_L\right)\sin\left(\beta_L\right)\right) + \ldots$$

$$- I_L\frac{k_\omega^3}{\rho_b}\left(\cos\left(\beta_L\right)\sinh\left(\beta_L\right) + \cosh\left(\beta_L\right)\sin\left(\beta_L\right)\right) + \ldots$$

$$+ I_L m_L\frac{k_\omega^4}{\rho_b^2}\left(1 - \cos\left(\beta_L\right)\cosh\left(\beta_L\right)\right) = 0, \tag{4.4.6}$$

37

which agrees with the results Luca and Siciliano (1989, 1991) present. Additionally, the choice $I_L = m_L = 0$ results in the characteristic equation of the clamped-free cantilever found in fundamental textbooks on the mechanics of vibrations (Dukkipati and Srinivas 2005; Meirovitch 2001).

The characteristic equations (4.4.5) and (4.4.6) represent transcendental equations. They have an infinite number of roots $\beta_{L,r}$, which implies that the beam has an infinite number of natural frequencies ω_r with $r = 1, 2, \ldots \infty$.

From the definition of the wave number k_ω in equation (4.3.3) the natural frequencies ω_r compute to:

$$\omega_r = \beta_{L,r}^2 \sqrt{\frac{EI_z}{\rho_b L^4}}. \tag{4.4.7}$$

In turn, from equation (4.3.6) we find a natural mode shape function $\Phi_r(x)$ for each natural frequency ω_r. The mode shape functions represent the set of possible beam deformations under the given boundary conditions. Since equation (4.3.4) is homogenous, they can only be determined up to a scale. The normalization derived in the appendix B.3 ensures that the mode shapes are orthogonal, so that the total spatial deflection function $\Phi(x)$ can be expressed as a linear combination of all mode shapes. This leads to the absolutely convergent series:

$$\Phi(x) = \sum_{u=1}^{n_u} w_u \, \Phi_u(x), \quad \text{with } n_u \to \infty. \tag{4.4.8}$$

where for the example of a perfectly rigid clamping the weights w_u are defined according to:

$$w_u = \int_0^L \rho_L \Phi_u(x)\Phi(x)\mathrm{d}x + m_L \Phi_u(x)_{|x=L}\Phi(x)_{|x=L} + \ldots$$
$$+ I_L \frac{\mathrm{d}\Phi_u(x)}{\mathrm{d}x}_{\Big|x=L} \frac{\mathrm{d}\Phi(x)}{\mathrm{d}x}_{\Big|x=L}. \tag{4.4.9}$$

In practice the weights w_u must be identified experimentally. Therefore the dynamic deflection has to be observed from distributed strain (Garcia, Feliu and Somolinos 2001; Pisoni et al. 1995) or acceleration (Hillsley and Yurkovich 1993) measurements or directly measured using markers and an external camera sensor (Feliu, Rattan and Brown 1992; Li and Chen 2002).

4.5. Natural frequencies under varying boundary conditions

One question arising from the previous section asks how the natural frequencies change with a variation in the boundary conditions. First, a perfectly rigid clamping is assumed, so that K_r tends to infinity and the characteristic equation (4.4.6) can be used. The variable parameters in the equation are the total load mass m_L as well as the total load inertia I_L normalized by the beam density per unit length ρ_b. Initial values for the frequencies are obtained by graphical inspection of the characteristic equation. The accurate values are determined using Brent's method (Brent 1972, ch. 4).
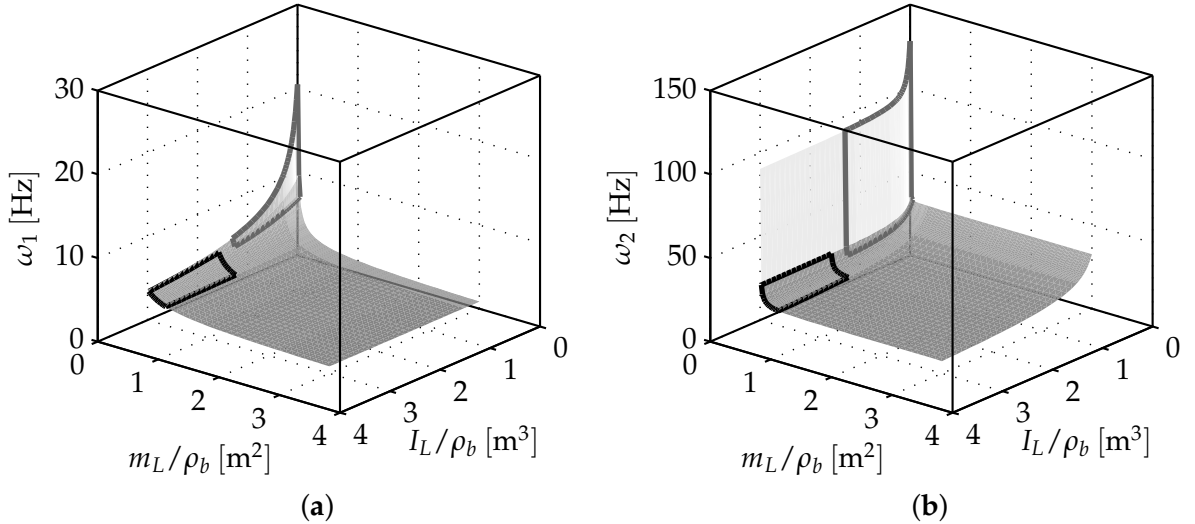
Figure 4.3.: First (**a**) and second (**b**) natural frequency of a rigidly clamped beam with varying ratios of the total load mass m_L as well as the total load inertia I_L to the beam density per unit length ρ_b. The thick lines enclose the frequency regions of the second (*black*) and third (*gray*) link of TUDOR when mounting mass plates with m_L between 0 and 0.6 kg and I_L from 0 to $3.3 \cdot 10^{-4}$ kgm^2 at the end effector. Note, that for the second link the third joint-link-module contributes to the load mass m_L and inertia I_L.

The figures 4.3 (**a**) and (**b**) show the theoretical variation of the first two natural frequencies ω_1 and ω_2. It is visible that the frequencies vary drastically if any of the ratios is below or close to 1. If the load mass or inertia is large, compared to the beam mass, only slight variations in the frequencies can be observed. The latter situation converges to the case where the load may be considered to be connected to a massless spring.

With TUDOR the applied test masses m_L at the end effector range from 0 to 600 g. The associated rotary inertia are between 0 to $3.3 \cdot 10^{-4}$ kgm^2. The framed regions in both figures indicate the corresponding frequencies obtained from the characteristic equation. The black frames belong to the second link which also has the third joint and link as load. The first frequency $^2\omega_1$ ranges from 2.2 Hz to 4.5 Hz. The second frequency $^2\omega_2$ theoretically ranges between 8.6 Hz and 21.8 Hz.

The gray frame belongs to the third link which carries just the test payload. The first frequency $^3\omega_1$ ranges from 4.5 Hz to 20.5 Hz. The second frequency $^3\omega_2$ ranges between 17.2 Hz and 128.2 Hz.

A second question arising from the previous section concerns the boundary condition at the joint hub. So far perfectly rigid clamping has been assumed. For an elastic link actuated by a revolute joint this assumption is intuitive regarding the beam deflection. However, the situation is different regarding the bending angle. In practice, at least a moderate compliance in the joints is likely to be observed due to harmonic gears, long joint shafts, flanges or transmission belts. Reaction torques from the link oscillations feed back to the joint. The joint controller may have a strong but finite disturbance rejection capability. Thus, the joint control also introduces certain compliance.

The figure 4.4 depicts the natural frequencies for a variation in the rotary clamping
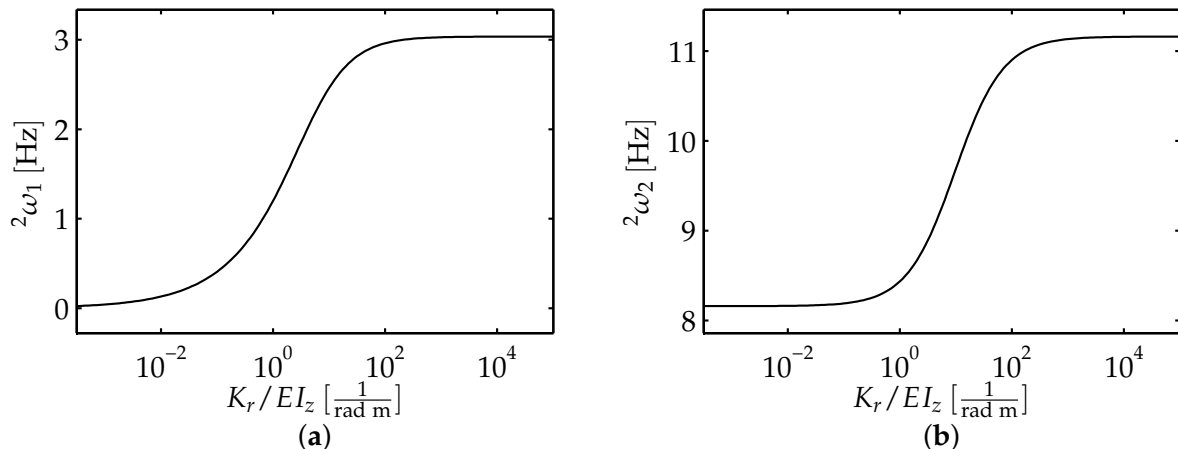
Figure 4.4.: First (**a**) and second (**b**) natural frequency of a beam with varying clamping stiffness.

stiffness K_r in the characteristic equation (4.4.5). The clamping stiffness is normalized by the beam stiffness EI_z. The underlying scenario is the second link of TUDOR carrying the third joint and third link as well as a test payload of $m_L = 0.3\,\text{kg}$ and $I_L = 1.6 \cdot 10^{-4}\,\text{kgm}^2$.

It is visible that the frequencies drop by about 3 Hz in the range of $10^{-2}\,\frac{1}{\text{rad m}} < K_r/EI_z < 10^2\,\frac{1}{\text{rad m}}$. This is a change of 99 % for the first and 26 % for the second frequency. The variation saturates beyond this range.

In view of the boundary conditions a conclusion is that rather stiff elastic links interfere with moderately elastic joints. Furthermore the joint controller can be expected to have an influence on the actually observed values of the natural frequencies.

4.6. Mode shapes under varying load mass and inertia

The load dependent variation of the natural frequencies is strongly connected with a change in the normalized mode shapes. Consider the second link of TUDOR carrying the third joint and third link as well as end effector test masses m_L in the range of 0 to 600 g as load. The clamping is assumed to be perfectly rigid, so that the characteristic equation (4.4.6) holds. For each test mass it is convenient to normalize the mode shapes according to equation (B.3.20). The resulting assumed mode shapes are depicted in figure 4.5.

With increasing load the maximum absolute values of the mode shape functions grow. This agrees with growing end effector oscillation amplitudes observed in experiments with TUDOR. The difference between subsequent mode shapes shrinks for larger payloads. This is in accordance with figure 4.3, where the frequency variation flattens for higher ratios m_L/ρ_b and I_L/ρ_b.

The interpretation of the graphs in the context of elastic link robots is that the boundary conditions must be well known in order to infer the pose of any point along the links using a finite approximation of equation (4.4.8). In fact, the computation of the kinematics already involves knowledge about the arm dynamics.
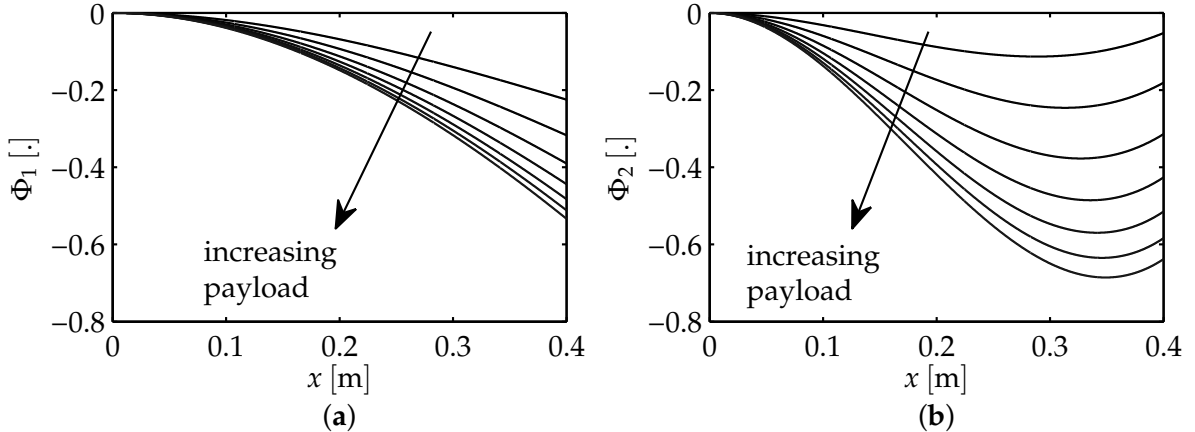
Figure 4.5.: First (**a**) and second (**b**) normalized modeshape for the second link of TUDOR, which carries the third joint, the third link as well as varying end effector masses as load.

4.7. Frequency measurements

In order to verify the theoretical relations between the load and the natural frequencies experimentally, a few provisions must be made. The gearboxes of TUDOR's joints show a backlash. The joint controllers would display an additional compliance. To minimize such effects the second link is detached from the second joint and directly clamped to the robot base. The third joint is mounted to the end of the second link. To minimize the effect of backlash and to disburden the joint brakes in the case of deactivated joint controllers, the flange of the third link is rigged with an additional fixture.

Figure 4.6 (**a**) shows strain measurement time series. The strain measurement has been acquired simultaneously on both elastic links of TUDOR during a hammer excitation at the end effector. The strain amplitude on the second link is significantly larger than on the third link. Both oscillations are slightly damped. The oscillations last more than a minute. In both measurements the higher order dynamics decay within one second and the long-lasting predominant lower frequency oscillation is clearly in phase. The evaluation of the phase information obtained from a Discrete Fourier Transform (DFT) prove that this is the case up to a frequency range of 20 Hz.

The normalized amplitude spectra depicted in figure 4.6 (**b**) are computed by a DFT on the whole time series presented in figure 4.6 (**a**). It must be noted that all visible frequency peaks in the measurements of one link are individually present in the spectra obtained on the other link. The peaks at 2.0 Hz and 9.9 Hz are shifted about 1 Hz leftwards from the theoretical values of the second link with corresponding load. Similarly the rather small peak at 6.3 Hz is one 1 Hz larger compared to theoretical first natural frequency of the third link. The deviations between the actually measured frequencies and the theoretical ones are presumed to originate from the still imperfect clamping, inaccurate knowledge about the rotary inertias, neglected masses such as the supply cables for the third joint and the sensors. This is plausible against the background that in this thesis all such influences have been mathematically shown to reduce the natural frequencies as observed (see fig. 4.3).

From additional measurements it can be summarized that two frequencies are al-
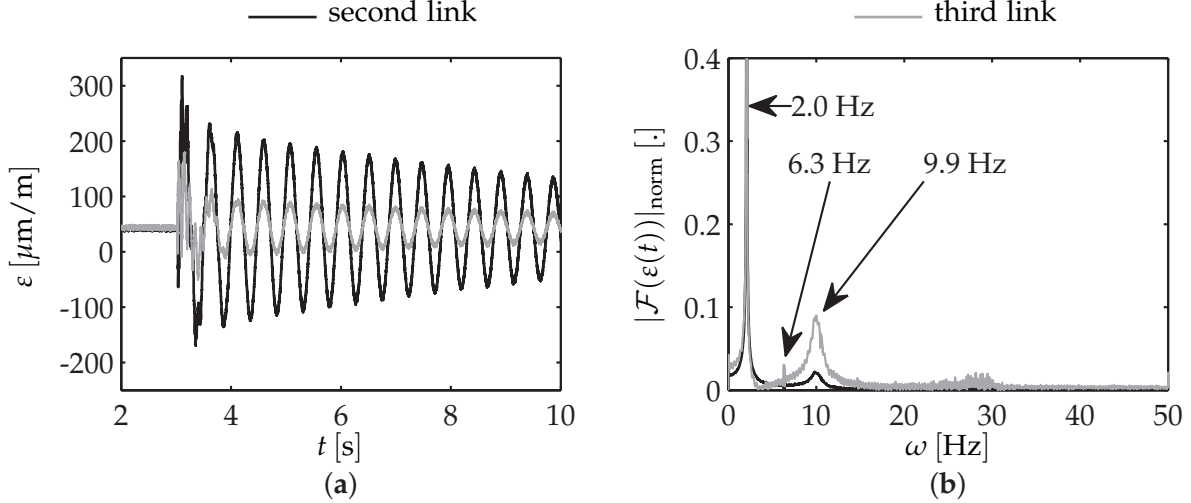
Figure 4.6.: Link surface strain time series (**a**) measured close to the hub on the second (*black*) and third (*gray*) link after a hammer excitation of TUDOR at the end effector. The corresponding spectra are shown in (**b**). The payload mass is $m_L = 300$ g. The payload inertia is $I_L = 1.6 \cdot 10^{-4}\,\mathrm{kgm}^2$.

ways predominant in the spectra. Their contributions to the oscillation signal power are orders of magnitude larger than the contribution of the other frequencies. From the measurements and the theoretical investigations in section 4.6 this work focuses on a frequency range up to a maximum of 30 Hz with a special emphasis on the two dominant frequencies further denoted by ω_1 and ω_2.

Figure 4.7 shows the average, minima and maxima of the two frequencies ω_1 and ω_2 determined from ten repetitions of a hammer excitation experiment for each payload with m_L between 0 and 0.6 kg as well as the inertia I_L between 0 and $3.3 \cdot 10^{-4}\,\mathrm{kgm}^2$.

Again, it is visible that the two dominant frequencies are equivalently measurable on both elastic links. Even though there is an offset between the actually measured and the theoretical frequency values, the strong inversely proportional relation between the load and the frequency as expected from figure 4.3 as well as the frequency range are experimentally validated.

4.8. Impact of backlash under gravity

The provisions made in the previous section are intended to validate the theoretical relations derived before. However, during operation of TUDOR the second link is attached to the second joint while the extra fixture to the third joint flange is removed, so that gear backlash is in effect. The joint controllers designed in section 3.2 are active. In this work the interplay between the backlash and the link orientation with respect to gravity has been observed to introduce a significant variance to the natural frequencies as well as to the intrinsic oscillation damping.

Malzahn et al. (2011a) carry out an initial investigation to this interplay for a single elastic link of TUDOR with payload. Malzahn et al. (2011b) extent the results to both links of TUDOR. The main result is depicted in figure 4.8.

The whole operation range of the second and third joint angles θ_2 and θ_3 has been
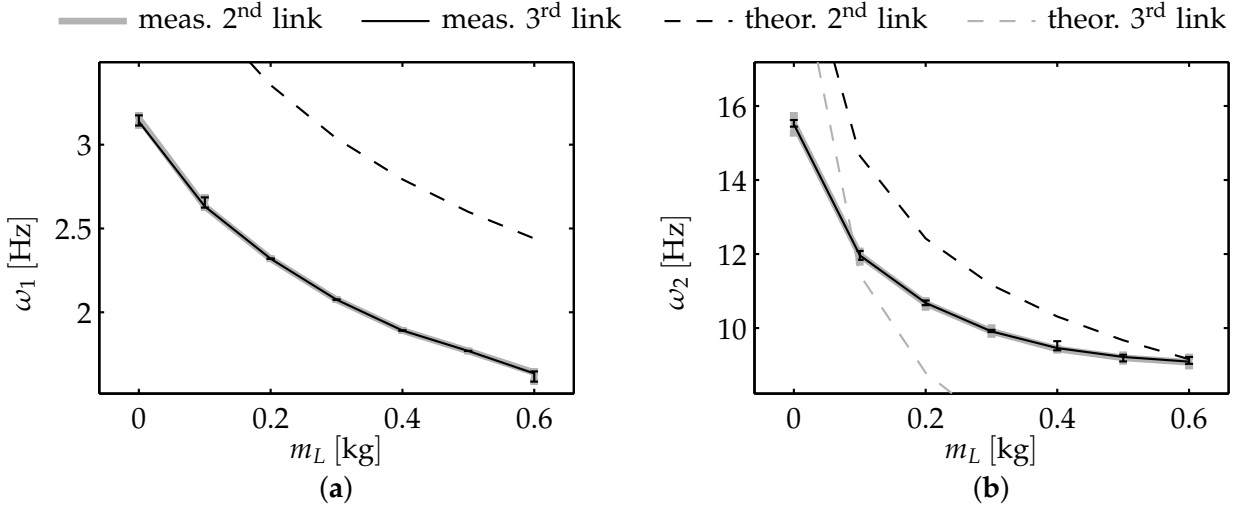
Figure 4.7.: First (**a**) and second (**b**) dominant frequencies determined for varying payloads from strain measurements on the second (*solid, gray*) and third link (*solid, black*). The averages, minima and maxima are obtained from ten hammer excitation experiments per payload. Additionally the theoretical values for the first two natural frequencies of the second link (*dashed, black*) and the first natural frequeny of the third link (*dashed, gray*) are shown.

sampled in steps of $10°$. The arm carries a test payload of $m_L = 0.3\,\text{kg}$ and $I_L = 1.6 \cdot 10^{-4}\,\text{kgm}^2$. Figure 4.8 (**a**) shows the map of the first dominant frequency ω_1 for all sampling points. The frequency ranges between 1.56 Hz and 2.74 Hz.

Figure 4.8 (**b**) contains a map of the logarithmic decrement ζ_1 associated with the first dominant frequency ω_1 for all sampling points. The logarithmic decrement is estimated using the procedure described in the appendix B.3. The absolute decrement values range between 0.03 and 1.24.

Both maps describe merely smooth variations of the quantities. Nevertheless, both diagrams show two equivalent "'canyons'" where the frequency as well as the logarithmic decrement drop abruptly. These "'canyons'" are found along $\theta_2 + \theta_3 = 90°$ and $\theta_2 = 90°$. In those particular joint configurations at least one link is oriented vertically and moving freely within the backlash limits.

While the link moves within the backlash limits the translational degree of freedom at this end is still fixed. Simultaneously the rotational degree can be considered to be free, similar to a simply supported beam. Once the link hits a backlash limit the boundary conditions instantly alter. For more horizontal link orientations gravity pulls the link to one end of the backlash limit. In such a case the imperfect clamping is still present with less impact. Frequent transitions between the boundary conditions may occur after an excitation and the underlying physics is very challenging to model. In fact, presumably because of the energy dissipation during percussions with the limits, the backlash causes an increased intrinsic structural damping.

Two approaches to deal with the situation are conceivable. The first one would be to use more expensive gears without backlash, such as harmonic gears. The second approach is to design a robust controller which dampens the oscillations in spite of the backlash and the varying plant parameters. This work aims at the latter solution.
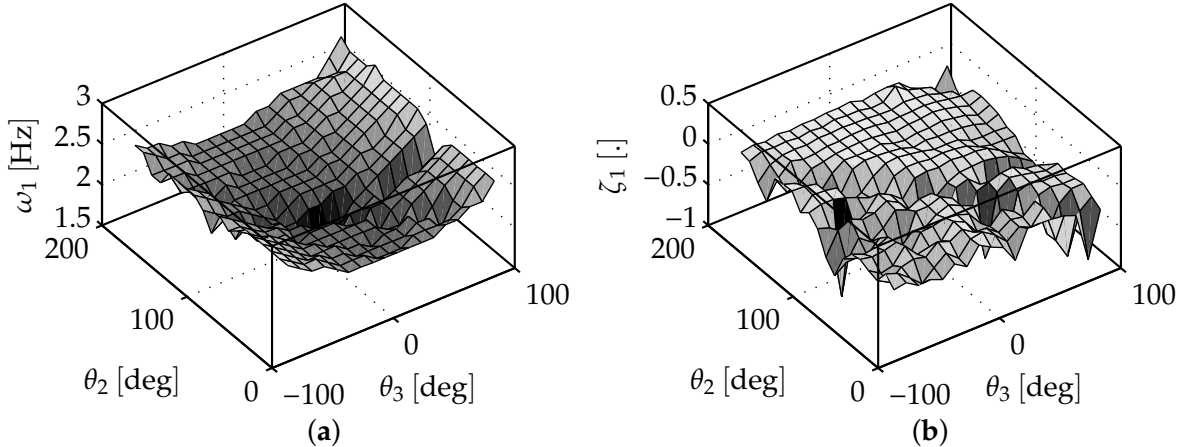
Figure 4.8.: Maps of the first dominant frequency ω_1 **(a)** as well as the logarithmic decrement ζ_1 **(b)** in dependance on the joint angles θ_2 and θ_3 acquired from strain measurements on the second link with an end effector payload of $m_L = 0.3 \, \text{kg}$ and $I_L = 1.6 \cdot 10^{-4} \, \text{kgm}^2$.

4.9. Conclusions for elastic link robots

As one major contribution of this work, this chapter summarizes a theoretical analysis of a broad range of practically relevant impact factors on the oscillatory dynamics of multi-elastic-link robots in terms of eigenfrequencies and mode shape functions. All theoretical investigations are supported by experiments. The impact factors include payload changes, varying operating points throughout the whole robot workspace as well as uncertain knowledge about the required boundary conditions for each link.

Boundary value problems for beams admit exact analytical solutions for a limited number of examples only. Mostly the examples are restricted to very basic boundary conditions as well as homogenous and uniform beams, such that stiffness and mass properties are constant along the beam length. With more complicated geometries and boundary conditions approximate methods such as the Rayleigh Ritz approach, Galerkin's method or numerical finite element techniques have to be applied (Dukkipati and Srinivas 2005; Meirovitch 2001). The exact as well as most approximate solutions to the boundary value problem usually result in a transcendental characteristic equation. This equation must be solved numerically, which leads to an infinite number of natural frequencies along with their mode shapes. The actual spatio-temporal deflection function is thus expressed as the infinite sum of the individual modes. In practice, only a limited number of so called assumed modes can be considered. The mode shapes can only be determined up to a scale. A proper orthogonalization, normalization and scaling has to be found to relate the assumed modes to the true beam deflection. A variation in the boundary conditions requires the frequency computation and the entire mode shape determination to be redone.

At this point it is worth discussing the implications associated with these properties of the boundary value problem for the practical control of general multi-elastic-link robots. In order to precisely compute the dynamic pose of a point along the structure based on a finite number of assumed modes, a boundary value problem of type (4.3.4) must be solved for each beam. The boundary conditions are generally governed by the mass, geometry and relative configuration of the subsequent links. Note that the

inertia of all subsequent bodies have to be expressed with respect to the tip bending axis using the parallel axis theorem. As also pointed out by Luca and Siciliano (1991), the load inertia I_L in general varies with the robot joint configuration. This way the mode shape functions become a function of time, which contradicts equation (4.3.1). Based on the knowledge of the joint values and under the assumption of comparably slow changes or piecewise constant boundary conditions, an idea could be to recompute the natural frequencies online. This process is computationally involved and difficult to implement under the hard real-time constraints required for control. Alternatively a direct mapping from the joint configuration to the natural frequencies and mode shapes in the sense of figure 4.8 would be conceivable. However, this approach is limited to inspection robots. If the elastic link robot is intended to perform manipulation tasks, such as Pick-and-Place, the varying and possibly a priori unknown payload mass and payload inertia may significantly influence the boundary conditions on each link. During physical contact with the environment or physical human robot interaction the impedance of the contact point may impose arbitrary unknown boundary conditions to the robot.

The uncertainties in the boundary conditions lead to poorly calibrated orthogonality relations. This renders the model based decoupling of modes infeasible. A controller based on a finite order model at runtime is likely to excite the wrong modeled or even unmodeled oscillations modes. Similarly, observers suffer from the poor decoupling of the individual modes and most probably provide insufficient estimates. This effect is called modal spillover and is illustrated in more detail for example by Vepa (2010, p. 338).

Under the painted circumstances and constraints it seems questionable whether it is practically feasible to realize a stabilizing centralized controller for a multi-elastic-link robot that dampens structural oscillations and precisely positions the end effector based on a single holistic plant model including payloads and contact boundary conditions.

Against this background it seems more convenient to follow a divide-and-conquer strategy. First a decentralized controller modifies the system dynamics of each individual link to virtually increase the apparent link damping in a wide frequency range. Such controllers are proposed in chapters 5 to 7. They are set free from the actual end effector positioning task and attenuate oscillations originating from the joint motions as well as external excitations and a variety of boundary conditions. On top of that an outer end effector control loop such as the ones presented in chapter 9, minimizes the pose error in the presence of joint configuration and load dependent static deflections due to gravity. Both controller stages ensure nominal plant dynamics. Deviations from this nominal dynamics are exploited in order to investigate the potentials of elastic link robots for planned as well as accidental physical contacts between the robot and the environment as proposed in chapter 11.

<div style="text-align: right; font-size: 4em; font-weight: bold;">5</div>

Proportional Oscillation Feedback

This is the first out of four subsequent chapters devoted to oscillation damping control. The oscillation damping control concept proposed here is based on a straightforward extension of the modal analysis presented in the previous chapter. The physical relations are converted into a truncated series of transfer functions superposed by a nonlinear static component.

5.1. Link transfer function model

Motivated by the workspace sampling results illustrated in figure 4.8 the parameters of the truncated transfer function model vary but are considered to be quasi static for a given joint configuration θ_0. The model structure together with the parameter range paves the way for the synthesis of the decentralized linear oscillation feedback controller in section 5.2. Malzahn et al. (2011b) provide an initial derivation of the model structure. Nevertheless, a more elaborate derivation is given in the following.

Modal parameters

From the results in section 4.7 it is known that the oscillations of each individual link can be perceived on the other links in the chain under preservation of phase alignment. Therefore the whole arm structure is interpreted as a chain of joint-link-modules. Each joint-link-module virtually possesses all perceivable oscillation modes as if they were actually obtained as solutions of the modal analysis for the particular link.

The module consists of a series connection of the joint transfer function (3.1.7) and a nonlinear transfer function capturing the oscillatory dynamics for the connected virtual elastic link. Due to the high gear ratios a feedback from the elastic link dynamics to the joint model can be assumed to be inconsequentially small. The joint-link-modules are therefore treated independently.

The nonlinear elastic link transfer function model has the joint angle θ as input and the strain measured close to the hub as output. Consider the beam partial differential equation (4.2.8) augmented by the effects of viscous and mass proportional damping effects summarized in the damping coefficient k_d:

$$EI_z \frac{\partial^4 y(x,t)}{\partial x^4} + k_d \frac{\partial}{\partial t} y(x,t) + \rho_b \frac{\partial^2 y(x,t)}{\partial t^2} = f_{ext}(x,t). \qquad (5.1.1)$$

For simplicity of derivation but without loss of generality the elastic link is assumed to be rigidly clamped at the hub with quasi static load mass and load inertia as discussed in section 4.4.

Equation (5.1.1) is multiplied by a particular shape function Φ_u and integrated over the link length:

$$\int_0^L \Phi_u(x)\, EI_z\, \frac{\partial^4 y(x,t)}{\partial x^4} dx + \int_0^L \Phi_u(x)\, k_d\, \frac{\partial}{\partial t} y(x,t) dx + \ldots$$

$$+ \int_0^L \Phi_u(x)\, \rho_b \frac{\partial^2 y(x,t)}{\partial t^2} dx = \int_0^L \Phi_u(x)\, f_{ext}(x,t) dx. \quad (5.1.2)$$

Using the series expansion derived in the appendix B.3 the solution $y(x,t)$ has the form:

$$y(x,t) = \sum_{u=1}^{\infty} \Phi_u(x)\, v_u(t). \quad (5.1.3)$$

Exploiting the orthonormality of modes enables the definition of so called modal parameters from the individual summands of equation (5.1.2). The first summand yields the modal stiffness c_u:

$$c_u = \int_0^L \Phi_u(x)\, EI_z\, \frac{\partial^4 \Phi_u(x)}{\partial x^4} dx, \quad (5.1.4)$$

the second summand is the modal damping d_u:

$$d_u = \int_0^L \Phi_u(x)\, k_d\, \Phi_u(x) dx, \quad (5.1.5)$$

the third summand is the modal mass m_u:

$$m_u = \int_0^L \Phi_u(x)\, \rho_b \Phi_u(x) dx \quad (5.1.6)$$

and the modal force f_u computes to:

$$f_u = \int_0^L \Phi_u(x)\, f_{ext}(x,t) dx. \quad (5.1.7)$$

With the modal parameters the partial differential equation (5.1.1) transforms to a set of independent modal ordinary differential equations:

$$m_u \frac{d^2 v_u(t)}{dt^2} + d_u \frac{d v_u(t)}{dt} + c_u\, v_u(t) = f_u(t). \quad (5.1.8)$$

In analogy to equation (5.1.3) the strain measured at a sensor location x_s can be written as:

$$\varepsilon(x_s,t) = y_b \sum_{u=1}^{\infty} \frac{d^2}{dx^2} \Phi_u(x)_{|x_s}\, v_u(t), \quad (5.1.9)$$

with

$$\varepsilon_u(x_s,t) = y_b \frac{d^2}{dx^2} \Phi_u(x)_{|x_s}\, v_u(t), \quad (5.1.10)$$
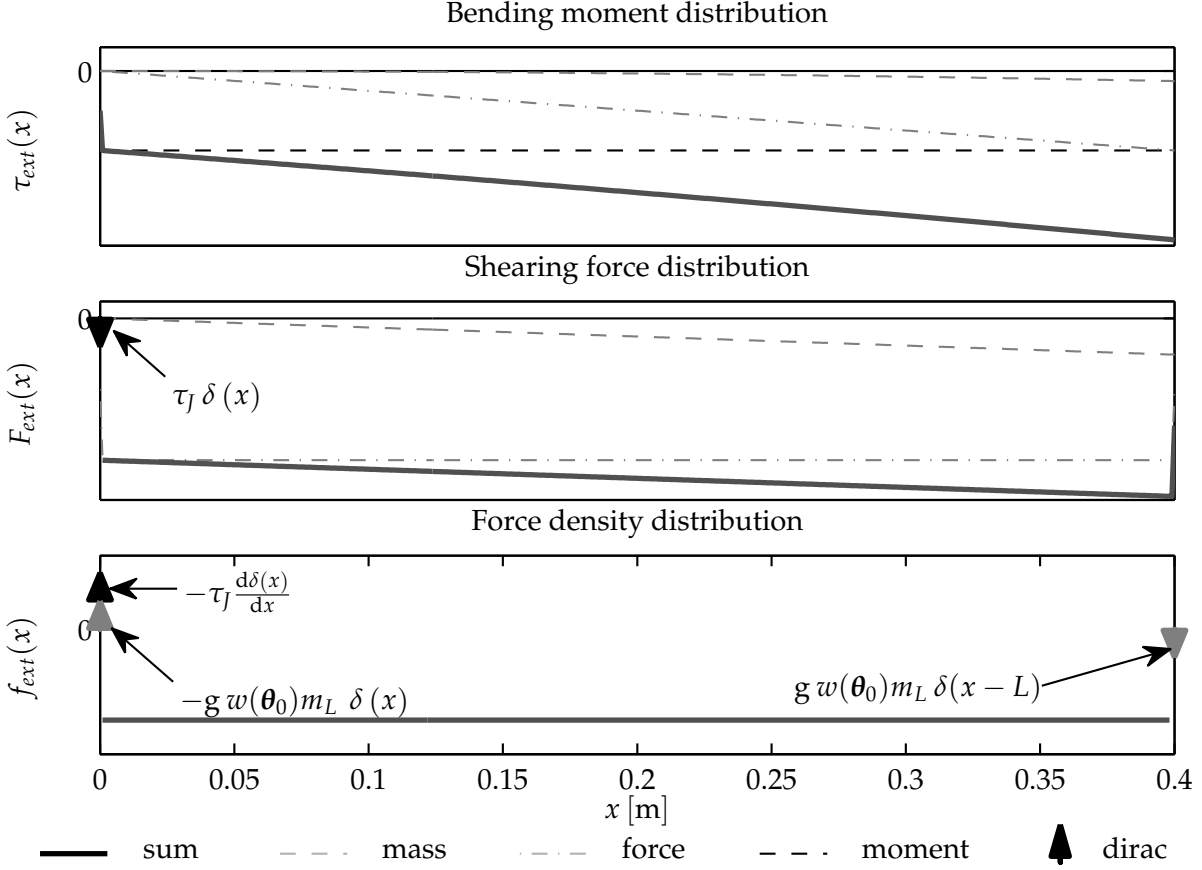
Figure 5.1.: Qualitative illustration of the bending moment distribution (*thick black, top*), shearing force distribution (*thick black, center*) and shearing force density distribution (*thick black, bottom*) together with the individual contributions of the mass density (*dashed gray*), load force (*dash-dotted gray*) as well as the constant bending moment (*dashed black*).

so that the modal amplitude ν_u computes to:

$$\nu_u(t) = \frac{1}{y_b \frac{\mathrm{d}^2}{\mathrm{d}x^2} \Phi_u(x)_{|x_s}} \, \varepsilon_u(x_s, t). \tag{5.1.11}$$

This way the modal differential equations can be expressed in terms of the modal strain at the sensor location:

$$m_u \frac{\mathrm{d}^2 \varepsilon_u(x_s, t)}{\mathrm{d}t^2} + d_u \frac{\mathrm{d}\varepsilon_u(x_s, t)}{\mathrm{d}t} + c_u \, \varepsilon_u(x_s, t) = y_b \frac{\mathrm{d}^2}{\mathrm{d}x^2} \Phi_u(x)_{|x_s} \, f_u(t). \tag{5.1.12}$$

Force density distribution

Up to this point only the homogenous case $f_{ext} = 0$ has been considered. The external force density function $f_{ext}(x, t)$ includes contributions of the static configuration dependent load forces and moments due to gravity as well as the moments imposed by the joints or contacts with the environment.

The external moment distribution $\tau_{ext}(x)$ for $0 \leq x \leq L$ is a result of external influences that have not been incorporated in the boundary conditions depicted in

figure 4.2. By inspection of the figure the distribution can be written as the balance about the joint axis:

$$\tau_{ext}(x) = (\tau_M + \tau_L(\boldsymbol{\theta}_0)) \; H(x) + \dots$$
$$+ \mathrm{g}\, w(\boldsymbol{\theta}_0) \left(\rho_b \frac{x^2}{2} - m_L(x - L)\, H(x - L) + x\, m_L\, H(x) \right). \quad (5.1.13)$$

The resulting distribution is shown in the top of figure 5.1. The weight function $w(\boldsymbol{\theta}_0)$ scales the gravitational acceleration g according to the link unit x-direction $\mathbf{e}_x$ with respect to the gravitational acceleration vector $\mathbf{a}_g$. The gravitational load moment $\tau_L(\boldsymbol{\theta}_0)$ scales analogously with the joint configuration.

The function $H(x)$ is the Heaviside function. It approximates the domain restrictions and enables the application of distribution theory to compute the derivatives of τ_{ext}. The first derivative yields the force distribution $F_{ext}(x)$ as depicted in the center of figure 5.1:

$$F_{ext}(x) = (\tau_M + \tau_L(\boldsymbol{\theta}_0)) \; \delta(x) + \mathrm{g}\, w(\boldsymbol{\theta}_0)\, (\rho_b\, x + m_L\, (H(x) - H(x - L))), \quad (5.1.14)$$

where $\delta(x - x_g)$ denotes the Dirac distribution. The second derivative yields the force density distribution $f_{ext}(x)$ shown in the bottom of figure 5.1:

$$f_{ext}(x) = (\tau_M + \tau_L(\boldsymbol{\theta}_0)) \; \frac{\mathrm{d}\delta(x)}{\mathrm{d}x} + \mathrm{g}w(\boldsymbol{\theta}_0)\, (\rho_b + m_L\, (\delta(x) - \delta(x - L))). \quad (5.1.15)$$

The mechanical torque τ_M provided by the joint can be replaced by:

$$\tau_M(t) = I_M\, \ddot{\theta}(t). \quad (5.1.16)$$

Transfer function

Equation (5.1.14) can be split into a static and a dynamic part. At a sensor location x_s the first part including the load mass m_L, the load moment τ_L as well as the mass per unit length ρ_b constitutes the static part for a given joint configuration $\boldsymbol{\theta}_0$. The dynamic part depends on the joint acceleration $\ddot{\theta}(t)$.

With this insight the combination of the modal strain differential equation (5.1.12) and the modal force equation (5.1.7) yields the modal transfer function after Laplace transformation for vanishing initial conditions:

$$\varepsilon_u(x_s, s) = \frac{k_{dyn,u}\, s^2}{s^2 + 2D_u\omega_u\, s + \omega_u^2} \theta(s) + \frac{k_{stat,u}(\boldsymbol{\theta}_0)}{s^2 + 2D_u\omega_u\, s + \omega_u^2}, \quad (5.1.17)$$

where the dynamic modal gain $k_{dyn,u}$ is:

$$k_{dyn,u} = \frac{y_b}{m_u} \frac{\mathrm{d}^2}{\mathrm{d}x^2} \Phi_u(x)_{|x_s}\, I_M \int_0^L \Phi_u(x)\, \delta(x)\mathrm{d}x \quad (5.1.18)$$

and the static modal gain $k_{stat,u}$ computes to:

$$k_{stat,u}(\boldsymbol{\theta}_0) = \frac{y_b}{m_u} \frac{\mathrm{d}^2}{\mathrm{d}x^2} \Phi_u(x)_{|x_s} \int_0^L \Phi_u(x) \left(\tau_L(\boldsymbol{\theta}_0) \frac{\mathrm{d}\delta(x)}{\mathrm{d}x} + \dots \right.$$
$$\left. + \mathrm{g}w(\boldsymbol{\theta}_0) \left(\rho_b + m_L \left(\delta(x) - \delta(x - L) \right) \right) \right) \mathrm{d}x. \quad (5.1.19)$$

The attenuation factor D_u is related to the logarithmic decrement ζ_u as well as the modal damping d_u and mass m_u properties:

$$D_u \omega_u = \frac{1}{2}\frac{d_u}{m_u} = -\zeta_u. \tag{5.1.20}$$

From the equations (5.1.4) and (5.1.6) along with equation (4.3.2) it can be verified that the frequency ω_u replaces the modal mass and stiffness according to:

$$\omega_u = \sqrt{\frac{c_u}{m_u}}. \tag{5.1.21}$$

Finally, with equation (5.1.9) the total beam transfer function can be written in the form:

$$\varepsilon(x_s, s) = \theta(s)\, s^2 \sum_{u=1}^{n_\omega} \frac{k_{dyn,u}}{s^2 + 2D_u\omega_u\, s + \omega_u^2} + \sum_{u=1}^{n_\omega} \frac{k_{stat,u}(\boldsymbol{\theta}_0)}{s^2 + 2D_u\omega_u\, s + \omega_u^2}. \tag{5.1.22}$$

The dimension of this transfer function is theoretically infinite. Practically only a finite number n_ω of oscillation modes can be taken into account for the controller synthesis and analysis.

Provided that the configuration dependent static strains $\varepsilon_{\text{stat}}$ can be removed by appropriate filtering, the remaining dynamic strain transfer function $G_B(s)$ is characterized by:

$$G_B(x_s, s) = \frac{\varepsilon_{\text{dyn}}(x_s, s)}{\theta(s)} = s^2 \sum_{u=1}^{n_\omega} \frac{k_{dyn,u}}{s^2 + 2D_u\omega_u\, s + \omega_u^2}. \tag{5.1.23}$$

This transfer function model serves as a basis for the synthesis of the controller described in the next section.

5.2. Controller synthesis

The assumption of a perfect static strain cancellation renders the remaining plant dynamics entirely linear. Thus, the Evans root locus may be used to design a proportional strain feedback for the series connection of the cascaded joint controller and remaining beam transfer function (5.1.23). Motivated by the observations in section 4.7 the beam model $G_B(s)$ in the root locus analysis combines the predominant eigenfrequencies of all links together. This way the controller is designed to also damp the oscillations due to inter-link couplings.

The proportional strain feedback discussed here is strongly related to the work reported by Luo (1993); Luo and Guo (1995). The authors introduce the concept of so called A-dependent operators to proof the stability of a proportional as well as integral strain feedback for a single link in the horizontal plane. In their experiments the joint angle is left uncontrolled in the first place. In a second step it is controlled by a single loop PID controller with the actuator input voltage as set value. In contrast to that, this work operates with a multi-link arm under gravity and chooses the extended cascaded joint controller from section 3.2 complemented by the jerk minimizing online trajectory planner provided in appendix B.6. The set value is the amplifier voltage proportional to the actuator electrical current.
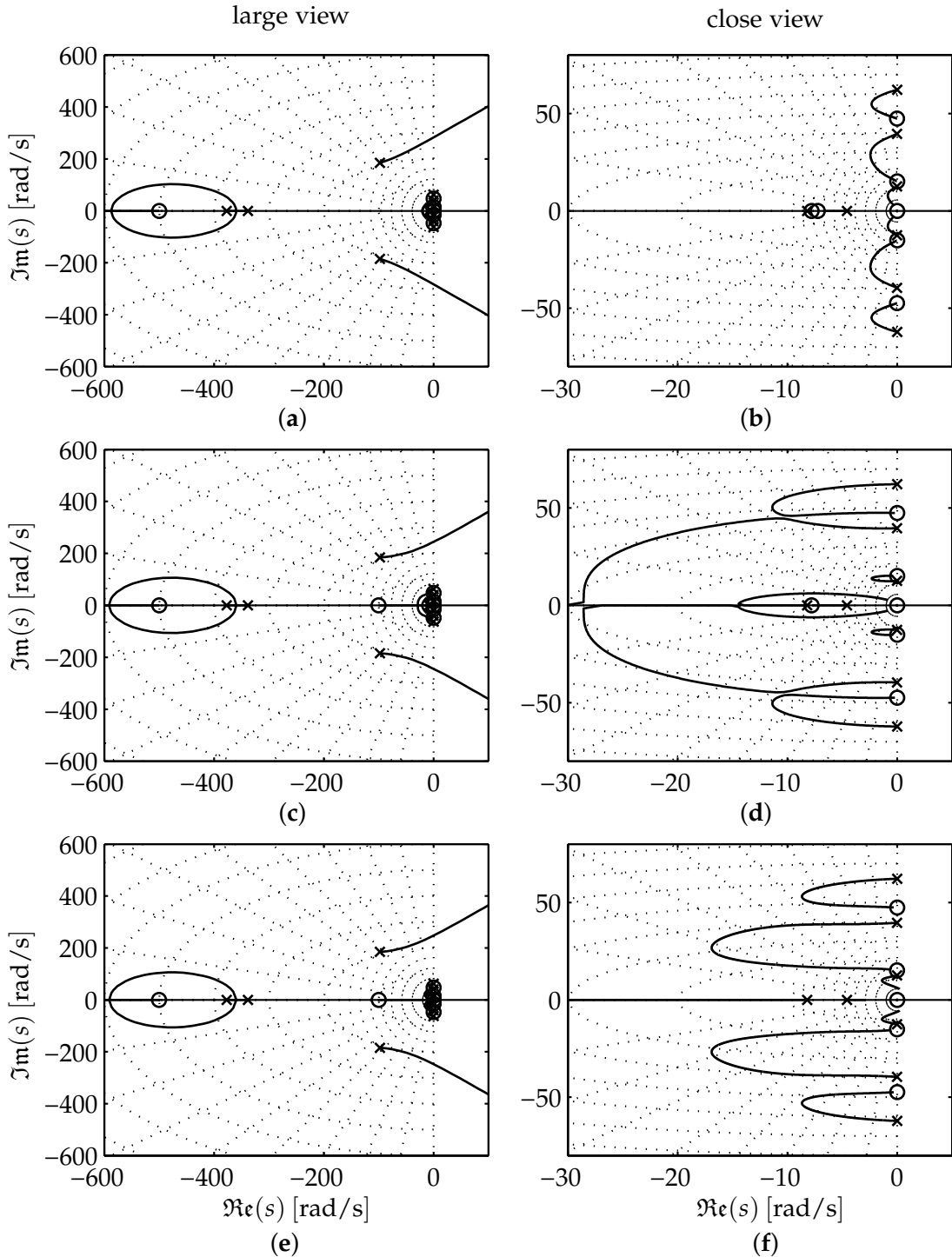
Figure 5.2.: Evans root locus for the proportional oscillation feedback at the position controller summation point (**a**) with close view (**b**), at the summation point of the velocity controller (**c**) with close view (**d**) as well as the power amplifier input (**e**) with close view (**f**). The poles and zeros on the imaginary axis originate from the beam transfer function $G_B(x_s, s)$.

In this chapter, the proportional strain feedback is considered. The integral feedback is discussed within the scope of chapter 6.

The cascaded structure enables the investigation of the three different feedback insertion points indicated in figure 3.3: at the position controller input, velocity controller input and at the amplifier voltage input. Figure 5.2 exemplifies the root locus computed from each of the insertion points to the strain output. The left column depicts overviews of the whole root locus, while the right column provides the corresponding close-ups to the complex pole and zero pairs on the imaginary axis. They originate from the flexible beam transfer function (5.1.23).

For the feedback insertion point at the position controller input (see figure 5.2 (**b**)), the flexible beam poles reside in the stable left-half plane. However, they show poor damping while approaching the origin of the complex *s*-plane.

For the feedback insertion point at the velocity controller input (see figure 5.2 (**d**)) the beam poles move to the left and one pole pair finally joins the real axis. This way, with increasing feedback gain, we observe a slightly decreasing dominant frequency and a significantly improving damping.

The insertion point at the voltage input (see figure 5.2 (**f**)) shows a similar behaviour compared to the insertion point at the velocity input. However, the lowest beam eigenfrequency rapidly approaches the origin of the complex *s*-plane. The path of this pole pair leads through regions of poor damping.

In summary the insertion point at the velocity controller is most advantageous in terms of achievable shift of the elastic link poles towards regions of higher damping in the complex *s*-plane. The control law is:

$$\dot{\theta}_\varepsilon = -k_\varepsilon\, \tilde{\varepsilon}(x_s, t). \tag{5.2.1}$$

In all three overview plots (left column of figure 5.2) it is visible that a complex pole pair tends to the right half of the complex *s*-plane with increasing feedback gain. This pole pair originates from the PD position controller. The strain feedback gain is therefore upper bounded to preserve closed loop stability. Nevertheless, the pole pair possesses a higher eigenfrequency and experiences additional damping due to the low-pass characteristics of the remaining plant poles. Moreover, it shapes the root locus of the considered elastic link pole pairs and keeps them in the left half plane.

The critical drawback behind the presented controller synthesis arises from the restriction to a finite number of oscillatory modes. As already mentioned in section 1.2, there exists no technique that guarantees stability with respect to the neglected eigenfrequencies.

The closed loop dynamics including the elastic link poles could be more generally influenced with full state feedback control. However, a practically important merit of the control concept is the simplicity of tuning.

Changes in the plant parameters as observed in figure 4.8 marginally distort the root locus but the general root locus geometry does not alter for a broad range of parameter variations. For a more tangible explanation of this fact, consider the already small natural damping to be negligible. In this case, the complex poles and zeros belonging to the beam transfer function are exactly located on the imaginary axis. A variation to the natural frequencies due to payload changes, physical contacts or altered joint configurations results in a vertical scaling of the root locus only. Increased
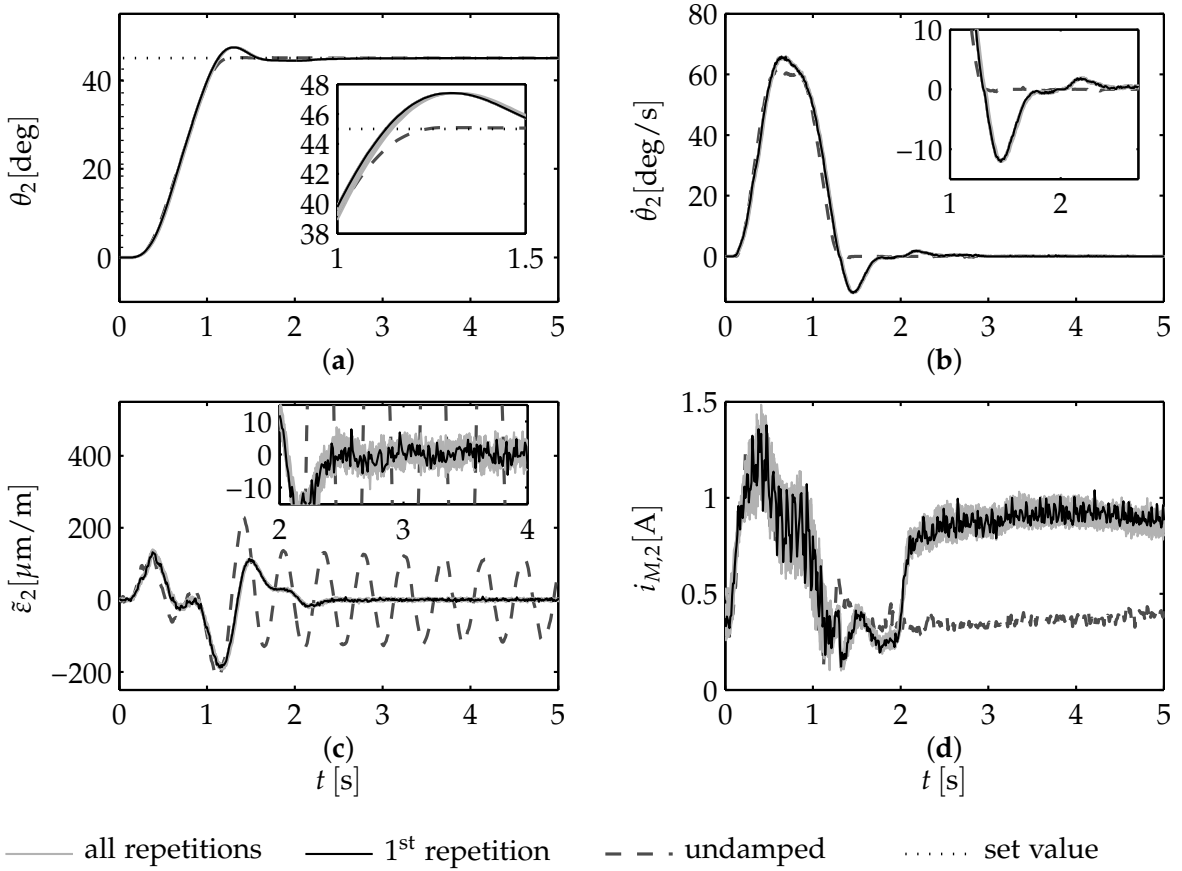
Figure 5.3.: Time series the joint angle (**a**), angular velocity (**b**), link strain (**c**) and motor current (**d**) measured on the second joint link module during twenty repetitions (*solid light gray*) of a point-to-point motion from $\theta = [0°, 0°, 0°]^T$ to $\theta = [0°, 45°, -45°]^T$. The first repetition is highlighted (*solid black*). For comparison the graphs show the same experiment without damping (*dashed gray*).

oscillation amplitudes due to additional payloads act as additional gain and vary the closed loop poles along the root locus branches. Therefore, stability with respect to the considered modes is preserved and robustness to plant variations is accomplished.

5.3. Controller evaluation

Starting with small values, the single vibration feedback gain for each joint-link-module can be tuned even manually without any explicit beam dynamics model being available. For the experiments provided in chapter 8 the gains are tuned through auto-mated and constrained hardware in the loop optimization using sequential quadratic programming. The gains are constrained to have an upper bound. This ensures closed loop stability. The cost function to minimize is the integral time weighted absolute strain surface criterion (see B.4).

Figure 5.3 exemplifies damping results obtained with the proportional strain feed-back on TUDOR. The small difference between the graphs of each repetition evid-ences the repeatability of the experiments. The damping action performed by the

actuator can be seen in the overshoot of the angular response, which is absent in the undamped case. Similarly, Figure 5.3 (**b**) illustrates the damping action as a brief motion reversal right before the deflections vanish. The accomplished rapid damping is clearly visible in the strain measurements 5.3 (**c**). Malzahn and Bertram (2013, at 0:36 min) provide an online available video comprising oscillation damping results with the proportional strain feedback at the velocity cascade level.

<div style="text-align: right; font-size: 3em; font-weight: bold;">6</div>

Lumped Parameter Wave Echo Control

This is the second out of four subsequent chapters devoted to oscillation damping control. The transfer function model in chapter 5 is based on a truncated series of transfer functions. As outlined in section 1.2 lumped parameter models constitute a widely applied alternative. O'Connor (2007b) investigates the wave-like propagation of motions and forces in serial open chains consisting of an arbitrary number of lumped masses interconnected through linear springs. Since it circumvents issues with neglected higher order modes, the concept is promising and relevant for the scope of this thesis. Up to now, it has been mainly studied in simulations or with single link setups under exclusion of gravitational effects (O'Connor et al. 2009). As one contribution, this work applies it to a multi-link experimental setup with gravity. In the following, the theory is briefly revisited and transferred to the equivalent description with rotary springs, which is more illustrative in the context of elastic link robots. The theory leads to the lumped parameter wave echo controller originally proposed by O'Connor. As a second contribution the chapter performs a structural reduction of the control scheme and reveals the close relation to the control approach presented in the previous chapter.

6.1. Wave properties in a lumped mass model

A chain of mass elements connected by rotary springs is depicted in figure 6.1.

The relation between the bending angle $\theta_{b,i}$ at the i-th spring and the bending angle $\theta_{b,i+1}$ at the next spring in the chain is described by the transfer function $G_l(s)$:

$$\theta_{b,i+1}(s) = G_l(s)\,\theta_{b,i}(s) \tag{6.1.1}$$
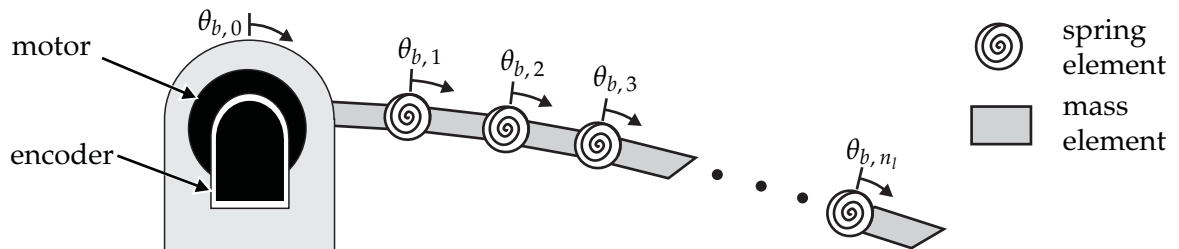
Figure 6.1.: Illustration of the lumped mass approximation of a single joint link module.

and consequently:

$$\theta_{b,i+n_l} = G_l^{n_l}\,\theta_{b,i}, \tag{6.1.2}$$

where n_l is the integer number of lumped masses considered.

The equation of motion for a lumped spring mass system is characterized by the lumped inertia I_l and a spring stiffness k_l:

$$I_l\ddot{\theta}_{b,i}(t) = k_l\,(\theta_{b,i-1}(t) - 2\,\theta_{b,i}(t) + \theta_{b,i+1}(t)), \tag{6.1.3}$$

which after Laplace transformation and rearrangement yields the quadratic equation in $G_l(s)$:

$$G_l^2(s) - \left(2 + \frac{s^2}{\omega_l^2}\right)G_l(s) + 1 = 0, \tag{6.1.4}$$

where $\omega_l = \sqrt{\frac{k_l}{I_l}}$. The quadratic equation has the two solutions $^+G_l(s)$ and $^-G_l(s)$:

$$^+G_l(s) = 1 + \frac{1}{2}\,(s/\omega_l)^2 - (s/\omega_l)\,\sqrt{1 + (s/2\omega_l)^2}, \tag{6.1.5}$$

$$^-G_l(s) = 1 + \frac{1}{2}\,(s/\omega_l)^2 + (s/\omega_l)\,\sqrt{1 + (s/2\omega_l)^2}. \tag{6.1.6}$$

Note, that the first solution (6.1.5) is causal, while the other one (6.1.6) shows an acausal phase lead. A closer look reveals two symmetries between both solutions. The first one is a spatial symmetry mathematically expressed by the inverse:

$$^+G_l(s) = {}^-G_l^{-1}(s), \quad {}^-G_l(s) = {}^+G_l^{-1}(s), \tag{6.1.7}$$

meaning that the elastic dynamics are reciprocal. The second symmetry is temporal:

$$^+G_l(-s) = {}^-G_l(s), \quad {}^-G_l(-s) = {}^+G_l(s). \tag{6.1.8}$$

The combination of both symmetries leads to:

$$^+G_l(s) = {}^+G_l^{-1}(-s), \quad {}^-G_l(s) = {}^-G_l^{-1}(-s), \tag{6.1.9}$$

which gives the physical interpretation of the acausality in the transfer functions from the perspective of propagating motion waves. Looking from the left towards the right end of the beam a motion propagating along the structure in the viewing direction at finite speed appears causal. An observed acausal bending motion propagates in the opposite direction and must have been initiated at a distal location previously in time. Consequently the bending angle $\theta_{b,i}$ of an i-th spring-beam-element consists of two components:

$$\theta_{b,i}(s) = {}^+G_l(s)\,C_{1,i}(s) + {}^-G_l(s)\,C_{2,i}(s), \tag{6.1.10}$$

with the functions $C_{1,i}(s)$ and $C_{2,i}(s)$ to be further specified, while the motion wave caused by a source on the left side of the link and propagating rightwards within the structure is given as $^+\check{\theta}_{b,i}(s) = {}^+G_l(s)\,C_{1,i}(s)$. Vice versa $^-\check{\theta}_{b,i}(s) = {}^-G_l(s)\,C_{2,i}(s)$ corresponds to the motion wave propagating leftwards within the structure, originating from the right side of the link, so that:

$$\theta_{b,i}(s) = {}^+\check{\theta}_{b,i}(s) + {}^-\check{\theta}_{b,i}(s). \tag{6.1.11}$$

This superposition relation analogously exists for the velocity as well as bending moment propagation in the lumped structure:

$$\dot{\theta}_{b,i} = {}^{+}\check{\dot{\theta}}_{b,i} + {}^{-}\check{\dot{\theta}}_{b,i}, \tag{6.1.12}$$

$$\tau_{b,i} = {}^{+}\check{\tau}_{b,i} + {}^{-}\check{\tau}_{b,i}. \tag{6.1.13}$$

Exploiting the reciprocity relation (6.1.7) enables the simplified notation ${}^{+}G_l(s) = {}^{-}G_l^{-1}(s) = G_l(s)$, where only the causal transfer function is used in different directions of propagation. This defines $C_{1,i}(s)$ and $C_{2,i}(s)$ in (6.1.10) as:

$$C_{1,i}(s) = {}^{+}\check{\theta}_{b,i-1}(s) \quad \text{and} \quad C_{2,i}(s) = {}^{-}\check{\theta}_{b,i+1}(s), \tag{6.1.14}$$

which yields:

$$\theta_{b,i}(s) = G_l(s) \, {}^{+}\check{\theta}_{b,i-1}(s) + G_l(s) \, {}^{-}\check{\theta}_{b,i+1}(s), \tag{6.1.15}$$

or equivalently:

$$\theta_{b,i}(s) = G_l(s) \, {}^{+}\check{\theta}_{b,i-1}(s) + G_l^{-1}(s) \, {}^{-}\check{\theta}_{b,i-1}(s). \tag{6.1.16}$$

O'Connor (2007b) calls $G_l(s)$ the wave transfer function (WTF).

6.2. Wave absorption

The wave echo control concept described in the following goes back to a series of papers by O'Connor (O'Connor 2007a,b; O'Connor and Donogh 1998; O'Connor et al. 2009). Even though the synthesis is based on the discrete representation of the elastic link provided in section 6.1, the controller derived with the gained insights finally waives the need for an online computation of a truncated or discretized plant dynamics model. It focuses on measurements at the interface between the actuation mechanism and the elastic structure.

Given a point-to-point motion task with goal θ_w, the idea behind the wave echo controller is to launch a motion wave of ${}^{+}\check{\theta}_{b,0}$ and then to absorb the echoed wave component ${}^{-}\check{\theta}_{b,0}$ to damp the induced oscillations. The question now is, what wave amplitude ${}^{+}\check{\theta}_{b,0}$ the actuator should launch in order to precisely arrive at the desired goal with all oscillations being completely attenuated. To answer this question, O'Connor (2007a) assumes free boundary conditions at the link end opposite to the actuator. At the "free end" he provides an intuition for a total reflection of the incoming wave component ${}^{+}\check{\theta}_{n_l}$ by introduction of virtual masses beyond the n-th mass, which mirror the physical plant. The wave echo ${}^{-}\check{\theta}_{n_l}$ is equal to the incoming wave, but propagating in the opposite direction. Once the wave echo arrives at the actuator, the unit gain of the transfer function $G_l(s)$ leads to ${}^{+}\check{\theta}_{b,0} = {}^{-}\check{\theta}_{b,0}$ at steady state. The actuator should thus launch the wave component ${}^{+}\check{\theta}_{b,0} = \frac{1}{2}\theta_w$. This way the actuator is commanded to move half the desired distance. The wave echo ${}^{-}\check{\theta}_{b,0}$ coming back to the actuator is computed by means of equation (6.3.5) and added to the commanded value. Ideal joint position controller dynamics assumed, the actuator absorbs the wave echo and arrives at the goal without residual oscillations.

6.3. Wave component separation

Equally to the continuous wave variables, the left- and rightwards propagating wave components in (6.1.11) to (6.1.13) cannot be measured directly. To implement the wave echo controller it is required to extract them from physical measurements.

Consider a bending wave $^{+}\check{\theta}_{b,0}(s)$ being launched by the actuator ($i = 0$) according to:

$$^{+}\check{\theta}_{b,0}(s) = \theta_{b,0}(s) - {}^{-}\check{\theta}_{b,0}(s).$$ (6.3.1)

The motion of the neighboring mass element with $i = 1$ computes to:

$$\theta_{b,1} = {}^{+}\check{\theta}_{b,1}(s) + {}^{-}\check{\theta}_{b,1}(s) = G_l(s)\,{}^{+}\check{\theta}_{b,0}(s) + G_l^{-1}(s)\,{}^{-}\check{\theta}_{b,0}(s),$$ (6.3.2)

which is rearranged to obtain the echo $^{-}\check{\theta}_{b,0}(s)$ to the launched wave $^{+}\check{\theta}_{b,0}(s)$:

$$^{-}\check{\theta}_{b,0}(s) = G_l(s)\,\left(\theta_{b,1} - G_l(s)\,{}^{+}\check{\theta}_{b,0}(s)\right).$$ (6.3.3)

The result eliminates $^{-}\check{\theta}_{b,0}(s)$ in equation (6.3.1):

$$^{+}\check{\theta}_{b,0}(s) = \frac{\theta_{b,0}(s) - G_l(s)\,\theta_{b,1}}{1 - G_l^2(s)},$$ (6.3.4)

which is the separated rightwards propagating wave component expressed in the physically measurable variables $\theta_{b,0}$ and $\theta_{b,1}$ at the actuator-link-interface. The echoed wave motion $^{-}\check{\theta}_{b,0}$ is obtained analogously by plugging result (6.3.4) back into equation (6.3.3):

$$^{-}\check{\theta}_{b,0}(s) = G_l\,\frac{\theta_{b,1}(s) - G_l(s)\,\theta_{b,0}}{1 - G_l^2(s)}.$$ (6.3.5)

The required physical measurements are the motor angle $\theta_{b,0}$ as well as the angle of a first spring element $\theta_{b,1}$. It is one measurement on each side of the interface between the actuator and the elastic structure. With both measurements the launched wave component $^{+}\check{\theta}_{b,0}$ as well as the echoed wave component $^{-}\check{\theta}_{b,0}$ can be reconstructed at any time instant using relations (6.3.4) and (6.3.5).

However, the exact WTFs obtained as the solutions of 6.1.4 are hard to implement for real-time control. It is not rational and has fractional order. O'Connor (2007b) discusses different approximations such as "a combination of Bessel functions" or the "convolution with a suitably truncated impulse response" but finally applies the linear underdamped second order transfer function:

$$G_l(s) \approx \frac{\omega_l^2}{s^2 + \omega_l\,s + \omega_l^2}.$$ (6.3.6)

6.4. Lumped wave impedance

Using the approximation (6.3.6) to the WTF, O'Connor et al. (2009) observe a steady state error arising during fast point-to-point motions in experimental results with a single link setup under exclusion of gravitational influence. The authors discuss

different alternatives to alleviate the steady state error for this particular scenario. They arrive at the reconstruction of the returning wave component at the actuator from joint angle and link bending torque measurements to be the best solution. Again, this is one physical measurement on each side of the interface between the actuator and the elastic structure. They define a wave impedance Z_w such that:

$$\dot{\theta}_{b,i} = \frac{\tau_{b,i}}{Z_w} \tag{6.4.1}$$

and

$$\dot{\theta}_{b,i} = \frac{^{+}\check{\tau}_{b,i}}{Z_w} - \frac{^{-}\check{\tau}_{b,i}}{Z_w} . \tag{6.4.2}$$

The negative sign in equation (6.4.2) can be understood from the convention that the rightwards propagating angular bending velocity is counted positively, while the leftwards propagating angular bending velocity is counted negatively. This also aggrees with the propagating wave amplitudes in the continuous case, as seen from the matrix elements in equation (7.1.5). With this definition it can be verified from (6.1.13) and addition that:

$$^{+}\check{\tau}_{b,i} = \frac{1}{2} \left(\tau_{b,i} + \dot{\theta}_{b,i}\, Z_w \right) \tag{6.4.3}$$

and symmetrically

$$^{-}\check{\tau}_{b,i} = \frac{1}{2} \left(\tau_{b,i} - \dot{\theta}_{b,i}\, Z_w \right) . \tag{6.4.4}$$

Similarly equation (6.1.12) yields:

$$^{+}\check{\theta}_{b,i} = \frac{1}{2} \left(\frac{\tau_{b,i}}{Z_w} + \dot{\theta}_{b,i} \right) , \tag{6.4.5}$$

while:

$$^{-}\check{\theta}_{b,i} = \frac{1}{2} \left(\frac{\tau_{b,i}}{Z_w} - \dot{\theta}_{b,i} \right) . \tag{6.4.6}$$

The echoed angular wave component is then obtained from (6.4.6) after integration:

$$^{-}\check{\theta}_{b,0}(t) = \frac{1}{2} \left(\theta_{b,0}(t) - \int \frac{\tau_{b,1}(t)}{Z_w} dt \right) . \tag{6.4.7}$$

6.5. Controller reduction

For control, the bending moment $\tau_{b,1}$ is replaced by the mean liberated strain measurements $\tilde{\varepsilon}$ close to the joint hub using equation (4.2.2), so that in the Laplace domain the approximation of the echoed wave component used as feedback θ_ε becomes:

$$\theta_\varepsilon(s) = {}^{-}\check{\theta}_{b,0}(s) = \frac{1}{2} \left(\theta(s) - \frac{k_\varepsilon}{s} \varepsilon(x_s, s) \right) , \tag{6.5.1}$$

where the gain k_ε computes to:

$$k_\varepsilon = -\frac{E I_z}{y_b\, Z_w} . \tag{6.5.2}$$
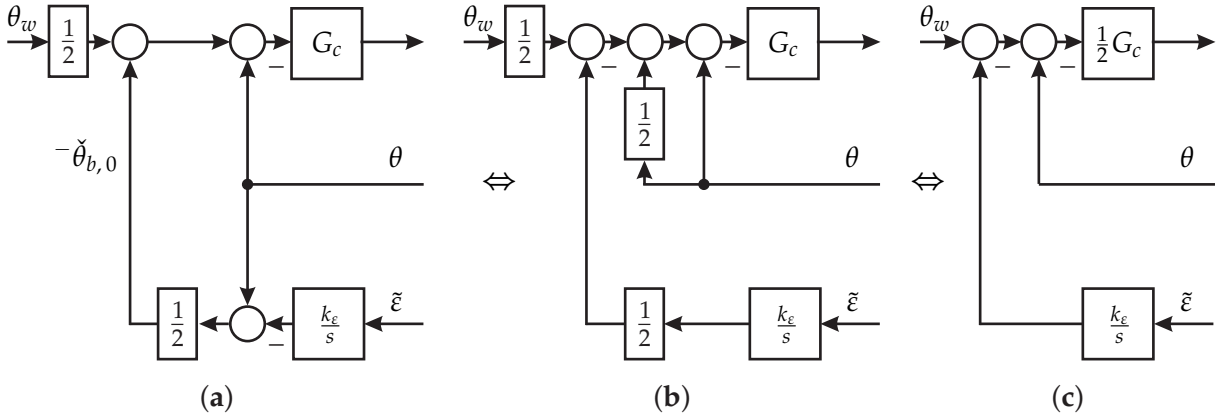
Figure 6.2.: Block scheme of the discrete wave echo control scheme **(a)** with reduction steps **(b)** and **(c)**.

The block scheme for the control law (6.5.1) is illustrated in figure 6.2 **(a)**. With the intermediate step illustrated in figure 6.2 **(b)** the control law may be simplified to yield the block scheme sketched in figure 6.2 **(c)**. The controller turns out to be an integral strain feedback at the position cascade level:

$$\theta_\varepsilon(s) = {}^-\check{\theta}_{b,0}(s) = -\frac{k_\varepsilon}{s}\, \varepsilon(x_s,\, s)\,, \tag{6.5.3}$$

with the initial position controller gains halved. The differentiation of control law (6.5.3) with respect to time or the repetition of the reduction steps based on equation 6.4.6 equivalently yield:

$$\dot{\theta}_\varepsilon(s) = {}^-\check{\theta}_{b,0}(s) = -k_\varepsilon\, \varepsilon(x_s,\, s)\,. \tag{6.5.4}$$

Strikingly, this equation is identical to (5.2.1). The main difference to the proportional feedback covered in chapter 5 is the division of the joint motion controller gains by two. Obviously, the tuning of the strain feedback k_ε depends on the gains determined for the joint motion controller. This is intuitively plausible, since a lower gain motion controller already complies to the echoed wave component, which is actually part of the physical coupling treated as a disturbance in section 3.2.

A purely torque based wave echo controller can be realized on the basis of equation 6.4.4 and oscillation rate measurements obtained from a gyroscope. However, experiments show the practical limitation in the case of TUDOR. Since the joints are current controlled but not truly torque controlled, the joint friction deteriorates the achievable damping and position accuracy.

O'Connor et al. (2009) selects the wave impedance Z_w to be $\frac{2}{\sqrt{k\,m}}$. In the present thesis, the complete gain k_ε is tuned through the same automated hardware in the loop optimization procedure already explained in section 5.3.

Since the proportional strain feedback at the velocity cascade level is already evaluated in chapter 5, figure 6.3 depicts the results obtained from twenty repetitions of a point-to-point maneuver using the integral control law 6.5.1 at the position cascade level.
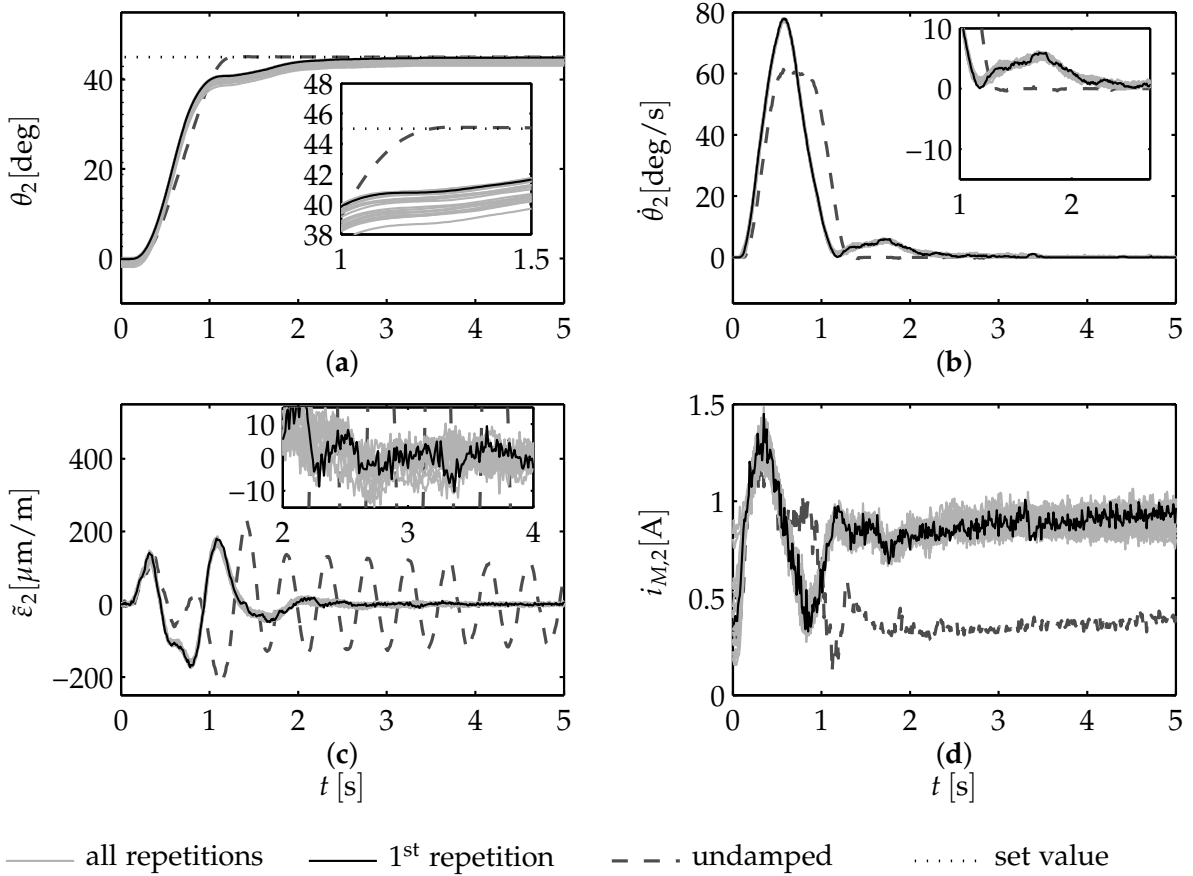
Figure 6.3.: Time series the joint angle (**a**), angular velocity (**b**), link strain (**c**) and motor current (**d**) measured on the second joint link module during twenty repetitions (*solid light gray*) of a point-to-point motion from $\boldsymbol{\theta} = [0°, 0°, 0°]^{\mathrm{T}}$ to $\boldsymbol{\theta} = [0°, 45°, -45°]^{\mathrm{T}}$ and the integral control law 6.5.1. The first repetition is highlighted (*solid black*). For comparison the graphs show the same experiment without damping (*dashed gray*).

6.6. Controller evaluation

O'Connor et al. (2009) move away from the WTF approximation (6.3.6) in favor of equation (6.5.3) to alleviate steady state positioning errors in the absence of gravity. However, from the joint angle in figure 6.3 (**a**) it is apparent, that in the presence of static deflections due to gravity the integration of the imperfectly mean liberated strain reintroduces the steady state positioning errors. This also explains the difference in the joint currents for the damped and undamped case visible in figure 6.3 (**d**).

In section 5.3 the damping action of the proportional strain feedback has been observed in the form of a motion reversal. In contrast, figure 6.3 (**b**) illustrates the damping action for the integral strain feedback to consist of a second acceleration phase, which reminds of feedforward input shapers discussed by Singer, Singhose and Seering (1999). In spite of the steady state error growing with each repetition, the light gray curves in figure 6.3 (**c**) evidence an ideally repeatable damping result comparable to the proportional strain feedback discussed in chapter 5. Malzahn, Balachandran and Bertram (2013) provide an online available video of the damping results.

7

Spatially Continuous Wave Echo Control

This is the third out of four subsequent chapters devoted to oscillation damping control. In this work, the controllers derived in the chapters 5 and 6 have been shown to be structurally equivalent. However, the derivations involve either a spatial discretization or a modal truncation. While the neglecting higher order dynamics can theoretically endanger the closed loop stability as already discussed in section 1.2, the lumped parameter view focuses on bending angles and torques. It neglects shearing forces and transversal deflections. The theory of spatially continuous mechanical waves provides an alternative way to incorporate all effects of the elastic link dynamics without truncation or discretization. The controller derived in the following is based on the active modification of the boundary conditions at the actuator side of the links. Parts of this chapter have been previously published by Malzahn and Bertram (2014).

7.1. Continuous wave variables

The theory starts with a reinterpretation of the general exponential solution (4.3.5) to the boundary value problem. Again, the whole arm is seen as a chain of independent joint-link-modules. Similar to chapter 6, the oscillations at any point along a link are considered to result from the superposition of mechanical wave components. However, the wave components consist of propagating components accompanied by near fields. This way equation (4.3.5) is redefined as follows:

$$y(x) = {}^+a + {}^-a + {}^+a_N + {}^-a_N. \tag{7.1.1}$$

The wave variables

$${}^+a = {}^+\hat{a}\,e^{-jk_\omega x} \quad \text{and} \quad {}^-a = {}^-\hat{a}\,e^{jk_\omega x} \tag{7.1.2}$$

denote the components of the forward and backward propagating waves. Analogously

$${}^+a_N = {}^+\hat{a}_N\,e^{-k_\omega x} \quad \text{and} \quad {}^-a_N = {}^-\hat{a}_N\,e^{k_\omega x} \tag{7.1.3}$$

are termed the attenuating near field wave components emerging at both link ends.
   The wave components are grouped into the vectors:

$${}^+\mathbf{a} = \begin{bmatrix} {}^+a, {}^+a_N \end{bmatrix}^\mathrm{T} \quad \text{and} \quad {}^-\mathbf{a} = \begin{bmatrix} {}^-a, {}^-a_N \end{bmatrix}^\mathrm{T}, \tag{7.1.4}$$

and the deflection y, bending angle θ_b, bending moment τ_b and shearing force F_y can be expressed in terms of the wave variables in the compact matrix form:

$$\begin{bmatrix} y \\ \frac{1}{k_\omega}\frac{\partial y}{\partial x} \\ \frac{1}{EIk_\omega^2}\tau_b \\ \frac{1}{EIk_\omega^3}F_y \end{bmatrix} = \begin{bmatrix} 1 & 1 & 1 & 1 \\ -j & -1 & j & 1 \\ -1 & 1 & -1 & 1 \\ j & -1 & -j & 1 \end{bmatrix} \begin{bmatrix} {}^+\mathbf{a} \\ {}^-\mathbf{a} \end{bmatrix}. \tag{7.1.5}$$

7.2. Reflection and transmission at junctions and boundaries

A travelling wave ${}^+\mathbf{a}$ reaching a junction or a boundary splits into a reflected wave component ${}^-\mathbf{a}$ and a transmitted wave component ${}^+\mathbf{b}$. The reflected component ${}^-\mathbf{a}$ computes to:

$$ {}^-\mathbf{a} = \mathbf{\Psi}\, {}^+\mathbf{a}. \tag{7.2.1}$$

The generally complex valued matrix $\mathbf{\Psi}$ is called the reflection matrix. The transmitted wave component ${}^+\mathbf{b}$ computes to:

$$ {}^+\mathbf{b} = \mathbf{\Omega}\, {}^+\mathbf{a}. \tag{7.2.2}$$

The generally complex valued matrix $\mathbf{\Omega}$ is called the transmission matrix. Note, in the case of the transversal oscillations of strings, the longitudinal oscillations of rods or the torsional oscillation of shafts near field components do not exist. The reflection and transmission would be governed just by a reflection and a transmission factor which corresponds to the top left elements of the matrices $\mathbf{\Psi}$ and $\mathbf{\Omega}$. For beam bending the matrix form implies that travelling bending waves arriving at boundaries or junctions may evoke new travelling wave components. Moreover travelling wave components can be converted into near field components and vice versa.

Consider a launched wave ${}^+\mathbf{a}$, which passes a constraining junction or support at $x = 0$. At this point the wave splits into a reflected wave component ${}^-\mathbf{a}$ and a transmitted wave component ${}^+\mathbf{b}$. The deflection at this location is characterized by:

$$ {}^-y(x) = {}^+a + {}^-a + {}^+a_N + {}^-a_N, \quad x \le 0, \tag{7.2.3}$$

$$ {}^+y(x) = {}^+b + {}^+b_N, \quad x \ge 0. \tag{7.2.4}$$

Following Mace (1984), the imposed constraints are modeled as the rotational and translational stiffnesses $\hat{K}_r$ and $\hat{K}_t$.

Assuming continuity in the deflection variables:

$$ {}^+y_{|x=0} = {}^-y_{|x=0} \quad \text{as well as} \quad \partial\, {}^+y(x,t)/\partial x_{|x=0} = \partial\, {}^-y(x,t)/\partial x_{|x=0} \tag{7.2.5}$$

and exploiting the first two rows of equation (7.1.5) in terms of ${}^-\mathbf{a}$, ${}^+\mathbf{a}$ and ${}^+\mathbf{b}$ results in:

$$ \begin{bmatrix} 1 & 1 \\ -j & -1 \end{bmatrix} {}^+\mathbf{a} + \begin{bmatrix} 1 & 1 \\ j & 1 \end{bmatrix} {}^-\mathbf{a} = \begin{bmatrix} 1 & 1 \\ -j & -1 \end{bmatrix} {}^+\mathbf{b}. \tag{7.2.6}$$

Next, the equilibrium of the bending torques and forces is assumed, so that:

$$ \hat{K}_r\, \theta_{b|x=0} = {}^+\tau_{b|x=0} - {}^-\tau_{b|x=0} \quad \text{and} \quad \hat{K}_t\, y_{|x=0} = {}^-f_{y|x=0} - {}^+f_{y|x=0}. \tag{7.2.7}$$

Both expressions can be reformulated using the bottom two rows along with the top right 2-by-2 submatrix of equation (7.1.5):

$$\begin{bmatrix} -1 & 1 \\ j & -1 \end{bmatrix} {}^{+}\mathbf{a} + \begin{bmatrix} -1 & 1 \\ -j & 1 \end{bmatrix} {}^{-}\mathbf{a} = \begin{bmatrix} -1 & 1 \\ j & -1 \end{bmatrix} {}^{+}\mathbf{b} + \begin{bmatrix} jK_r & K_r \\ K_t & K_t \end{bmatrix} {}^{+}\mathbf{b}, \qquad (7.2.8)$$

where the normalized stiffnesses

$$K_t = \frac{\hat{K}_t}{EI\,k_\omega^3} \quad \text{and} \quad K_r = \frac{\hat{K}_r}{EI\,k_\omega} \qquad (7.2.9)$$

abbreviate the notation.

The reflection matrix (7.2.1) and the transmission matrix (7.2.2) allow for the elimination of $^{-}\mathbf{a}$ and $^{+}\mathbf{b}$. After rearrangement the reflection and transmission matrix are expressed in terms of the boundary stiffnesses:

$$\mathbf{\Omega} = \mathbf{E} + \eta_t\,\mathbf{C}_t - \eta_r\,\mathbf{C}_r, \qquad \mathbf{\Psi} = \eta_t\,\mathbf{C}_t + \eta_r\,\mathbf{C}_r, \qquad (7.2.10)$$

with:

$$\mathbf{C}_t = \begin{bmatrix} j & j \\ 1 & 1 \end{bmatrix}, \ \mathbf{C}_r = \begin{bmatrix} -j & -1 \\ j & 1 \end{bmatrix}, \ \eta_t = \frac{K_t}{4 - (1+j)K_t}, \ \eta_r = \frac{K_r}{4 + (1-j)K_r}. \qquad (7.2.11)$$

The normalized stiffnesses K_r and K_t are the characteristic parameters of the reflection and transmission matrices at boundaries and junctions of beams. The controller described in section 7.4 makes use of this relation.

7.3. Near field contribution

Without natural damping the absolute value of the travelling waves persists along the whole beam. The near field wave components are special to bending waves and do not exist in the case of the transversal oscillations of strings, the longitudinal oscillations of rods or the torsional oscillation of shafts. It becomes apparent in the previous section, that the absence of near field components would facilitate the analyses and it is worth investigating the share of the near fields in the overall oscillation.

The absolute value of the near field components attenuates with the constant $1/k_\omega$, so that for sufficiently long links and higher natural frequencies the near field components can be neglected. To give a tangible example, consider the absolute value of the near field component emerging at one end of a single TUDOR link body. At the opposite link end this absolute value drops to about 70 % for $\omega = 1$ Hz and down to 10 % for $\omega = 30$ Hz. Obviously, the near field components substantially contribute to the deflections over the whole link length and in the frequency range of interest.

To give a graphical notion, figure 7.1 shows the contribution of all wave variables for the first two theoretical frequencies on the second link of TUDOR. This link carries the third joint, the third link as well as the end effector payload. The case of no end effector payload is visible in the figures 7.1 (**a**) and (**b**). The case with $m_L = 0.6$ kg and $I_E = 3.3 \cdot 10^{-4}$ kgm^2 is displayed in figures 7.1 (**c**) and (**d**). The load configuration corresponds to the lower and upper bounds already discussed with the aid of figure 4.5.
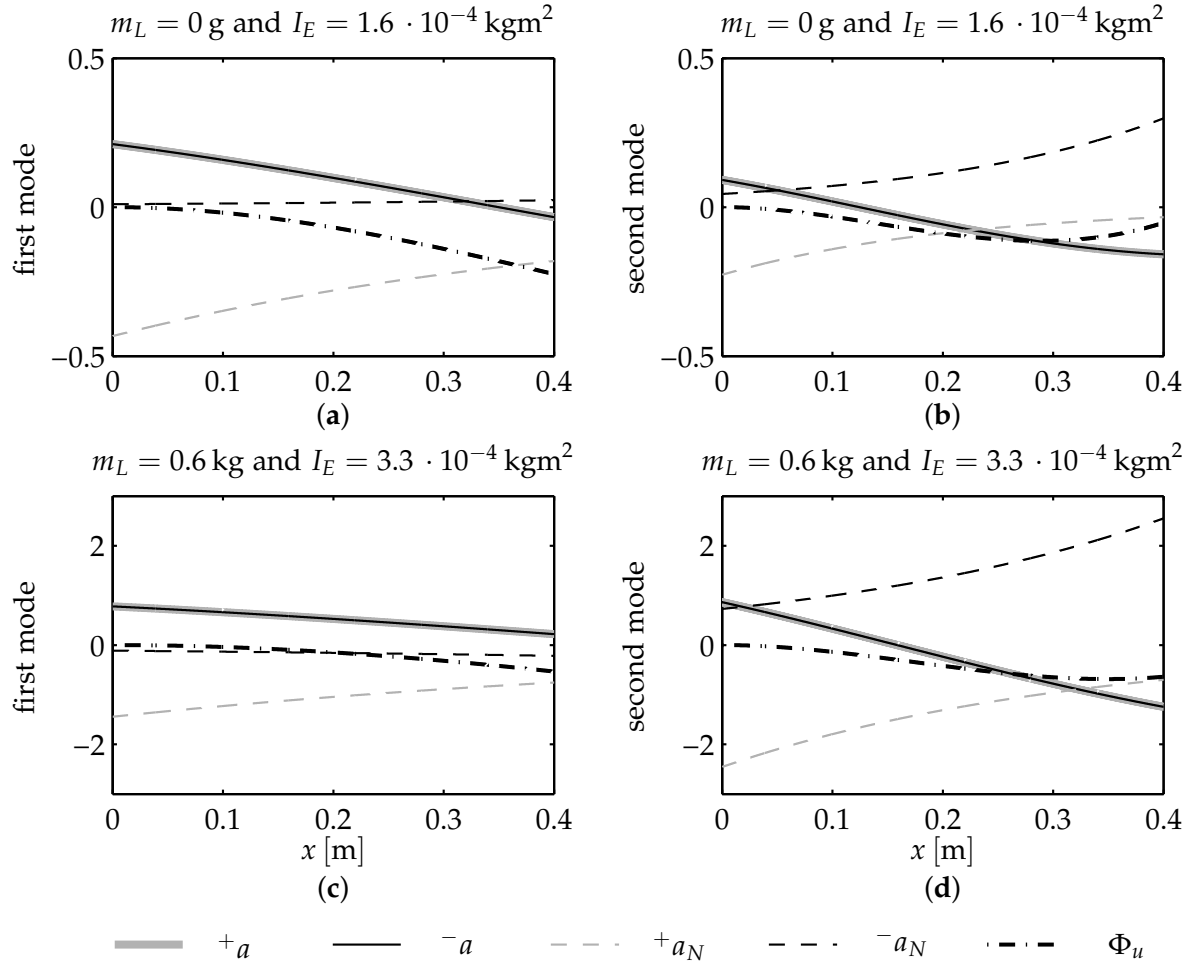
Figure 7.1.: Normalized travelling wave and near field wave components without (*top*) and with (*bottom*) tip load ($m_L = 0.6 \, \text{kg}$ and $I_E = 3.3 \cdot 10^{-4} \, \text{kgm}^2$).

It is clearly visible that the near field components significantly contribute to the shape function of the first two modes. Only for the first frequency the near field component ^-a_N is inconsequentially small. This is effected by the boundary conditions at the load end. As a conclusion for TUDOR, the near field components must not be neglected in the spatially continous wave model just by implication. It may be even argued, whether the near fields play the most important role in the comparatively short links. This would agree with the vanishing dispersion observed for the dominant frequencies in section 4.7.

7.4. Reflection matrix shaping

With an elastic-link robot at least one actuated joint is attached to each link. The joint can be controlled to actively shape the boundary conditions at this particular end. Equation (7.2.11) models the constraints at junctions and boundaries by translational and rotational stiffnesses K_t and K_r. These stiffnesses characterize the reflection and transmission of wave components at such points.

In the present work the robot comprises revolute joints. Therefore the translational
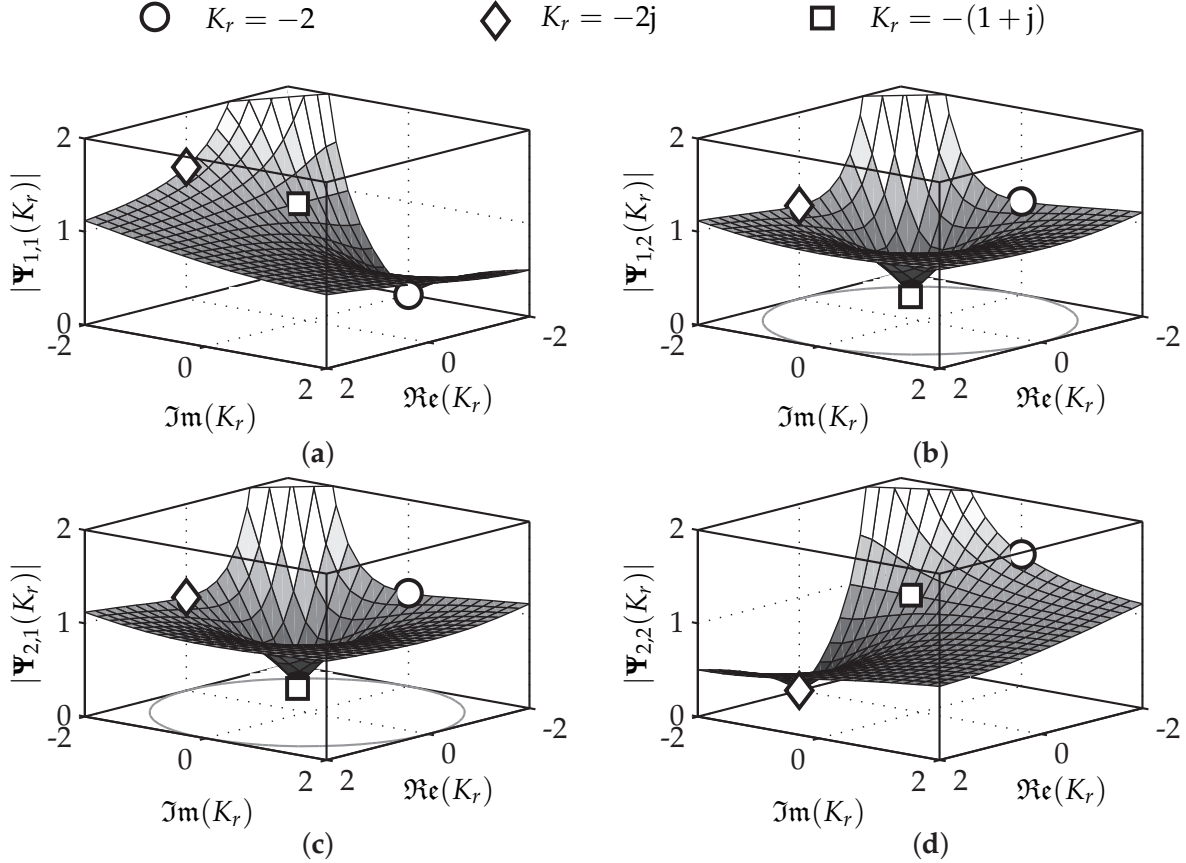
Figure 7.2.: Absolute values of the top left (**a**), top right (**b**), bottom left (**c**) and bottom right (**d**) reflection matrix entry for varying complex stiffnesses K_r.

stiffness K_t at all joints can be assumed to be large. The application of l'Hopital's rule to η_t for a real valued constant K_t in expression (7.2.11) yields:

$$\eta_t \approx \lim_{K_t \to \infty} \frac{K_t}{4 - (1+j)K_t} = \lim_{K_t \to \infty} \frac{1}{-(1+j)} = \frac{1}{\sqrt{2}} e^{-j\frac{5}{4}\pi}, \tag{7.4.1}$$

so that the reflection and transmission matrices at the joint location solely depend on the rotational stiffness K_r:

$$\mathbf{\Omega} = \begin{bmatrix} \frac{jK_r}{4+K_r(1-j)} + \frac{1-j}{2} & \frac{K_r}{4+K_r(1-j)} - \frac{1+j}{2} \\ -\frac{jK_r}{4+K_r(1-j)} + \frac{-1+j}{2} & -\frac{K_r}{4+K_r(1-j)} + \frac{1+j}{2} \end{bmatrix}, \tag{7.4.2}$$

$$\mathbf{\Psi} = \begin{bmatrix} -\frac{jK_r}{4+K_r(1-j)} - \frac{1+j}{2} & -\frac{K_r}{4+K_r(1-j)} - \frac{1+j}{2} \\ \frac{jK_r}{4+K_r(1-j)} + \frac{-1+j}{2} & \frac{K_r}{4+K_r(1-j)} + \frac{-1+j}{2} \end{bmatrix}. \tag{7.4.3}$$

The idea is to develop an oscillation feedback control law which augments the independent joint angle controller described in section 3.2 and actively shape the reflected rotational stiffness $\hat{K}_r$ with respect to the mean liberated strain measurement $\tilde{\varepsilon}(x_s, t)$.

If the strain gauges are applied very close to the joint hub, the gravity liberated net bending torque at the joint can be approximated with negligible error:

$$-\tilde{\tau}_{b|x=0} - {}^+\tilde{\tau}_{b|x=0} \approx \frac{EI_z}{y_b}\,\tilde{\varepsilon}_{|x=x_s}. \tag{7.4.4}$$

The rotational stiffness $\hat{K}_r$ relates this expression to the bending angle $\theta_{b|x=0}$ at the joint:

$$\hat{K}_r\,\theta_{b|x=0} = \frac{EI_z}{y_b}\,\tilde{\varepsilon}_{|x=x_s}. \tag{7.4.5}$$

The rearrangement of (7.4.5) with $\theta_\varepsilon = \theta_{b|x=0}$ using the normalized rotational stiffness K_r introduced in (7.2.9) and inserting the definition of k_ω from (4.3.3) yields the generic form of the oscillation damping control law:

$$\theta_\varepsilon = \frac{1}{K_r}\frac{1}{\sqrt{\omega}\,y_b}\sqrt[4]{\frac{EI_z}{\rho_b}}\,\tilde{\varepsilon}_{|x=x_s}. \tag{7.4.6}$$

Note, that this generic control law is frequency dependent and, by principle, it is set free from the boundary conditions at the opposite link end as well as the actual oscillation excitation source. No critical model truncation is involved.

The design objective is to find the rotational stiffness K_r, which modifies the transmission and reflection matrices, so that excited oscillations vanish as fast as possible.

A straight forward idea is to demand absolutely no wave reflection to take place at the joint. Mathematically this is equivalent to a singular reflection matrix $\mathbf{\Psi}$, which requires:

$$\det\mathbf{\Psi} = \frac{K_r(-1+\mathrm{j})}{4 + K_r(1-\mathrm{j})} = 0 \tag{7.4.7}$$

and consequently $K_r = 0$. Looking at (7.4.6), this implies an infinite gain controller, which is practically infeasible to realize. However, the obtained result is intuitively plausible. A controlled joint that does not act against the external torque admits to be driven back and absorbs any incoming wave components.

Figure 7.2 shows the absolute values of the individual elements of $\mathbf{\Psi}$ for varying normalized stiffnesses K_r. The graphs suggest a closer view at the three emphasized characteristic choices of K_r.

A finite gain controller with $K_r = -2$ causes the reflection coefficient $\Psi_{1,1}$ to vanish. In the absence of near fields or in the case of negligible near field components this would be a highly desired situation. Travelling wave components arriving at the joint do not initiate a reflected travelling wave. The total reflection matrix becomes:

$$\mathbf{\Psi} = \begin{bmatrix} 0 & -\mathrm{j} \\ -1 & -1+\mathrm{j} \end{bmatrix} \tag{7.4.8}$$

If near field components are not negligible an incoming wave is converted into a near field component while reaching near field components from the opposite end also start new reflected propagating waves. The associated control law (7.4.6) results in:

$$\theta_\varepsilon = -\frac{1}{\sqrt{\omega}}\frac{1}{2\,y_b}\sqrt[4]{\frac{EI_z}{\rho_b}}\,\tilde{\varepsilon}_{|x=x_s}, \tag{7.4.9}$$

which consists of a frequency dependent gain.

Another remarkable choice is $K_r = -2\mathrm{j}$, for which the reflection matrix computes to:

$$\mathbf{\Psi} = \begin{bmatrix} -(1+\mathrm{j}) & -1 \\ \mathrm{j} & 0 \end{bmatrix} \tag{7.4.10}$$

and shows vanishing near field reflection. Looking at the normalized wave components illustrated in figure 7.1, it can be expected that the control law:

$$\theta_\varepsilon = -\frac{1}{2\mathrm{j}} \frac{1}{\sqrt{\omega}} \frac{1}{y_b} \sqrt[4]{\frac{EI_z}{\rho_b}} \, \tilde{\varepsilon}_{|x=x_s} \tag{7.4.11}$$

significantly reduces structural oscillations. Moreover the temporal derivative computes to:

$$\dot{\theta}_\varepsilon = -\frac{\sqrt{\omega}}{2\, y_b} \sqrt[4]{\frac{EI_z}{\rho_b}} \, \tilde{\varepsilon}_{|x=x_s}. \tag{7.4.12}$$

A comparison with the previously introduced control law (5.2.1) allows the interpretation of (7.4.12) to be a frequency adaptive generalization of the proportional strain feedback presented in chapter 5. However, the frequency adaption is hard to realize in practice. An explicit online frequency estimation is likely too slow and by nature gets constantly more difficult with increasing damping success.

The most promising choice is the complex valued stiffness $K_r = -(\mathrm{j}+1)$. It yields the reflection matrix:

$$\mathbf{\Psi} = \begin{bmatrix} -1 & 0 \\ 0 & -1 \end{bmatrix}, \tag{7.4.13}$$

which causes both, incoming propagating waves as well as near field components, to be directly reflected with the opposite sign. In the absence of natural damping, which is implied by the real valued wave number k_ω, incoming and reflected waves destructively interfere. A conversion between reflected propagating waves and near field components is inhibited. The insertion into the generic control law (7.4.6) yields after rearrangement:

$$\theta_\varepsilon = -\frac{1}{(1+\mathrm{j})\sqrt{\omega}} \frac{1}{y_b} \sqrt[4]{\frac{EI_z}{\rho_b}} \, \tilde{\varepsilon}_{|x=x_s} = -\frac{1}{\sqrt{\mathrm{j}\omega}} k_\varepsilon \, \tilde{\varepsilon}_{|x=x_s}, \tag{7.4.14}$$

which is the Fourier domain transfer function of a so-called half-integrator and a gain:

$$k_\varepsilon = \frac{1}{\sqrt{2}\, y_b} \sqrt[4]{\frac{EI_z}{\rho_b}}. \tag{7.4.15}$$

In comparison to the transfer function of the commonly known full-integrator $\frac{1}{\mathrm{j}\omega}$, the slope of the logarithmic frequency magnitude is half as steep. The constant phase angle of the half-integrator is also half the phase angle of the full-integrator.

Flotow and Schäfer (1986) report that feeding back the tip deflection to the actuator control torque leads to the similar half-differentiator as a wave based controller. Using strain feedback at the velocity cascade level also leads to the half-differentiator:

$$\dot{\theta}_\varepsilon = -\mathrm{j}\omega \, \frac{1}{(1+\mathrm{j})\sqrt{\omega}} \frac{1}{y_b} \sqrt[4]{\frac{EI_z}{\rho_b}} \, \tilde{\varepsilon}_{|x=x_s} = -\sqrt{\mathrm{j}\omega}\, k_\varepsilon \, \tilde{\varepsilon}_{|x=x_s}. \tag{7.4.16}$$
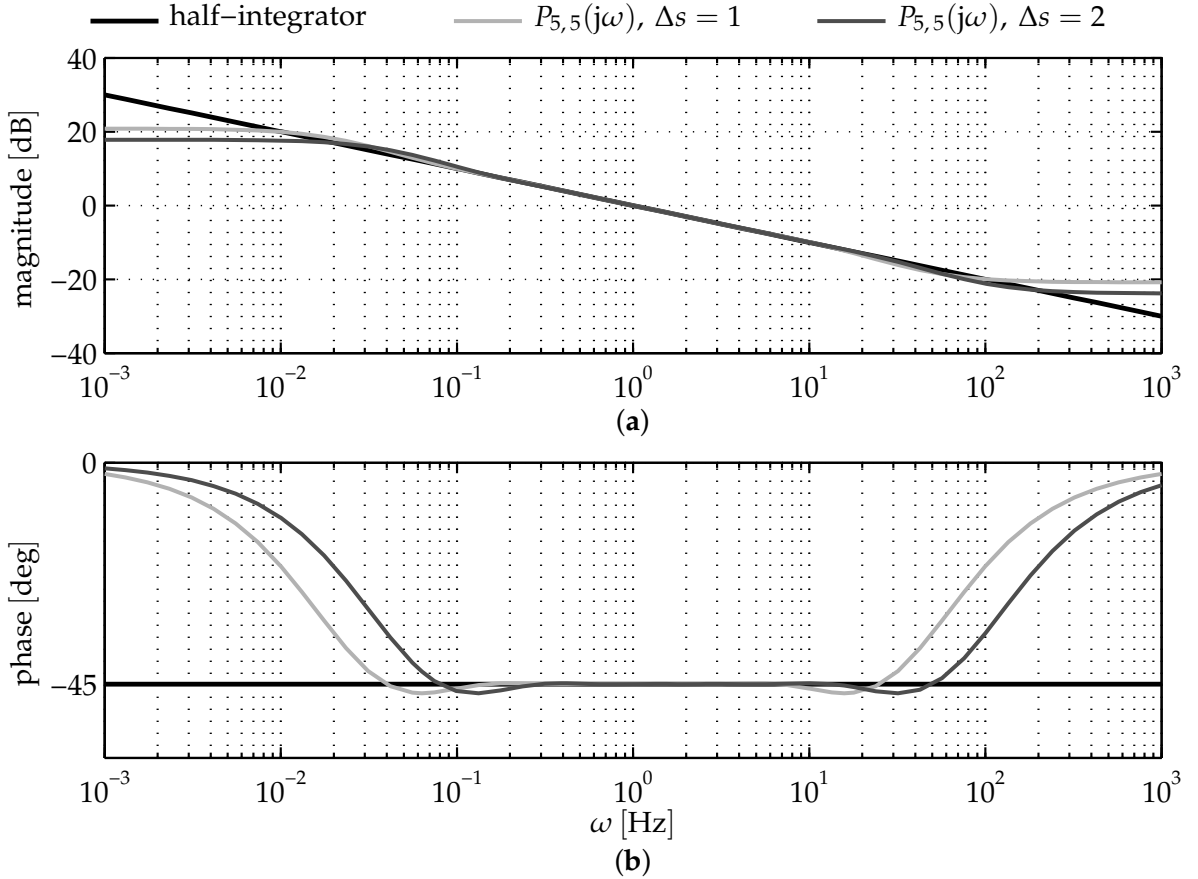
Figure 7.3.: Bode diagram with magnitude (**a**) as well as phase (**b**) of the half-integrator and its approximations.

Neither of these controllers can be exactly realized by means of standard linear transfer elements.

7.5. Approximation of the half-integrator

Flotow and Schäfer (1986); Podlubny et al. (2002) approximate the behavior of the half-differentiator by Lattice hardware circuits. More recently Takyar and Georgiou (2007) discuss different software approximations of the half-integrator such as RC ladders and the Padé approximation. While the half-differentiator has an acausal phase lead by nature, a shifted version of the 5th order Padé approximation by Takyar and Georgiou (2007) is employed to realize the causal half-integrator in the present thesis:

$$P_{5,5}(s) = \frac{1}{\sqrt{\Delta s}} \frac{\hat{s}^5 + 55\hat{s}^4 + 330\hat{s}^3 + 462\hat{s}^2 + 165\hat{s}^1 + 11}{11\hat{s}^5 + 165\hat{s}^4 + 462\hat{s}^3 + 330\hat{s}^2 + 55\hat{s}^1 + 1} \approx \frac{1}{\sqrt{s}}, \qquad (7.5.1)$$

with $\hat{s} = \frac{s}{\Delta s}$ and Δs being the frequency shift factor introduced for better approximation in the frequency range of interest as shown in figure 7.3.

------ all repetitions   ——— 1st repetition   – – · undamped   · · · · · · set value
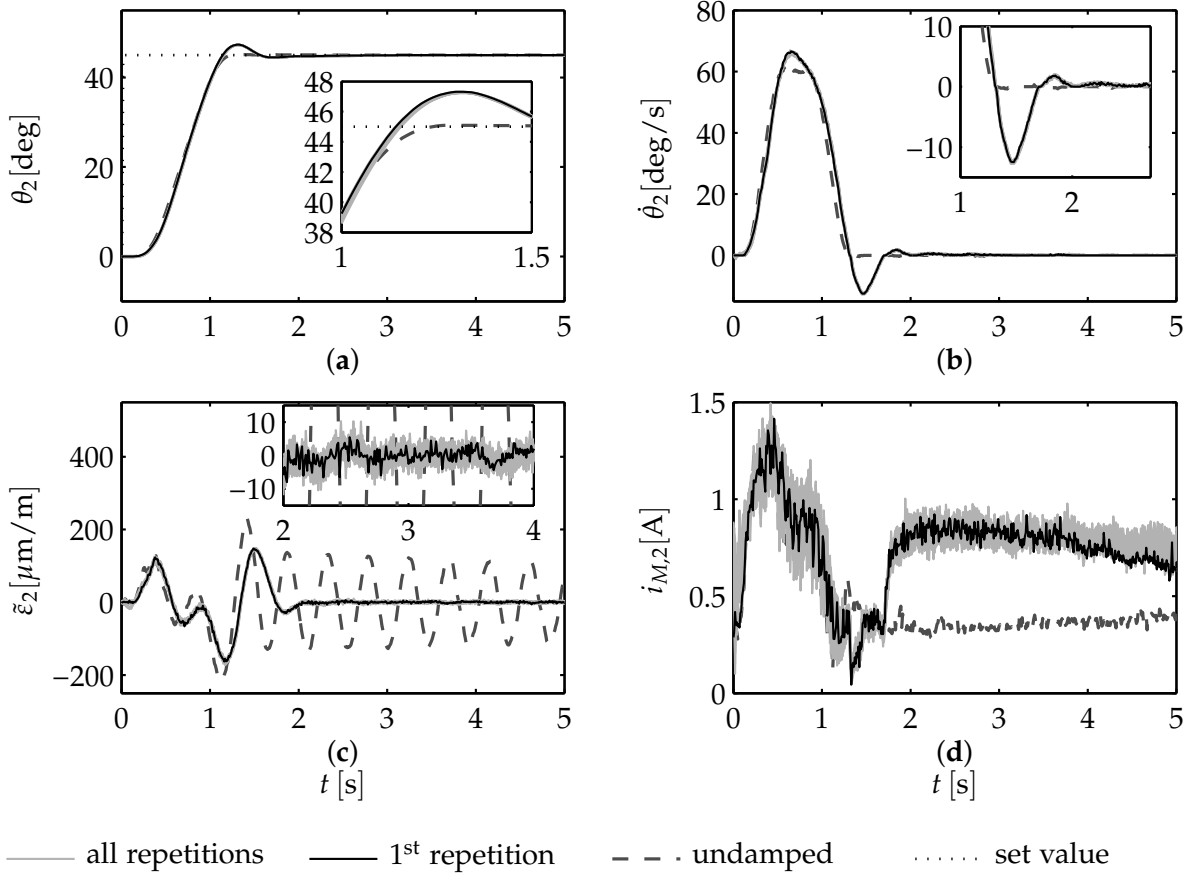
Figure 7.4.: Half-integrator damping results. Time series the joint angle (**a**), angular velocity (**b**), link strain (**c**) and motor current (**d**) measured on the second joint link module during twenty repetitions (*solid light gray*) of a point-to-point motion from $\theta = [0°, 0°, 0°]^T$ to $\theta = [0°, 45°, -45°]^T$. The first repetition is highlighted (*solid black*). For comparison the graphs show the same experiment without damping (*dashed gray*).

7.6. Controller evaluation

Oscillation damping results with the half-integrator wave reflection controller are exemplified in figure 7.4. Equally to chapters 5 and 6 the gain k_ε has been automatically tuned through the hardware in the loop optimization reported in section 5.3. The time series presented in the figure are very similar to those observed with the proportional strain feedback in chapter 5. The damping action is observed as an overshoot in the joint angle in figure 7.4 (**a**) and a corresponding motion reversal in the joint angular velocity in figure 7.4 (**b**). The slim distribution of the measurements of all twenty repetitions indicate a high repeatability of the damping result without steady state positioning error. The rapid damping evidenced through the strain measurements presented in figure 7.4 (**c**). The evolution of the joint current in figure 7.4 (**d**) also reminds of the proportional feedback results in figure 5.3 (**d**).

8

Experimental Damping Comparison

This is last out of four subsequent chapters devoted to oscillation damping control. Chapter 5 discusses the proportional strain feedback at different cascade levels of the independent joint motion controller designed in chapter 3. From the root locus analysis carried out in chapter 5, the proportional feedback at the velocity cascade level is identified to be the best choice. Chapter 6 identifies wave properties in chains of lumped mass-spring-systems. The derivations arrive at the same damping controller structure at velocity cascade level and alternatively propose an integral feedback at position level. A more precise modeling perspective in terms of continuous propagating waves and near fields leads to fractional order feedback laws in chapter 7. With the following sections the work contributes an experimental comparison of the proportional strain feedback at the velocity cascade level along with the integral as well as half-integral strain feedback at the position cascade level.
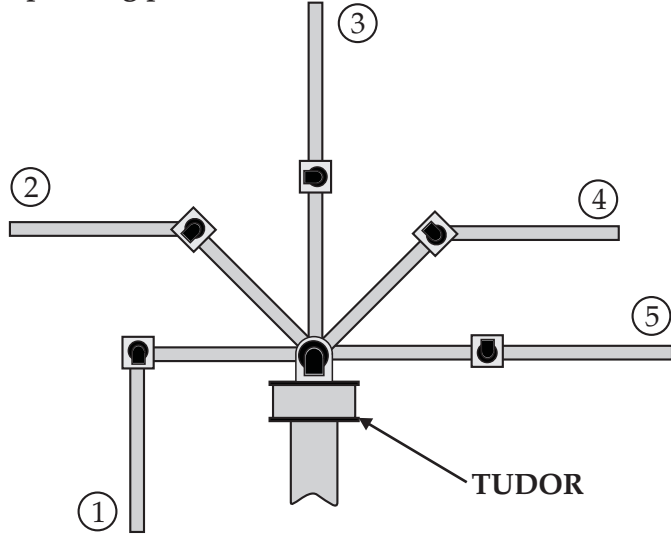
8.1. Experiment design

The oscillation damping results provided in the chapters 5 to 7 are based on the automated hardware in the loop optimization of the oscillation damping gains with respect to the integral absolute time weighted strain surface criterion (see B.4) for the particular point-to-point motion from $\boldsymbol{\theta} = [0°, 0°, 0°]^{\mathrm{T}}$ to $\boldsymbol{\theta} = [0°, 45°, -45°]^{\mathrm{T}}$. The accomplished results provided in these chapters represent a principal proof of concept for the synthesized controllers.

Tuning gains for a single motion task may be adequate for a few low-level tasks in industrial mass production. However, a robot is actually expected to be equally functional in the whole workspace and arbitrary motions within that workspace. The experiments presented in this chapter are therefore carried out around as well as in between of the operating points illustrated and indexed in figure 8.1. Among all operating points ③ and ⑤ are special. The straight vertical pose in operating point ③ maximizes the effect of joint backlash. The straight horizontal pose in operating point ⑤ maximizes the effect of gravity.

All joint motions are performed with a maximum speed of 60 deg/s as well as a maximum acceleration of 200 deg/s^2. The basic payload is $m_L = 300$ g. All experiments in this chapter are repeated 20 times. The results are given as mean and standard deviation over all repetitions. The medium step motion indexed by 06 cor-

operating points:

experiment index:

small steps	**01:** ① + $[0°,5°,5°]^{\mathrm{T}}$	
	02: ② + $[0°,5°,5°]^{\mathrm{T}}$	
	03: ③ + $[0°,5°,5°]^{\mathrm{T}}$	
	04: ④ + $[0°,5°,5°]^{\mathrm{T}}$	
	05: ⑤ + $[0°,5°,5°]^{\mathrm{T}}$	
medium steps	**06:** ① ⟶ ②	
	07: ② ⟶ ③	
	08: ③ ⟶ ④	
	09: ④ ⟶ ⑤	
large steps	**10:** ① ⟶ ③	
	11: ③ ⟶ ⑤	
	12: ⑤ ⟶ ②	

Figure 8.1.: Operating points and experiment naming.

responds to the experiment employed in the chapters 5 to 7. The gains tuned for this case remain fixed for all experiments throughout the present chapter.

The comparison criteria applied in the sections 8.2 and 8.3 are the maximum absolute strain amplitude $\max(|\tilde{\varepsilon}_2|)$ measured on the second joint-link-module, the strain settling time $T_{CS}(\tilde{\varepsilon}_2)$ (see B.4) for the same strain measurement as well as the spectral amplitude $|\mathcal{F}(\omega_1)|$ at the first dominant eigenfrequency. The integral absolute time weighted strain surface $\mathrm{IATS}(\varepsilon_2)$ may be understood to be information provided by the maximum strain amplitude as well as settling time aggregated in a single integral criterion. It penalizes strain overshoots as well as long lasting oscillations.

The impact of the damping action on the joint positioning is judged by the joint angle settling time $T_{CS}(\theta_2)$ (see B.4) as well as the integral absolute time weighted angular error $\mathrm{IATE}(\theta_2)$ (see B.4).

8.2. Whole workspace step responses

For the oscillation damping control concepts under consideration the performance in the whole workspace is assessed from small, medium and large scale point-to-point motions. The small motions range five degrees in the second and third joint starting from the five operating points visible in the left of figure 8.1. The medium steps are point-to-point motions between neighboring operating points. The large steps from ① to ③ as well as from ③ to ⑤ just skip the operating point in between. The motion from ⑤ to ② is the largest step, which also passes the straight vertical arm pose. This means, that the static load torque along with the static strain changes sign. The inclusion of this scenario is important against the background, that Franke et al. (2009) discovered such a sign change to cause stability problems in some damping approaches.

All metrics are normalized to the corresponding values of the undamped case. Consequently their values are given in percent. Since the undamped oscillations can last
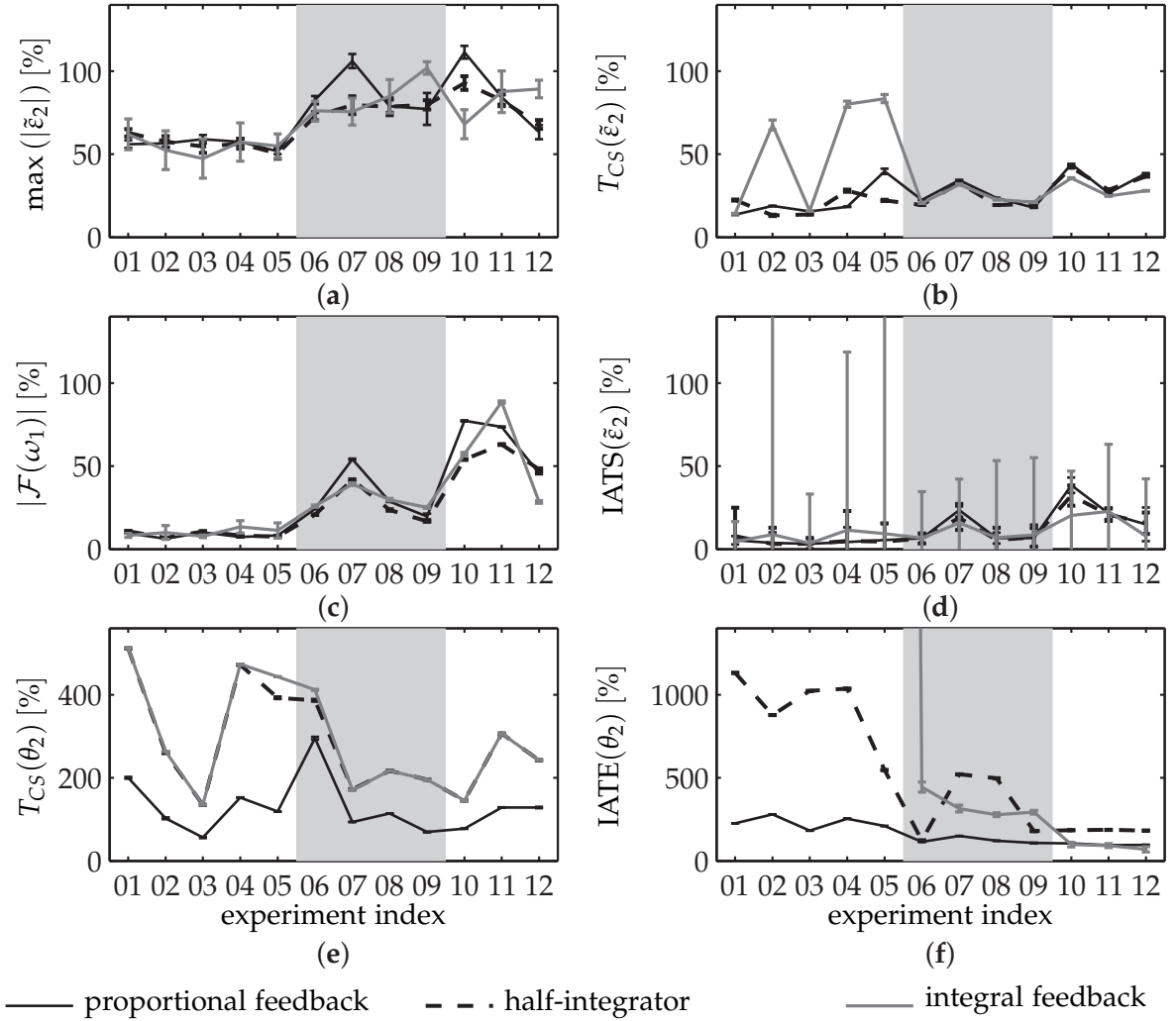
Figure 8.2.: Damping metrics in the whole workspace with the robot carrying a payload of $m_L = 300\,\mathrm{g}$.

for minutes, the strain settling time $T_{CS}(\tilde{\varepsilon}_2)$ is normalized by the fixed time horizon of ten seconds.

For the small motions all three control schemes succeed to significantly reduce the maximum strain amplitude as visible in figure 8.2 (**a**). For medium and large motions this reduction becomes rather insignificant for the proportional and integral feedback. Only the half-integrator scheme reliably keeps the amplitude about 75 % of the undamped case. The results with the integral concept spread wider than the results obtained with the other two schemes.

Figure 8.2 (**b**) evidences that all three control approaches drastically and reliably reduce the strain settling times throughout the whole workspace. The proportional feedback as well as the half-integrator feedback are almost equal. Strikingly, the integral feedback performs significantly worse during the small motions than the other two.

The inspection of the relative spectral amplitude of the dominant eigenfrequency in figure 8.2 (**c**) shows only inconsequential differences between the individual approaches. The spectral amplitude drops below 10 % for the small motions. A reduced
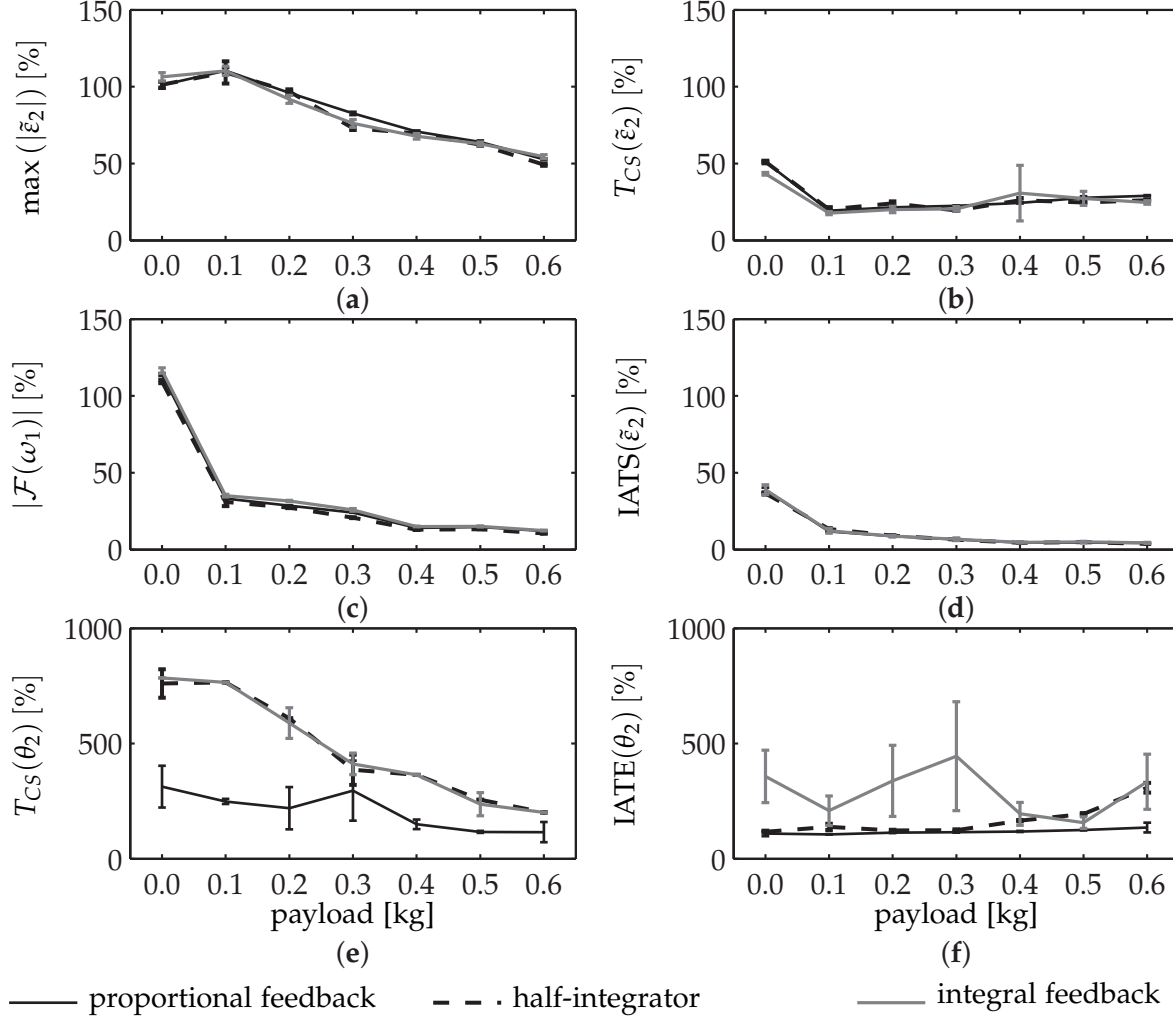
Figure 8.3.: Damping metrics for experiment 06 with varying payloads.

damping effect can be observed for experiment 07 and 11. With the experiment 07 the motion target is the straight vertical pose where backlash has a maximum impact so that damping actions cannot develop their full effect. Experiment 11 stops at the straight horizontal pose, where the actuators have to operate under the largest load.

On average, the integral time weighted strain surface in figure 8.2 (**d**) is equivalently minimized by all three controllers. However, the integral feedback exhibits very irregular results.

Looking at the joint angle metrics in figures 8.2 (**e**) and (**f**) reveals that the damping actions have the least impact on the joint motion augmented by the proportional feedback at the velocity cascade level. The strongest impact is observed with the full integral feedback at the position controller level.

8.3. Varying payloads

The robustness assessment of the three oscillation damping controllers with respect to varying payloads bases on the point-to-point motion experiment 06. While the

gains are tuned and fixed for the default payload of $m_L = 300$ g using three test mass plates, the investigated payload variation ranges from zero to six test mass plates so that $m_L \in \{0\,\text{g}, 100\,\text{g}, 200\,\text{g}, 300\,\text{g}, 400\,\text{g}, 500\,\text{g}, 600\,\text{g}\}$. Again, all metrics are normalized to the corresponding values of the undamped case, just as described in the previous section.

Figure 8.3 (**a**) shows that a relative reduction in the maximum strain amplitude becomes increasingly significant with larger payloads. This is also observed from the spectral amplitude of the first dominant eigenfrequency in the graph 8.3 (**c**). The maximum strain amplitude as well as the spectral amplitude of the first eigenfrequency are slightly increased by the damping action for payload masses of 0 g and 100 g. This can be understood as an over reactive damping behavior, due to the fixed gains tuned for a payload of $m_L = 300$ g.

Nevertheless, except for zero payload all three damping controllers accomplish an almost constant abbreviation of the settling time by about 80 % as visible in figure 8.3 (**b**).

At zero payload the relative reduction of the settling time appears less because of the normalization to 10 s. A result of 50 % is equivalent to 5 seconds already incorporating the actual point-to-point motion taking a little less than 2 seconds.

The relative decrease of the integral time weighted strain surface presented in figure 8.3 (**d**) is significant for all three damping approaches. As with the metrics before, the damping action becomes increasingly significant with growing payload masses. In summary all three control schemes robustly damp oscillations for a wide range of payloads.

Looking at the joint angle metrics in figure 8.3 (**e**) and (**f**), the conclusion to be drawn is identical to the experiments with constant payload but varying operating points in the whole robot workspace. The proportional strain feedback operating at the velocity controller level affects the joint motion way less than the other two approaches operating at the position cascade level. The full integral feedback shows a drastically spread distribution around the average metric values. The reason for that is the aggregation of imperfectly cancelled static strains.

8.4. Disturbance rejection

The previous two sections considered the joint motion to be the only source of oscillations excited in the link structure. Interactions between the robot and the environment are another practically relevant source of oscillations. Their exact amplitude as well as location of action along the structure is commonly unknown. The disturbance may be impulsive, step-like or even periodical.

Periodic excitation

The periodic disturbance is generated using a DC motor attached to the robot end effector as depicted in figure 8.4 (**a**). The DC motor carries an unbalanced load. The deviative reaction moments excite the oscillations at the motor frequency of rotation. This frequency is manually tuned close to resonance with the first dominant eigenfrequency by adjusting the motor input voltage.

(a)

(b)

(c)

(d)
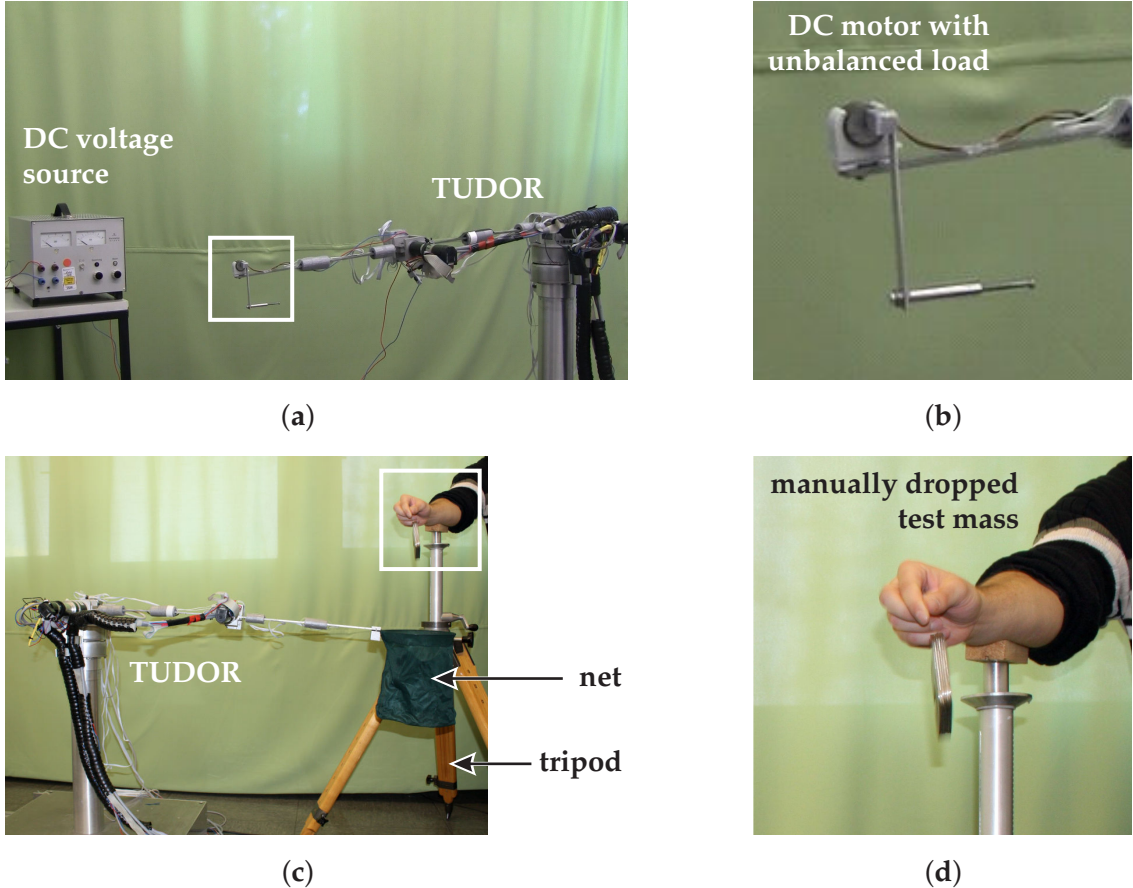
Figure 8.4.: Experimental setups to generate periodic (**a**)-(**b**) and step-like disturbances (**c**)-(**d**).

In all experiments the arm resides in the horizontally stretched out joint zero config-uration, which represents the maximum load configuration for the actuators. During the first two seconds of each repetition the oscillation damping gain is zero. After ap-proximately two seconds the gains are set to the default ones tuned in the chapters 5 to 7.

Figure 8.5 shows the time series of strain measurements (**a**) and (**b**) as well as joint angular velocity measurements (**c**) and (**d**) for the proportional strain feedback as well as the half-integrator controller. Experimental results with the full integral feedback at the joint position cascade level are omitted here. The excited oscillations are large enough to interfere with the static strain cancellation. The interference accumulates in the integral control law and introduces a drift in the joint angle, so that results are not comparable to the other control approaches.

The close to resonance strain amplitude is equally visible in the left of figures 8.5 (**a**) and (**b**). In spite of the large gear ratios, the strong oscillations also affect the joint angles. During the first two seconds in figures 8.5 (**c**) and (**d**) the cascaded independ-ent joint controllers have to visibly compensate for the strong oscillations.

With the activation of the oscillation damping, the strain amplitude abruptly drops from close to 400 μm/m to approximately 100 μm/m. The half-integrator achieves a slightly smaller strain amplitude in figure 8.5 (**b**) compared to the proportional feedback in figure 8.5 (**a**) with apparently the same effort as visible in figures 8.5 (**c**) and (**d**).
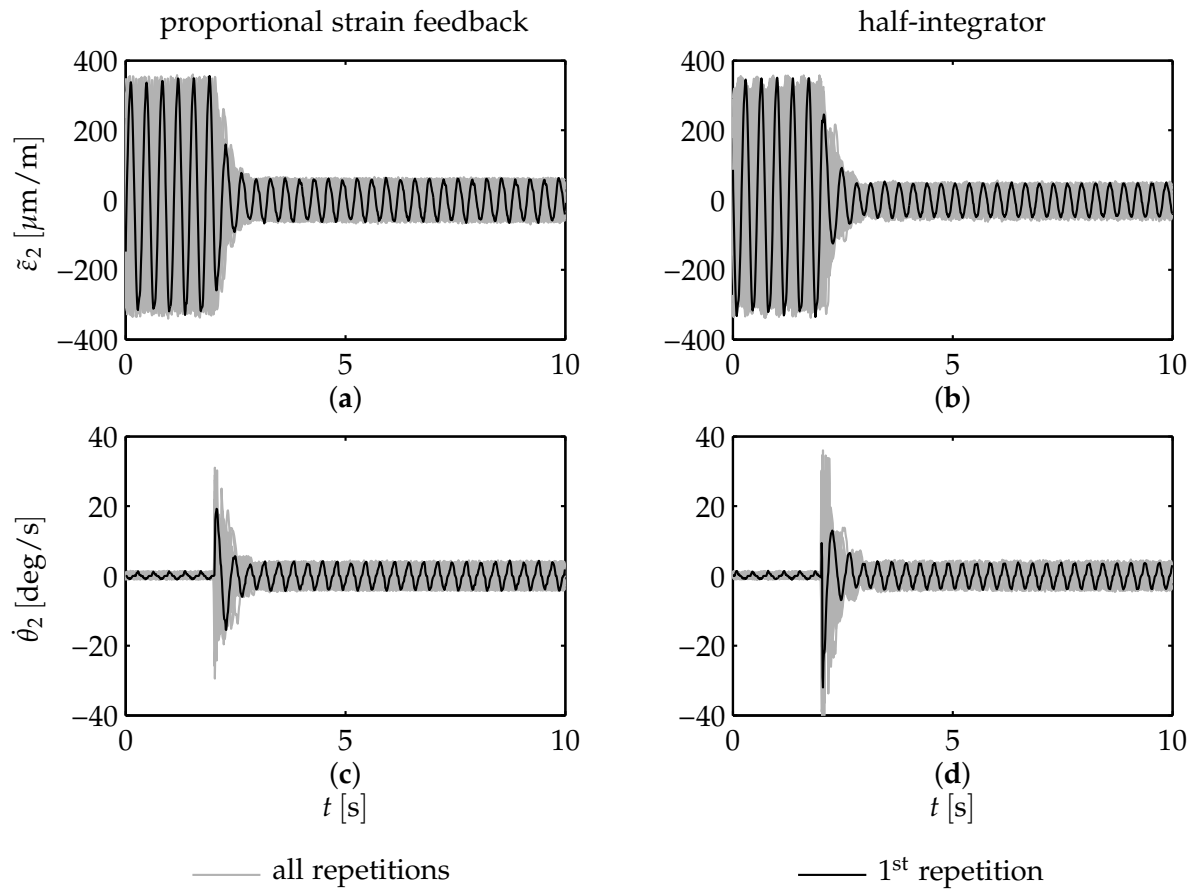
Figure 8.5.: Harmonic disturbance results.

The twenty repetitions of each experiment vary in the timing. In every repetition the damping controller gets activated in a different oscillation phase. This melts the individual repetitions drawn as gray graphs in figure 8.5. Nevertheless the graphs prove the reliable repeatability of the damping results irrespective of the initial phase.

Malzahn and Bertram (2013, at 0:48 min) demonstrate the periodic disturbance experiment in an online available video. The video shows the excitation at a constant frequency as well as a frequency sweep.

Disturbance steps

The rejection of step-like disturbances is investigated using a net attached to the end effector in operating point ⑤ as visible in figure 8.4 (**b**). The net with fixture has a mass of 120 g. Besides the net, the end effector initially carries no load. The step-like disturbances are generated by manually dropping an additional test mass of 600 g into the net. The height from the initial test mass position to the net bottom amounts to approximately 50 cm. The manual experiment execution is the reason for the temporal misalignment between the graphs of different repetitions as well as irregularities in the excitation amplitude.

Again, the results for the full integral strain feedback are omitted, because the momentous and potentially growing steady state error practically disqualifies the approach.
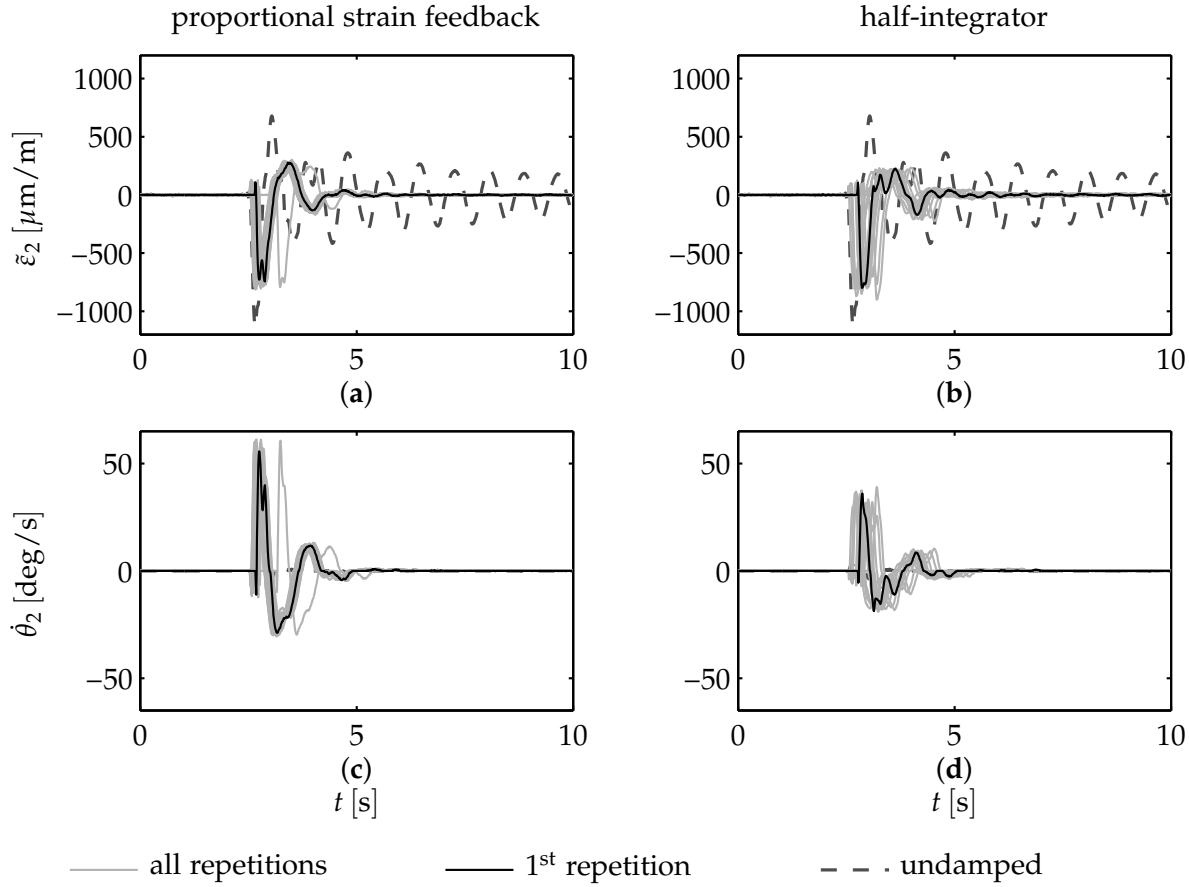
Figure 8.6.: Step disturbance results.

The strain measurements in the figures 8.6 (**a**) and (**b**) evidence rapid attenuation of the excited oscillations as well as the static strain due to the additional payload. Similar to the periodic disturbance rejection the figures 8.6 (**c**) and (**d**) indicate, that the half-integrator controller seems to require less effort in terms of joint motion to achieve the oscillation damping. The proportional strain feedback controller appears to comply more under the external disturbance. In summary, the proportional feedback as well as the half-integrator control properly dampen the oscillations within about two seconds.

8.5. Damping with a single actuator

The frequency measurements in section 4.7 show that the dominant eigenfrequencies of each individual link are measurable on the other link in the chain under preservation of phase alignment. This leads to the corollary that each joint can damp the oscillations of the whole arm structure. In order to prove that, experiment 06 repeated twenty times with the damping gains for the second joint-link-module set to zero and only the third joint employed for damping the oscillations.

Figure 8.7 (**a**) and (**b**) show the resulting strain measurements on the second joint-link-module, whereas figure 8.7 (**c**) and (**d**) display the angular velocity measurements including the damping actions on the *third* joint-link-module.

proportional strain feedback · half-integrator
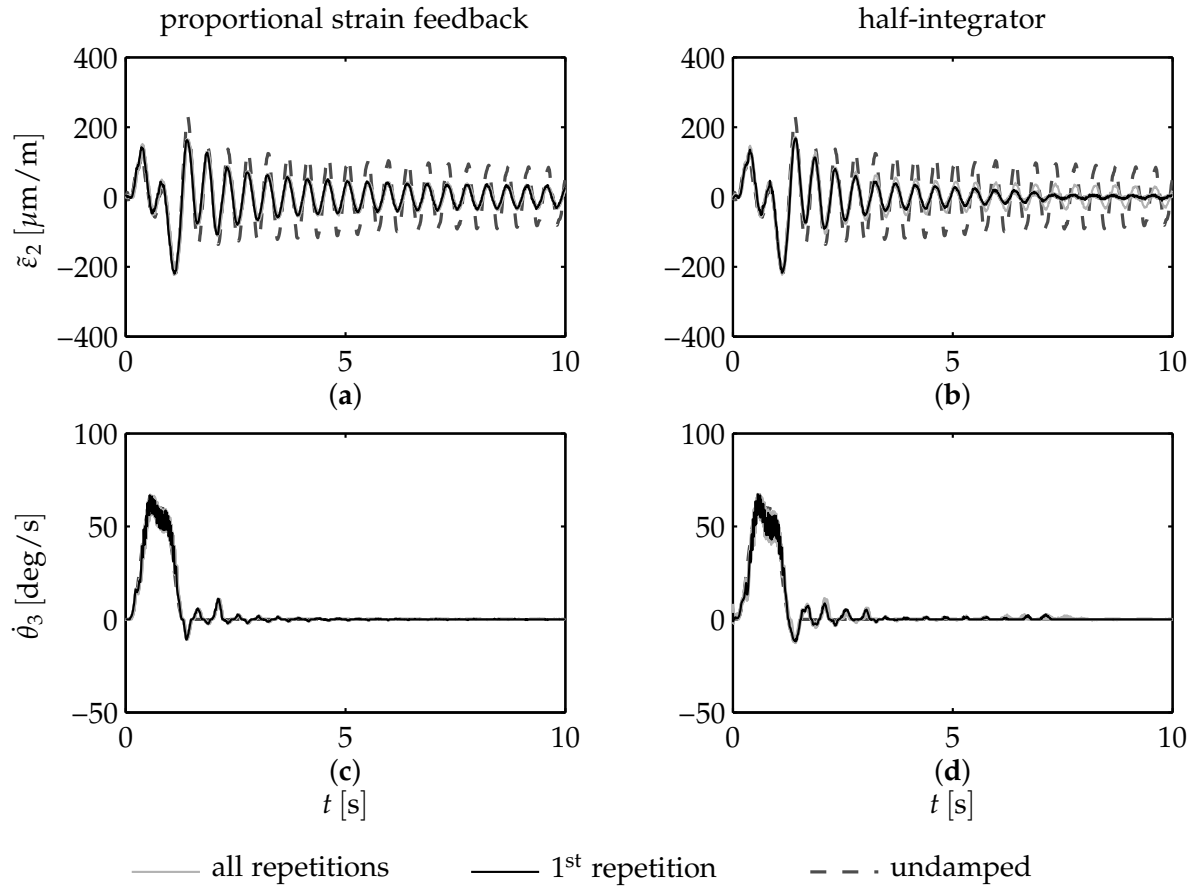
Figure 8.7.: Results with only the third actuator performing damping actions. The arm carries a payload of $m_L = 300 \, \text{g}$

Of course, the damping result achieved with a single actuator cannot compete with the results obtained using both actuators. Nevertheless the damping improvements with both, the proportional feedback as well as the half-integrator feedback are clearly visible. The half-integrator accomplishes the superior damping among the two concepts.

8.6. Discussion

First of all, it has to be observed that all three investigated damping control concepts robustly attenuate structural oscillations under the applied changes in payload as well as altered operating points.

The full-integral feedback at the position cascade level suffers from steady state errors growing over time. The clearly wider standard deviations of the metrics compared to the other approaches evidence an unsatisfactory smaller repeatability. The reason is the imperfect static strain cancellation frequently charging and discharging the feedback integrator state. Any practically implemented model of the static strain only has finite accuracy. Thus, the imperfection would also occur if the static strain cancellation would have been performed using a model based approach. As a conclusion, full-integral strain feedback is not recommended for elastic link robots operating

under gravity.

The half-integrator at the position cascade level as well as the proportional strain feedback at the velocity cascade level show very similar results. Both control methods demand for no explicit model knowledge about the actual link dynamics. They feature just a single additional controller gain per joint-link-module to be tuned. The dampen oscillations irrespective of their excitation source.

The half-integrator requires the least efforts to reject external disturbances, the proportional strain feedback has the smallest impact on the actual joint positioning. With the damping results being almost equal to the half-integrator, the proportional feedback is therefore the favored oscillation damping controller in the remainder of this thesis. Nevertheless, the half-integrator concept would produce equivalent results with respect to the remaining chapters of this thesis. In this regard, the compensation of the first undesired effect associated with the intentionally introduced link elasticity, namely the structural oscillations, is accomplished for the scope of this thesis.

9

End Effector Control

With the structural oscillations readily damped, the forward and inverse kinematics modeling simplifies. A reconstruction of the end effector location based on a truncated series of oscillation modes or a finite number of lumped parameters may be omitted. It is sufficient to focus on the compensation of the static deflections in order to accurately position the end effector.

The oscillation damping controllers derived in chapters 5 to 7 waive the need for any dynamics model at runtime. It is consistent and desirable to investigate an end effector positioning approach, which relinquishes any additional modeling compared to conventional robots. Section 9.1 follows this paradigm using the eye-in-hand mounted camera detailed in section 2.3.

Alternatively, the forward and inverse kinematics have to be modelled under consideration of the static configuration and load dependent deflections in order to position the end effector. In comparison to conventional robots the additional static strains estimated in section 2.2 are required. The data-based load estimation and kinematics presented in section 9.2 are originally developed for TUDOR and published by Phung et al. (2011a). Continuatively, Malzahn, Phung and Bertram (2012a) demonstrate the positioning speed and accuracy of the inverse kinematics with integrated oscillation damping through the realization of the ball catching task detailed in section 9.3.

9.1. Visual servoing

Visual servoing controllers with an eye-in-hand mounted camera minimize the relative pose error between a current view and a goal view of the scene. Today visual servoing is a well understood topic in literature. An early tutorial is given by Hutchinson, Hager and Corke (1996). A decade later Chaumette and Hutchinson (2006, 2007) summarize fundamental concepts and also provide an introduction to more advanced visual servoing techniques. Visual servoing controllers are categorized as position based visual servoing controllers (PBVS) or image based visual servoing controllers (IBVS). PBVS also known as 3D visual servoing controllers use the image information to explicitly estimate the camera poses and infer the control error with respect to a coordinate frame of reference. In IBVS or 2D visual servoing the control error is directly formulated in the 2D image space. Hybrid concepts exist, which are basically IBVS approaches involving a partial pose estimate or measurement. While the concepts

have their individual merits and shortcomings, they all operate on the pure basis of differential robot kinematics. This is a beneficial property for the end effector control of elastic link robots. The visual servoing controller commands a camera velocity $\mathbf{v}_c$, which may be interpreted as a relative direction towards the goal rather than a particular absolute metric path to the goal. Outside kinematically singular configurations the inverse of the end effector referred robot Jacobian $^E\mathbf{J}_r(\boldsymbol{\theta})$ transforms the relative camera motion vector into the joint space:

$$\dot{\boldsymbol{\theta}} = {}^E\mathbf{J}_r^{-1}(\boldsymbol{\theta})\,\mathbf{v}_c \qquad (9.1.1)$$

In the joint space the direction of the rotations $\dot{\boldsymbol{\theta}}$ computed for the individual joints from the rigid body differential kinematics pretty well agrees with the elastic case almost irrespective of the static deflections.

Visual servoing control law

TUDOR has three actuated degrees of freedom. The present work employs a hybrid IBVS concept augmented by the depth readings of the RGB-D sensor to control the translational degrees of freedom of the end effector.

Using a number of point features extracted from the camera images, the classical IBVS control law is:

$$\mathbf{v}_c = -\mathbf{K}_c\,\mathbf{J}_c^\dagger(u_i,\,v_i,\,\Delta z)\,\mathbf{e}_{uv}. \qquad (9.1.2)$$

Therein $\mathbf{v}_c = \begin{bmatrix} v_{cx}, & v_{cy}, & v_{cz} \end{bmatrix}^\mathrm{T}$ denotes the commanded translational camera velocity vector. The controller gain matrix $\mathbf{K}_c$ is chosen to be positive and diagonal. The pairwise error between image point features extracted in the goal view and their correspondences in the image of the current view is $\mathbf{e}_{uv}$. $\mathbf{J}_c^\dagger(u_i,\,v_i,\,\Delta z)$ represents the pseudoinverse of the image feature Jacobian $\mathbf{J}_c(u,\,v,\,\Delta z)$. The image feature Jacobian $\mathbf{J}_c(u_i,\,v_i,\,\Delta z)$ consists of one column for each considered camera degree of freedom and two rows per point feature correspondence. In the present case the reduced image Jacobian for a single point feature computes to:

$$\mathbf{J}_c(u_i,\,v_i,\,\Delta z) = \begin{bmatrix} \frac{\Lambda}{\Delta z}, & 0, & -\frac{u_i}{\Delta z} \\ 0, & \frac{\Lambda}{\Delta z}, & -\frac{v_i}{\Delta z} \end{bmatrix}, \qquad (9.1.3)$$

where Λ is the focal length known from a camera calibration, u_i and v_i are the horizontal and vertical image coordinates of the point feature, Δz is the distance between the camera coordinate frame and the scene point represented by the point feature. The Jacobian (9.1.3) provides two coupled equations per point feature. With respect to the three degrees of freedom controllable with TUDOR, classical IBVS requires at least two image features to be extracted for end effector control. In the general case of 6 degrees of freedom, a minimum of three features are required.

With a conventional monocular camera the distance Δz is unknown. IBVS control concepts "traditionally" involve an online estimation or use approximations. The RGB-D sensor used in this work already provides distance measurements. Point features are usually extracted from the images with subpixel accuracy. A depth value can be assigned to each such 2D features by interpolation of the depth measurements. With

square pattern to be centered

(a)

× start pose   ○ goal pose   —— viewing direction
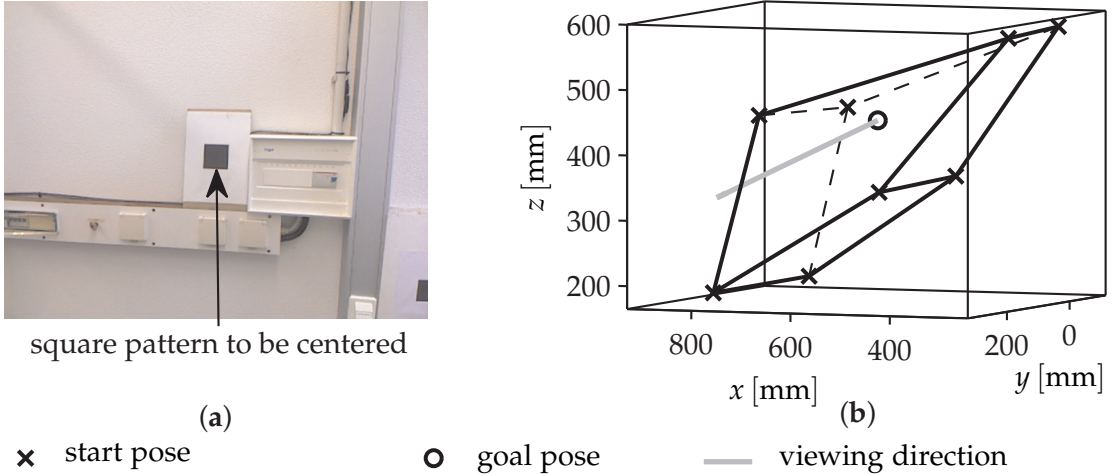
Figure 9.1.: Visual servoing experiment. Goal view (**a**) observed with the eye-in-hand camera and polyhedral configurations of goal and starting poses expressed in the robot base frame (**b**).

the depth for each point feature being available a decoupled control law is applied by replacing the Jacobian with the interaction matrix $\mathbf{L}_c$:

$$\mathbf{L}_c(\Delta z) = \begin{bmatrix} \frac{\Lambda}{\Delta z}, & 0, & 0 \\ 0, & \frac{\Lambda}{\Delta z}, & 0 \\ 0, & 0, & 1 \end{bmatrix}. \tag{9.1.4}$$

With this interaction matrix a single image point feature with associated scene depth is mathematically sufficient to control the considered translational degrees of freedom using the control law:

$$\mathbf{v}_c = -\mathbf{K}_c \, \mathbf{L}_c^{-1}(\Delta z) \, [e_u, \, e_v, \, e_z]^{\mathrm{T}}. \tag{9.1.5}$$

Increased robustness against image distortions and measurement noise as well as outliers can be achieved by using multiple point features. Nevertheless, the control law (9.1.5) is suitable to demonstrate the potentials of visual servoing controllers in the presence of static configuration and load dependent link deflections.

Experiments on pose repeatability and error dynamics

In visual servoing a goal pose is taught to the robot by virtue of an image capturing the view of the scene at the desired location. The associated performance metric is the pose repeatability. It describes the ability of the robot to repeatedly return to this view. ISO 9283 (1999) defines the repeatability in terms of the translational end effector degrees of freedom to be the radius of the sphere enclosing all actual poses attained from the same direction. The sphere centroid is the center of mass of all actual poses. The limited degrees of freedom do not allow to follow ISO 9283 (1999) in all details, but the following investigation is motivated by the standard.

In the present work the repeatability is assessed using the stereo camera system detailed in section 2.4. The visual servoing controller is used to center the black square pattern on a white ground within the image. The square pattern is visible in
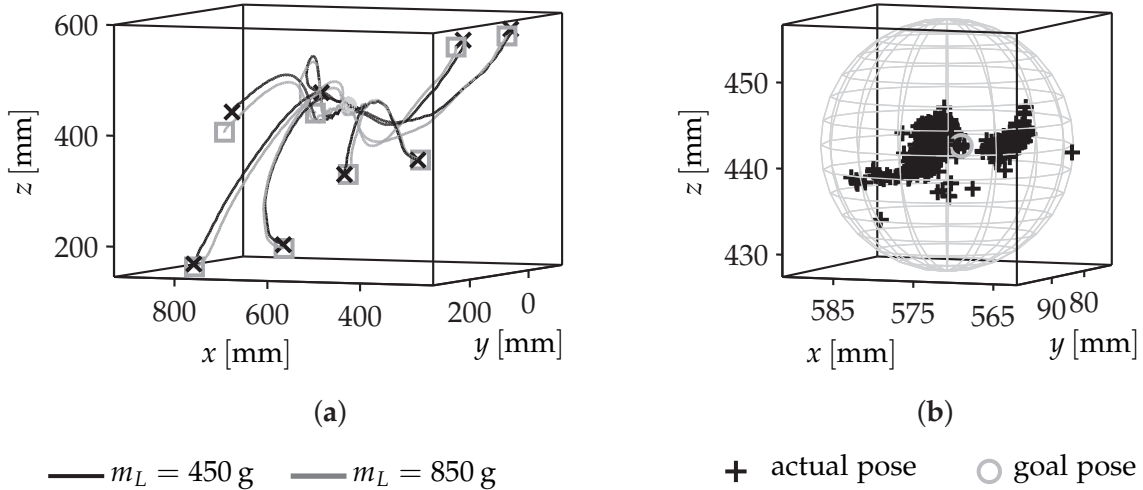
Figure 9.2.: Transitions from the eight start configurations towards the goal pose (**a**) and close up to the goal pose (**b**) with actual poses attained during all 480 experiments.

figure 9.1 (**a**). The centroid of the black square provides the single image point feature required to control all three translatory degrees of freedom. The goal view is attained from a total of eight different start poses. ISO 9283 (1999) suggest the start poses to be the corners of a cuboid around the goal pose. In this work, the start poses locate the square pattern close to the image corners. Four poses are as close as possible to the square pattern. The other four are located as distant as feasible from the pattern. In the workspace these start poses form the corners of a polyhedron, which is the largest emulation of the cuboid feasible with TUDOR.

Figure 9.1 (**b**) depicts the location of the goal pose with camera viewing direction, the utilized start poses as well as the polyhedron enclosing the considered workspace volume. The experiments beginning at each starting point are repeated with payloads of 0 g, 200 g and 400 g in addition to the eye-in-hand camera. With the camera the maximum payload adds to 850 g. All experiments are repeated 20 times.

Figure 9.2 (**a**) depicts single realizations of transitions from all individual start poses towards the goal pose. The curves represent the case of 0 g and 400 g additional payload. The start poses are remembered in the joint space without additional payload. The altered static deflections in the start poses due to the additional payload become visible as the displacement between the rectangles and crosses in the figure. Nevertheless, all end effector trajectories equivalently converge to the goal pose.

Figure 9.2 (**b**) is a close view on the goal pose. The crosses represent the attained actual poses of all 480 experiments and the enclosing sphere. Note, that ISO 9283 (1999) just investigates the repeatability under identical load conditions and a single approaching direction. A few outliers render the radius to be 14 mm, while 90 % of the measured errors are smaller than 8 mm. The average pose error amounts to only 4 mm. These values are less than 10 % of the static deflection already introduced by the additional payload mass.

Beyond the steady state positioning error, figure 9.3 (**a**) illustrates the transient dynamics of the workspace error. The corresponding image space error is depicted in figure 9.3 (**b**). The workspace error as well as the image space error both smoothly
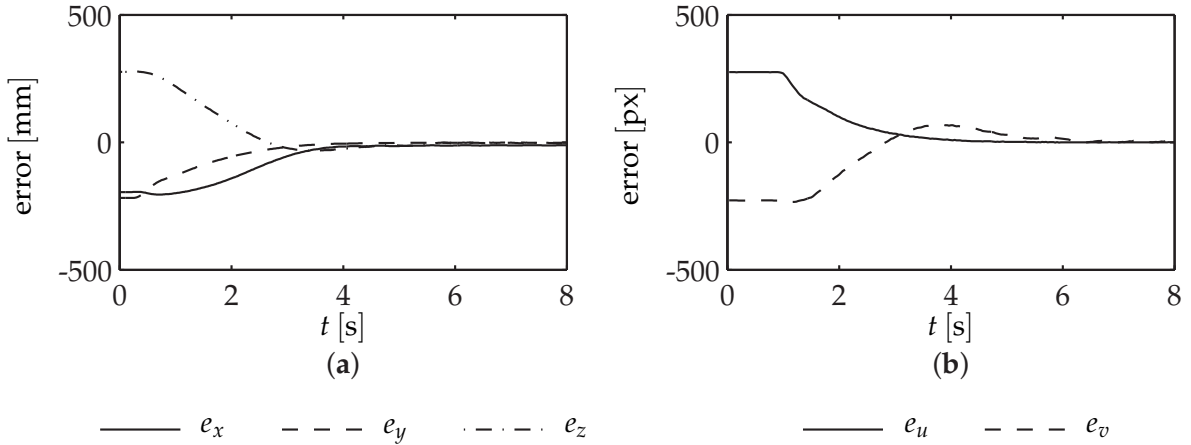
Figure 9.3.: Error dynamics in the workspace (**a**) as well as the image space (**b**).

converge. Malzahn et al. (2011d) demonstrate the tracking of a moving square pattern in an online available video, which complements the results provided in this thesis.

9.2. Data based kinematics

Phung et al. (2011a) compare linear regression, local linear model trees, multi-layer perceptron (MLP) networks as well as radial basis function networks for learning the forward and inverse kinematics of the multi-elastic-link robot arm TUDOR. Based on this comparison, the Levenberg-Marquardt algorithm is applied here to obtain parameters of MLP networks through nonlinear regression. Following a divide and conquer approach, separate networks are used to learn a payload estimator, the forward kinematics as well as the inverse kinematics. Phung et al. (2011a) show that this strategy simplifies the learning task and improves the inverse kinematics accuracy.

Training data

The training data set is recorded using the stereo-camera setup introduced in section 2.4. The robot joint space is sampled in $10°$ increments between $0°$ and $180°$ for joint two as well as between $-90°$ and $90°$ for joint three. Payloads range between 0 g and 400 g. The payloads are varied in 100 g steps. In the resulting 1805 static poses, the joint values θ_2 and θ_3, the settled strain measurements ε_2, ε_3 as well as the end-effector position ${}^B x_E$ and ${}^B z_E$ are recorded.

Forward kinematics

With TUDOR the elastic deflections dominantly occur in the vertical plane and are independent of the joint variable θ_1. Regarding the forward kinematics this allows to model just the two end effector coordinates ${}^B x_E$ and ${}^B z_E$ for ${}^B y_E = 0$ in terms of the joint angles θ_2 and θ_3 as well as the link strains ε_2 and ε_3. The full actual end effector pose is obtained from a rotation by an angle θ_1 about axis ${}^B z \equiv {}^1 z$.

The data set is divided into 70 % for training, 15 % for validation and the remaining 15 % as test data to estimate the generalization error. The number of neurons is

limited to a hundred. The winning forward kinematics MLP network for ${}^B x_E$ and ${}^B z_E$ comprises a single hidden layer with eight perceptrons.

While the strain measurements are directly applied as inputs to the network, the joint angles are transformed into the nonlinear regressors $\cos(\theta_2)$, $\sin(\theta_2)$, $\cos(\theta_2 + \theta_3)$, $\sin(\theta_2 + \theta_3)$. These regressors appear as the original regressors in the analytical forward kinematics of the equivalent rigid arm. In particular for ${}^B z_E$ Phung et al. (2011a) demonstrate that these nonlinear regressors drastically improve the model accuracy compared to the original features θ_2 and θ_3. The root mean squared error on the unseen testing data set including varying payloads reduces from 4.17 mm in ${}^B x_E$ and 5.84 mm in ${}^B z_E$ to 1.76 mm in ${}^B x_E$ and 1.36 mm in ${}^B z_E$.

Load estimation

A MLP with a single hidden layer as well as 10 perceptrons is employed for the load estimation. This way TUDOR operates as a weighing machine. The inputs to the network are the joint angles θ_2 and θ_3 as well as the strains ε_2 and ε_3. The data sets with 0, 200, 300 and 400 g are used to train the network. The root mean squared training error (RMSE) computed over all joint space samples amounts to 5.7 g. The generalization RMSE is determined for the unseen 100 g payload and amounts to 9.3 g. This is less than 10 % of the used payload increments.

Figure 9.4 (a) visualizes the estimated payload for each data point against ground truth. For some data points a drastical increase in the estimation error is visible. A visualization of the normalized RMSE (NRMSE, see B.4) against the orientation of the second and third link in the figures 9.4 (b) and 9.4 (c) provides a plausible explanation for this observation. The NRMSE for the training as well as the testing data set disproportionally increases the more any of the two links aligns with the gravitation vector. The full alignment occurs for $\theta_2 = 90°$ and $\theta_2 + \theta_3 = 90°$. The alignment minimizes the static deflections due to gravity, which aggravates the estimation principle based on the weighing machine.

Nevertheless, outside of such joint configurations, the payload estimation is considered as accurate for the purpose of this work.

Multimodel inverse kinematics

The inverse kinematics with respect to the first joint angle θ_1 is equivalent to rigid robots. From the experiences gained during forward kinematics learning, the end effector coordinates ${}^B x_E$ and ${}^B z_E$ are converted into the nonlinear regressors:

$$Y_1 = \mathrm{atan}_2\left({}^B x_E, {}^B z_E\right), \tag{9.2.1}$$

$$Y_2 = \mathrm{asin}\left(\frac{l_3^2 - ({}^B x_E^2 + {}^B z_E^2 + l_2^2)}{2 l_2 \sqrt{{}^B x_E^2 + {}^B z_E^2}}\right). \tag{9.2.2}$$

These expressions appear in the closed-form inverse kinematics of the equivalent rigid arm. The atan$_2$-function represents the two argument arc tangent defined on $[-\pi; \pi]$.

A testing result for a trained inverse kinematics MLP network using the coordinates ${}^B x_E$ and ${}^B z_E$ as well as the estimated payload for the input and the joint angles
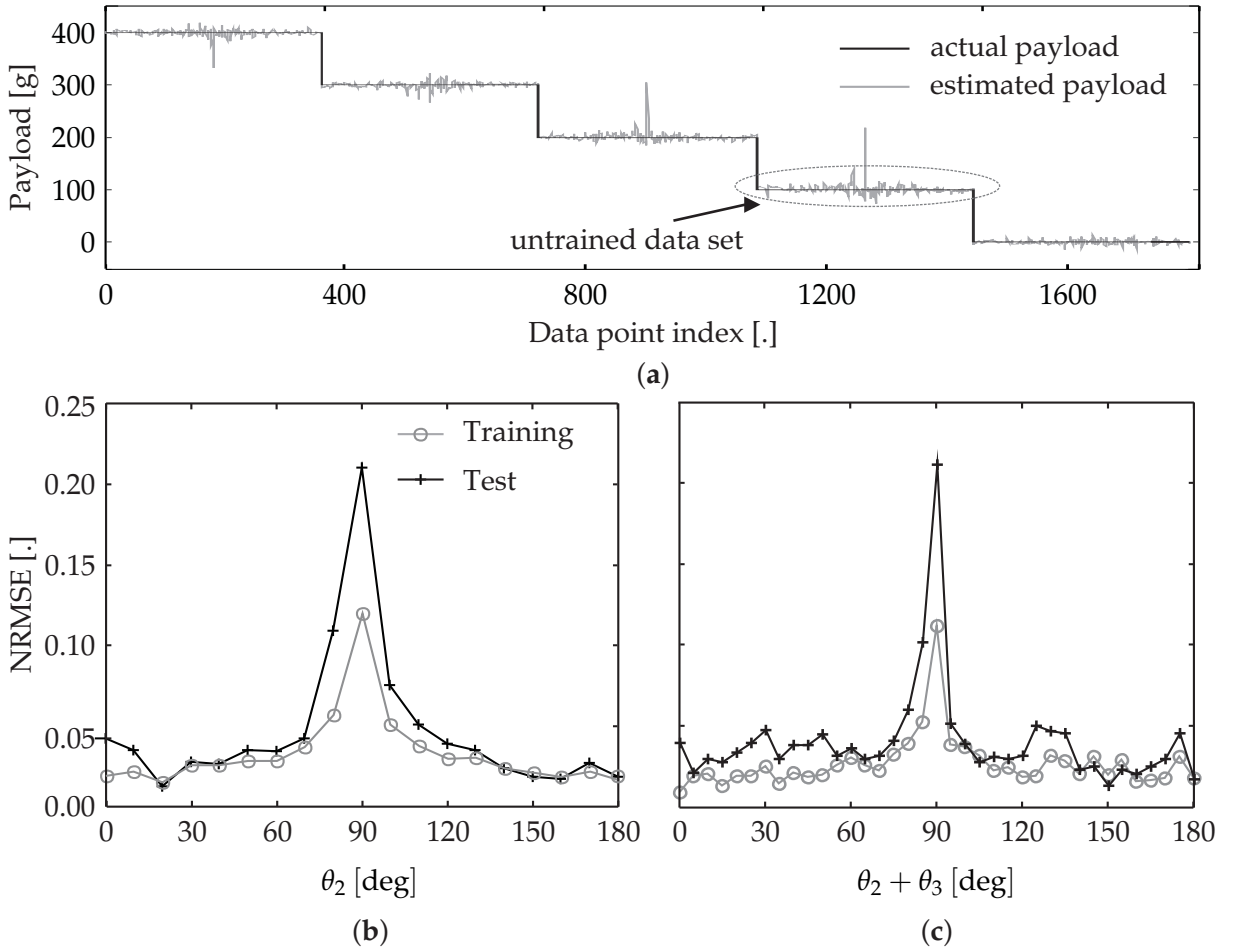
Figure 9.4.: Load estimation results with seen and unseen payloads (**a**). NRMSE for the load model computed from all payloads and plotted against θ_2 (**b**) and $\theta_2 + \theta_3$ (**c**).

θ_2, θ_3 as outputs, is illustrated in figure 9.5 (**a**). The data partitioning is identical to the forward kinematics learning. Remapping the computed joint angles into the workspace using the corresponding strain measurements in conjunction with the learned forward kinematics results in the RMSE of 20.6 mm for the $^B x_E$ and 24.3 mm for $^B z_E$. This poor remapping is obtained even with the nonlinear regressors.

For serial chain robot arms the inverse kinematics is generally ambiguous. With TUDOR the ambiguity with respect to the first joint is identical to rigid robots. Regarding the second and third joint, some poses are only reachable in the elbow-up configuration, while other poses can only be approached in the elbow-down pose. The corresponding part of the workspace is highlighted as uni-solution area in figure 9.5 (**b**). A third class of poses may be attained in both configurations, which introduces another ambiguity in the inverse kinematics solution. The corresponding workspace region is indicated as the multi-solution area in figure 9.5 (**b**).

The remedy to diminish the remapping error is to learn separate networks for the elbow-up and elbow-down postures. Therefore, the training data is split into two subsets. One subset for $\theta_3 > 0°$ and the other for $\theta_3 \leq 0°$.

For each given target pose, the inverse kinematic models output two alternative joint configurations. The ambiguity is resolved in two steps. Solutions are discarded, if they are outside the joint limits, otherwise the solution that is closer to the current
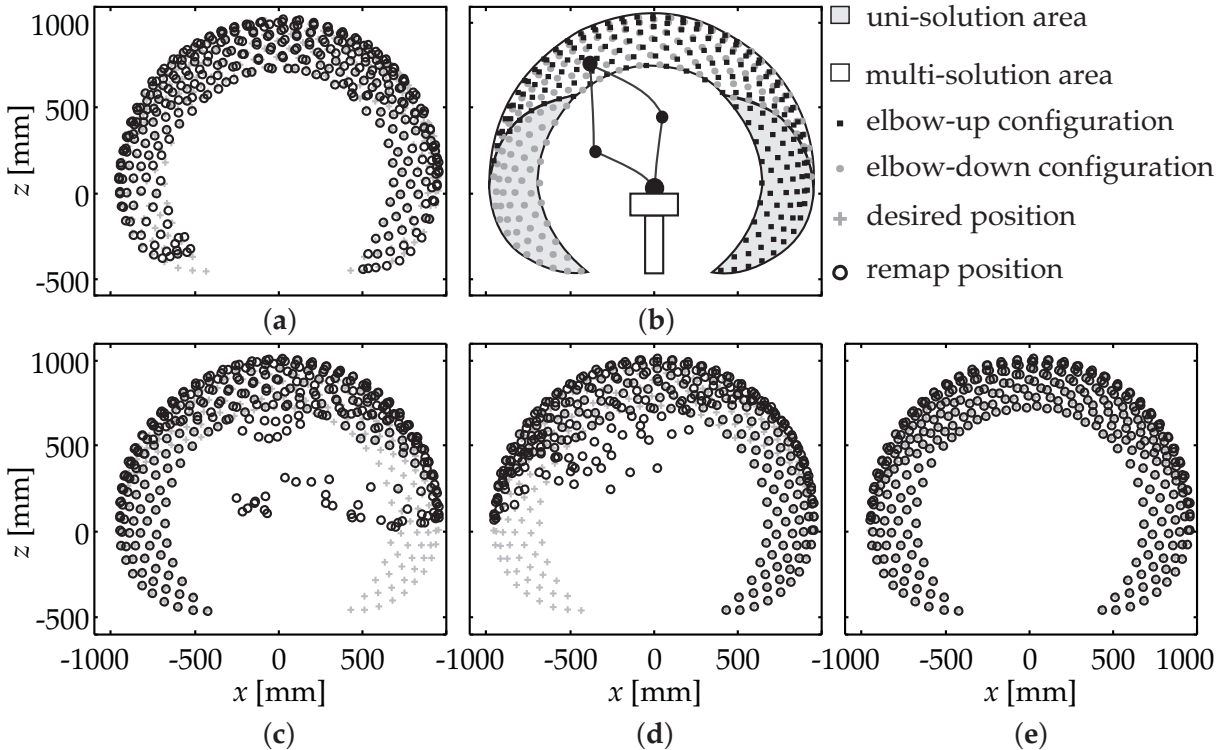
Figure 9.5.: Remapped positions using a single neural network for the inverse kinematics model (**a**). Workspace samples as well as uni- and multi-solution areas for the inverse kinematics model (**b**). Distribution of reference and remapped positions for the model with $\theta_3 > 0°$ (**c**), $\theta_3 \leq 0°$ (**d**) and the multi-model (**e**).

joint configuration is selected.

The testing results for the individual submodels are shown in the figures 9.5 (**c**) and (**d**). The outliers correspond to poses, which are not reachable with the particular submodel. Figure 9.5 (**e**) represents the remapping result for the obtained multi-model with ambiguity resolution. The combined multi-model achieves a remapping RMSE of 2.6 mm in both the ^Bx_E and ^Bz_E. This value is close to the measurement accuracy of the stereo camera as well as the absolute accuracy of many conventional robots.

9.3. Ball catching

In industrial production robots are required to perform tasks in a given cycle time with a predefined precision. Enabling TUDOR to catch multiple balls, which are sequentially but irreproducibly thrown by a human, is a graspable demonstration of the general feasibility to perform such tasks with an elastic link robot in practice.

Scenario

The ball catching scenario is illustrated in figure 9.6 (**a**). A human consecutively throws soft balls towards TUDOR. The distance between TUDOR and the thrower is about 6 meters. The RGB-D camera used for visual servoing is mounted to the wall behind the thrower. The thrown balls are detected based on the background
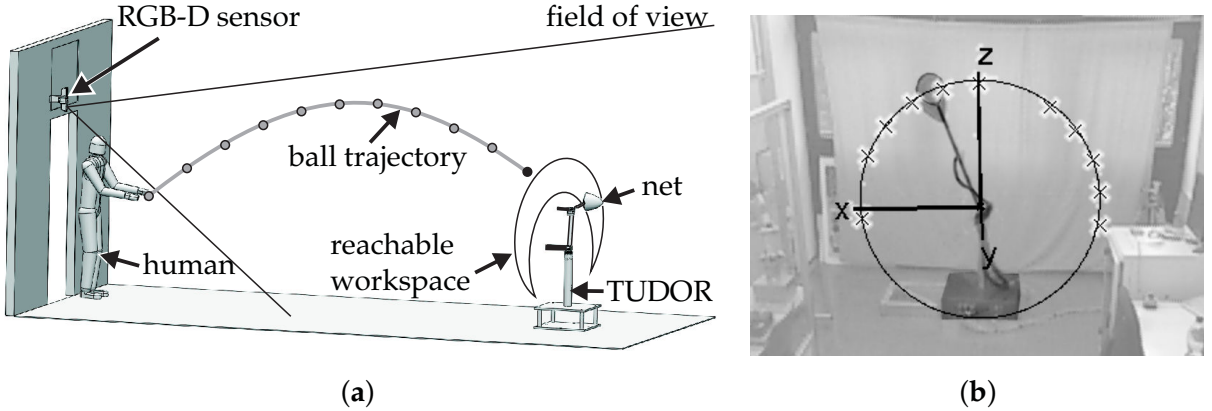
Figure 9.6.: Ball Catching Scenario (**a**) and RGB-D sensor to robot calibration (**b**).

subtraction algorithm explained by Frese et al. (2001). It is assumed that the ball is the only moving object within a distance of 4.5 m from the RGB-D sensor. The ball trajectory is tracked and predicted in the successively recorded image sequences by an extended Kalman filter. The tracking algorithm is also taken from Frese et al. 2001, who use a wide baseline stereo camera setup instead of the Kinect. The intersection between the predicted ball trajectory and the planar workspace of TUDOR visible in figure 9.6 (**a**) is intended to be the ball intercept location. Once the predicted intercept location falls into the robot workspace, the error covariances of the extended Kalman filter are constantly supervised. If they are sufficiently small, the intercept location is passed to the inverse kinematics algorithm, which commands the robot to intercept the ball with the net mounted at the end effector. The diameter of the ball is 9 cm. The diameter of the net amounts to 18 cm.

The balls already present in the net constitute an additional payload increasing with each successful catching operation. Furthermore, the previously caught balls behave as pendulums and induce disturbances at the end effector in response to any arm motion. The inverse kinematics has to compensate for the additional load, while the oscillation damping has to attenuate the motion induced oscillations as well as the disturbances readily in time to successfully catch the next approaching ball.

RGB-D Sensor to Robot Calibration

The calibration of coordinate transformation $^W_B\mathbf{T}$ between the robot base frame and the wall-mounted RGB-D sensor is performed by sampling the operating range of the second joint with $\theta_1 = \theta_3 = 0°$.

A solid disc is inserted into the net used to catch the thrown balls. The camera perceives the disc as a circular region of uniform depth readings. This region is segmented through thresholding based on a manually given seed. The centroid of the segment during the i-th sample step provides the coordinates of the end-effector location $^W\mathbf{p}_i$ in the RGB-D sensor frame.

All end effector coordinates recorded during the sampling procedure are considered to be located on the perimeter of a circular plane. Figure 9.6 (**b**) depicts the recorded samples in addition to the circle fitted to these points. The RMSE of this circle fit is 4.82 cm and therefore below the experimentally determined depth measurement

accuracy of the RGB-D sensor at this distance (see figure 2.5 (**c**)).

The center of the fitted circle constitutes the origin $^{W}\mathbf{o}_B$ of the robot base frame with respect to the wall-mounted camera. The z-axis $^{W}\mathbf{z}_B$ of the robot base frame is the unit vector in parallel to the connection from $^{W}\mathbf{o}_B$ to the end effector location $^{W}\mathbf{p}_6$ in the straight vertical posture with $[\theta_1, \theta_2, \theta_3]^{\mathrm{T}} = [0°, 90°, 0°]^{\mathrm{T}}$, where the arm is nearly undeformed.

An initial estimate $^{W}\hat{\mathbf{y}}_B$ of the y-axis $^{R}\mathbf{y}_B$ is the normal to the circular plane through the circle center. The cross product $^{W}\mathbf{y}_B \times {}^{W}\mathbf{z}_B$ determines the x-axis $^{W}\mathbf{x}_B$. Subsequently $^{W}\mathbf{y}_B = {}^{W}\mathbf{z}_B \times {}^{W}\mathbf{x}_B$ yields the orientation of the robot base frame as a right-handed trihedron $^{W}_{B}\mathbf{R} = [^{W}\mathbf{x}_B, {}^{W}\mathbf{y}_B, {}^{W}\mathbf{z}_B]$.

Catching results

A sequence of images recorded by the wall-mounted RGB-D sensor during a ball catching experiment is illustrated in figure 9.7.

Figure 9.7 (**a**) sketches the boundaries of the reachable workspace. The picture captures the instant after a first ball has been caught and right before a second ball is thrown. The black circle marks the predicted intercept location, which for each throw is initialized at the robot base. A history of previously sensed ball positions as well as the updated intercept location are shown in figure 9.7 (**b**). It is visible in figure 9.7 (**c**), that the inertia causes the previously caught ball in the net, to lag behind the expedited end effector. In figure 9.7 (**d**) the robot finally positions the net at the correctly predicted intercept location properly in time and catches the ball. The success rate is larger than 66 %, provided that the ball trajectory intersects the robot workspace. Malzahn et al. (2011c) provide an online available video demonstrating the ball catching experiments with and without the active vibration damping.

(**a**)

(**b**)

(**c**)

(**d**)
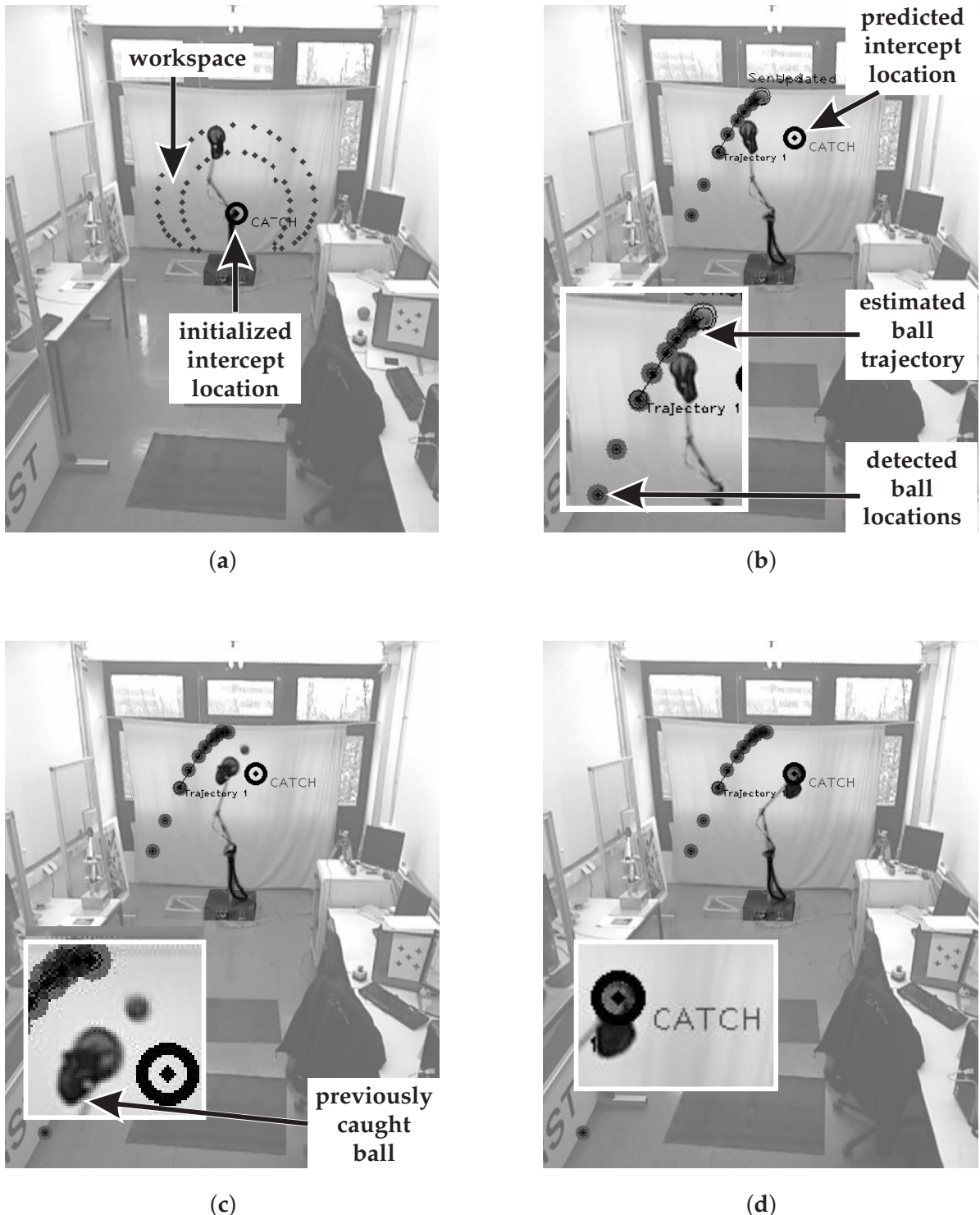
Figure 9.7.: Sequence of images captured by the wall-mounted RGB-D sensor during a ball catching experiment.

10

Damped Dynamics Modelling

As a final step before exploiting link elasticity for sensing contact forces, the work contributes two analytical real-time capable models for the remaining damped arm dynamics in this chapter. Parts of this chapter have been previously published by Malzahn, Reinhart and Bertram (2014).

The first model explains the joint currents. The second one models the per link strain measurements. Both models are derived and also related to each other through the investigation of the load torque distribution in the links. Mathematically the model equations share exactly the same structure. A data-driven neural network models the same outputs without any prior structural knowledge about the dynamics. The data driven model works on exactly the same input/output data as the analytical models and provides a benchmark for them. All models are efficiently identified using linear regression techniques and validated by experiments with multiple payloads under gravitational influence.

10.1. Motor current model

Consider the motor torque balance given in equation (3.1.1) using the nonlinear friction model for τ_F (3.1.3). The vector $\boldsymbol{\tau_J} = \boldsymbol{\tau_{L|x=0}}$ collects the load torques the robot arm bodies and contact torques $\boldsymbol{\tau_c}$ exert on the individual joints according to:

$$\boldsymbol{\tau_J} - \boldsymbol{\tau_c} = \mathbf{I}(\boldsymbol{\theta})\ddot{\boldsymbol{\theta}} + \mathbf{C}(\boldsymbol{\theta}, \dot{\boldsymbol{\theta}})\dot{\boldsymbol{\theta}} + \mathbf{g}(\boldsymbol{\theta}). \tag{10.1.1}$$

Therein $\mathbf{I}$ describes the symmetric positive definite robot inertia matrix. The matrix $\mathbf{C}$ includes the Coriolis and centrifugal terms. The vector $\mathbf{g}$ represents the load torque due to gravity.

At first, consider $\boldsymbol{\tau_c} = \mathbf{0}$. The expressions for the mechanical torque τ_M, the friction torque τ_F as well as the load torque τ_J in equation (10.1.1) are all linear in their parameters. For parameter identification from experimental data equation (3.1.1) can be rearranged to form the linear regression problem:

$$\mathbf{i}_M = \mathbf{Y}_i(\boldsymbol{\theta}, \dot{\boldsymbol{\theta}}, \ddot{\boldsymbol{\theta}}) \, \boldsymbol{\chi}_i. \tag{10.1.2}$$

The motor currents $\mathbf{i}_M$ are measurable at each individual joint. The regressor $\mathbf{Y}_i$ only incorporates measurable joint angles and their derivatives. The vector $\boldsymbol{\chi}_i$ is the minimal set of identifiable base dynamics parameters. Khalil and Dombre (2004)
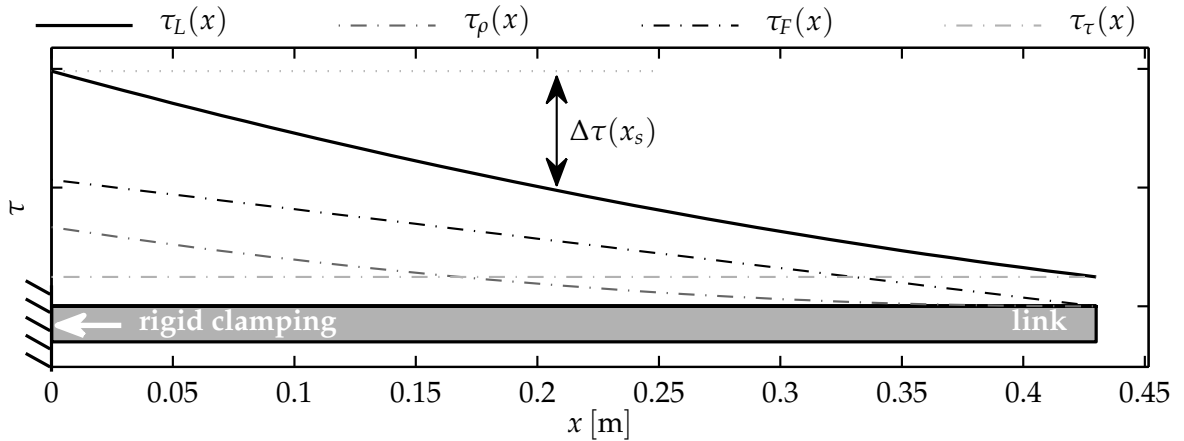
Figure 10.1.: The load torque distribution $\tau_L(x)$ along a link (*gray bar*) can be expressed as the superposition of the three components τ_ρ, τ_F as well as τ_τ.

describes two symbolic and one numerical approach for finding the base parameters. This work follows the numerical approach analyzing the space span by the columns of $\mathbf{Y}_i$ and solves equation (10.1.2) using a linear least-squares technique.

10.2. Link strain model

The derivation of a model for the link strains is based on the question for the difference between the load torque $\tau_L(x)$ "seen" at each individual joint shaft $\tau_J = \tau_L(0)$ and the load torque $\tau_L(x_s)$ causing the strain measured at a strain gauge position x_s along the link attached to this particular joint shaft. Equation (4.2.2) relates the link surface strain ε and load torque. With assumption 4.1.1 (**f**) the parameters of this relation become constant.

For a load free cantilever with the mass density per unit length ρ_b the bending torque originates from the weight of the link itself. The associated torque distribution $\tau_\rho(x)$ computes to:

$$\tau_\rho(x) = \rho_b \frac{L^2}{2EI_z}\left(1 - 2\left(\frac{x}{L}\right) + \left(\frac{x}{L}\right)^2\right). \tag{10.2.1}$$

Consider a constant load force F_L acting at the tip of a single massless cantilever. For a robot link the load force reflects the weight of subsequent links, a payload or contact force. The corresponding torque distribution $\tau_F(x)$ computes to:

$$\tau_F(x) = F_L \frac{L}{EI_z}\left(1 - \left(\frac{x}{L}\right)\right). \tag{10.2.2}$$

In robotic links a constant bending torque τ_b may arise at the tip due to the weights of distal links and payloads or as a result from a contact situation. For the massless cantilever the associated torque distribution $\tau_\tau(x)$ is constant along the link:

$$\tau_\tau(x) = \tau_b. \tag{10.2.3}$$

Based on assumption 4.1.1 (**e**) the individual components (10.2.1) to (10.2.3) may be superposed as illustrated in figure 10.1:

$$\tau_L(x) = \tau_\rho(x) + \tau_F(x) + \tau_\tau(x). \tag{10.2.4}$$

The relation models the load conditions for any link member in the kinematic chain of a robot arm.

The torque $\tau_L(0)$ exerted on a single joint differs from the torque $\tau_L(x_s)$ causing the strain on a subsequent link in a distance x_s by $\Delta\tau$:

$$\Delta\tau = \tau_L(0) - \tau_L(x_s) = \frac{\rho_b(x_s)}{EI_z(x_s)}\left(L\,x_s - \frac{1}{2}x_s^2\right) + \frac{F_L}{EI_z(x_s)}x_s. \tag{10.2.5}$$

For any particular strain sensor, the first summand is constant. The load force F_L governs the second summand. This force remains the same for any configuration of the subsequent links. Thus, in the presence of a constant payload and in the absence of external contact forces, the difference $\Delta\tau_L$ is constant as well.

Under this condition there exists a linear mapping between the strain ε measured at a location x_s along the link and the load torque $\tau_J = \tau_L(0)$ acting on the joint shaft. Combining equations (4.2.3) and (10.2.5) the mapping is:

$$\tau_J = \frac{EI_z(x_s)}{y_b(x_s)}\varepsilon(x_s) + \Delta\tau. \tag{10.2.6}$$

Due to the linearity of this mapping the effect of link motions on the perceived surface strain can be described in analogy to equation (10.1.1) using exactly the same mathematical structure:

$$\boldsymbol{\varepsilon}(\mathbf{x}_s) = \mathbf{I}_\varepsilon(\boldsymbol{\theta})\ddot{\boldsymbol{\theta}} + \mathbf{C}_\varepsilon(\boldsymbol{\theta},\dot{\boldsymbol{\theta}})\dot{\boldsymbol{\theta}} + \mathbf{g}_\varepsilon(\boldsymbol{\theta}). \tag{10.2.7}$$

where the subscript ε indicates the reference to the strain measurements. A linear regression problem equivalent to equation (10.1.2) can be formulated with respect to the link strains:

$$\boldsymbol{\varepsilon} = \mathbf{Y}_\varepsilon(\boldsymbol{\theta},\dot{\boldsymbol{\theta}},\ddot{\boldsymbol{\theta}})\,\boldsymbol{\chi}_\varepsilon, \tag{10.2.8}$$

The key difference between the equations (10.1.2) and (10.2.8) is that the latter excludes the joint parameters, most importantly the joint friction. Joint friction torques cannot be measured directly. They have to be observed. The parameters of equation (3.1.3) frequently vary over time due to temperature dependances, changes in lubrication, wear and tear (Bona and Indri 2005). A link strain referred dynamics model such as equation (10.2.7) assesses the actual mechanical load set free from the joint friction. The links with the applied strain gauges resemble load side torque sensors.

Malzahn (2013) contributed the Matlab code written to derive the dynamics in symbolic form and to automatically generate real-time compatible Simulink code as a generic module to the Robotics Toolbox by Corke (2011).

10.3. Data-driven reference model

In the field of machine learning a broad variety of general purpose techniques for non-linear function approximation exist. An analytical model is generally preferred for control. Nevertheless, the capability of available data driven techniques to approximate arbitrary nonlinear functions without prior structural knowledge provides a benchmark for the analytical models.

This work applies feedforward neural networks within a learning scheme known from Huang, Zhu and Siew (2004) as Extreme Learning Machine (ELM). The data driven reference model describes the same dynamics structure with identical inputs and outputs as the analytical joint current as well as the link strain models derived before, but it uses "problem agnostic" input features.

Within the ELM scheme the input weights and biases are randomly drawn from a normal distribution. They nonlinearly project the inputs into a single high dimensional hidden layer with sigmoidal activation functions. After normalization of the input/output data the actual training is restricted to the read-out layer and consists of simple offline linear regression. The denormalization is performed online.

The good generalization properties together with the fact that training any ELMs comes down to a linear regression task outweighs the increased number of required hidden neurons compared to other feedforward network types (Huang, Zhu and Siew 2006). A total of 100 neurons are used for both the current as well as the strain models in this work.

10.4. Identification

Excitation signal

The design of optimal excitation signals for the identification of the robot dynamics parameters is well studied in literature (Armstrong 1989). For example, band limited periodic sinusoidal signals parameterized by finite Fourier series elegantly allow for computation of higher order measurement derivatives even in the presence of noise (Swevers, Verdonck and Schutter 2007). The Fourier coefficients can be tuned according to trajectory optimization criteria such as the condition numbers and singular values of the regression matrices developed in earlier works (Presse and Gautier 1993).

In the following amplitude-modulated pseudo-random binary (APRBS) stimuli (see Isermann and Münchhof (2011, p. 174)) serve as excitation signals for the analytical as well as the data driven models. APRBS are generic stimuli for the identification of nonlinear systems. They are well suited for training the ELM reference networks and result in good condition numbers and smallest singular values of the regression matrices $\mathbf{Y}_i$ and $\mathbf{Y}_\varepsilon$.

Experiment design

This chapter focuses on the damped dynamics modeling of the elastic links. Without loss of generality the first joint is therefore kept at zero position. During data acquisition an individual stimulus is simultaneously applied to each of the other two position controlled joints.

For each individual payload between $m_L \in \{0\,\text{g},\ 100\,\text{g},\ 200\,\text{g},\ 300\,\text{g},\ 400\,\text{g}\}$ a total of 10 stimulus responses with a duration of 80 s are recorded at 100 Hz. The data is subsampled to 20 Hz and randomly split into 50 % for identification and 50 % for validation. The joint angle amplitude modulation bandwidth is one Hertz. The amplitudes equally cover the entire joint operating range. The maximum planned
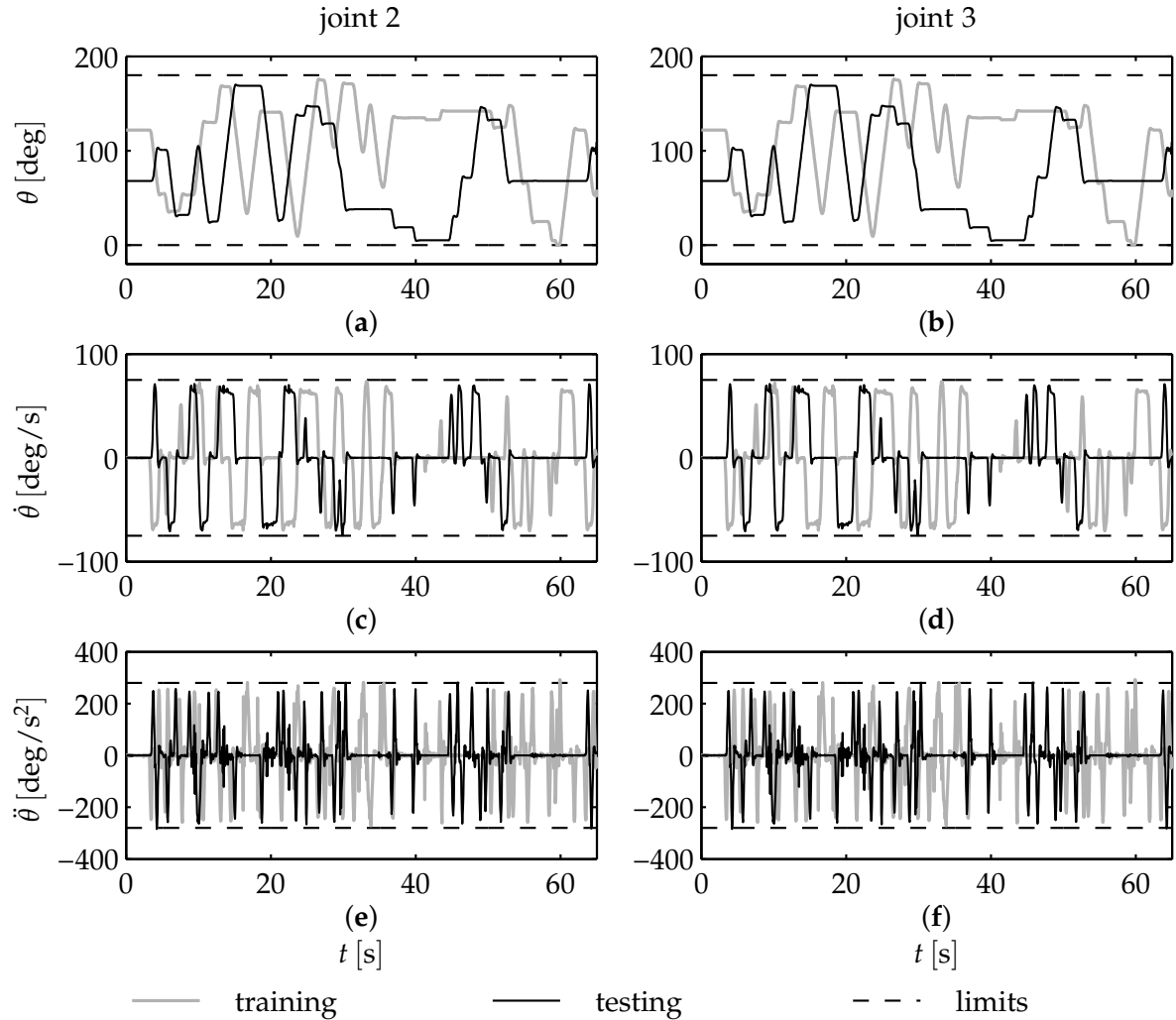
Figure 10.2.: Joint angles in (**a**) and (**b**) along with angular velocities in (**c**) and (**d**) as well as accelerations in (**e**) and (**f**) exemplified for two joint stimulus responses recorded at the second and third actuator.

acceleration is 200 deg/s^2. The maximum planned speed is 70 deg/s. For both joints figure 10.2 exemplifies a stimulus response from the training and one from the validation data set.

The analytical models as well as the ELM reference share the same inputs and outputs. The inputs are $[\theta_2, \theta_3, \dot{\theta}_2, \dot{\theta}_3, \ddot{\theta}_2, \ddot{\theta}_3]^{\mathrm{T}}$. The velocities are obtained from numerical differentiation and filtering with a first order filter and a cut-off frequency of 80 Hz. The accelerations are obtained from a subsequent numerical differentiation filtering of the velocity signal with a cut-off frequency of 20 Hz.

The outputs are either the actuator currents $\mathbf{i}_M = [i_{M,2}, i_{M,3}]^{\mathrm{T}}$ for the current referred model (10.1.2) or the strains measured close to the joint hubs on the elastic links $\boldsymbol{\varepsilon} = [\varepsilon_{21}, \varepsilon_{31}]^{\mathrm{T}}$ for the strain referred model (10.2.8).
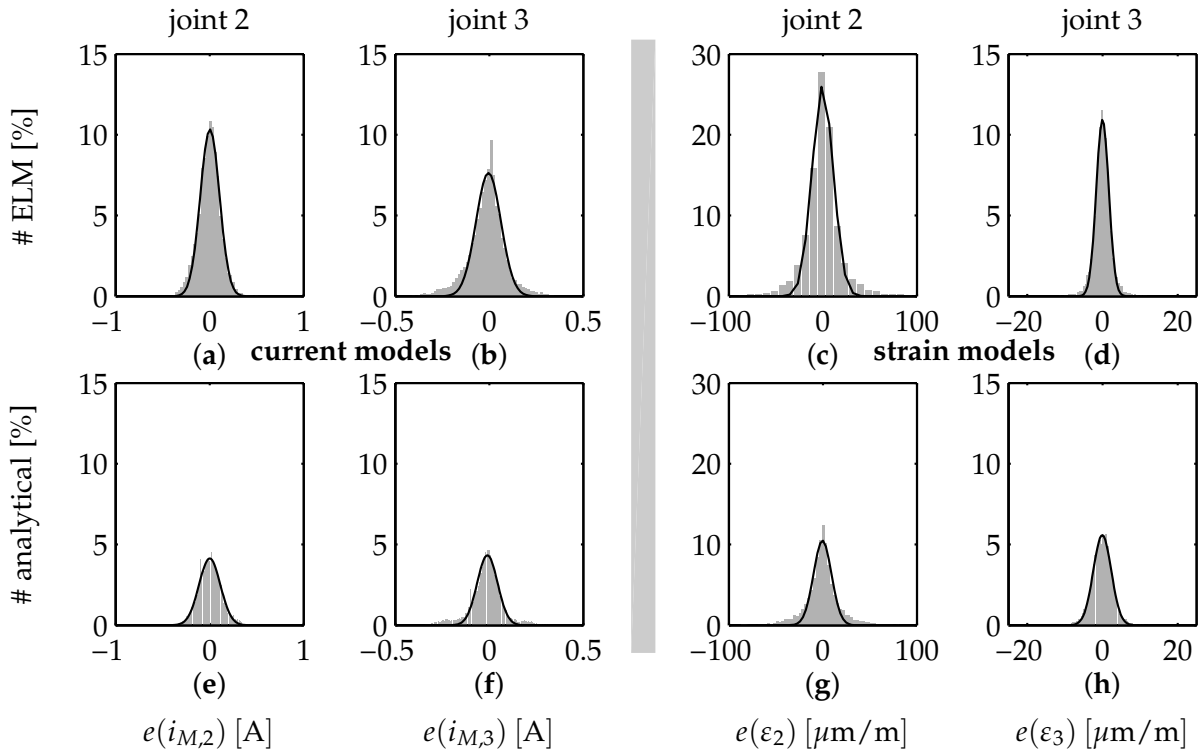
Figure 10.3.: Error histograms (*gray*) with 150 bins for the current models (*left*) and the strain models (*right*) obtained from the validation data set combining all payloads. Estimated normal distributions are indicated by the *black curves*.

10.5. Validation

In the first validation step the model errors obtained from the validation data set are combined for all payloads and visualized in the histograms provided in figure 10.3. It can be seen, that the distributions for the analytical as well as the data-driven reference model are well described by normal distributions. The statement holds for the motor currents as well as the per link strains. The normal distributions show a close to zero mean. The standard deviation of the data-driven model and the analytical model are almost equal. The data-driven models generally show a stronger error discretization, which results in higher Gaussian amplitudes and wider spacing between populated bins.

The modeling error can be interpreted as a bias free purely random variable. This indicates that the derived model structure properly explains all significant deterministic effects of the damped arm dynamics with different payloads. The data-driven reference models exhibit equivalent error statistics as the analytical models, which supports this implication.

Table 10.1 separately collects the identification and validation results on all models for each individual payload. The listed metrics are the root mean squared error (RMSE) aggregated on both dimensions of the model output along with the associated standard deviation σ_E and the goodness of fit metric (see B.4).

Regarding the current models the goodness of fit metrics for the analytical model identification basically range around 60 %. On average, the data-driven model shows

Table 10.1.: Identification results for the analytical (AN) as well as the data-driven model (ELM) with payloads $m_L = 0 \ldots 400$ g.

m_L	[g]	ELM	AN	ELM	AN	ELM	AN	ELM	AN	ELM	AN
			0		100		200		300		400
current models											
Identification											
RMSE	[A]	0.11	0.12	0.16	0.19	0.13	0.17	0.20	0.22	0.22	0.24
σ_E	[A]	0.07	0.07	0.11	0.10	0.09	0.08	0.13	0.12	0.15	0.14
fit	[%]	71.02	69.32	57.99	53.36	69.19	38.60	62.97	59.36	63.53	61.28
Validation											
RMSE	[A]	0.15	0.13	0.20	0.19	0.23	0.22	0.23	0.22	0.28	0.26
σ_E	[A]	0.10	0.08	0.16	0.11	0.23	0.12	0.14	0.13	0.46	0.16
fit	[%]	58.92	63.96	50.13	55.65	47.62	52.75	54.50	54.78	40.21	56.96
strain models											
Identification											
RMSE	[μm/m]	12.19	13.11	18.15	19.93	24.86	28.30	28.48	31.83	47.65	53.77
σ_E	[μm/m]	14.22	16.04	18.60	20.63	30.76	33.44	30.22	34.61	62.20	67.19
fit	[%]	92.26	91.44	90.40	89.41	87.16	85.83	87.71	86.03	80.07	78.05
Validation											
RMSE	[μm/m]	17.76	14.92	26.72	25.77	28.86	27.73	33.36	32.36	57.27	54.71
σ_E	[μm/m]	21.84	17.44	40.54	32.45	32.11	27.85	34.92	32.97	78.35	69.44
fit	[%]	88.30	90.59	82.02	84.59	86.58	87.75	85.28	85.88	76.02	77.78

larger values compared to the analytical model. The situation changes on the validation data set. Here the analytical model shows 5 % larger values in proportion to the data-driven model. Similarly the data-driven model shows an improved identification fit metric compared to the analytical model. In the case of the strain measurements this improvement approximately amounts to insignificantly meager 2 %. The analytical model exhibits the equivalent 2 % improvement compared to the data-driven model on the validation data set.

These consistent reciprocal goodness of fit results on the identification and validation data sets may indicate a moderate overfitting of the data-driven model. A reduction of the number of hidden neurons provides a remedy. Nevertheless, this indication is inconsiderable especially with respect to the current models. Here the data-driven as well as the analytical model consistently stay away from the 80 % threshold. Values above the threshold commonly suggest that a model well explains the signal standard deviation.

A closer look at the time series reveals an answer to that observation. A time slice of a validation result is exemplified in figure 10.4 (**a**) and (**b**). During the first seconds, where the motors are at rest, the motor currents incorporate substantial noise. During this period the analytical model chatters between two discrete values. The data-driven model completely ignores the higher signal dynamics and predicts a motor current with a clearly visible offset to the measurement. Either model errors effect the comparatively low goodness of fit values.

Once the joint stimulus motion starts, the chattering of the analytical model stops. The model responses acceptably agree with the measurements.

The chattering in the analytical model obviously originates from the nonlinear switching functions in the friction model (3.1.3). The alternative choice of continu-
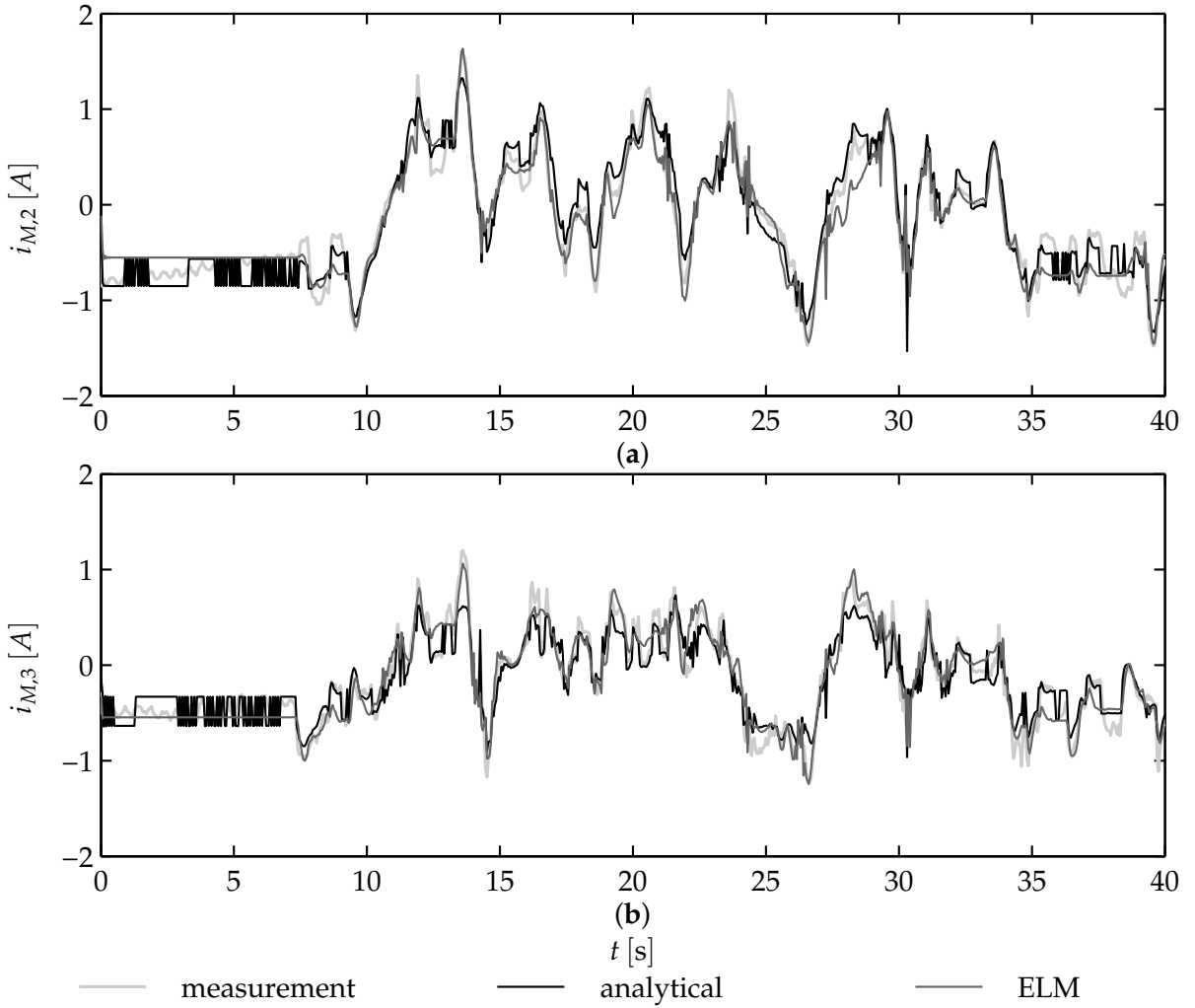
Figure 10.4.: Example validation result for the motor currents measured in the second (**a**) and third (**b**) joint for $m_L = 400\,g$.

ously differentiable switching functions does not make a difference. The remedy to the chattering is the reduction of the friction model to a single direction independent viscous friction term. On the other hand, the drastically poorer explanation of the dynamic motor currents during the stimulus motions leads to even lower goodness of fit values with this approach.

The analytical strain models reach well above the goodness of fit metric threshold of 80 % during identification as well as validation. Individual evaluations even reach 90 %. Only for $m_L = 400\,g$ it drops slightly below the threshold. A time slice of a validation result with $m_L = 400\,g$ is thus exemplified in figure 10.5.

The responses of the analytical model as well as the data-driven model almost coincide. Both models match the static strain without any chattering during rest. In total the models tightly track the measurements. Imperfect oscillation damping sporadically raises a modeling error. Examples for the imperfect oscillation damping can be seen in figure 10.5

The imperfect oscillation damping is visible in figure 10.5 (**a**) and (**b**) around $t = 30\,s$. Heavier payloads effect that strain peaks during fast motion reversals are par-
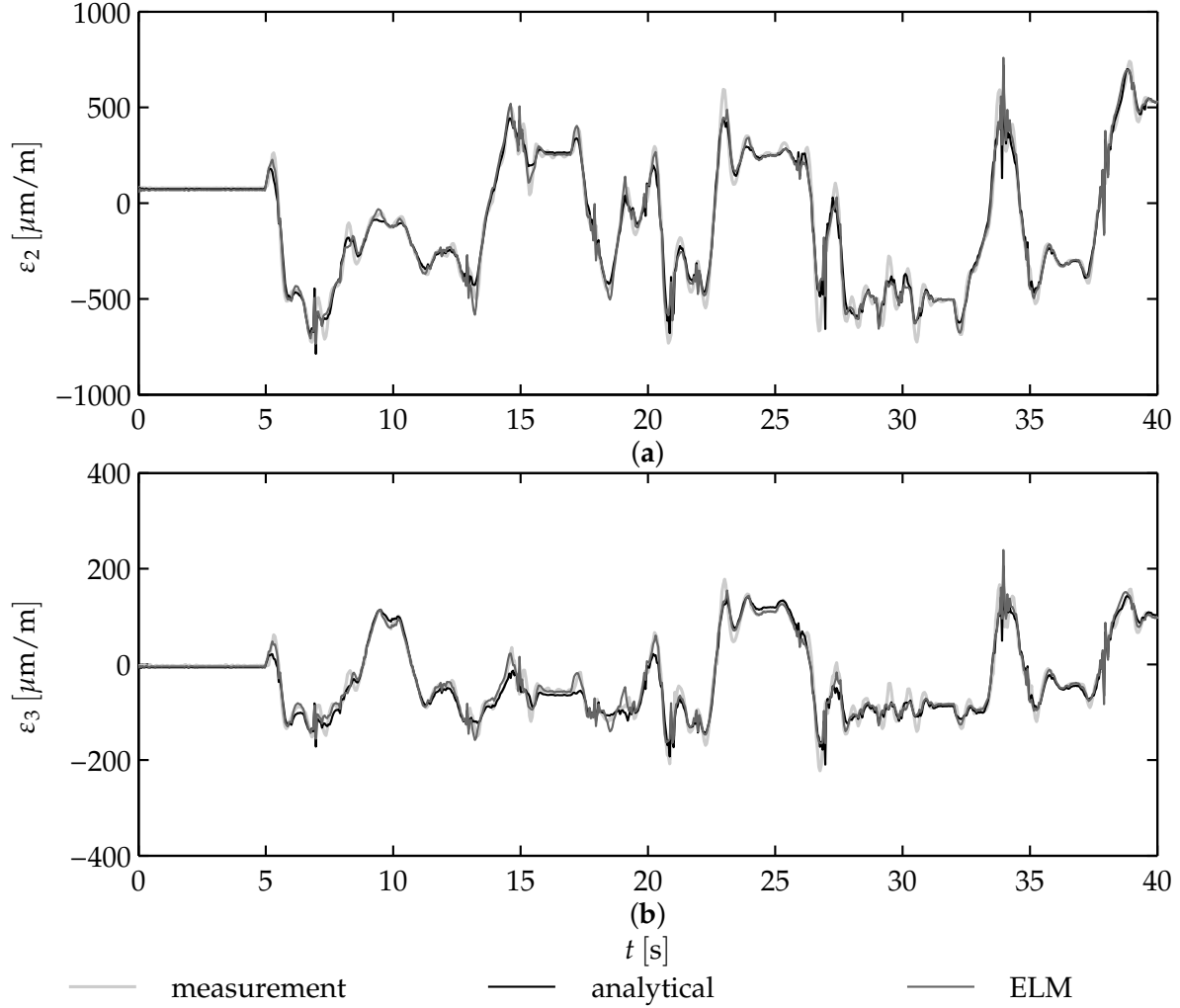
Figure 10.5.: Example validation result for the strains measured on the second (**a**) and third (**b**) link for $m_L = 400$ *g*.

tially explained by the models. This becomes visible around second 23 as well as 27 for instance.

10.6. Discussion

With this chapter the work contributes a linear relation between the joint torques τ_J as well as the load torque $\tau_L(x_s)$ effecting the strain at a strain sensor location x_s. On the basis of the inner loop oscillation damping controller, the oscillatory link dynamics are negligible. This way the derived theory suggests that the joint referred dynamics as well as the link strain dynamics of a damped multi-elastic-link robot arm can be modeled using the identical mathematical structure known from conventional rigid robots.

The zero centered Gaussian shaped modeling error histograms computed from extensive dynamics identification experiments including different payloads together with the slight superiority over the nescient data-driven model validate the theory.

The identified analytical model is valid to explain the pivotal deterministic portion of the strain measurements. The figures 10.4 and 10.5 emphasize that the RMSE as well as the standard deviations presented in table 10.1 are indeed just a small fraction of the de facto appearing signal ranges.

Equivalent statements hold for the joint current models, even though they have to be gently alleviated. The key difference between the equations (10.1.2) and (10.2.8) is that equation (10.1.2) includes the joint friction parameters. Tribology is a very broad topic. In this work the friction model (3.1.3), which is widely used in robotics, has been selected because it covers broad range of friction effects and fits into the efficient linear regression framework. More sophisticated friction models, which include phenomena such as Stribeck friction or hysteretic effects may improve the achievable results at the cost of parameter non-linearity and aggravated identification. Note that the friction parameters likely vary over time due to temperature dependance, wear and tear as well as changes in lubrication (Bona and Indri 2005). Additionally the gears show backlash. All these impact factors deteriorate the modeling accuracy. The investigation of the individual impacts of these influence factors is a challenging topic for future works.

The link strain models are set free from the joint friction, so that the applied strain gauges directly operate as load side torque sensors. The derived models can be applied in real-time control such that the proposed modeling technique paves the way for online payload estimation aiming at onward load adaptation for the inner loop oscillation damping controller. A further research direction is the development of direct force control concepts.

11

Collision Detection and Reaction

The biological inspiration by the whiskers of rodents and pinnipeds in section 1.1 contributes a major motivation of the present work. It gives reasons for the hypothesis that the intrinsic link compliance can be exploited to sense contact forces between the robot and its environment, once the undesired oscillations and deflections have been sufficiently compensated. The end effector control in the presence of varying static deflections presented in chapter 9, the oscillation damping evaluated in chapter 8 along with the evident accuracy of the identified damped arm dynamics in chapter 10 strongly confirm these prerequisites to be fulfilled. The way has been paved to investigate the validity of the initial hypothesis in this chapter. The following sections apply the real-time capable damped dynamics model for the detection of accidental collisions and supplement fast reaction strategies. The reaction strategies are extended to allow intentional physical human robot interaction.

11.1. Collision detection and isolation

The collision detection is realized by the computation of an appropriate residual signal. This section introduces and discusses two such residuals.

Direct Strain Residual

The identified strain referred damped dynamics model computes an expectation for the strain measurements at each time step. Unexpected collisions between the robot and its environment cause a discrepancy between the expectation and the actual measurement. A quantitative measure of discrepancy is the direct strain residual:

$$\mathbf{r}_{\varepsilon} = \boldsymbol{\varepsilon} - \mathbf{I}_{\varepsilon}(\boldsymbol{\theta})\ddot{\boldsymbol{\theta}} - \mathbf{C}_{\varepsilon}(\boldsymbol{\theta}, \dot{\boldsymbol{\theta}})\dot{\boldsymbol{\theta}} - \mathbf{g}_{\varepsilon}(\boldsymbol{\theta}). \tag{11.1.1}$$

The residual vector $\mathbf{r}_{\varepsilon}$ indicates a collision, if the absolute value of any element exceeds a predefined threshold. The directional information is contained in the sign of the particular elements. The link involved in the collision can be determined as the last link in the kinematic chain showing the threshold violation.

The major difficulty of this straightforward residual design lies in the requirement of the joint angular acceleration to be available. In this work the joint angular acceleration is computed through double differentiation of the encoder readings. The res-

ulting amplified noise level deteriorates the detection sensitivity and makes a strong low-pass filtering necessary. The low-pass reduces the detection reactiveness.

Generalized momentum based residual

The alternative technique proposed by Luca and Mattone (2004) and extended by Luca and Mattone (2005); Luca et al. (2006) circumvents the computation of the second order derivatives. It is based on the generalized momentum $\mathbf{p}$ of the robot arm, which is defined as the product of the robot inertia matrix and the joint velocity vector.

As a modification to the original approach the linear relation (10.2.6) is applied in order to define the strain based equivalent to the generalized momentum:

$$\mathbf{p}_\varepsilon = \mathbf{I}_\varepsilon(\boldsymbol{\theta})\dot{\boldsymbol{\theta}}. \tag{11.1.2}$$

The derivation of the strain based generalized momentum residual based on this equation is analogous to the one from Luca and Mattone (2005), except that it uses the strain referred equivalents of the inertia matrix $\mathbf{I}_\varepsilon$, Coriolis matrix $\mathbf{C}_\varepsilon$ as well as gravitational load vector $\mathbf{g}_\varepsilon$. A well-known property of the robot dynamics equations is the skew symmetry of the expression:

$$\dot{\mathbf{I}}_\varepsilon(\boldsymbol{\theta}) - 2\mathbf{C}_\varepsilon(\boldsymbol{\theta}, \dot{\boldsymbol{\theta}}) = -\left(\dot{\mathbf{I}}_\varepsilon(\boldsymbol{\theta}) - 2\mathbf{C}_\varepsilon(\boldsymbol{\theta}, \dot{\boldsymbol{\theta}})\right)^{\mathrm{T}}. \tag{11.1.3}$$

Using the symmetry of $\dot{\mathbf{I}}_\varepsilon(\boldsymbol{\theta})$, it allows to write:

$$\dot{\mathbf{I}}_\varepsilon(\boldsymbol{\theta}) = \mathbf{C}_\varepsilon(\boldsymbol{\theta}, \dot{\boldsymbol{\theta}}) + \mathbf{C}_\varepsilon^{\mathrm{T}}(\boldsymbol{\theta}, \dot{\boldsymbol{\theta}}). \tag{11.1.4}$$

The temporal derivative of the generalized momentum (11.1.2) yields:

$$\dot{\mathbf{p}}_\varepsilon = \boldsymbol{\varepsilon} + \mathbf{C}_\varepsilon^{\mathrm{T}}(\boldsymbol{\theta}, \dot{\boldsymbol{\theta}})\dot{\boldsymbol{\theta}} - \mathbf{g}_\varepsilon(\boldsymbol{\theta}). \tag{11.1.5}$$

In addition to equation (11.1.2), a second option to compute the generalized momentum is the integration of (11.1.5), which incorporates the actual strain measurements. The acceleration free generalized momentum based residual is thus defined as the difference between both options:

$$\mathbf{r}_p = \mathbf{K}_I \left[\mathbf{p}_\varepsilon - \int_0^t \boldsymbol{\varepsilon} + \mathbf{C}_\varepsilon^{\mathrm{T}}(\boldsymbol{\theta}, \dot{\boldsymbol{\theta}})\dot{\boldsymbol{\theta}} - \mathbf{g}_\varepsilon(\boldsymbol{\theta}) \mathrm{d}t - \mathbf{p}_\varepsilon(0) \right], \tag{11.1.6}$$

where $\mathbf{K}_I$ is a positive diagonal gain matrix.

In the case of a collision, the strain measurement $\boldsymbol{\varepsilon}$ is the nominal collision free strain measurement $\boldsymbol{\varepsilon}_f$ superposed by the collision strain $\boldsymbol{\varepsilon}_c$. Assuming $\mathbf{p}_\varepsilon(0) = 0$ the residual shows the first order dynamics:

$$\dot{\mathbf{r}}_p = -\mathbf{K}_I \, \mathbf{r}_p + \mathbf{K}_I \, \boldsymbol{\varepsilon}_c. \tag{11.1.7}$$

Each row in $\mathbf{r}_p$ can be expressed as the output of a transfer function of type:

$$r_{p,i} = \frac{K_{I,i}}{s + K_{I,i}} \, \varepsilon_{c,i}. \tag{11.1.8}$$
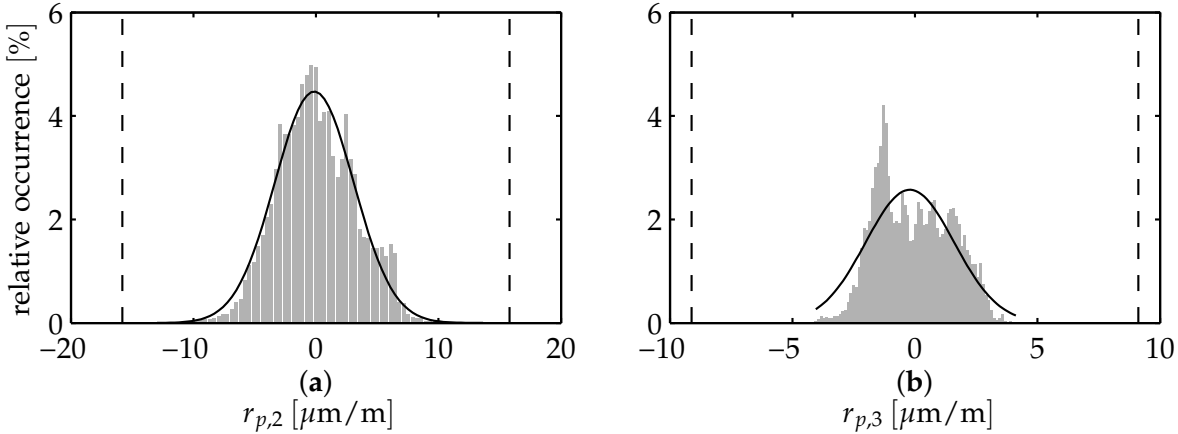
Figure 11.1.: Generalized momentum residual histogram with 75 bins computed on the whole validation data set described in section 10.5. Estimated gaussian distribution (*solid black*) as well as six sigma detection thresholds (*dashed black*).

From this transfer function the residual may be interpreted as the strain measurement filtered by a first order filter. Most importantly, the residual involves numerical integration, but it is stationary for static contacts and drops back to zero for vanishing collision strain. This is crucial for the residual based collision reaction in section 11.2. The isolation of the collided link works identically to the direct strain residual $\mathbf{r}_\varepsilon$ discussed before. Again, the absolute residual values indicate whether a collision has occurred, while the sign carries the directional information.

The cut-off frequencies are tunable through $\mathbf{K_I}$ and trade off the detection reactiveness and noise sensitivity. Compared to the low-pass filtering required for the direct strain alternative, the absence of a second order numerical derivative enables larger cut-off frequencies on behalf of an improved detection reactiveness. Therefore, the generalized momentum based collision detection is employed in this work.

Tuning thresholds

Next to the measurement noise, the dynamics model accuracy dominates the tuning of the residual thresholds and hence, the collision detection sensitivity. Figure 11.1 shows the histograms for the generalized momentum based residual. The histograms are computed on the whole validation data set as described in section 10.5. It includes the results for all test payloads between 0 g and 400 g.

Both histograms are well approximated by the estimated Gaussians. Only the histogram for the third joint-link module shows a slightly irregular error accumulation around $-1.3\,\mu$m/m. The detection thresholds are chosen to be six times the standard deviation identified from the Gaussian distribution estimated on each residual. This way, the irregular error accumulation of the third joint-link-module does not have any practical impact on the collision detection.

Luca and Mattone (2004) propose an adaptive thresholding technique for collision detection. It has been successfully applied to conventional rigid link and elastic joint robots. The transfer to the elastic link case is left for future investigations.
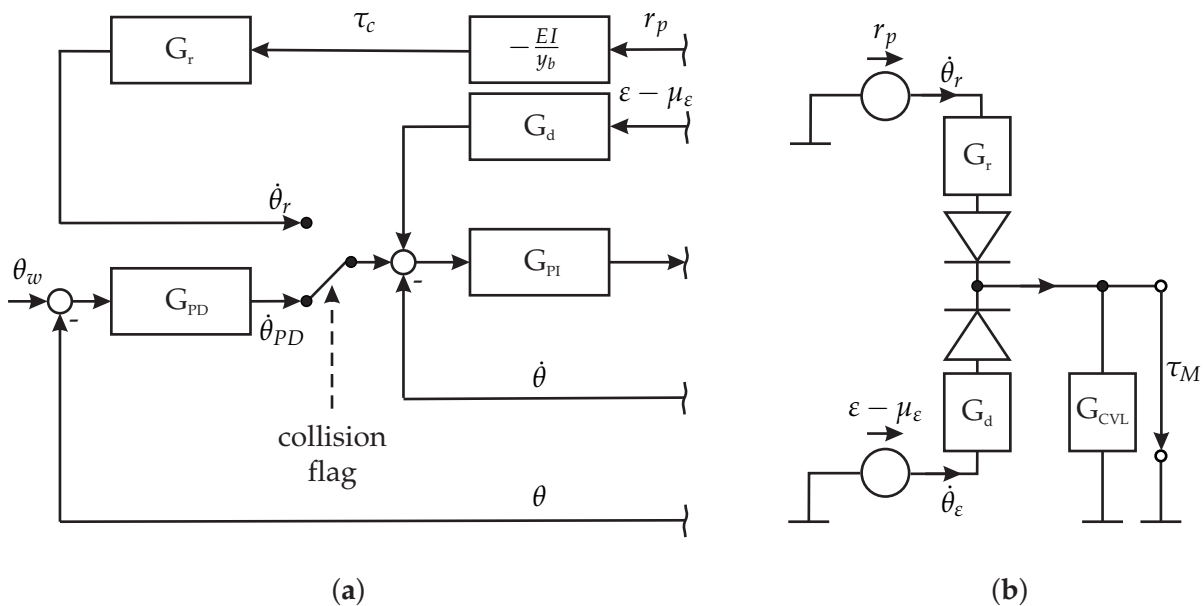
Figure 11.2.: Integration of the collision reaction scheme into the independent joint controllers at the velocity controller level (**a**) and network illustration of the interaction between collision reaction and oscillation damping (**b**).

11.2. Collision reaction

The idea behind the collision reaction is to generate a joint motion command, which limits hazardous effects of the impact in the post collision phase. With an elastic link robot simultaneously the oscillation damping has to be properly maintained during the evasive maneuver.

Reaction admittance

Luca et al. (2006) perform the collision reaction on a torque controller level. In this work the collision reaction is integrated into the existing general controller architecture described in section 3.2. The integration can be elegantly done on the velocity controller level for each individual joint. This is visible in figure 11.2 (**a**), which represents an extended extract of figure 3.3. The integration also reduces the effect of joint friction on the reactive motion. At the instant of a collision detection, the nominal reference $\dot{\theta}_{PD}$ to the velocity controller is replaced by the reaction velocity $\dot{\theta}_r$.

Expression (4.2.3) transforms the residual, which is a low-pass filtered copy of the collision strain ε_c, into the equivalent collision torque τ_c acting on the joint-link-module. The relationship between the commanded collision reaction velocity $\dot{\theta}_r$ and this collision torque τ_c is defined by introduction of the generic reaction admittance G_r:

$$G_r(s) = \frac{\dot{\theta}_r(s)}{r_p(s)} = \frac{k_{or}}{m_r\,s + f_r + k_r/s}. \tag{11.2.1}$$

Therein m_r, f_r and k_r are the inertial, resistive and capacitive components. The gain k_{or} can be tuned to generate an overreactive retreat maneuver in the case of a detected collision by choosing $k_{or} > 1$.

During the post collision phase the total input to the velocity controlled joint-link-module G_{CVL} originates from two branches of the network diagram 11.2 (**b**). It is driven by two sources: the residual source with the effort variable r_p in the upper branch as well as the oscillation source with the effort $\varepsilon - \mu_\varepsilon$ in the lower branch. The reaction admittance G_r as well as the damping admittance G_d convert the efforts into the flow variables $\dot{\theta}_r$ and $\dot{\theta}_d$, which add to the velocity controller input flow.

Even though a collision inevitably excites oscillations on one hand and strong oscillations yield non-zero residuals on the other hand, both branches can be seen as decoupled from each other. The oscillation feedback with damping admittance G_d has been shown to stably suppress oscillations irrespective of their origin. The residual is stationary during contact and vanishes with the collision strain. Thus, with a stable reaction admittance G_r, the stability of the total damped system with integrated collision reaction is plausible.

Reaction strategies

A variety of reaction strategies are considerable. Three choices are exemplified with the multi-elastic-link arm TUDOR in this work.

Just stop: The simplest reaction strategy is to just stop all motions by commanding $\dot{\theta}_r = 0$.

Reflex behavior: The directional information encoded in the sign of the residual is employed to implement an escaping reflex behavior. This is achieved by choosing small inertial m_r and friction f_r parameters, while the spring constant k_r is set to zero. With this setting the robot mimics a small mass gliding on a low friction surface and colliding with a presumably larger mass. As a result the robot bounces back from any collision point. An overreaction gain $k_{or} > 1$ amplifies this behavior.

Physical interaction mode: During a physical interaction such as a kinesthetic teaching scenario, the human operator desires to easily reconfigure the arm. This can be achieved by setting the overreaction gain $k_{or} = 1$ and the spring constant $k_r = 0$. The inertial m_r and friction f_r parameters are tuned to provide a convenient haptic feedback to the operator. This tuning however depends on the particular task to be taught as well as the individual user preferences.

11.3. Experimental results

This section provides experimental results for the collision detection and reaction for blunt as well as sharp impacts and physical interaction with a human. Additional results are provided in appendix C. The experiments utilize the force sensing contact cube described in subsection 2.4.
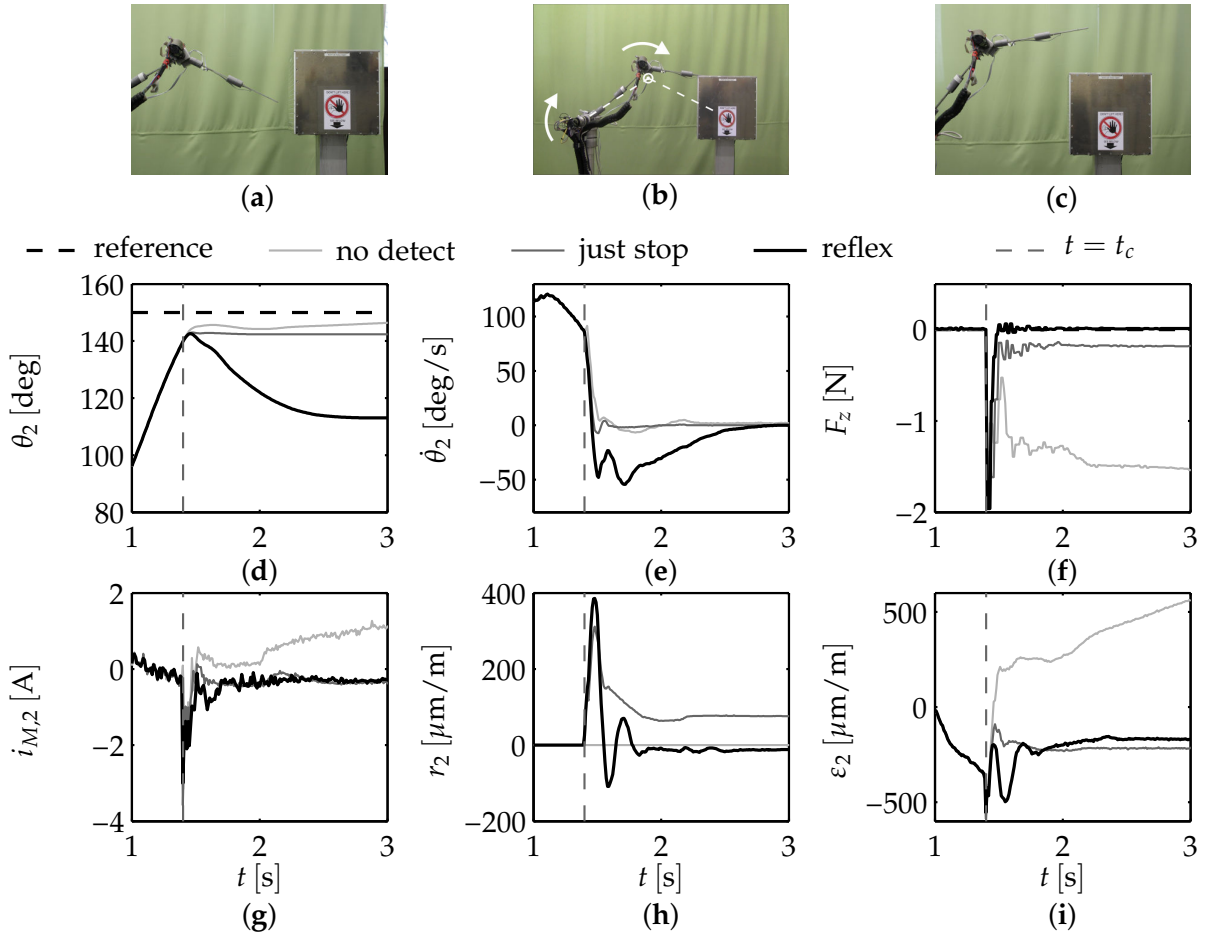
Figure 11.3.: Collision detection and reaction results for *blunt* impacts with the contact cube. Photograph illustrating the commanded pose (**a**) as well as the collision instant (**b**) and the rest position after collision reaction using the admittance-strategy (**c**). Time evolution of the second joint angle (**d**) and angular velocity (**e**) for the different reaction strategies along with the normal force F_z at the contact cube, the current (**g**), the residual (**h**) and the strain (**i**) belonging to the second joint.

Blunt impacts with the contact cube

The first collision detection and reaction experiments are blunt direct collisions with the contact cube introduced in subsection 2.4. Figure 11.3 (**a**) illustrates the commanded robot goal pose $\theta = [0°, 150°, 60°]^T$ with the contact cube put aside. The robot starts in the joint configuration $\theta = [0°, 45°, -45°]^T$ while the contact cube is placed in the path as visible in figure 11.3 (**b**).

If the collision detection is deactivated the joint controller continues to minimize the joint angle position error after the contact. This is visible for the second joint angle in figure 11.3 (**d**), the angular velocity not settling in 11.3 (**e**) and the steadily increasing motor current in 11.3 (**g**). The joint angle indeed reaches the commanded value, while the elastic link strain depicted in figure 11.3 (**i**) constantly increases with the contact force provided in figure 11.3 (**f**).

Using the stop-strategy the angular velocity immediately drops to zero. A small
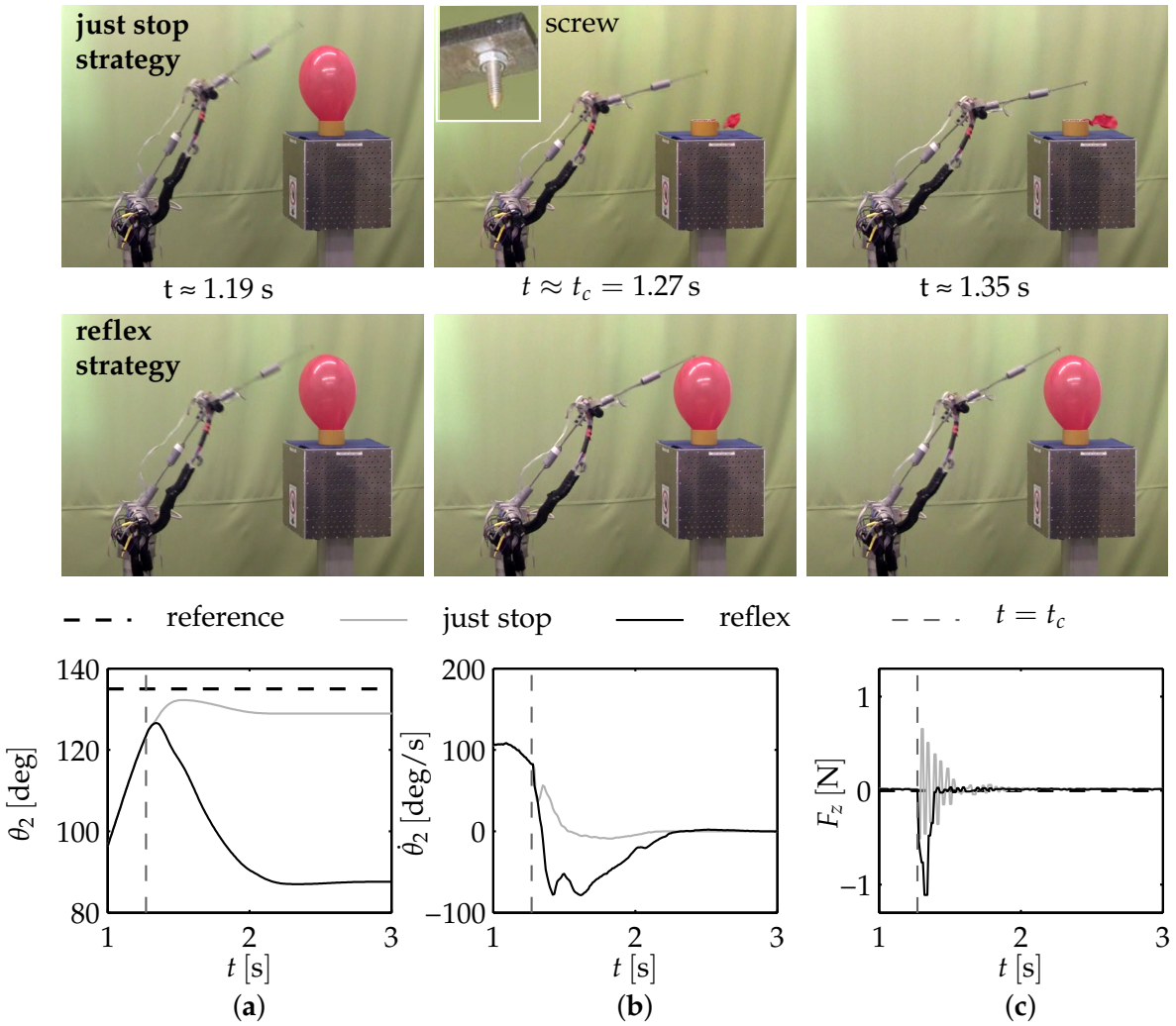
Figure 11.4.: Collision detection and reaction results for *sharp* impacts with a balloon placed as *compliant* object on the contact cube. Snapshots applying the stop-strategy (**top row**) as well as the admittance strategy (**second row**) before (**left column**), during (**center column**) and after (**right column**) the instant of collision. Angle (**a**) and angular velocity (**b**) for the second joint along with the normal force measured at the contact cube (**c**).

overshoot followed by a quick undershoot in the corresponding velocity graph 11.3 (**e**) are visible right after the collision. They attribute to the oscillation damping, which suppresses repeated bounces against the cube. The residual belonging to the second joint is drawn in figure 11.3 (**h**). After the impact it reaches a steady state value indicating the persistence of the contact situation. The curves for the contact force 11.3 (**f**) as well as the strain 11.3 (**i**) settle at a constant level.

The admittance-strategy causes the robot to move back from the cube to the rest position depicted in figure 11.3 (**c**). Equivalent to the stop-strategy the oscillation damping action is clearly visible in the joint angular velocity signal 11.3 (**e**). After the retreat maneuver the residual 11.3 (**h**) and the contact force 11.3 (**f**) come back to zero. From the force measurement at the cube the total contact duration is determined to be 10 ms.

The maximum absolute force measured at the cube is 1.90 N and equal for both the

stop- as well as the admittance-strategy. With 0.17 N the steady state contact force using the stop-strategy is just about 8 % of the maximum contact force.

Sharp impacts with a balloon

In view of the oscillatory dynamics investigated in chapter 4, the contact reflects a sudden change to unknown boundary conditions. The contact cube is a rather rigid body. Experiments with a balloon placed on the contact cube demonstrate the behavior of the oscillation damping as well as the surrounding collision detection and reaction scheme during contact with a compliant object.

Results with blunt impacts and no collision detection, using the stop- as well as the admittance-strategy are provided in the appendix C.1. In this subsection the effectiveness of the collision detection and reaction with an elastic link robot is demonstrated in figure 11.4 based on sharp impacts with the balloon. The sharp impacts are realized with screw fixed to the end effector. The screw has been manually sharpened using a drill machine and a file.

The top row of figure 11.4 makes it clearly visible that just stopping all joint motions indeed limits but does not minimize the consequences of an impact. The robot does not crash into the contact cube, but the screw bursts the balloon. The blast excites link oscillations as visible in figure 11.4 (c). In contrast, the reflex strategy immediately causes the robot to reverse the joint motion, which saves the balloon.

Malzahn and Bertram (2013, at 2:37 min) provide an online available video with this experiment.

Physical interaction with a human

In this experiment the robot is commanded to continuously move between the two joint configurations $\theta = [0°, 45°, -45°]^T$ and $\theta = [0°, 135°, 45°]$. Figure 11.5 (**a**) collects the joint angles and figure 11.5 (**b**) the joint angular velocity for this experiment. While performing the task the residuals for both links are zero as visible in figure 11.5 (**c**). At second 5.17 a human has entered the robot workspace and interrupts the performed task by blocking the robots way as shown in figure 11.6 (**d**). This is equivalent to the experiments on blunt impacts presented in subsection C.1. The absolute residuals in both links impulsively increase driving the reflex-strategy to move the robot back immediately. The robot comes to rest at second 5.80 in a distance to the actual contact point as illustrated in figure 11.6 (**e**). After that, the robot switches to interaction mode. As an alternative to the more cautious reflex-strategy the stop-strategy could have been chosen to directly start the interaction with the robot at the location of task interruption.

At second 7.02 the human touches the robot as depicted in figure 11.6 (**f**) and guides the robot to the new pose depicted in figure 11.6 (**g**). The interaction mode admits to do this with just a fingertip at the end effector. Measurements with a force meter show that the required force is less than 1 N. The manual guidance causes irregular changes in the per link residuals with high frequency content. The reflected admittance nevertheless filters this input and yields a smooth joint motion.
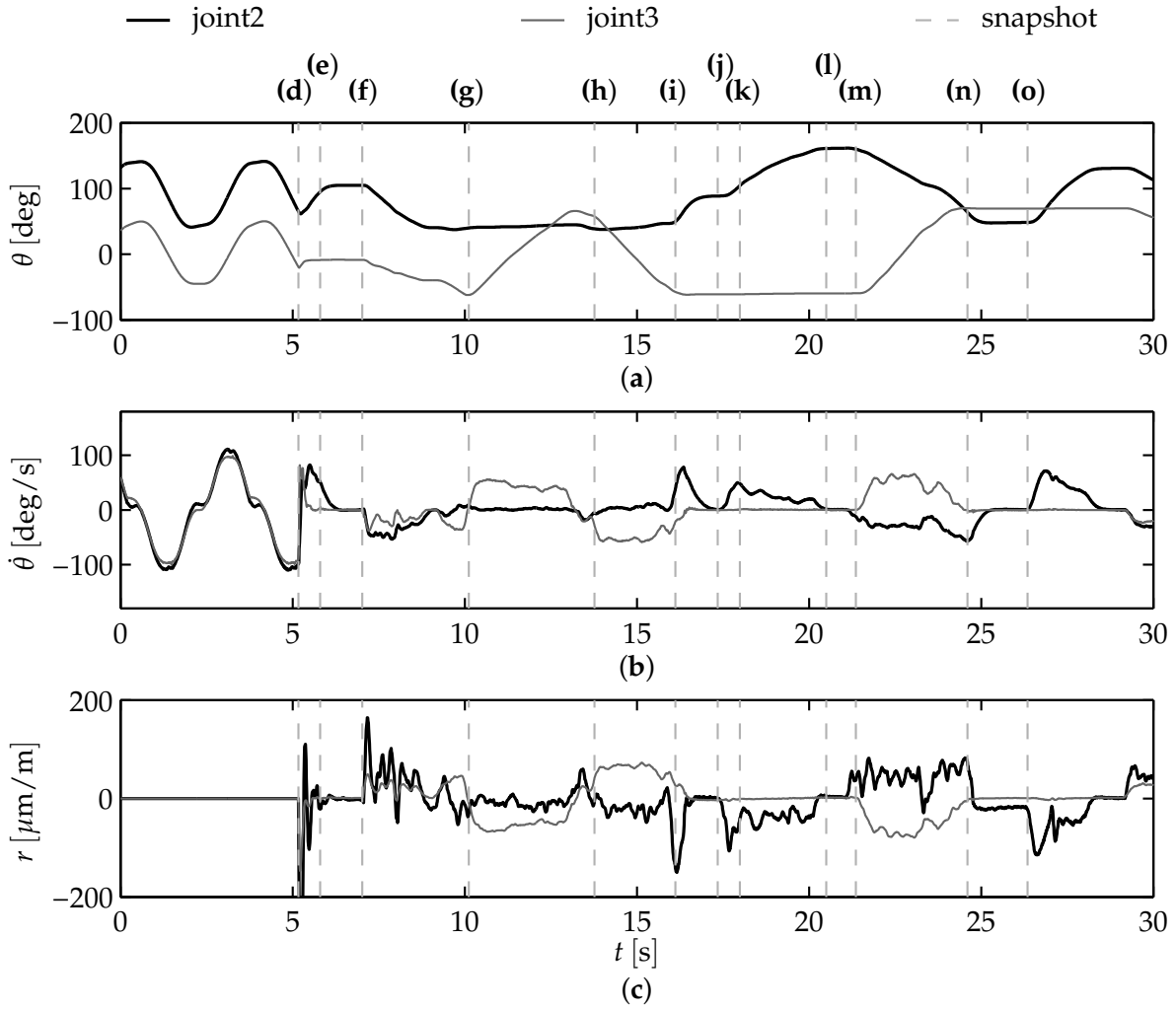
Figure 11.5.: Measurements for the joint angles (**a**), joint velocities (**b**) and residuals (**c**) during physical human-robot-interaction. The marked time instants correspond to the snapshots presented in figure 11.6 (**d**)-(**o**).

In the next step multiple contacts occur. The generalized momentum based approach yields decoupled residuals for each link and isolates the individual contacts as long as the contact force vector has a component normal to the preceding links. This allows for independent contact reactions on each link. To demonstrate this, the human places another finger at the end of the second link and reverses the interaction force exerted at the end effector around second 9.83. The action results in a reconfiguration from the elbow-up to the elbow-down pose shown in figure 11.6 (**h**).

Back in the elbow-up pose (see figure 11.6 (**i**)), an impulsive interaction force at the end effector is directed in parallel to the third link. This way, the human shoves the robot without significantly altering the relative configuration between the second and third joint as visible in figure 11.6 (**j**). The impulsive interaction is visible in the residual for the second joint only.

A short time after the shove the robot comes to rest at the joint configuration shown in figure 11.6 (**k**). The distance travelled in response to the shove can be arbitrarily adjusted to the human's requests in a broad range through the virtual friction modeled
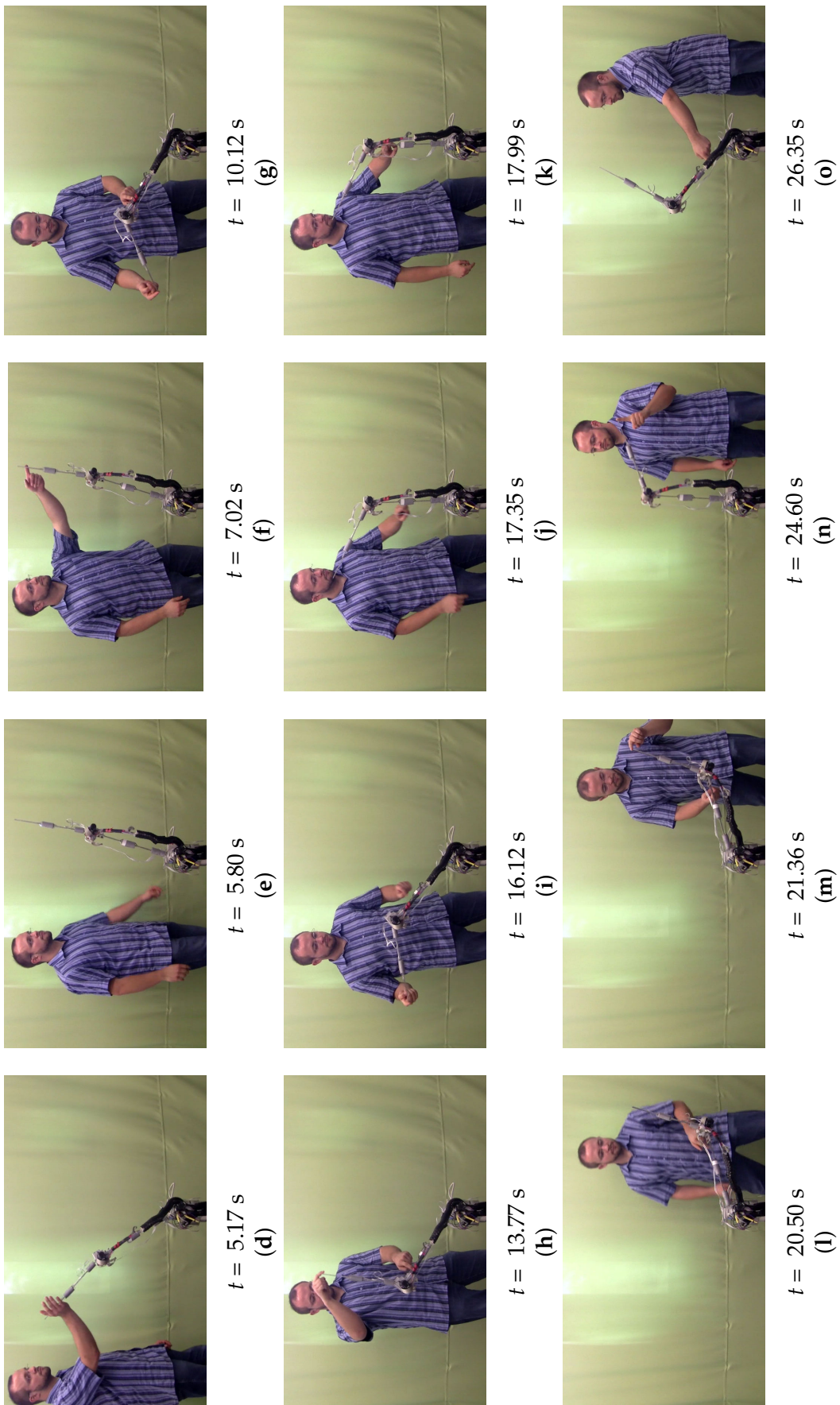
Figure 11.6.: Snapshots of the particular time instants during the physical human-robot-interactions (**d**)-(**o**). The snapshots correspond to the dashed lines in figure 11.5.

111

in the interaction admittance.

The transition between the figures 11.6 (**k**) and (**l**) supplements the previous demonstration of the contact isolation. The robot can not only be guided by a contact at the end effector, but also by pushing at the end of the second link. The figures 11.6 (**k**) and (**l**) exemplify the reconfiguration between the elbow-up and elbow-down pose in the other half of the robot workspace. The shove from figure 11.6 (**n**) to (**o**) mirrors the previous example. Finally figure 11.6 (**o**) illustrates the interaction by grasping the second arm in the vicinity of the strain gauges close to the joint.

Malzahn and Bertram (2013, at 3:47 min) provide an online available video with this experiment.

11.4. Discussion

The chapter experimentally demonstrates the collision detection and reaction with a multi-elastic-link robot arm under gravitational influence. This way, it puts the biological inspiration drawn from the whiskers of rodents and pinnipeds into real practice.

The experimental results demonstrate different reaction strategies. Each presented strategy has its merits and shortcomings. During constrained collisions the stop strategy would mean that a person or object will remain clamped between the robot and the constraining surface. Any contact force would persist and potentially experienced as a threat to a human. The alternative reflex behavior causes the robot to bounce back from any collision point. While the balloon experiment descriptively demonstrates the improved sensitivity of this approach, the challenge is to tune the parameters of bouncing behavior. Consider a service robot carrying a cup of coffee. If the escape motion is too dynamic, the robot would spill the coffee or cause new collisions. Furthermore, after the danger of collision is successfully averted, the robot should finish the originally given task.

The appropriate strategy selection and tuning is a challenging research direction, which involves higher level cognition, situation awareness and reasoning performed by the robot.

With this chapter the present work proves for the first time the practical feasibility to provide the required low level functionalities for such higher level decision processes with a multi-elastic-link robot arm. Up to now this has only been achieved with elastic joint robots. It ennobles intrinsic link elasticity from "just a problem" to a factual opportunity for physical interaction between the robot and its environment.

12

Conclusion and Outlook

Link elasticity is frequently considered an undesired effect in the mechanical design of robot arms and comparable machines. The driving motivation behind this work originates from the contrary perspective of exploiting the intrinsic compliance to grant elastic link robots force sensing capabilities and to simultaneously reduce the overall arm masses. The underlying hypothesis proposes that link elasticity is not necessarily just a problem, which degrades positioning accuracy and prolongs settling times. The thesis contributes new theoretical concepts confirmed by extensive experimental results in the fields of oscillation damping and end effector positioning for a multi-elastic-link arm in the presence of load and joint configuration dependent static deflections under gravity. On top of that, the work practically demonstrates the general feasibility of detecting and reacting to external contact forces with a multi-elastic-link robot operating under gravity. The contact scenarios include unpredicted or accidental collisions between the robot and the environment as well as intentional contacts for physical human robot interaction. A guideline, which summarizes the major steps required to deploy the techniques developed in this thesis, is provided in appendix D.

Experimental setup and arm dynamics

Multi-elastic-link robots operating under gravitational influence, which allow to test devised modeling and control algorithms in real experiments, are very rare. Therefore, the work starts from scratch with the development of an experimental setup. The complete experimental system consists of the three degree of freedom robot TUDOR along with external sensory equipment to assess the true end effector position and contact forces as reference.

The work comprises a comprehensive literature review and contributes an investigation towards the sensitivity of the plant dynamics with respect to joint configuration and payload changes, the effect of backlash and imperfect link clamping as well as generally unknown boundary conditions during physical contacts with the environment. The theoretical investigation is supported by extensive experiments.

With the gained insights the present work proposes a decentralized control architecture. The kinematic chain is subdivided into independent joint link modules, for which joint angular and oscillation damping controllers are individually tuned.

Oscillation damping control

Three different approaches for strain based oscillation damping are investigated. All three approaches are set free from a computation of the plant dynamics at runtime or the explicit knowledge of all boundary conditions.

The first proposed oscillation damping controller utilizes a truncated model of the oscillatory dynamics and is devised using the root locus method applied to the linearized plant. The second approach has originally been proposed by O'Connor and identifies wave propagation properties in a lumped parameter model. This thesis contributes a unified view on both approaches by revealing their identical controller structure with minor differences in the parameter tuning. The third proposed control approach considers the distributed nature as well as continuous wave dynamics of elastic beams and waives the need for any truncation or discretization. Structural similarities with the previous approaches suggest that it represents a frequency adaptive generalization of these schemes. A thorough theoretical investigation with the objective of deriving a global unified view on wave based controllers for elastic link robots is a promising future research direction.

The work contributes the derivation, practical application and comparison of the individual oscillation damping concepts at different levels within the underlying cascaded joint angular controller. As a conclusion the oscillation damping controllers operating on the velocity level prove to be most robust with respect to imperfect static strain cancellations in the presence of gravitational influences and joint friction. At the same time they have the least impact on the overall joint positioning behavior. As a concluding remark, full integral strain feedback laws for elastic-link robots under gravitational influence are definitely not recommended. Imperfect static strain cancellations yield growing steady state errors and deteriorate repeatability.

All presented concepts effect a rapid decay of structural oscillations induced by joint accelerations and step-like or periodic disturbances, even near resonance. All these results are robust to the backlash present in the gears. Of course, more homogenous experimental results can be expected throughout the entire workspace, if backlash can be eliminated by hardware.

This thesis focuses on multi-elastic-link arms, which predominantly oscillate in a single plane. Future research should be concerned with the extension of the presented oscillation damping controllers to multiple planes of oscillation. A major challenge to solve in this case is to maintain the controllability of the oscillatory degrees of freedom. One option is to avoid uncontrollable joint configurations in analogy to kinematic singularities. In contrast, it should be asked and investigated, if an elastic link robot with multiple planes of oscillations can be designed without the existence of such configurations. In fact, the present work already illustrates that a single joint link module can be used to dampen oscillations in distant joint-link-modules. Exploiting inter module couplings could be a key.

End effector position control

With the readily damped oscillations, the divide and conquer strategy to the control of elastic link robot arms already pays off in regard to the end effector positioning.

Only the static deflections remain to be compensated in comparison to conventional arms. The thesis presents two methods to solve the end effector positioning task. The first approach is a visual servoing technique, which preserves the idea of relying on only marginal model knowledge during the controller design. Well established visual servoing control schemes minimize the relative pose error between a current and a desired view of the scene. To approach the goal view they command the direction of rotation for each individual joint through the differential robot kinematics. The work demonstrates the sufficiency of the differential kinematics approximation for the elastic link arm TUDOR on the basis of the equivalent rigid robot Jacobian.

In spite of the elegance and minimal modeling efforts associated with the visual servoing approach, a shortcoming is the dependance of the control result on the actual scene structure, which has to be adequately rich in visual features. This motivates the second positioning concept proposed in this work. It is based on the data driven learning of the forward and inverse kinematics along with a payload estimator using MLP neural networks. The key to obtain precise models is to transform the original input features into nonlinear features using the regressors known from the analytical rigid body forward and inverse kinematics. In the case of the inverse kinematics the estimated payload is an additional aggregated feature.

A conventional six degree of freedom robot arm usually provides up to sixteen solutions for a given pose within the dexterous workspace. The ambiguity is resolved by selecting the feasible solution being the closest to the current joint configuration. Similar to that the ambiguity resolution in the inverse kinematics of TUDOR is achieved by the multi-model approach, in which one dedicated model is trained for the elbow-up and elbow-down postures.

The work exemplifies the speed and accuracy of the kinematics model in conjunction with the underlying oscillation damping controller by realizing ball catching experiments with a multi-elastic-link robot arm. The balls are sequentially but irreproducibly thrown by a human. The robot intercepts the ball with a net at the piercing point of the ball trajectory with the robot workspace.

Since the successful experiments contribute a major step regarding point-to-point maneuvers, future works should be dedicated to extensions for precise trajectory control of multi-elastic-link arms under gravity. Looking at the actually rather imprecise human motion apparatus it becomes apparent that a lot of human skills emerge from learned and continuously adapted perception-action-mappings working in a feed-forward sense. From this inspiration, it can be expected that the augmentation of the controllers devised in this work by suitable feed-forward schemes leads to fruitful results. Additionally, the work has proven that the link strains as well as the joint angles carry the required information to compute the forward and inverse kinematics. Since analytical solutions are favorable, investigations to derive them should be pushed forward in this direction by continuing research.

Collision detection and physical interaction

The oscillation damping and the end effector positioning address the originally undesired challenges associated with link elasticity. The accomplished results finally allow for the investigation of the suspected potentials in this thesis. The conducted

investigations reveal a linear relationship between the damped link strains and the joint load torques. The main difference originates from the friction present in the joints. In the absence of friction, the link strains could be directly transformed into the actuator electrical torques and vice versa. The linear mapping is valid in the whole workspace for a constant given payload.

The mathematical structure of the joint referred arm dynamics known from conventional rigid robots can be directly applied to describe the strain referred damped arm dynamics. As a consequence, collision detection and reaction schemes originally developed for rigid and elastic joint robots may be straightly applied to damped elastic link robots. The work verifies these findings in illustrative experiments including blunt and also sharp collisions with intrinsically compliant or fragile objects as well as a human arm. A stopping and a reflex behavior is implemented as reaction strategy to detected collisions. Both strategies are shown to visibly reduce the harm potential of an unforeseen impact situation with a variety of contact impedances.

Beyond the detection and reaction to accidental collisions the work demonstrates how the force sensing capabilities may be extended to switch the robot into a backdrivable mode. This enables intentional physical human robot interaction such as kinesthetic teaching of frequently varying tasks by a non-robotic specialist.

A consequential next step for future work is to take advantage of the force sensing capabilities evidenced in this work for analytical payload identification. This will help to automatically adapt the collision detection scheme and to even improve the oscillation damping as well as end effector positioning results. The controllers proposed in the present work enable ongoing research to be engaged with the development of direct and hybrid force controllers with a multi-elastic-link robot.

Conclusion

Within the big picture of the affordable and intrinsically safe "household automaton [...] about the price of a good automobile" (Heinlein 1957) it must be humbly kept in mind, that TUDOR is a three degree of freedom multi-elastic-link robot with oscillations taking place mainly in the vertical plane. While short- and mid-term research directions are given above, long-term research must spawn elastic link robots arms with six to seven degrees of freedom and strive for the realization of practically relevant robotics tasks.

The contributed concept of the present work follows a divide-and-conquer strategy in that it separates the control objectives of low-level joint control, oscillation damping and finally end effector positioning as well as collision detection and reaction.

The results achieved and exemplified with TUDOR strongly confirm that it is indeed feasible to have a lightweight robot with intrinsic force sensing capabilities by relaxing the persistently strong demands for robot link stiffness. The commonly undesired link elasticity is intentionally and visibly introduced in the structure of TUDOR. The devised control algorithms alleviate the detrimental effects and successfully exploit the potentials. This confirms:

Link elasticity is not ultimately "just a problem".

A

Hardware Parameters

This appendix summarizes the hardware properties of all important components of TUDOR as well as the sorrounding reference systems detailed in chapter 2.

A.1. Elastic links

The elastic links are spring steel blades with rectangular cross section.

parameter	symbol	unit	link 1	link 2	link 3
length	l_B	mm	0	430	410
width	b_B	mm	0	15	15
height	$2\,y_b$	mm	0	4	4
density	ρ_b	$10^3 \mathrm{kg/m}^3$		7.8	7.8
Youngs modulus	E	$10^9\ \mathrm{N/m}^2$		200	200

A.2. Computer systems

All employed computer systems are standard desktop PCs (compare figure 2.9).

parameter	unit	xPC	console	stereo cam	eye in hand
operating system		xPC Target	Win XP	Win XP	Ubuntu 12.04 LTS
type		TL-Electronic CL41xx	DELL Optiplex 755	DELL Optiplex GX280	DELL Optiplex 755
CPU name		Intel Pentium 4	Intel Core 2 E6650	Intel Pentium 4	Intel Core 2 Duo E6750
CPU clock	GHz	3.8	2.33		2.66
RAM	MB	2048	2048	2048	3072
RAM clock	MHz	533	400	266	800

A.3. Actuators

parameter	symbol		unit	actuator 1	actuator 2	actuator 3
model				EC-max 40	EC-max 40	EC-max 30
overall length	l_M		mm	185.3	198.8	150.9
Ø motor	d_M		mm	40	40	30
Ø gear	d_G		mm	52	52	32
gear ratio	n_M			156:1	230:1	246:1
gear backlash			deg	<1	<1	<1
rotor and gear inertia*	I_M	10^{-6}	kgm^2	9.19	9.41	0.82
pos. viscous friction*	k_v^+	10^{-5}	Nms/rad	2.21	1.86	0.26
neg. viscous friction*	k_v^-	10^{-5}	Nms/rad	2.11	1.86	0.23
pos. coulomb friction*	k_c^+	10^{-3}	Nm	0.46	3.34	1.49
neg. coulomb friction*	k_c^-	10^{-3}	Nm	7.25	1.15	2.40
torque constant	k_τ	10^{-3}	Nm/A	44.8	44.8	12.9
joint ranges			deg	$[-170, 180]$	$[-14, 192]$	$[-102, 102]$
maximum speed			deg/s	184	125	146
max. continous current			A	3.95	3.95	2.85
max. intermittent current			A	11.85	11.85	8.55
max. continous torque			Nm	30	30	6
max. intermittent torque			Nm	45	45	7.5
encoder resolution			1/rev.	500	500	500
amplifier gain*	k_{amp}		A/V	1.39	1.39	1.39
amplifier cut-off frequency*	ω_{amp}		Hz	833	833	833
mass*			kg	0.5410	1.6680	0.5885

Parameters marked with an asterisk (*) have been experimentally identified within this work (see section 3.1). All other parameters are taken from the vendor's datasheets. Joint ranges, maximum joint speeds as well as continuous and intermittent torques are referred to the gear output.

A.4. Sensors

Strain sensors

The strain sensors applied in this work are FAE-12S-35-S6E-P type strain gages manufactured by Vishay Precision Group. The measurement amplifiers are GSV-1L by ME-Messsysteme GmbH.

parameter	symbol	unit	value
sensing element			foil-gage
alloy			constantan
carrier material			polyamide
total gage length		mm	5.61
total gage width		mm	2.67
active gage length		mm	3.18
gage resistance		Ω	$350 \pm 0.2\%$
creep compensation			8.5
temperature compensation		$10^{-6}/{}^{\circ}C$	10.8

Inertial measurement unit

The inertial measurement sensor is a CHR-6D unit consists of a LPR510AL 3-axes MEMS rotation rate sensor as well as a ADXL335 3-axes accelerometer. It ships with a 32 bit ARM Cortex processor operating at 64 Mhz.

parameter	symbol	unit	value
supply voltage		V	3.3
resolution		bit	16
gyroscope range		$^{\circ}/\text{s}$	± 400
acceleromenter range		$9.81\frac{\text{m}}{\text{s}}$	± 3
mass		g	1.5
FIR cutoff frequency		Hz	$[10, 140]$

Stereo camera system

The stereo camera system comprises of two VRmC-3+ cameras manufactured by VRmagic. Both are equipped with a wide angle lens.

parameter	symbol	unit	value
horizontal resolution		px	638
vertical resolution		px	478
horizontal pixel size		μm	6
vertical pixel size		μm	6
pixel clock		MHz	[5, 26.6]
frame rate		Hz	50
length		mm	27.0
width		mm	36.0
height		mm	36.0
focal length		mm	4.2
shutter			rolling

Contact cube

The 6D force/torque sensor of type FT Gamma manufactured by ATI constitutes the core of the contact cube described in section 2.4.

parameter	symbol	unit	value
mass		g	225
range F_x, F_y		N	±65
range F_z		N	±200
range τ_x, τ_y		Nm	±5
range τ_z		Nm	±5
resolution F_x, F_y		N	$\pm1/40$
resolution F_z		N	$\pm1/20$
resolution τ_x, τ_y		Nm	$\pm1/667$
resolution τ_z		Nm	$\pm1/667$

B

Mathematical Definitions and Derivations

This appendix contains mathematical definitions and derivations to support the material provided in this work. It is intended to render the document self-contained.

B.1. Equivalences of trigonometric, hyperbolic and exponential functions

The general solution of the mode shape ODE can be written using exponential or hyperbolic functions. The derivation of their equivalence as well as the transformation between the corresponding coefficients requires knowledge about the mathematical relationship between:

- ...trigonometric and exponential functions:

$$\mathrm{e}^{\mathrm{j}x} = \cos(x) + \mathrm{j}\,\sin(x)\,, \tag{B.1.1}$$

$$\mathrm{e}^{-\mathrm{j}x} = \cos(x) - \mathrm{j}\,\sin(x)\,, \tag{B.1.2}$$

$$\mathrm{e}^{y+\mathrm{j}x} = \mathrm{e}^{y}\left(\cos(x) + \mathrm{j}\,\sin(x)\right)\,, \tag{B.1.3}$$

$$\sin(x) = \frac{\mathrm{e}^{\mathrm{j}x} - \mathrm{e}^{-\mathrm{j}x}}{\mathrm{j}2}\,, \tag{B.1.4}$$

$$\cos(x) = \frac{\mathrm{e}^{\mathrm{j}x} + \mathrm{e}^{-\mathrm{j}x}}{2}\,; \tag{B.1.5}$$

- ...trigonometric and hyperbolic functions:

$$\sin(x) = -\mathrm{j}\,\sinh(\mathrm{j}x)\,, \tag{B.1.6}$$

$$\cos(x) = \cosh(\mathrm{j}x)\,, \tag{B.1.7}$$

$$\sinh(x) = -\mathrm{j}\,\sin(\mathrm{j}x)\,, \tag{B.1.8}$$

$$\cosh(x) = \cos(\mathrm{j}x)\,; \tag{B.1.9}$$

$$\tag{B.1.10}$$

- ...hyperbolic and exponential functions:

$$e^x = \cosh(x) + \sinh(x), \tag{B.1.11}$$

$$e^{-x} = \cosh(x) - \sinh(x), \tag{B.1.12}$$

$$\sinh(x) = \frac{e^x - e^{-x}}{2}, \tag{B.1.13}$$

$$\cosh(x) = \frac{e^x + e^{-x}}{2}. \tag{B.1.14}$$

B.2. Derivatives of general solutions to the boundary value problem

The derivation of particular solutions to the elastic beam boundary value problem requires the spatial derivatives of the general solution.

- In the hyperbolic notation the derivatives are:

$$\Phi(x) = \hat{a}_1 \, \sinh(k_\omega \, x) + \hat{a}_2 \, \cosh(k_\omega \, x) + \ldots$$
$$+ \hat{a}_3 \, \sin(k_\omega \, x) + \hat{a}_4 \, \cos(k_\omega \, x), \tag{B.2.1}$$

$$\frac{\mathrm{d}\Phi(x)}{\mathrm{d}x} = k_\omega \, (\hat{a}_1 \, \cosh(k_\omega \, x) + \hat{a}_2 \, \sinh(k_\omega \, x) + \ldots$$
$$+ \hat{a}_3 \, \cos(k_\omega \, x) - \hat{a}_4 \, \sin(k_\omega \, x)), \tag{B.2.2}$$

$$\frac{\mathrm{d}^2\Phi(x)}{\mathrm{d}x^2} = k_\omega^2 \, (\hat{a}_1 \, \sinh(k_\omega \, x) + \hat{a}_2 \, \cosh(k_\omega \, x) + \ldots$$
$$- \hat{a}_3 \, \sin(k_\omega \, x) - \hat{a}_4 \, \cos(k_\omega \, x)), \tag{B.2.3}$$

$$\frac{\mathrm{d}^3\Phi(x)}{\mathrm{d}x^3} = k_\omega^3 \, (\hat{a}_1 \, \cosh(k_\omega \, x) + \hat{a}_2 \, \sinh(k_\omega \, x) + \ldots$$
$$- \hat{a}_3 \, \cos(k_\omega \, x) + \hat{a}_4 \, \sin(k_\omega \, x)). \tag{B.2.4}$$

- In the exponential notation the derivatives compute to:

$$\Phi(x) = {}^+\hat{a} \, e^{-\mathrm{j}k_\omega \, x} + {}^-\hat{a} \, e^{\mathrm{j}k_\omega \, x} + {}^+\hat{a}_n \, e^{-k_\omega \, x} + {}^-\hat{a}_n \, e^{k_\omega \, x}, \tag{B.2.5}$$

$$\frac{\mathrm{d}\Phi(x)}{\mathrm{d}x} = k_\omega \left(-\mathrm{j} \, {}^+\hat{a} \, e^{-\mathrm{j}k_\omega \, x} + \mathrm{j} \, {}^-\hat{a} \, e^{\mathrm{j}k_\omega \, x} - {}^+\hat{a}_n \, e^{-k_\omega \, x} + {}^-\hat{a}_n \, e^{k_\omega \, x} \right), \tag{B.2.6}$$

$$\frac{\mathrm{d}^2\Phi(x)}{\mathrm{d}x^2} = k_\omega^2 \left(-1 \, {}^+\hat{a} \, e^{-\mathrm{j}k_\omega \, x} - {}^-\hat{a} \, e^{\mathrm{j}k_\omega \, x} + {}^+\hat{a}_n \, e^{-k_\omega \, x} + {}^-\hat{a}_n \, e^{k_\omega \, x} \right), \tag{B.2.7}$$

$$\frac{\mathrm{d}^3\Phi(x)}{\mathrm{d}x^3} = k_\omega^3 \left(\mathrm{j} \, {}^+\hat{a} \, e^{-\mathrm{j}k_\omega \, x} - \mathrm{j} \, {}^-\hat{a} \, e^{\mathrm{j}k_\omega \, x} - {}^+\hat{a}_n \, e^{-k_\omega \, x} + {}^-\hat{a}_n \, e^{k_\omega \, x} \right). \tag{B.2.8}$$

B.3. Characteristic equation of the boundary value problem

This section derives the characteristic equation of the boundary value problem defined in section 4.4. The boundary conditions are given in the equations (4.4.1) to (4.4.4).

The first boundary condition (4.4.1) together with the general solution to the boundary value problem (4.3.6) yields:

$$\Phi(x)_{|x=0} = \hat{a}_4 + \hat{a}_2 = 0 \Leftrightarrow \hat{a}_4 = -\hat{a}_2. \tag{B.3.1}$$

From the second boundary condition (4.4.1) and the derivatives (B.2.2) as well as (B.2.3) $\hat{a}_3$ computes to:

$$\hat{a}_3 = \frac{2EI_z k_\omega}{k_r} \hat{a}_2 - \hat{a}_1. \tag{B.3.2}$$

With these results the equations (B.2.1) to (B.2.4) simplify to:

$$\Phi(x) = \hat{a}_1 \left(\sinh(k_\omega x) - \sin(k_\omega x) \right) + \dots$$
$$+ \hat{a}_2 \left(\cosh(k_\omega x) + \frac{2EI_z k_\omega}{k_r} \sin(k_\omega x) - \cos(k_\omega x) \right), \tag{B.3.3}$$

$$\frac{\mathrm{d}\Phi(x)}{\mathrm{d}x} = k_\omega \left(\hat{a}_1 \left(\cosh(k_\omega x) - \cos(k_\omega x) \right) + \dots \right.$$
$$\left. + \hat{a}_2 \left(\sinh(k_\omega x) + \frac{2EI_z k_\omega}{k_r} \cos(k_\omega x) + \sin(k_\omega x) \right) \right), \tag{B.3.4}$$

$$\frac{\mathrm{d}^2\Phi(x)}{\mathrm{d}x^2} = k_\omega^2 \left(\hat{a}_1 \left(\sinh(k_\omega x) + \sin(k_\omega x) \right) + \dots \right.$$
$$\left. + \hat{a}_2 \left(\cosh(k_\omega x) - \frac{2EI_z k_\omega}{k_r} \sin(k_\omega x) + \cos(k_\omega x) \right) \right), \tag{B.3.5}$$

$$\frac{\mathrm{d}^3\Phi(x)}{\mathrm{d}x^3} = k_\omega^3 \left(\hat{a}_1 \left(\cosh(k_\omega x) + \cos(k_\omega x) \right) + \dots \right.$$
$$\left. + \hat{a}_2 \left(\sinh(k_\omega x) - \frac{2EI_z k_\omega}{k_r} \cos(k_\omega x) - \sin(k_\omega x) \right) \right). \tag{B.3.6}$$

The coefficient $\hat{a}_2$ can now be expressed solely in terms of $\hat{a}_1$ by combining boundary condition (4.4.3) with the results (B.3.4) and (B.3.5):

$$\hat{a}_2 = \left(\rho_b \left(\sin(\beta_L) + \sinh(\beta_L) \right) + I_L k_\omega^3 \left(\cos(\beta_L) - \cosh(\beta_L) \right) \right) \cdot \dots$$
$$\cdot \left(2\frac{EI_z}{k_r} \left(k_\omega \rho_b \sin(\beta_L) + I_L k_\omega^4 \cos(\beta_L) \right) + \dots \right.$$
$$- \rho_b \left(\cosh(\beta_L) + \cos(\beta_L) \right) + \dots$$
$$\left. + I_L k_\omega^3 \left(\sinh(\beta_L) + \sin(\beta_L) \right) \right)^{-1} \hat{a}_1. \tag{B.3.7}$$

In combination with the simplified expressions (B.3.3) and (B.3.6) the fourth bound-

ary condition (4.4.4) finally yields the characteristic equation:

$$
\frac{k_\omega EI_z}{K_r} \left(\cos\left(\beta_L\right) \sinh\left(\beta_L\right) - \cosh\left(\beta_L\right) \sin\left(\beta_L\right) + \ldots\right.
$$

$$
-\frac{2k_\omega m_L}{\rho_b} \sin\left(\beta_L\right) \sinh\left(\beta_L\right) - \frac{2k_\omega^3 I_L}{\rho_b} \cos\left(\beta_L\right) \cosh\left(\beta_L\right) + \ldots
$$

$$
-\frac{k_\omega^4 I_L m_L}{\rho_b} \left(\cos\left(\beta_L\right) \sinh\left(\beta_L\right) + \cosh\left(\beta_L\right) \sin\left(\beta_L\right)\right)\left. \right) + \ldots
$$

$$
+ m_L \frac{k_\omega}{\rho_b} \left(\cos\left(\beta_L\right) \sinh\left(\beta_L\right) - \cosh\left(\beta_L\right) \sin\left(\beta_L\right)\right) + \ldots
$$

$$
- I_L \frac{k_\omega^3}{\rho} \left(\cos\left(\beta_L\right) \sinh\left(\beta_L\right) + \cosh\left(\beta_L\right) \sin\left(\beta_L\right)\right) + \ldots
$$

$$
+ I_L m_L \frac{k_\omega^4}{\rho_b^2} \left(1 - \cos\left(\beta_L\right) \cosh\left(\beta_L\right)\right) + \ldots
$$

$$
+ 1 + \cos\left(\beta_L\right) \cosh\left(\beta_L\right) = 0, \quad \text{(B.3.8)}
$$

where $\beta_L = k_\omega L$.

Orthogonality of modes and normalization

Consider two solutions $y_u(x,t)$ and $y_v(x,t)$ to the boundary value problem with the conditions (4.4.1) to (4.4.4). The associated natural frequencies are ω_u and ω_v. In search for a convenient normalization and orthogonality relations, the beam equation of motion (4.2.8) is written for the case $\rho_{ext}(x,t) = 0$:

$$
- EI_z \frac{\mathrm{d}^4 y_u(x)}{\mathrm{d}x^4} = \rho_b \omega_u^2\, y_u(x), \tag{B.3.9}
$$

where the result of equation (4.3.8) allows to omit the time argument.

The two solutions $y_u(x)$ and $y_v(x)$ are joined by multiplication of (B.3.9) with y_v. The integration over the beam length yields:

$$
- \int_0^L EI_z\, y_v(x) \frac{\mathrm{d}^4 y_u(x)}{\mathrm{d}x^4}\mathrm{d}x = \int_0^L \rho_b \omega_u^2\, y_v(x) y_u(x)\mathrm{d}x, \tag{B.3.10}
$$

The idea for the derivation of the orthogonality relations is to level the derivative orders of $y_u(x)$ and $y_v(x)$ on the left side of this equation. This is done with two steps of integration by parts. The first step yields:

$$
- \int_0^L EI_z\, y_v(x) \frac{\mathrm{d}^4 y_u(x)}{\mathrm{d}x^4}\mathrm{d}x = - \left(EI_z\, y_v(x) \frac{\mathrm{d}^3 y_u(x)}{\mathrm{d}x^3}\right)\Bigg|_0^L + \ldots
$$

$$
+ \int_0^L EI_z \frac{\mathrm{d}y_v(x)}{\mathrm{d}x} \frac{\mathrm{d}^3 y_u(x)}{\mathrm{d}x^3}\mathrm{d}x. \tag{B.3.11}
$$

The second integration step is performed on the new integral:

$$\int_0^L EI_z \frac{\mathrm{d}y_v(x)}{\mathrm{d}x}\frac{\mathrm{d}^3 y_u(x)}{\mathrm{d}x^3}\mathrm{d}x = - \left(EI_z \frac{\mathrm{d}y_v(x)}{\mathrm{d}x}\frac{\mathrm{d}^2 y_u(x)}{\mathrm{d}x^2} \right)\Bigg|_0^L + \dots$$
$$- \int_0^L EI_z \frac{\mathrm{d}^2 y_v(x)}{\mathrm{d}x^2}\frac{\mathrm{d}^2 y_u(x)}{\mathrm{d}x^2}\mathrm{d}x. \quad \text{(B.3.12)}$$

At this point the derivative orders are levelled in the integrand. The boundary conditions (4.4.1) and (4.4.4) simplify the first summand of the first step (B.3.11):

$$- \left(EI_z \, y_v(x)\frac{\mathrm{d}^3 y_u(x)}{\mathrm{d}x^3} \right)\Bigg|_0^L = -m_L \omega_u^2 \, y_v(x)_{|x=L}\, y_u(x)_{|x=L} \,. \quad \text{(B.3.13)}$$

Assuming the clamping to be very stiff, the boundary condition (4.4.2) tends to zero. Together with boundary condition (4.4.3) first summand of the second step simplifies to:

$$- \left(EI_z \frac{\mathrm{d}y_v(x)}{\mathrm{d}x}\frac{\mathrm{d}^2 y_u(x)}{\mathrm{d}x^2} \right)\Bigg|_0^L = -I_L \omega_u^2 \frac{\mathrm{d}y_v(x)}{\mathrm{d}x}\Bigg|_{x=L}\frac{\mathrm{d}y_u(x)}{\mathrm{d}x}\Bigg|_{x=L}. \quad \text{(B.3.14)}$$

Insertion of (B.3.13) and (B.3.14) in (B.3.9) results in:

$$\int_0^L \rho_b \omega_u^2 \, y_v(x) y_u(x)\mathrm{d}x = -I_L \omega_u^2 \frac{\mathrm{d}y_v(x)}{\mathrm{d}x}\Bigg|_{x=L}\frac{\mathrm{d}y_u(x)}{\mathrm{d}x}\Bigg|_{x=L} + \dots$$
$$- m_L \omega_u^2 \, y_v(x)_{|x=L}\, y_u(x)_{|x=L} \,. \quad \text{(B.3.15)}$$

An analogous result is obtained by writing (B.3.9) in terms of y_v and following the same steps as before:

$$\int_0^L \rho_b \omega_v^2 \, y_u(x) y_v(x)\mathrm{d}x = -I_L \omega_v^2 \frac{\mathrm{d}y_u(x)}{\mathrm{d}x}\Bigg|_{x=L}\frac{\mathrm{d}y_v(x)}{\mathrm{d}x}\Bigg|_{x=L} + \dots$$
$$- m_L \omega_v^2 \, y_u(x)_{|x=L}\, y_v(x)_{|x=L} \,. \quad \text{(B.3.16)}$$

The subtraction of both equations yields:

$$\left(\omega_u^2 - \omega_v^2 \right) \left(\int_0^L \rho_b \, y_v(x) y_u(x)\mathrm{d}x + \dots \right.$$
$$\left. + I_L \frac{\mathrm{d}y_u(x)}{\mathrm{d}x}\Bigg|_{x=L}\frac{\mathrm{d}y_v(x)}{\mathrm{d}x}\Bigg|_{x=L} + m_L \, y_u(x)_{|x=L}\, y_v(x)_{|x=L} \right) = 0. \quad \text{(B.3.17)}$$

For $u \neq v$ this can only be satisfied if:

$$\int_0^L \rho_b \, y_v(x) y_u(x)\mathrm{d}x + I_L \frac{\mathrm{d}y_u(x)}{\mathrm{d}x}\Bigg|_{x=L}\frac{\mathrm{d}y_v(x)}{\mathrm{d}x}\Bigg|_{x=L} + \dots$$
$$+ m_L \, y_u(x)_{|x=L}\, y_v(x)_{|x=L} = \delta_{uv}, \quad \text{(B.3.18)}$$

where

$$\delta_{uv} = \begin{cases} 1 & u = v \\ 0 & u \neq v \end{cases}. \tag{B.3.19}$$

This implies the orthogonality of the natural modes $y_u(x)$ and $y_v(x)$. Therefore equation (B.3.18) is known as the orthogonality relation. From the characteristic equation the mode shapes can only be computed up to scale. The orthogonality relation implies to normalize to mode shapes to satisfy:

$$\int_0^L \rho_b \, y_u^2(x) \mathrm{d}x + I_L \left(\frac{\mathrm{d}y_u(x)}{\mathrm{d}x} \right)^2_{|x=L} + m_L \, y_u^2(x)_{|x=L} = 1. \tag{B.3.20}$$

The interpretation of this result yields that the natural modes form an orthonormal basis of all possible dynamic deflections $y(x,t)$. In other words: any dynamic deflection $y(x,t)$ can be expressed by a linear combination of the infinite number of modes. The linear coefficients are the temporal amplitudes v_u:

$$y(x,t) = \sum_{u=1}^{\infty} \Phi_u(x) \, v_u(t). \tag{B.3.21}$$

Adding:

$$\omega_u^2 \left(I_L \frac{\mathrm{d}y_u(x)}{\mathrm{d}x}\bigg|_{x=L} \frac{\mathrm{d}y_v(x)}{\mathrm{d}x}\bigg|_{x=L} + \ldots + m_L \, y_u(x)_{|x=L} \, y_v(x)_{|x=L} \right) \tag{B.3.22}$$

to both sides of equation (B.3.10) yields:

$$-\int_0^L E I_z \, y_v(x) \frac{\mathrm{d}^4 y_u(x)}{\mathrm{d}x^4} \mathrm{d}x + \ldots$$
$$+ \omega_u^2 \left(I_L \frac{\mathrm{d}y_u(x)}{\mathrm{d}x}\bigg|_{x=L} \frac{\mathrm{d}y_v(x)}{\mathrm{d}x}\bigg|_{x=L} + m_L \, y_u(x)_{|x=L} \, y_v(x)_{|x=L} \right) = \ldots$$
$$+ \omega_u^2 \left(\int_0^L \rho_b \, y_v(x) y_u(x) \mathrm{d}x + I_L \frac{\mathrm{d}y_u(x)}{\mathrm{d}x}\bigg|_{x=L} \frac{\mathrm{d}y_v(x)}{\mathrm{d}x}\bigg|_{x=L} + m_L \, y_u(x)_{|x=L} \, y_v(x)_{|x=L} \right), \tag{B.3.23}$$

so that:

$$-\int_0^L E I_z \, y_v(x) \frac{\mathrm{d}^4 y_u(x)}{\mathrm{d}x^4} \mathrm{d}x + \ldots$$
$$+ \omega_u^2 \left(I_L \frac{\mathrm{d}y_u(x)}{\mathrm{d}x}\bigg|_{x=L} \frac{\mathrm{d}y_v(x)}{\mathrm{d}x}\bigg|_{x=L} + m_L \, y_u(x)_{|x=L} \, y_v(x)_{|x=L} \right) = \omega_u^2 \, \delta_{uv}. \tag{B.3.24}$$

After rearranging the combination of equations (B.3.13) and (B.3.14) to replace the right of (B.3.10) yields:

$$-\int_0^L E I_z \frac{\mathrm{d}^2 y_v(x)}{\mathrm{d}x^2} \frac{\mathrm{d}^2 y_u(x)}{\mathrm{d}x^2} \mathrm{d}x = \omega_u^2 \, \delta_{uv}. \tag{B.3.25}$$

The equations (B.3.24) and (B.3.25) are known as the companion orthogonality relations (Meirovitch 2001).
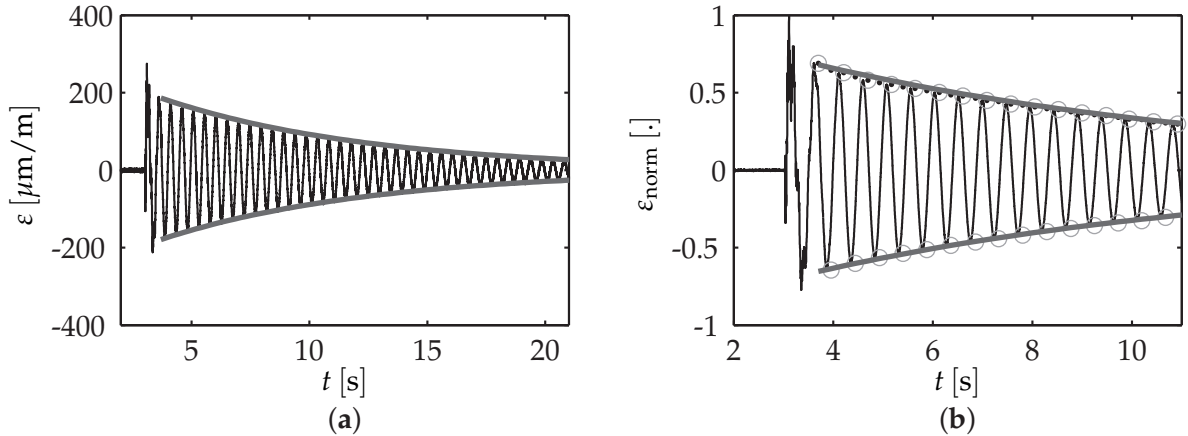
Figure B.1.: Measured oscillation strain signal with envelope defined by the logarithmic decrement (**a**). Close-up with detected and refined extremal values used to identify the logartihmic decrement (**b**).

Logarithmic decrement estimation

The logarithmic decrement is estimated from a measured oscillation signal such as the one depicted in figure B.1 (**a**) applying a two-step procedure. The first step is a detection of the extrema ε_{ex} of the normalized and mean liberated oscillation strain signal visible in figure B.1 (**a**). The extrema are initialized based on the signal frequency as indicated by the circles and refined by a absolute maximum search on a window around these initial locations. According to:

$$\bar{\zeta}_1 = \frac{1}{n_k} \sum_{k=1}^{n_K-1} \frac{1}{t(k+1) - t(k)} \ln \frac{|\varepsilon_{ex}(k)|}{|\varepsilon_{ex}(k+1)|} \tag{B.3.26}$$

the found extremal points provide an initial guess $\bar{\zeta}_1$ for the decrement. In the second step this initial guess along with the first absolute extremum $|\varepsilon|_{ex}(1)$ initialize a Levenberg-Marquardt curve fit of a decaying exponential function. The curve fit yields the final estimate ζ_1.

B.4. Performance metrics

Throughout the thesis different performance metrics are used to evaluate and compare control concepts as well as modeling techniques. Their definitions are summarized in this section.

Normalized Root Mean Squared Error

The root mean squared error between a quantity x and its reference x_{ref} normalized by the error standard deviation yields the normalized root mean squared error (NRMSE). The NRMSE is given in percent:

$$\text{NRMSE}(x) = 100 \frac{\|x - x_{\text{ref}}\|}{\|x - \bar{x}_{\text{ref}}\|} \quad [\%] . \tag{B.4.1}$$

The goodness of fit

The goodness of fit metric used in this work is defined as one minus the normalized root mean squared error $(1 - \mathrm{NRMSE})$ and given in in percent:

$$\mathrm{fit}(x) = 100 - \mathrm{NRMSE}, \quad [\%]. \tag{B.4.2}$$

The goodness of fit reflects the percentage of the standard deviation in a reference signal x_{ref} explained by the model. A model that achieves a goodness of fit value above 80 % is commonly accepted as a good model.

Integral of absolute time weighted error

The integral of absolute time weighted error (IATE) computes to:

$$IATE(x,t) = \int_0^t t \left| x(t) - x_{ref}(t) \right| \, \mathrm{d}t. \tag{B.4.3}$$

It penalizes errors that persist for a longer period more than initial errors.

Integral absolute time weighted strain surface

The integral absolute time weighted strain surface computes to:

$$IATS(x,t) = \int_0^t t \left| \varepsilon(t) \right| \, \mathrm{d}t. \tag{B.4.4}$$

It may be understood as the IATE with $x = \varepsilon$ and $x_{ref} = 0$.

Settling time

The strain settling time T_{CS} is the time elapsed until the error $x - x_{ref}$ resides within a given band. Again, in the case of strain based oscillations measurements $x = \varepsilon$, whereas $x_{ref} = 0$. For joint angles an error band of 0.01 degrees is used. The error band for strain based oscillations measurements amounts to $15\,\mu\mathrm{m/m}$.

B.5. Stereo camera accuracy

The theoretical accuracy of the stereo camera setup is approximated within a supervised thesis by Bürger (February 2011). The conservative assumption is that the tracking object centers are localized in the images with integer pixel accuracy. A single pixel covers a field of view with a pyramidal volume. At any point within the robot workspace the pyramidal volumes of the two cameras intersect. The intersection volume is enclosed by a cuboid, with the edges parallel to the stereo camera reference frame. The edge lengths of the cuboid represent the approximated localization error.

The computed errors along the x- and z-axes of the stereo camera frame are visualized by isometric lines in figure B.2. Within the workspace of TUDOR the conservative approximation of the absolute accuracy amounts to 3.5 to 4.5 mm along the x-axis and 3 to 8 mm along the z-axis. Despite sensor noise and segmentation errors the tracking
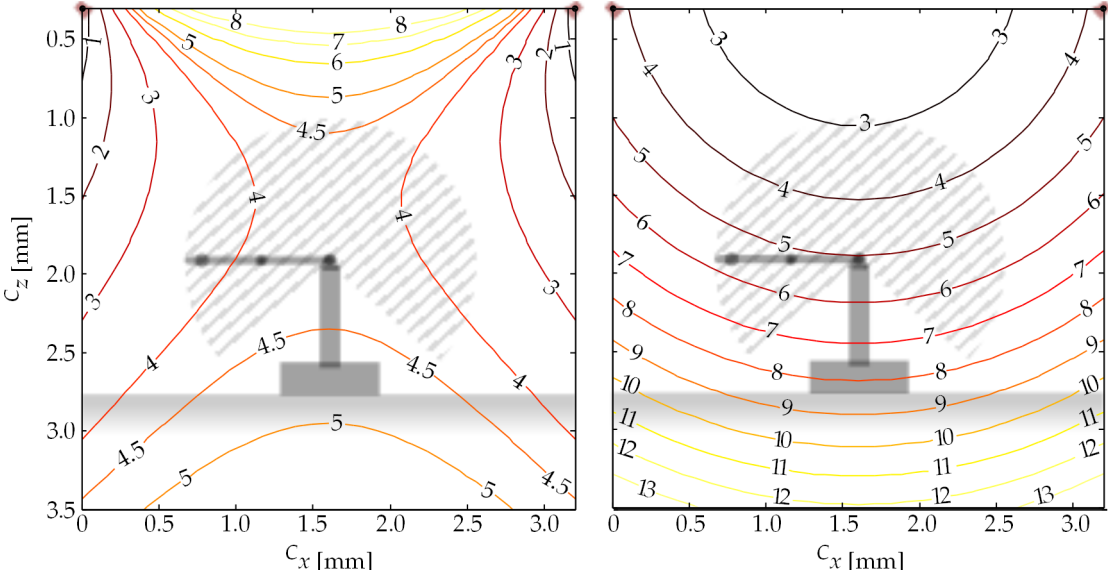
Figure B.2.: Conservative theoretical approximation of the stereo camera absolute accuracy determined by Bürger (February 2011). Isolines of the absolute error in mm along the *x*-coordinate (*left*) and the *z*-coordinate (*right*) referred to the stereo camera frame.
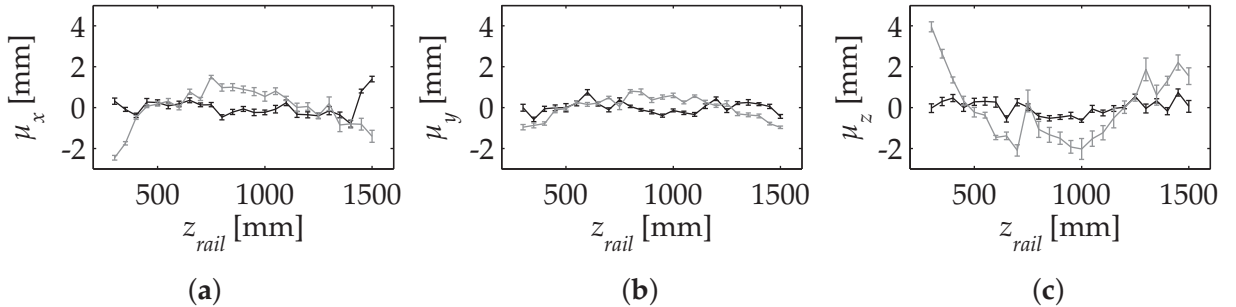

Figure B.3.: Results of experimental precision evaluation at the center (*black*) and at the border (*gray*) of the TUDOR workspace along the x-axis (**a**), y-axis (**b**) and z-axis (**c**) of the stereo camera system.

object centers are detected with subpixel accuracy. Hence, the practically observed error is smaller.

For the experimental evaluation of the measurement accuracy the tracking spheres are mounted on a slider attached to a vertical rail of 1.50 m length. The rail is placed in the center and at a distance of 0.85 m to the center along the ^1x-axis. In the latter position the rail is tangent to the robot workspace. The slider is shifted in 50 mm steps from 300 to 1500 mm above the floor. At each step 100 images are recorded. The orientation of the rail is not perfectly aligned with the axes of the stereo camera frame. Nevertheless the detected locations of the tracking spheres are supposed to lie on a straight line. The mean errors as well as the standard deviation between the measurements and the fitted straight line model are depicted in figure B.3. It is visible that inside the workspace of TUDOR the error remains within a 2 mm band for all degrees of freedom. Only outside the workspace the error in the *z*-direction grows out of this band.

B.6. Joint acceleration profile

The motion of each joint used with TUDOR is planned using the sinusoidal acceleration profile described in Wenz 2008, p. 89. A motion is subdivided into three acceleration segments. Consider a point-to-point motion with zero initial and final acceleration. The profile is given by:

$$
\ddot{\theta} = \begin{cases}
\ddot{\theta}_{max} \sin^2\left(\frac{\pi}{t_1}t\right), & 0 \leq t \leq t_1 \\
0, & t_1 \leq t \leq t_2 \\
-\ddot{\theta}_{max} \sin^2\left(\frac{\pi}{t_3-t_2}(t-t2)\right), & t_2 \leq t \leq t_3.
\end{cases}
\tag{B.6.1}
$$

The corresponding velocity profile is:

$$
\dot{\theta} = \begin{cases}
\dot{\theta}(0) + \ddot{\theta}_{max}\left(\frac{1}{2}t - \frac{t_1}{4\pi}\sin\left(\frac{2\pi}{t_1}t\right)\right), & 0 \leq t \leq t_1 \\
\dot{\theta}_{max}, & t_1 \leq t \leq t_2 \\
\dot{\theta}_{m}ax - \ddot{\theta}_{max}\left(\frac{1}{2}(t-t_2) - \frac{t_3-t_2}{4\pi}\sin\left(\frac{2\pi}{t_3-t_2}(t-t_2)\right)\right), & t_2 \leq t \leq t_3.
\end{cases}
\tag{B.6.2}
$$

$$
\theta = \begin{cases}
\theta(0) + \dot{\theta}(0)t + \ddot{\theta}_{max}\left(\frac{1}{4}t^2 + \frac{t_1^2}{8\pi^2}\left(\cos\left(\frac{2\pi}{t_1}t\right) - 1\right)\right), & 0 \leq t \leq t_1 \\
\theta(0) + \dot{\theta}_{max}t - \frac{\dot{\theta}_{max}-\dot{\theta}(0)}{2}t_1, & t_1 \leq t \leq t_2 \\
\theta(t_3) + \dot{\theta}_{max}(t-t_3) + \frac{(\dot{\theta}_{max}-\dot{\theta}(t_3))^2}{\ddot{\theta}_{max}} + \dots \\
\quad + \frac{\ddot{\theta}_{max}}{2}\left(\frac{(t_3-t_2)^2}{4\pi^2}\left(1 - \cos\left(\frac{2\pi}{t_3-t_2}(t-t_2)\right)\right) - \frac{1}{2}(t-t_2)^2\right), & t_2 \leq t \leq t_3.
\end{cases}
\tag{B.6.3}
$$

C

Supplemental Collision Experiments

In addition to the experimental collision detection results provided in section 11.3 this appendix complements blunt impacts with the balloon, sharp impacts with a stiff but fragile object as well as sharp collisions with a human arm.

C.1. Blunt impacts with a compliant object

Prior to the sharp collision impacts presented with the balloon in section 11.3 blunt collision experiments are carried out. During blunt impacts the balloon remains undamaged, even without collision detection. However, an emerging strong deformation of the balloon is clearly observed in the top right photograph and in the force level measured at the contact cube in figure C.1 (**c**). The strong deformation as well as the increasing force level is absent when the stop strategy is used (center row, right photograph). Without collision detection, the force level grows until the joint angles reach the commanded position as visible in figure C.1 (**a**).

The velocity measurements for the case with no collision detection as well as the stop strategy being enabled show a short sequence of significant over- and undershoot right after the collision time instant. Such a sequence is not observed with the blunt impacts on the rigid contact cube in figure 11.3 (**e**). It originates from the compliance of the balloon.

The effect of the admittance strategy is illustrated in the bottom row of photographs in figure C.1. Remarkably, in this case there is hardly any difference visible in the blunt impact measurements depicted in the figures C.1 (**a**) to (**b**), when compared with the corresponding sharp impact results sensor readings in figure 11.4.

Malzahn and Bertram (2013, at 2:10 min) published an online available video with this experiment.

C.2. Sharp impacts with a fragile object

Compared to the balloon, the Christmas sphere is a rather stiff object.

Without collision detection, the link with the sharpened screw penetrates the Christmas sphere. It is visible in the top right photograph of figure C.2 that at $t \approx 1.57$ s the end effector already went right through the Christmas sphere. Finally it hits the
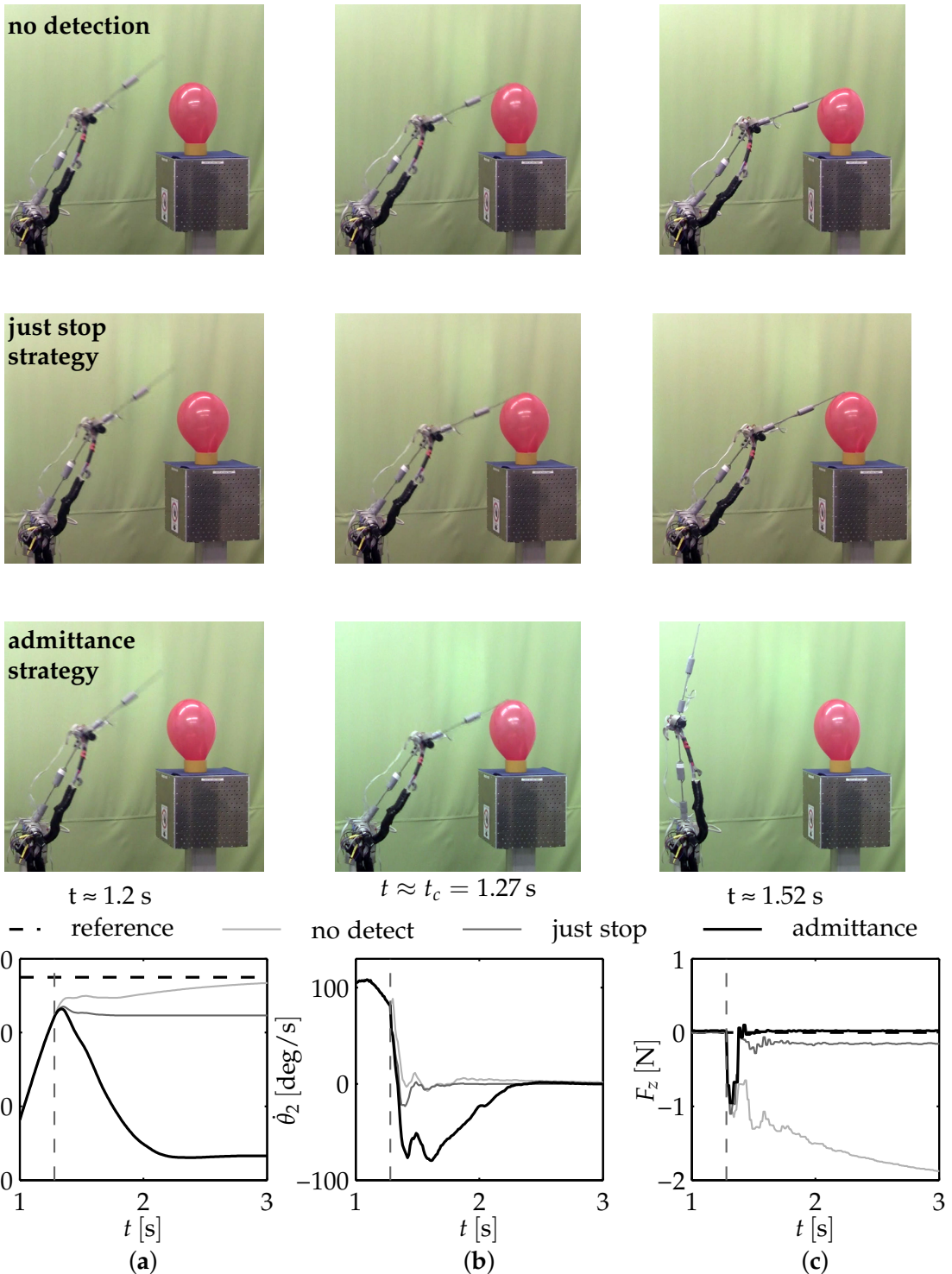
Figure C.1.: Collision detection and reaction results for *blunt* impacts with a balloon placed as *compliant* object on the contact cube. Snapshots in the absence of any collision detection (**top row**), with the stop-strategy (**second row**) as well as the admittance strategy (**third row**) before (**left column**), during (**center column**) and after (**right column**) the moment of collision. Angle (**a**) and angular velocity (**b**) for the second joint along with the normal force measured at the contact cube (**c**).
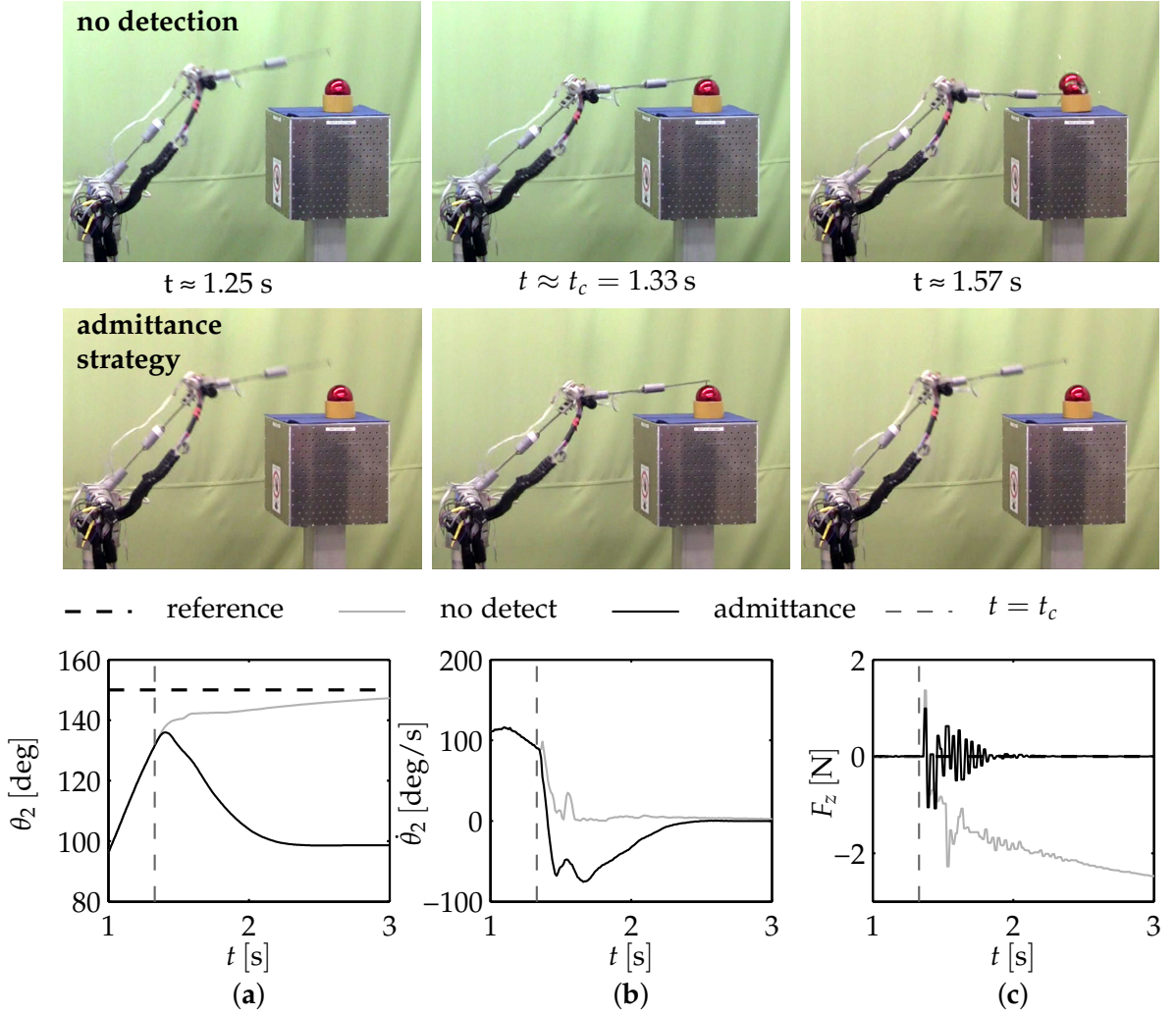
Figure C.2.: Collision detection and reaction results for sharp impacts with a Christmas ball placed as *fragile* object on the contact cube.

contact cube. At this moment, a second impact is visible in the force readings of figure C.2 (**b**). With some delay, the Christmas sphere starts burst asunder. Individual debris begin to lift into the air.

Just as before, the joint angles reach the targeted position, while the robot links absorb the contact force in their deflections.

Identical to the sharp impact experiments with the balloon, the reflex strategy saves the Christmas sphere. The measurements provided in the figures C.2 (**a**) to (**c**) are very similar to those observed with the balloon in figure 11.4. As a major difference, the spheres are made from rather thick glass. Thus, they are sturdy enough to also survive the impacts when the stop strategy is applied.

Malzahn and Bertram (2013, at 3:02 min) published an online available video of this experiment.
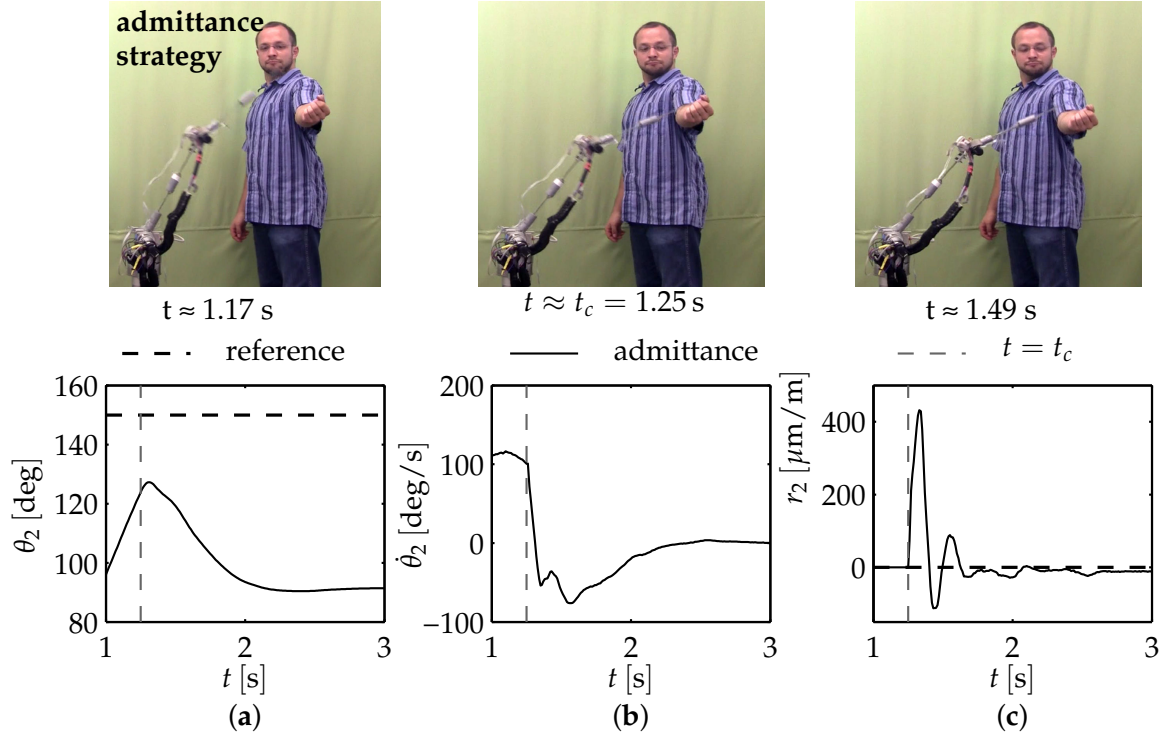
Figure C.3.: Collision detection and reaction results for sharp impacts with a human arm.

C.3. Sharp impacts on a human arm

The results obtained from the collision experiments with the balloon as well as the Christmas sphere confirm a significant reduction of the harm potential associated with the sharpened screw at the end effector. The results are convincing enough to give a demonstration where the sharp collisions are effected with a human arm. Of course, the reflex strategy is used in this scenario.

Figure C.3 shows photographs and measurements recorded during this experiment. The sequence of measurements for the second joint angle and joint angular velocity are equivalent to those obtained during the other collision experiments before. The residual r_2 is visible in figure C.3 (**c**). It instantly grows and indicates the collision right after the contact.

This way, the collision is rapidly detected and injuries to the human are properly averted. Malzahn and Bertram (2013, at 3:23 min) published an online available video with three repetitions of this experiment.

D
Steps to Deploy the Techniques

The following guideline summarizes the major steps required to deploy the techniques developed in this work.

Initial situation: The arm hardware as well as the reference sensors are set up and ready for operation.

1. Actuator identification and control: The actuator vendor commonly provides datasheets with good initial values for all parameters required to implement the controller design used in this work. With the tuned controller, the values for the individual initial parameters can be verified or refined by additional identification experiments, as done in this work.

chapter:	sensors:	parameters per joint-link-module:	#
3	current sensors, encoders	I_M, k_M, k_v, k_{PI}, t_{PI}, t_d, k_{PD}, t_{PD}, t_l	9

2. Oscillation damping: For oscillation damping the work suggest to proportionally feed the mean liberated strain measurements back to the velocity controller cascade level for each individual joint-link-module. Therefore, the FIR based high pass filter for mean liberation is tuned (see 2.2) for the desired frequency range. Next, the proportional feedback gains k_ε are determined in two steps. The first step is a careful manual tuning with determination of the stability limit $k_{\varepsilon, max}$. The second step is the automated hardware in the loop optimization of the gains as described in section 5.3.

chapters:	sensor:	parameters per joint-link-module:	#
2.2, 5	strain sensor	N_{FIR}, k_ε, $k_{\varepsilon, max}$	3

3. Kinematics learning: In order to determine the weights of the data based kinematics models, end effector positions must be recorded together with static strains and joint angles by sampling the whole workspace with different payload masses.

chapter:	sensors:	parameters per joint-link-module:	#
9.2	strain gauges, encoders, external tip position sensor (stereo camera)	weights for the forward kinematics, inverse kinematics and load estimation network	

4. Damped dynamics identification: A set of APRBS stimuli for each joint is applied to the arm. During stimulus execution the joint angles, velocities and strains are recorded. The symbolic dynamics model of the equivalent rigid arm is derived. It is reduced to the robot base dynamics parameters and brought into the regression form (10.2.8). The identified base parameters are rewritten to yield the strain referred inertia and Coriolis matrix as well as the vector of gravitational strain load.

chapter:	sensors:		parameters per joint-link-module:	#
10	encoders, sensors	strain	base dynamics parameters	≤ 11

5. Collision detection: The known damped arm dynamics allow the computation of the strain referred generalized momentum based residual. In order to reliably detect contacts without false positives the detection thresholds for each joint-link-module are determined from a statistical analysis of the strain referred generalized momenta computed on the dynamics identification data sets.

chapter:	sensors:		parameters per joint-link-module:	#
11.1	encoders, sensors	strain	$k_{I,i}$, detection thresholds (pos. and neg.)	3

6. Collision reaction: The collision reaction strategy is implemented as generic reaction admittance defined by a second order transfer function. A set of parameters for this transfer function defines one particular reaction strategy. For each joint-link-module, the parameters encode the virtual inertial characteristic, damping and spring stiffness of the reaction behavior augmented by an additional overreaction gain to realize fast reflex reactions. The parameters are found empirically and are affected by the haptic preferences of the user, who performs the tuning.

chapter:	sensor:	parameters per joint-link-module:	#
11.2	strain sensors	m_r, f_r, k_r, k_{or}	4

Bibliography

References

Parts of the material presented in this work has been originally published in conferences and journals. These publications as well as the resources by other researchers are summarized in the following list:

Adams, R. and L. Bischof (1994): Seeded region growing. In: *Transactions on Pattern Analysis and Machine Intelligence*. Vol. 16, no. 6, pp. 641–647.

Alami, R., A. Albu-Schaeffer, A. Bicchi, R. Bischoff, R. Chatila, A. d. Luca, A. d. Santis, G. Giralt, J. Guiochet, G. Hirzinger et al. (2006): Safe and dependable physical human-robot interaction in anthropic domains: State of the art and challenges. In: *IROS Workshop on pHRI*. IEEE.

Argall, B., S. Chernova, M. Veloso and B. Browning (2009): A survey of robot learning from demonstration. In: *Robotics and Autonomous Systems*. Vol. 57, no. 5, pp. 469–483.

Armstrong, B. (1989): On finding exciting trajectories for identification experiments involving systems with nonlinear dynamics. In: *The International Journal of Robotics Research*. Vol. 8, no. 6, pp. 28–48.

Bailey, T. and J. E. Ubbard (1985): Distributed piezoelectric-polymer active vibration control of a cantilever beam. In: *Journal of Guidance, Control, and Dynamics*. Vol. 8, no. 5, pp. 605–611.

Balas, M. (1978): Feedback control of flexible systems. In: *IEEE Transactions on Automatic Control*. Vol. 23, no. 4, pp. 673–679.

Bascetta, L. and P. Rocco (2006a): End-point vibration sensing of planar flexible manipulators through visual servoing. In: *Mechatronics*. Vol. 16, no. 3-4, pp. 221–232.

Bascetta, L. and P. Rocco (2006b): Two-time scale visual servoing of eye-in-hand flexible manipulators. In: *IEEE Transactions on Robotics*. Vol. 22, no. 4, pp. 818–830.

Bazaei, A. and M. Moallem (2011): Improving Force Control Bandwidth of Flexible-Link Arms Through Output Redefinition. In: *IEEE/ASME Transactions on Mechatronics*. Vol. 16, no. 2, pp. 380–386.

Becedas, J., J. Trapero, V. Feliu and H. Sira-Ramirez (2009): Adaptive controller for single-link flexible manipulators based on algebraic identification and generalized proportional integral control. In: *IEEE Transactions on Systems, Man, and Cybernetics, Part B: Cybernetics*. Vol. 39, no. 3, pp. 735–751.

Behn, C., T. Schmitz, H. Witte and K. Zimmermann (2013): Animal Vibrissae: Modeling and Adaptive Control of Bio-inspired Sensors. In: *Advances in Computational Intelligence*. Springer, pp. 159–170.

Benosman, M. and G. Le Vey (2004): Control of flexible manipulators: A survey. In: *Robotica*. Vol. 22, no. 5, pp. 533–545.

Bicchi, A. and G. Tonietti (2004): Fast and soft-arm tactics. In: *IEEE Robotics Automation Magazine*. Vol. 11, no. 2, pp. 22–33.

Billard, A., S. Calinon and F. Guenter (2006): Discriminative and adaptive imitation in uni-manual and bi-manual tasks. In: *Robotics and Autonomous Systems*. Vol. 54, no. 5, pp. 370–384.

Bona, B. and M. Indri (2005): Friction compensation in robotics: an overview. In: *44th Conference on Decision and Control and European Control Conference*, pp. 4360–4367.

Book, W. J. (1984): Recursive Lagrangian dynamics of flexible manipulator arms. In: *The International Journal of Robotics Research*. Vol. 3, no. 3, p. 87.

Book, W. J. (1990): Modeling, design, and control of flexible manipulator arms: A tutorial review. In: *29th Conference on Decision and Control*, pp. 500–506.

Book, W. J. and M. Majette (1983): Controller design for flexible, distributed parameter mechanical arms via combined state space and frequency domain techniques. In: *Journal of dynamic systems, measurement and control*. Vol. 105, no. 4, pp. 245–254.

Boscariol, P., A. Gasparetto and V. Zanotto (2010): Model predictive control of a flexible links mechanism. In: *Journal of Intelligent and Robotic Systems*. Vol. 58, no. 2, pp. 125–147.

Bouguet, J. Y. (2008): Camera calibration toolbox for Matlab.

Brent, R. P. (1972): Algorithms for minimization without derivatives. Series in Automatic Computation. Englewood Cliffs: Prentice-Hall.

Cazzulani, G., C. Ghielmetti, H. Giberti, F. Resta and F. Ripamonti (2011): Overview on the truck mounted concrete boom pump: A dynamic numerical model for active control logic definition. In: *IFAC World Congress*. Vol. 18, pp. 4232–4237.

Chaumette, F. and S. Hutchinson (2006): Visual servo control, part I: Basic approaches. In: *IEEE Robotics and Automation Magazine*. Vol. 13, no. 4, pp. 82–90.

Chaumette, F. and S. Hutchinson (2007): Visual servo control, part II: Advanced approaches. In: *IEEE Robotics and Automation Magazine*. Vol. 14, no. 1, pp. 109–118.

Chen, W. (2001): Dynamic modeling of multi-link flexible robotic manipulators. In: *Computers & Structures*. Vol. 79, no. 2, pp. 183–195.

Corke, P. I. (2011): Robotics, Vision & Control: Fundamental Algorithms in Matlab. Springer.

Devol, G. C. (1961): Programmed Article Transfer. Pat. no. 2,988,237.

Diaz, I., E. Pereira, V. Feliu and J. Cela (2010): Concurrent design of multimode input shapers and link dynamics for flexible manipulators. In: *IEEE/ASME Transactions on Mechatronics*. Vol. 15, no. 4, pp. 646–651.

Dubus, G., O. David and Y. Measson (2009): Vibration Control of a Flexible Arm for the ITER Maintenance Using Unknown Visual Features From Inside the Vessel. In: *International Conference on Intelligent Robots and Systems*. IEEE/RSJ, pp. 5697–5704.

Dukkipati, R. V. and J. Srinivas (2005): Textbook of mechanical vibration. New Delhi: Prentice-Hall of India.

Dwivedy, S. and P. Eberhard (2006): Dynamic analysis of flexible manipulators, a literature review. In: *Mechanism and Machine Theory*. Vol. 41, no. 7, pp. 749–777.

Ens, J. and P. Lawrence (1993): An investigation of methods for determining depth from focus. In: *IEEE Transactions on Pattern Analysis and Machine Intelligence*. Vol. 15, no. 2, pp. 97–108.

Feliu, J. J., V. Feliu and C. Cerrada (1999): Load adaptive control of single-link flexible arms based on a new modeling technique. In: *IEEE Transactions on Robotics*. Vol. 15, no. 5, pp. 793–804.

Feliu, V., S. Rattan and B. H. Brown (1992): Modeling and Control of Single-Link Flexible Arms With Lumped Masses. In: *Journal of dynamic systems, measurement and control*. Vol. 114, no. 1, pp. 59–69.

Flotow, A. H. v. and B. Schäfer (1986): Wave-absorbing controllers for a flexible beam. In: *Journal of Guidance, Control and Dynamics*. Vol. 9, no. 6, pp. 673–680.

Franke, R., J. Malzahn, T. Nierobisch, F. Hoffmann and T. Bertram (2009): Vibration control of a multi-link flexible robot arm with Fiber-Bragg-Grating sensors. In: *International Conference on Robotics and Automation*, pp. 3365–3370.

Freedman, B., A. Shpunt, M. Machline and Y. Arieli (2008): Depth mapping using projected patterns. Pat. no. US 2008 0240502 A1,

Frese, U., B. Bauml, S. Haidacher, G. Schreiber, I. Schaefer, M. Hahnle and G. Hirzinger (2001): Off-the-shelf vision for a robotic ball catcher. In: *IEEE/RSJ International Conference on Intelligent Robots and Systems*. Vol. 3, pp. 1623–1629.

Garcia, A. and V. Feliu (2000): Force control of a single-link flexible robot based on a collision detection mechanism. In: *Control Theory and Applications*. Vol. 147, pp. 588–595.

Garcia, A., V. Feliu and J. A. Somolinos (2001): Gauge based collision detection mechanism for a new three-degree-of-freedom flexible robot. In: *International Conference on Robotics and Automation*. Vol. 4, pp. 3853–3858.

Ge, S., H. Lee and G. Zhu (1998): Improving regulation of a single-link flexible manipulator with strain feedback. In: *IEEE Transactions on Robotics*. Vol. 14, no. 1, pp. 179–185.

German Federal Ministry of Education and Research (2007): ICT 2020 - Research for innovations. URL: http://www.bmbf.de/pub/ict_2020.pdf (visited on 24/10/12).

Giannakouris, K. (2008): Population and social conditions: Ageing characterises the demographic perspectives of the European societies. Ed. by eurostat - statistics in focus.

Guizzo, E. and E. Ackerman (2012): The rise of the robot worker. In: *IEEE Spectrum*. Vol. 49, no. 10, pp. 34–41.

Halevi, Y. (2004): Control of flexible structures governed by the wave equation using infinite dimensional transfer functions. In: *Journal of dynamic systems, measurement and control*. Vol. 127, pp. 579–588.

Halevi, Y. and C. Wagner-Nachshoni (2006): Transfer function modeling of multi-link flexible structures. In: *Journal of Sound and Vibration*. Vol. 296, no. 1-2, pp. 73–90.

Ham, R. v., T. Sugar, B. Vanderborght, K. Hollander and D. Lefeber (2009): Compliant actuator designs. In: *Robotics & Automation Magazine, IEEE*. Vol. 16, no. 3, pp. 81–94.

Hansard, M., S. Lee, O. Choi and R. Horaud (2013): Time-of-flight cameras. Springer.

Hartley, R. and A. Zisserman (2006): Multiple view geometry in computer vision. 2. ed., 4. printing. Cambridge: Cambridge Univ. Press.

Heinlein, R. A. (1957): The Door Into Summer. 1st ed. Doubleday.

Hillsley, K. L. and S. Yurkovich (1993): Vibration control of a two-link flexible robot arm. In: *Dynamics and Control.* Vol. 3, no. 3, pp. 261–280.

Hu, A. (1993): A Survey of Experiments for Modeling Verification and Control of Flexible Robotic Manipulators. In: *First Regional Conference on Aerospace Control Systems.* IEEE, pp. 344–353.

Huang, G.-B., Q.-Y. Zhu and C.-K. Siew (2004): Extreme learning machine: a new learning scheme of feedforward neural networks. In: *IEEE International Joint Conference on Neural Networks.* Vol. 2, pp. 985–990.

Huang, G.-B., Q.-Y. Zhu and C.-K. Siew (2006): Extreme learning machine: theory and applications. In: *Neurocomputing.* Vol. 70, no. 1, pp. 489–501.

Hutchinson, S., G. D. Hager and P. I. Corke (1996): A tutorial on visual servo control. In: *IEEE Transactions on Robotics.* Vol. 12, no. 5, pp. 651–670.

Isermann, R. and M. Münchhof (2011): Identification of dynamic systems: An introduction with applications. Heidelberg and New York: Springer.

ISO 9283, E. N. (1999): Industrieroboter: Leistungskenngrößen und zugehörige Prüfmethoden. In: *Beuth-Verlag, Berlin.*

Jiang, X., A. Konno and M. Uchiyama (2007): A Vision-Based Endpoint Trajectory and Vibration Control for Flexible Manipulators. In: *International Conference on Robotics and Automation*, pp. 3427–3432.

Khalil, W. and E. Dombre (2004): Modeling, identification and control of robots. Butterworth-Heinemann.

Kharitonov, A., N. Zimmert and O. Sawodny (2007): Active Oscillation Damping of the Fire–Rescue Turntable Ladder. In: *International Conference on Control Applications.* IEEE, pp. 391–396.

Khatib, O., K. Yokoi, O. Brock, K. Chang and A. Casal (1999): Robots in human environments: Basic autonomous capabilities. In: *The International Journal of Robotics Research.* Vol. 18, no. 7, pp. 684–696.

Khorrami, F., I. Zeinoun and E. Tome (1993): Experimental results on active control of flexible-link manipulators with embedded piezoceramics. In: *International Conference on Robotics and Automation*, pp. 222–227.

Konno, A., M. Uchiyama and M. Murakami (1997): Configuration-dependent vibration controllability of flexible-link manipulators. In: *The International Journal of Robotics Research.* Vol. 16, no. 4, p. 567.

Konno, A. and M. Uchiyama (1996): Modeling of a flexible manipulator dynamics based upon Holzer's model. In: *International Conference on Intelligent Robots and Systems.* Vol. 1, pp. 223–229.

Korayem, M., R. Haghighi, A. Korayem, A. Nikoobin and A. Alamdari (2010): Determining maximum load carrying capacity of planar flexible-link robot: closed-loop approach. In: *Robotica.* Vol. 28, no. 7, pp. 959–973.

Krauss, R. (2012): Computationally efficient modeling of flexible robots using the transfer matrix method. In: *Journal of Vibration and Control.* Vol. 18, no. 5, pp. 596–608.

Krauss, R., W. J. Book et al. (2010): Transfer Matrix Modeling of Systems With Non-collocated Feedback. In: *Journal of dynamic systems, measurement and control*. Vol. 132, no. 6, pp. 13011–130111.

Krauss, R. W. (2006): An Improved Technique for Modeling and Control of Flexible Structures. Phd thesis. Atlanta: Georgia Institute of Technology.

Li, Y. F. and X. B. Chen (2002): End-point sensing and state observation of a flexible-link robot. In: *IEEE/ASME Transactions on Mechatronics*. Vol. 6, no. 3, pp. 351–356.

Luca, A. d. and R. Mattone (2004): An adapt-and-detect actuator FDI scheme for robot manipulators. In: *International Conference on Robotics and Automation*. Vol. 5, pp. 4975–4980.

Luca, A. d. and R. Mattone (2005): Sensorless robot collision detection and hybrid force/motion control. In: *International Conference on Robotics and Automation*, pp. 999–1004.

Luca, A. d., S. Panzieri and G. Ulivi (1998): Stable inversion control for flexible link manipulators. In: *International Conference on Robotics and Automation*. Vol. 1, IEEE/RSJ, pp. 799–805.

Luca, A. d. and B. Siciliano (1989): Trajectory control of a non-linear one-link flexible arm. In: *International Journal of Control*. Vol. 50, no. 5, pp. 1699–1715.

Luca, A. d. and B. Siciliano (1991): Closed-form dynamic model of planar multilink lightweight robots. In: *IEEE Transactions on Systems, Man and Cybernetics*. Vol. 21, no. 4, pp. 826–839.

Luca, A. d., A. Albu-Schaffer, S. Haddadin and G. Hirzinger (2006): Collision detection and safe reaction with the DLR-III lightweight manipulator arm. In: *International Conference on Intelligent Robots*. IEEE/RSJ, pp. 1623–1630.

Luo, Z.-H (1993): Direct strain feedback control of flexible robot arms: new theoretical and experimental results. In: *IEEE Transactions on Automatic Control*. Vol. 38, no. 11, pp. 1610–1622.

Luo, Z.-H. and B. Guo (1995): Further theoretical results on direct strain feedback control of flexible robot arms. In: *IEEE Transactions on Automatic Control*. Vol. 40, no. 4, pp. 747–751.

Mace, B. R. (1984): Wave reflection and transmission in beams. In: *Journal of Sound and Vibration*. Vol. 97, no. 2, pp. 237–246.

Malzahn, J. (2008): Modellierung und Regelung eines mehrgliedrigen elastischen Roboterarms. Diploma Thesis. Dortmund: TU Dortmund.

Malzahn, J. and T. Bertram (2014): Fractional Order Strain Feedback for Oscillation Damping of a Multi-Elastic-Link Arm Under Gravity. In: *45th International Symposium on Robotics and 8th German Conference on Robotics*, accepted.

Malzahn, J., A. S. Phung and T. Bertram (2012a): A Multi-Link-Flexible Robot Arm Catching Thrown Balls. In: *7th German Conference on Robotics*, pp. 411–416.

Malzahn, J., A. S. Phung and T. Bertram (2012b): Predictive delay compensation for camera based oscillation damping of a multi link flexible robot. In: *Intelligent Robotics and Applications*. Springer, pp. 93–102.

Malzahn, J., A. S. Phung and T. Bertram (2012c): Scene adaptive RGB-D based oscillation sensing for a multi flexible link robot arm in unstructured dynamic environments. In: *International Conference on Intelligent Robots and Systems*, pp. 1017–1022.

Malzahn, J., R. F. Reinhart and T. Bertram (2014): Dynamics Identification of a Damped Multi Elastic Link Robot Arm under Gravity. In: *International Conference on Robotics*, accepted.

Malzahn, J., M. Ruderman, A. Phung, F. Hoffmann and T. Bertram (2010a): Input shaping and strain gauge feedback vibration control of an elastic robotic arm. In: *Conference on Control and Fault-Tolerant Systems*, pp. 672–677.

Malzahn, J., A. S. Phung, R. Franke, F. Hoffmann and T. Bertram (2010b): Markerless Visual Vibration Damping of a 3-DOF Flexible Link Robot Arm. In: *41st International Symposium on Robotics (ISR) and 6th German Conference on Robotics (ROBOTIK)*, pp. 401–408.

Malzahn, J., A. Phung, F. Hoffmann, M. Ruderman and T. Bertram (2011a): Modellfreie Schwingungsdämpfung eines eingliedrigen elastischen Roboterarms unter Gravitationseinfluss. In: *Fachtagung Mechatronik*. Ed. by T. Bertram, B. Corves and K. Janschek. TU Dresden, pp. 89–94.

Malzahn, J., A. S. Phung, F. Hoffmann and T. Bertram (2011b): Vibration control of a multi-flexible-link robot arm under gravity. In: *International Conference on Robotics and Biomimetics*, pp. 1249–1254.

Malzahn, J., A. S. Phung, F. Hoffmann and T. Bertram (2012): Bildbasierte Regelung eines gliedelastischen Roboterarms mit einem RGB-D-Sensor. In: *at-Automatisierungstechnik*. Vol. 60, no. 5, pp. 246–259.

Mansour, T., X. Jiang, A. Konno and M. Uchiyama (2008): Experimental verification on vibration suppression of a flexible manipulator using MPID controller. In: *International Conference on Robotics and Automation*. IEEE, pp. 2896–2901.

Meirovitch, L. (2001): Fundamentals of vibrations. Boston: McGraw-Hill.

Miersch, L., W. Hanke, S. Wieskotten, F. D. Hanke, J. Oeffner, A. Leder, M. Brede, M. Witte and G. Dehnhardt (2011): Flow sensing by pinniped whiskers. In: *Philosophical Transactions of the Royal Society B: Biological Sciences*. Vol. 366, no. 1581, pp. 3077–3084.

Moallem, M. and R. V. Patel (2001): Vibration control of flexible-link manipulators using generalized output redefinition. In: *International Symposium on Computational Intelligence in Robotics and Automation*, pp. 23–28.

Singer, Singhose and Seering (1999): Comparison of Filtering Methods for Reducing Residual Vibration. In: *European Journal of Control*. Vol. 5, no. 2, pp. 208–218.

O'Connor, W. J. (2007a): Theory of wave analysis of lumped flexible systems. In: *American Control Conference*, pp. 4215–4220.

O'Connor, W. J. (2007b): Wave-based analysis and control of lump-modeled flexible robots. In: *IEEE Transactions on Robotics*. Vol. 23, no. 2, pp. 342–352.

O'Connor, W. J. and L. Donogh (1998): Position control of flexible robot arms using mechanical waves. In: *Journal of dynamic systems, measurement and control*. Vol. 120, no. 3, pp. 334–339.

O'Connor, W. J., F. La Ramos de Flor, D. McKeown and V. Feliu (2009): Wave-based control of non-linear flexible mechanical systems. In: *Nonlinear Dynamics*. Vol. 57, no. 1, pp. 113–123.

Oliensis, J. (1999): A multi-frame structure-from-motion algorithm under perspective projection. In: *International Journal of Computer Vision*. Vol. 34, no. 2-3, pp. 163–192.

Phung, A. S., J. Malzahn, F. Hoffmann and T. Bertram (2011a): Data based kinematic model of a multi-flexible-link robot arm for varying payloads. In: *International Conference on Robotics and Biomimetics*, pp. 1255–1260.

Pisoni, A. C., C. Santolini, D. E. Hauf and S. Dubowsky (1995): Displacements in a Vibrating Body by Strain Gage Measurements. In: *13th International Conference on Modal Analysis*. Vol. 2460, Society for Experimental Mechanics, p. 119.

Podlubny, I., I. Petras, B. M. Vinagre, P. O'Leary and L. Dorcak (2002): Analogue realizations of fractional-order controllers. In: *Nonlinear Dynamics*. Vol. 29, no. 1-4, pp. 281–296.

Presse, C. and M. Gautier (1993): New criteria of exciting trajectories for robot identification. In: *IEEE International Conference on Robotics and Automation*, pp. 907–912.

Pridgen, B., E. Maleki, W. Singhose, W. Seering, U. Glauser and L. Kaufmann (2011): A small-scale cherrypicker for experimental and educational use. In: *American Control Conference*, pp. 681–686.

Rong, B., X. Rui, G. Wang and F. Yang (2010): Discrete time transfer matrix method for dynamics of multibody system with real-time control. In: *Journal of Sound and Vibration*. Vol. 329, no. 6, pp. 627–643.

Santis, A. d., B. Siciliano, A. d. Luca and A. Bicchi (2008): An atlas of physical human–robot interaction. In: *Mechanism and Machine Theory*. Vol. 43, no. 3, pp. 253–270.

Sawada, H., H. Ueno, M. Oda, S. Matunaga and K. Konoue (2005): Input Shaping Experiment for Damping Vibration in Manual Operation of a Large Robotic Arm. In: *Proceedings of The 8th International Symposium on Artificial Intelligence, Robotics, and Automation in Space, Sept. 5*. Vol. 8,

Schröder, D. (2009): Elektrische Antriebe - Regelung von Antriebssystemen. 3rd ed. Berlin and Heidelberg: Springer Berlin Heidelberg.

Sciavicco, L. and B. Siciliano (2001): Modelling and Control of Robot Manipulators. Second. Berlin and Germany: Springer.

Scott, M. A., M. G. Gilbert and M. E. Demeo (1993): Active Vibration Damping of the Space Shuttle Remote Manipulator System. In: *Journal of Guidance, Control and Dynamics*. Vol. 16, no. 2, pp. 275–280.

Singhose, W. (2009): Command shaping for flexible systems: A review of the first 50 years. In: *International Journal of Precision Engineering and Manufacturing*. Vol. 10, no. 4, pp. 153–168.

Subbarao, M. and G. Surya (1994): Depth from defocus: a spatial domain approach. In: *International Journal of Computer Vision*. Vol. 13, no. 3, pp. 271–294.

Subudhi, B. and A. Morris (2009): Soft computing methods applied to the control of a flexible robot manipulator. In: *Applied Soft Computing*. Vol. 9, no. 1, pp. 149–158.

Swain, M. J. and D. H. Ballard (1990): Indexing via color histograms. In: *Third International Conference on Computer Vision*, pp. 390–393.

Swevers, J., W. Verdonck and J. d. Schutter (2007): Dynamic model identification for industrial robots. In: *IEEE Control Systems Magazine*. Vol. 27, no. 5, pp. 58–71.

Takyar, M. S. and T. T. Georgiou (2007): The fractional integrator as a control design element. In: *46th Conference on Decision and Control*, pp. 239–244.

Tao, W. M., M. J. Zhang, M. Liu and X. P. Yun (2006): Residual Vibration Analysis and Suppression for SCARA Robots in Semiconductor Manufacturing. In: *International Journal of Intelligent Control and Systems*. Vol. 11, no. 2, pp. 97–105.

Theodore, R. J. and A. Ghosal (1995): Comparison of the assumed modes and finite element models for flexible multilink manipulators. In: *The International Journal of Robotics Research*. Vol. 14, no. 2, pp. 91–111.

TNS Opinion and Social (2012): Public Attitudes Towards Robots: Report of the Special EB 382, Wave EB 77.1. Ed. by European Commission.

Tokhi, O. and K. A. Azad (2008): Flexible robot manipulators: Modelling, simulation and control. London: Inst. of Engineering and Technology.

Tsujisawa, T. and W. J. Book (1989): A reduced order model derivation for lightweight arms with a parallel mechanism. In: *IEEE International Conference on Robotics and Automation*, pp. 728–735.

Vaughan, J., A. Yano and W. Singhose (2008): Comparison of robust input shapers. In: *Journal of Sound and Vibration*. Vol. 315, no. 4, pp. 797–815.

Vepa, R. (2010): Dynamics of Smart Structures. Wiley.

Wang, D. and M. Vidyasagar (1991): Transfer functions for a single flexible link. In: *The International Journal of Robotics Research*. Vol. 10, no. 5, pp. 540–549.

Wenz, M. (2008): Automatische Konfiguration der Bewegungssteuerung von Industrierobotern. Dissertation. Karlsruhe: University Karlsruhe.

Whitney, D. E., W. J. Book and P. M. Lynch (1974): Design and control considerations for industrial and space manipulators. In: *15th Joint Automatic Control Conference, Austin (USA)*, pp. 591–598.

Wöhler, C. (2013): 3D computer vision: Efficient methods and applications. 2nd ed. X.media.publishing. London and New York: Springer.

Xuming Luan (2001): Experimental Investigation of Photonic Mixer Device and Development of TOF 3D Ranging Systems Based on PMD Technology. Dissertation. Siegen: Universität Siegen.

Zeng, H. (1999): Modeling, Identification and Control of a Multi-Link Lightweight Manipulator. Dissertation. Bochum: Ruhr-University Bochum.

Zimmert, N., A. Kharitonov and O. Sawodny (2008): A new Control Strategy for Trajectory Tracking of Fire–Rescue Turntable Ladders. In: *Proceedings of the 17th IFAC World Congress*, pp. 869–874.

Additional Publications

The research activities during preparation of this work have reached beyond the actual scope of this thesis. This lead to the authorship and co-authorship in the following additional publications:

Kracht, M., J. Malzahn, F. Hoffmann and T. Bertram (2010): Image Based Visual Servoing For Lane Keeping Assistance. In: *FISITA 2010 World Automotive Congress*. FISITA.

Malzahn, J. (February 2012): Einsatz eines RGB-D-Sensors zur schwingungsgedämpften Positionierung eines gliedelastischen Roboterarms. Boppard.

Malzahn, J. (October 2013): Link Elasticity in a Robot Arm: From a Problem to an Opportunity. München.

Malzahn, J., R. Franke, F. Hoffmann and T. Bertram (2009): Modellierung und Regelung eines mehrgliedrigen elastischen Roboterarms. In: *Automation 2009*. Vol. 2067, VDI-Berichte. VDI-Verl., pp. 153–157.

Nierobisch, T., K. V. Patel, J. Malzahn, F. Hoffmann and T. Bertram (2007): Rapid Prototyping of Visual Servoing Controllers with Virtual Reality. In: *System integration*. Ed. by E. Kallenbach. Wiss.-Verl. Thüringen.

Phung, A. S., J. Malzahn, F. Hoffmann and T. Bertram (2010): Lernen durch Demonstration und Kollisionsvermeidung mit Dynamischen Bewegungsprimitiven. In: *20. Workshop Computational Intelligence*. Ed. by F. Hoffmann. Vol. 33, KIT Scientific Pub., pp. 250–263.

Phung, A. S., J. Malzahn, F. Hoffmann and T. Bertram (2011b): Datenbasiere Modellierung der Kinematik eines dreigliedrigen elastischen Roboterarms. In: *21. Workshop Computational Intelligence*. Ed. by F. Hoffmann. Vol. 21, KIT Scientific Publishing, pp. 187–202.

Phung, A. S., J. Malzahn, F. Hoffmann and T. Bertram (2012): Tool centered learning from demonstration for robotic arms with visual feedback. In: *International Conference on Robotics and Biomimetics*, pp. 1117–1122.

Phung, A., J. Malzahn, F. Hoffmann and T. Bertram (2011d): Get Out of the Way-Obstacle Avoidance and Learning by Demonstration for Manipulation. In: *IFAC World Congress*. Vol. 18, pp. 11514–11519.

Published Software and Media

During preparation of this work the following media and sources have been published online under open licenses:

Malzahn, J. (2013): CodeGenerator-Module for the Robotic Toolbox by Peter Corke.

Malzahn, J., R. Balachandran and T. Bertram (2013): Video: Experiments on force control of a multi-fexible-link robot. URL: http://youtu.be/AJPZjF7HDxY (visited on 12/12/13).

Malzahn, J. and T. Bertram (2013): Video: Oscillation Damping, Collision Detection and Reaction with a Multi-Elastic-Link Robot Arm. URL: http://youtu.be/kJPuenyxeps (visited on 12/12/13).

Malzahn, J., A. S. Phung, F. Hoffmann and T. Bertram (2011c): Video: A multi-flexible-link robot arm under gravity catching thrown soft-balls. URL: http://youtu.be/P4_i_kGt2jA (visited on 12/12/13).

Malzahn, J., A. S. Phung, F. Hoffmann and T. Bertram (2011d): Video: Initial visual servoing experiments with a multi-flexible-link arm. URL: http://youtu.be/V2NnEU6yGEA (visited on 12/12/13).

Phung, A. S., J. Malzahn, F. Hoffmann and T. Bertram (2011c): Video: Tip position control of a multi-flexible-link robot arm for varying payloads using neural networks. URL: http://youtu.be/VQZ1FF3wAxA (visited on 12/12/13).

Supervised theses

A number of ideas grown during this work emerged from discussions in the context of the following supervised theses:

Balachandran, R. (November 2012): Experimental Evaluation of Wave-Based Concepts for Oscillation free Motion Control of a Flexible Link Robot Arm. Masterhtesis. Dortmund: Technische Universität Dortmund.

Breitenbach, T. (September 2009): Bildbasierte Regelung und Schwingungsdämpfung eines mehrgliedrigen elastischen Roboterarms. Diploma Thesis. Dortmund: Technische Universität Dortmund.

Bürger, F. (February 2011): Entwicklung eines kamerabasierten Messsystems zur 3D-Endeffektorlokalisierung für einen elastischen Roboterarm. Studienarbeit. Dortmund: Technische Universität Dortmund.

Bürger, F. (February 2012): Echtzeit-Schätzung der Endeffektor-Eigenbewegung eines gliedelastischen Roboterarms mittels einer 3D-Kamera. Diploma Thesis. Dortmund: Technische Universität Dortmund.

Gorczak, P. (November 2012): Fusion von RGB-D- und Inertial-Sensorik zur örtlich konzentrierten Schwingungsmessung an einem gliedelastischen Roboterarm unter Gravitationseinfluss. Bachelorthesis. Dortmund: Technische Universität Dortmund.

Kappen, J. (October 2012): Gravitationskompensation eines gliedelastischen Roboterarms. Bachelorthesis. Dortmund: Technische Universität Dortmund.

Koop, A. (May 2011): Adaptive Schwingungsdämpfung eines elastischen Roboterarms unter Gravitationseinfluss. Studienarbeit. Dortmund: Technische Universität Dortmund.

Koop, A. (October 2013): Physische Interaktion mit einem konventionellen Industrieroboter auf Basis verteilter Dehnungs-Sensorik. Diploma Thesis. Dortmund: Technische Universität Dortmund.

Sapadinski, A. (October 2011): Sensitivitätsanalyse für die Dynamik eines gliedelastischen Roboterarms unter Gravitationseinfluss. Bachelorthesis. Dortmund: Technische Universität Dortmund.

Wissing, C. (October 2013): Dual-Quaternionen zur Schätzung der Kamera Eigenbewegung aus RGB-D-Bildfolgen. Masterthesis. Dortmund: Technische Universität Dortmund.

Zimmert, M. (August 2010): 2D-Bildbasierte Regelung zur Realisierung eines Spurhalteassistenten für Kraftfahrzeuge. Studienarbeit. Dortmund: Technische Universität Dortmund.